

EFFECT OF POSTURE ON LOADING IN THE ANKLE USING AN  
FE MODEL

EVALUATION OF THE LOAD PATH THROUGH THE  
FOOT/ANKLE COMPLEX IN VARIOUS POSTURES  
THROUGH CADAVERIC AND FINITE ELEMENT MODEL  
TESTING

By CHRIS SMOLEN, B.Eng.

A Thesis Submitted to the School of Graduate Studies in Partial Fulfilment of the  
Requirements for the Degree Master of Applied Science

McMaster University © Copyright by Chris Smolen, September 2015

McMaster University Master of Applied Science (2015) Hamilton, Ontario (Mechanical Engineering)

TITLE: Evaluation of the Load Path Through the Foot/Ankle Complex in Various Postures Through Cadaveric and Finite Element Model Testing

AUTHOR: Chris Smolen, B.Eng.

SUPERVISOR: Cheryl E. Quenneville, B.Sc., M.E.Sc., Ph.D

NUMBER OF PAGES: xxii, 232

## **LAY ABSTRACT**

Ankle fractures are common occurrences that can lead to severe disability. Safety evaluations of the lower leg are often performed using computer models in a neutral ankle posture, which may underestimate the fracture tolerance in altered postures. The purpose of this study was to develop a computer model of the ankle that accounts for these changes.

A cadaveric leg was used to determine how the locations of and strains in the bones of the foot and ankle varied as ankle posture was adjusted. A computer model of the lower leg and ankle was developed, and its accuracy was evaluated by comparison with the experimental results.

The least vulnerable posture was neutral, and the hindfoot bones were the most likely to experience fracture in all postures. This model can be used in the future to evaluate new protective systems and develop comprehensive injury criteria for these altered postures.

## **ABSTRACT**

The foot/ankle complex (particularly the hindfoot) is frequently injured in a wide array of debilitating events, such as car crashes. Numerical models have been used to assess injury risk, but most are minimally validated and do not account for variations in ankle posture that frequently occur during these events. The purpose of this study was to develop an accurate finite element (FE) model of the foot and ankle that accounts for these positional changes.

The bone positions and load path in the foot and ankle were quantified throughout its natural range of motion. CT scans were taken of a male cadaveric leg in five postures in which fractures are commonly reported, while strains were recorded by strain gauges attached to the hindfoot bones in response to quasi-static, sub-failure loading. Substantial variations in bone displacements, rotations and strains were observed for all postures tested, highlighting the need for an FE model that accounts for these positional changes.

The CT scans were used as the basis of an FE model of the foot and ankle that was developed using TrueGrid<sup>®</sup> and LS-Dyna<sup>®</sup> software. The model met rigorous mesh quality criteria, and its properties were optimized to best represent the experimental plantar tissue compression and surface strains. The model was evaluated by comparing its bone position and strain responses to the experimental results in each posture.

The fracture thresholds and locations in each posture were estimated and were similar to those reported in the literature. The least vulnerable posture was neutral, and the talus and calcaneus exhibited the lowest fracture thresholds in all postures.

This work will be useful in developing improved injury limits for the ankle and postural guidelines to minimize injury. The model can be used to evaluate new protective systems to reduce the occurrence of lower leg injuries.

## **ACKNOWLEDGEMENTS**

First, I would like to thank my supervisor Dr. Quenneville for her guidance and support. She always remained optimistic, even during moments of frustration when things were not working as intended, and that, in turn, inspired me to stay positive and keep working at the problem until it was resolved. I also appreciate the very detailed feedback she would always provide on my writing. I cannot imagine how many hours she must have spent reading through the numerous drafts of my very long thesis, with a sometimes overwhelming (but always welcome!) number of comments and corrections written on every page.

I would also like to express my sincere gratitude to Dr. Tom Chow for his help in performing the CT scans and setting up the test frame in the CT scanner, and to Dr. Harjeet Ghandi for his assistance during the dissection of the specimen. These two men were a pleasure to work with and were invaluable to the completion of this thesis.

A big thanks to the machine shop guys: John, Ron, Mike and Mark, for offering great design advice and for bringing my machining abilities from nonexistent to competent. I would always look forward to spending a day in the machine shop learning something new and creating something cool, while shooting the breeze with the guys and listening to the radio.

A special thanks to my lab mates past and present: John, Vivega, Alberto and Avery, for making every day fun, as well as the lifelong friends I made outside the lab: Vicky, Salomon and Barnabus. Every single one of you has made the last two years a fantastic experience.

I must also acknowledge my two sources of funding: McMaster University and the Ontario Graduate Scholarship for making graduate school possible for me.

Last but not least, I would like to thank my family: Mom, Dad and Steph, for their unwavering support and understanding while I've been away at school for the last two years. I missed all of you immensely and I am looking forward to coming back home and being able to see you every day.

## TABLE OF CONTENTS

Descriptive Note .....	ii
Lay Abstract.....	iii
Abstract.....	iv
Acknowledgements.....	vi
Table of Contents .....	viii
List of Tables .....	xiv
List of Figures .....	xv
List of Abbreviations and Symbols.....	xix
Declaration of Academic Achievement .....	xxii
<b>CHAPTER 1 – Introduction .....</b>	<b>1</b>
1.1 Motivation.....	1
1.2 Anatomy of the Foot and Ankle .....	3
1.3 Bone Structure and Material Properties.....	6
1.4 Mechanisms of Foot and Ankle Injury .....	10
1.5 Experimental Injury Assessment of the Lower Leg .....	14
1.5.1 Injury Assessment in the Neutral Posture.....	15
1.5.2 Injury Assessment with Variation in Posture.....	16
1.6 Finite Element Analysis.....	17
1.7 Previous Finite Element Simulations of the Foot and Ankle .....	21
1.7.1 Tannous and Bandak, 1996, 2001 .....	21

1.7.2	Iwamoto et al., 2005.....	22
1.7.3	Shin et al., 2012 .....	24
1.7.4	Dong et al., 2013.....	26
1.8	Critique of Previous Finite Element Models of the Lower Limb.....	28
1.9	Overview of Validation Methods for Lower Limb Models.....	30
1.10	Strain Gauges.....	31
1.11	Study Rationale and Overview .....	33
1.12	Objectives and Hypotheses.....	34
1.13	References.....	35
<b>CHAPTER 2 – Cadaveric Testing.....</b>		<b>42</b>
2.1	Introduction.....	42
2.2	Methods .....	43
2.2.1	Specimen Preparation – Dissection .....	43
2.2.2	Specimen Preparation – Strain Gauge Selection .....	45
2.2.3	Specimen Preparation – Strain Gauge Placement.....	46
2.2.4	Specimen Preparation – Potting Procedure.....	51
2.2.5	Test Frame Construction.....	54
2.2.5.1	Design Objectives.....	54
2.2.5.2	Ankle Positioner .....	54
2.2.5.3	Test Frame .....	56
2.2.5.4	Ankle Positioner Modifications .....	60
2.2.5.5	Finite Element Stress Analysis .....	61

2.2.6	TESTING OF THE SPECIMEN .....	62
2.2.6.1	Neutral Posture .....	62
2.2.6.2	Non-Neutral Postures.....	66
2.2.7	Coordinate System Development and Data Analysis .....	67
2.3	Results.....	71
2.3.1	Bone Positions .....	71
2.3.2	Strains .....	73
2.4	Discussion.....	77
2.5	References.....	88
<b>CHAPTER 3 – Finite Element Model Development .....</b>		<b>91</b>
3.1	Introduction.....	91
3.2	Methods .....	92
3.2.1	Acquisition of Model Geometry .....	92
3.2.2	Mesh Generation.....	98
3.2.2.1	Meshing Techniques .....	98
3.2.2.2	Meshing of the Talus and Calcaneus .....	103
3.2.2.3	Meshing of the Fibula.....	106
3.2.2.4	Meshing of the Heel/Foot Pad .....	108
3.2.2.5	Mesh quality Evaluation .....	109
3.2.2.6	Meshing of the Midfoot/Forefoot Bones .....	111
3.2.3	Tibial Alignment.....	111
3.2.4	Finite Element Model Setup .....	114

3.2.4.1	Software Overview .....	114
3.2.4.2	Boundary Conditions and Contact.....	114
3.2.4.3	Bone Material Property Assignment .....	117
3.2.4.4	Ligament Positioning and Material Property Assignment....	118
3.2.4.5	Foot/Heel Pad Material Property Assignment.....	123
3.3	Results.....	123
3.3.1	Mesh Statistics and Evaluation .....	123
3.3.2	Tibial Alignment.....	127
3.3.3	Shell Thickness .....	127
3.3.4	Final Lower Leg Model .....	127
3.4	Discussion.....	131
3.5	References.....	136
<b>CHAPTER 4 – Model Verification and Injury Prediction .....</b>		<b>140</b>
4.1	Introduction.....	140
4.2	Methods .....	142
4.2.1	Tuning of Material Properties.....	142
4.2.2	Investigation of Friction Factor Sensitivity .....	143
4.2.3	Verification of Quasi-Static Strain Rates.....	143
4.2.4	Simulation with Original Tibial Geometry.....	144
4.2.5	Adjustment of Ankle Posture.....	145
4.2.6	Comparison of Simulation and Experiment.....	146
4.2.7	Injury Prediction .....	148

4.3	Results.....	148
4.3.1	Tuning of Material Properties.....	148
4.3.2	Investigation of Friction Factor Sensitivity .....	151
4.3.3	Verification of Quasi-Static Strain Rates.....	151
4.3.4	Effect of Original Tibial Geometry.....	155
4.3.5	Neutral Posture.....	155
4.3.6	Inversion–External Rotation .....	158
4.3.7	Eversion–External Rotation .....	161
4.3.8	Plantarflexion.....	165
4.3.9	Dorsiflexion-Inversion.....	165
4.3.10	Midfoot/Forefoot Bone Positions .....	169
4.3.11	Injury Prediction .....	172
4.4	Discussion.....	176
4.4.1	Heel Pad Properties.....	178
4.4.2	Bone Properties.....	179
4.4.3	Friction Factor Sensitivity.....	180
4.4.4	Strain Rates .....	180
4.4.5	Original Tibial Geometry.....	182
4.4.6	General Model Evaluation .....	184
4.4.7	Similarities and Differences Among All Postures .....	188
4.4.8	Talo-Crural and Talo-Calcaneal Joint Behaviour .....	190
4.4.9	Midfoot/Forefoot Bone Positions .....	192

4.4.10 Injury Prediction .....	194
4.5 References.....	200
<b>CHAPTER 5 – General Discussion and Conclusions .....</b>	<b>203</b>
5.1 Summary.....	203
5.2 Strengths and Limitations .....	205
5.3 Future Directions .....	208
5.4 Significance .....	211
5.5 References.....	212
<b>APPENDICES .....</b>	<b>213</b>
Appendix A – Glossary of Medical Terms .....	214
Appendix B – Estimated Radii of Curvature .....	218
Appendix C – Strain Gauge Attachment Protocol .....	219
Appendix D – Technical Drawings for Test Frame .....	220
Appendix E – Full Strain Table .....	230
Appendix F – Full Euler Angle and Displacement Tables .....	231
Appendix G – Previously-Validated Tibia Mesh Evaluation.....	232

## LIST OF TABLES

Table 2.1: Repeatability of Neutral Posture and Comparison with the Final Trial.....	72
Table 2.2: Maximum Euler Angles and Displacements of the Chosen Origin .....	72
Table 3.1: Tibia and Fibula Ligament Properties.....	119
Table 3.2: Calcaneus, Talus and Midfoot Bone Ligament Properties .....	121
Table 3.3: Forefoot Ligament Properties .....	122
Table 3.4: Jacobian Ranges and Means .....	125
Table 3.5: Angular Deviation Range and Mean.....	125
Table 3.6: Aspect Ratio Range and Mean.....	126
Table 4.1: Maximum Strains and Strain Rates in Each Bone for Short and Long Runs .....	154
Table 4.2: Maximum Distances between Simulated and Experimental Forefoot and Midfoot Bones at Each Ankle Posture.....	171
Table 4.3: Maximum Strain Locations in the Hindfoot for all Tested Postures .....	174
Table B.1: Estimated Radii of Curvature at the Strain Gauge Locations .....	218
Table E.1: Principal Strains and Direction of Principal Strain.....	230
Table F.1: Experimental Euler Angles and Displacements of the Talus and Calcaneus .....	231

## LIST OF FIGURES

Figure 1.1: Lower Leg Anatomy.....	4
Figure 1.2: Ligaments of the Medial Foot and Ankle .....	5
Figure 1.3: Foot and Ankle Anatomy .....	7
Figure 1.4: A Typical Stress-Strain Curve for Bone.....	9
Figure 1.5: Anatomy of the Calcaneus and Talus .....	11
Figure 1.6: Types of Elements .....	19
Figure 2.1: Accessing the Medial and Lateral Ankle Compartments .....	44
Figure 2.2: Strain Gauge Locations on the Lateral Side of the Foot.....	47
Figure 2.3: Strain Gauge Locations on the Plantar Surface of the Foot .....	47
Figure 2.4: Strain Gauge Locations on the Medial Side of the Foo.....	48
Figure 2.5: Talar Strain Gauge Locations .....	48
Figure 2.6: Calcaneal Fracture Lines .....	50
Figure 2.7: Alignment of the Potted Leg .....	53
Figure 2.8: Original and Modified Ankle Positioner .....	55
Figure 2.9: Test Frame .....	57
Figure 2.10: Experimental Setup and Test Device.....	63
Figure 2.11: Bone Coordinate Systems.....	69
Figure 2.12: Strain Readings at Each Position for the Tested Postures .....	75
Figure 2.13: The Lateral Aspect of the Talo-Calcaneal Joint .....	81
Figure 3.1: CT Scan of the Lower Leg and Ankle .....	93
Figure 3.2: Hindfoot Bone Thresholding Challenges and Polylines.....	94

Figure 3.3: 3D Geometry of the Foot Bones and Soft Plantar Tissues .....	97
Figure 3.4: Strain Gauge Location Identification .....	99
Figure 3.5: TrueGrid® Environment .....	101
Figure 3.6: The Butterfly Technique.....	102
Figure 3.7: Meshes of the Talus and Calcaneus.....	105
Figure 3.8: Fibula Mesh .....	107
Figure 3.9: Heel/Foot Pad Mesh .....	110
Figure 3.10: Alignment of the Two Tibial Geometries.....	113
Figure 3.11: Elements with Large Angular Deviations .....	126
Figure 3.12: Distance Map between the Two Tibias .....	128
Figure 3.13: Talus and Calcaneus Shell Thicknesses .....	129
Figure 3.14: Complete Lower Leg Model.....	130
Figure 4.1: Overall Summed Error Between Experimental and Simulated Heel/Foot Pad Thickness in the Neutral Posture at Maximum Load as Properties are Varied .....	149
Figure 4.2: Simulated and Experimental Heel/Foot Pad Thickness in the Neutral Posture at Maximum Load .....	150
Figure 4.3: Overall Summed Error Between Experimental and Simulated Strains in the Neutral Posture as Bone Elastic Modulus is Varied.....	152
Figure 4.4: Comparison of Euler Angles and Displacements at the Neutral Posture for the Calcaneus and Talus as Friction Factor is Adjusted.....	153
Figure 4.5: Comparison of Talar Strains in the Neutral Posture for the Specimen's	

	Original Tibial Geometry and the Previously Validated Tibia.....	156
Figure 4.6:	Comparison of Experimental and Simulated Euler Angles and Displacements at the Neutral Posture for the Calcaneus and Talus .....	157
Figure 4.7:	Comparison of Experimental and Simulated Strains at the Neutral Posture .....	159
Figure 4.8:	Comparison of Experimental and Simulated Euler Angles and Displacements in Inversion-External Rotation for the Calcaneus and Talus .....	160
Figure 4.9:	Comparison of Experimental and Simulated Strains at the Inversion- External Rotation Posture .....	162
Figure 4.10:	Comparison of Experimental and Simulated Euler Angles and Displacements in Eversion-External Rotation for the Calcaneus and Talus .....	163
Figure 4.11:	Comparison of Experimental and Simulated Strains at the Eversion- External Rotation Posture .....	164
Figure 4.12:	Comparison of Experimental and Simulated Euler Angles and Displacements in Plantarflexion for the Calcaneus and Talus .....	166
Figure 4.13:	Comparison of Experimental and Simulated Strains at the Plantarflexion Posture .....	167
Figure 4.14:	Comparison of Experimental and Simulated Euler Angles and Displacements in Dorsiflexion-Inversion for the Calcaneus and Talus ..	168
Figure 4.15:	Comparison of Experimental and Simulated Strains at the Dorsiflexion-	

Inversion Posture .....	170
Figure 4.16: Contour Plot of Bone Distance in the Neutral Posture .....	173
Figure 4.17: Predicted Failure Load in the Hindfoot for all Tested Postures .....	173
Figure 4.18: Contour Plots of Maximum Strain in Each Posture .....	175
Figure 4.19: Anterior View of the Ankle in the Neutral Posture .....	183
Figure D.1: Dimensioned Drawing of Ankle Positioner Modifications .....	220
Figure D.2: Dimensioned Drawing of Ankle Positioner Bottom Rail .....	220
Figure D.3: Dimensioned Drawing of Ankle Positioner Top Rail Piece .....	221
Figure D.4: Dimensioned Drawing of Test Frame Bottom Struts .....	222
Figure D.5: Dimensioned Drawing of Test Frame Top Struts .....	222
Figure D.6: Dimensioned Drawing of Test Frame Front End Plate .....	223
Figure D.7: Dimensioned Drawing of Test Frame Back End Plate .....	224
Figure D.8: Dimensioned Drawing of Test Frame Slotting Wing .....	225
Figure D.9: Dimensioned Drawing of Test Frame Cross Members .....	226
Figure D.10: Dimensioned Drawing of Test Frame Clamping Bar .....	227
Figure D.11: Dimensioned Drawing of Test Frame Pegs .....	228
Figure D.12: Dimensioned Drawing of Test Frame Potting Fixture .....	229

## LIST OF ABBREVIATIONS AND SYMBOLS

%	Percent
$\hat{x}$	Unit vector in the x-direction
$\hat{y}$	Unit vector in the y-direction
$\hat{z}$	Unit vector in the z-direction
“	Inch
°	Degree
1D	One-dimensional
2D	Two-dimensional
3D	Three-dimensional
ANOVA	Analysis of variance
ATD	Anthropomorphic test device
CAD	Computer aided design
cm	Centimeter
CT	Computed Tomography
DAQ	Data acquisition system
DF	Dorsiflexion
ELFORM	Element formulation
ER	External rotation
EV	Eversion
FE	Finite element
FEA	Finite element analysis

FEM	Finite element model
g	Gram
GPa	Gigapascals
h	Hour
HU	Hounsfield Units
Icune	Intermediate cuneiform
IED	Improvised explosive device
Int	Intermediate
INV	Inversion
IR	Internal rotation
kg	Kilogram
kN	Kilonewtons
kPa	Kilopascals
Lat	Lateral
lbs	Pounds
Lcune	Lateral cuneiform
m	Meter
Mcune	Medial cuneiform
Med	Medial
Meta	Metatarsal
mm	Millimeter
MPa	Megapascals

MRI	Magnetic Resonance Imaging
ms	Millisecond
N	Newtons
PF	Plantarflexion
R <sup>2</sup>	Coefficient of determination
s	Second
s <sup>-1</sup>	Per second
SD	Standard deviation
STL	Stereolithography file format
$\varepsilon$	Strain
$\mu\varepsilon$	Microstrain

## **DECLARATION OF ACADEMIC ACHIEVEMENT**

The following is a declaration that the research outlined in this thesis was completed by Chris Smolen and recognizes the contributions of Dr. Cheryl Quenneville, Dr. Harjeet Ghandi and Dr. Tom Chow. Chris Smolen contributed to the study design and was responsible for the experimental testing protocols, test fixture manufacturing and design, modification of existing test devices, data collection, data analysis, finite element model creation and evaluation, and writing of the manuscript. Dr. Cheryl Quenneville assisted with the study design and review of the manuscript. Dr. Harjeet Ghandi aided with the dissection of the cadaveric specimen and Dr. Tom Chow took the CT scans of the specimen.

---

## **CHAPTER 1 – Introduction**

---

### **1.1 MOTIVATION**

The ankle is the most common site of injury for occupants during frontal vehicular collisions (Morris et al., 1997). Furthermore, in combat zones such as Iraq and Afghanistan, improvised explosive devices (IEDs) are one of the greatest dangers to soldiers, and detonations from such weapons underneath vehicles can lead to serious damage to the ankles and lower limbs of an occupant (Ramasamy et al., 2011). In fact, it has been found that of all IED-related injuries, 87% involve the lower limbs (Ramasamy et al., 2008). Impacts with the ground after falling from a height are another common cause of ankle injury. As individual protective measures and medical care have improved over time, the number of fatalities due to such injuries have decreased (Ramasamy et al., 2011). However, the ankle contains a relatively low number of blood vessels, which means healing in this area is poor (Haddock et al., 2013). As a result, these injuries are still debilitating, often require amputation, and are associated with poor clinical results (Ramasamy et al., 2013). For example, in a study on U.K. military personnel who had suffered lower limb injuries from under-vehicle explosions between 2006 and 2008, it was found that 29% of the injured legs required amputation and after 33.3 months, and 74% of the wounded legs exhibited continued impairment (Ramasamy et al., 2013). The health care costs associated with ankle damage are very high, especially if amputation and a prosthetic limb replacement are required. It has been found that if reconstruction of the limb is possible, the long-term financial burden of such an injury is more than \$160,000 on average. For

patients who require amputation, this cost is over three times higher, at around \$510,000, including the cost of a prosthetic limb replacement (MacKenzie et al., 2007). This also says nothing of the impact on the quality of life of such victims. Along with loss of mobility, lower limb trauma can lead to chronic pain that may interfere with everyday activities and the ability to remain a productive member of society (Castillo et al., 2006). These injuries are also associated with a high incidence of emotional distress. One study found that 48% of patients who were admitted to main trauma centers in the US with limb-threatening injuries screened positive for psychological disorders three months following the event, and 42% two years following the event (McCarthy et al., 2003).

By understanding the factors that cause ankle injury, suitable protective systems can be designed. When implemented in military and civilian vehicles, these improved safety measures will lower the risks associated with these accidents, alleviating the financial and psychological burden on society and on individuals subjected to such injuries. Injury to the ankle in different loading scenarios has previously been evaluated experimentally using cadaveric specimens (*e.g.* Yoganandan et al., 1996), and numerically using computer simulations such as finite element (FE) modeling (*e.g.* Shin et al., 2012). These tests are usually performed with the ankle in a neutral position. However, the ankle can assume a wide variety of postures during these traumatic events. This variation may alter the load path through the hindfoot, with fractures having been noted in the tibia, fibula, talus and calcaneus (McKay and Bir, 2009). For falls involving the wrist, the orientation of the scaphoid and lunate have been found to affect both the fracture location and load in the radius bone of the forearm (Troy and Grabiner, 2007), and therefore, a similar

mechanism may operate at the ankle. An FE model that can predict injury in various postures would be very beneficial for assessment of injury risk.

## **1.2 ANATOMY OF THE FOOT AND ANKLE<sup>1</sup>**

The tibia and fibula are the two bones of the lower leg (Figure 1.1). The tibia is much larger than the fibula and bears the vast majority of the weight supported by the leg (90% or more) (Takebe et al., 1984). The tibia articulates with the femur at the knee and with the talus at the ankle. The fibula articulates minimally with the tibia at both a proximal and distal joint. The primary purpose of the fibula is to provide stabilization to the ankle joint by restricting lateral movement of the talus. Both the tibia and fibula have protrusions at the distal end known as the medial and lateral malleoli, respectively. These malleoli are attachment sites for numerous ankle ligaments that connect with the talus and calcaneus bones.

The foot is composed of 26 bones that articulate at 33 joints and are connected by over 100 ligaments (Figure 1.2). These ligaments are essential for controlling the relative movement of the bones of the foot and for the stability of the joints. Articular cartilage is present between bones at each joint and allows for nearly frictionless relative movement between bones. The two bones of the hindfoot are the talus and calcaneus (Figure 1.3). The talus is responsible for most of the movement allowed by the foot due to its articulation with the tibio-fibular complex at its superior surface (Lundberg et al., 1989). This is known

---

<sup>1</sup> Commonly used anatomical terms are defined in Appendix A due to the interdisciplinary nature of this work.

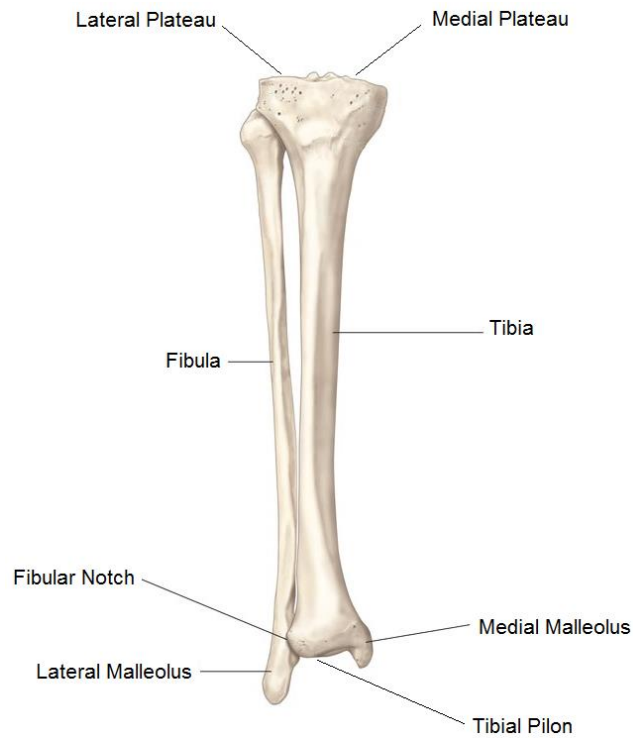


**Figure 1.1: Lower Leg Anatomy**

An anterior view of the tibia and fibula bones of the right leg. The tibia and fibula articulate with the talus at the distal end and with the femur at the proximal end (not shown). Adapted from (Maxwell, 1878).

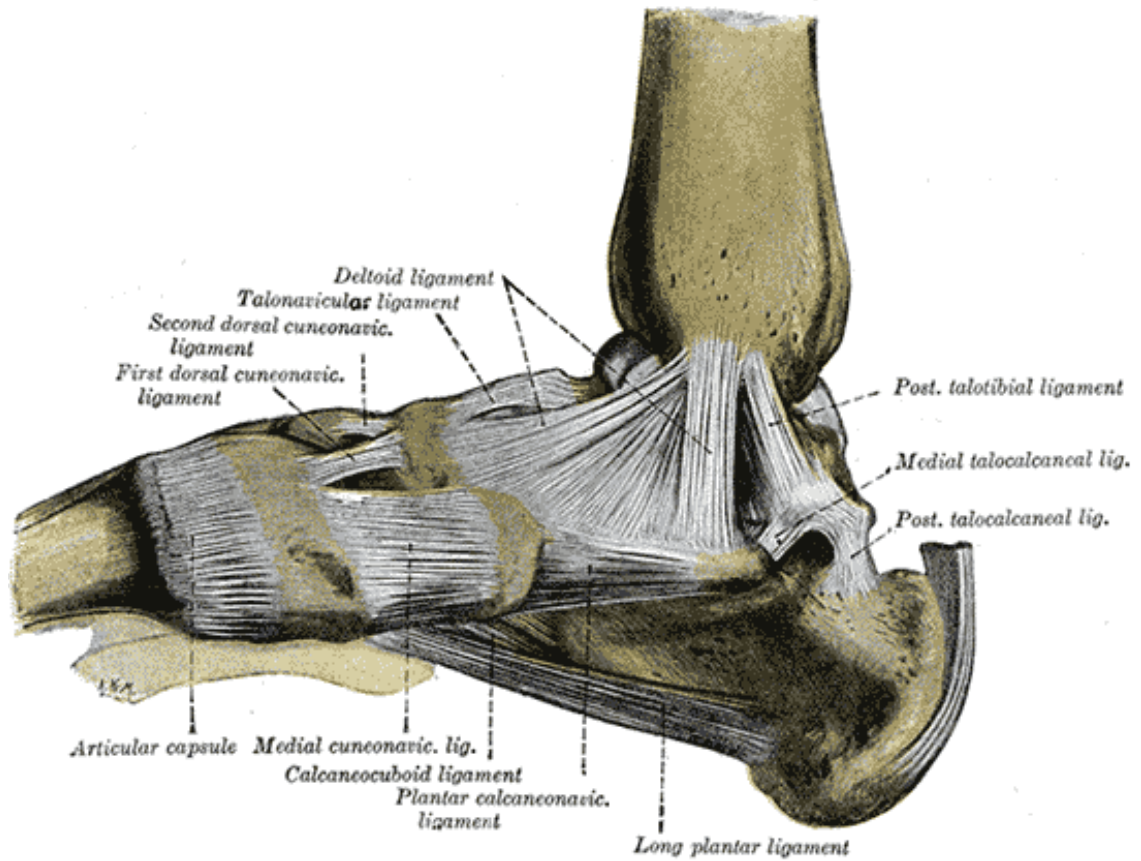


**Figure 1.2: Ligaments of the Medial Foot and Ankle**

Over 100 ligaments are present in the foot and ankle. These ligaments control the relative movement among the bones and provide stability to the joints. The major ligaments of the medial foot are shown (Gray, 2009).

as the talo-crural joint. This bone also articulates with the calcaneus at its inferior surface (the talo-calcaneal joint), and the navicular at its anterior surface (the talo-navicular joint). All load transmitted from the foot to the leg must pass through the talus. Furthermore, the talus has no muscle attachment sites, meaning that its position is entirely dependent on the positions of its neighbouring bones. The calcaneus makes up the heel of the foot and is one of the primary points of contact with the ground. Most of the load transmitted through the leg passes through the calcaneus. During the gait cycle, the peak loads at the heel/forefoot have been found to be around 75/35% bodyweight (Hutton and Dhanendran, 1979). Directly below the calcaneus is a heel pad made up of soft tissue that acts as a shock absorber (Noe et al., 1993). Along with the talus, the calcaneus also articulates with the cuboid bone at the anterior surface (talo-cuboid joint).

The midfoot and forefoot together are composed of 24 bones (Figure 1.3) including the cuboid, navicular, cuneiforms, metatarsals and phalanges. This region is a point of contact with the ground, and the numerous articulations in this region allow the foot to conform to irregular surfaces, acting as a stabilizer.

### **1.3 BONE STRUCTURE AND MATERIAL PROPERTIES**

Bone is comprised of two different microstructural components: cortical and cancellous (or trabecular) bone. Cortical bone forms the shafts of long bones, and serves as an outer dense shell covering regions of inner, less dense cancellous bone.

Cortical bone is made up of osteons, which are tightly packed cylindrical structures. Cancellous bone on the other hand is porous and is composed of a network of small rod

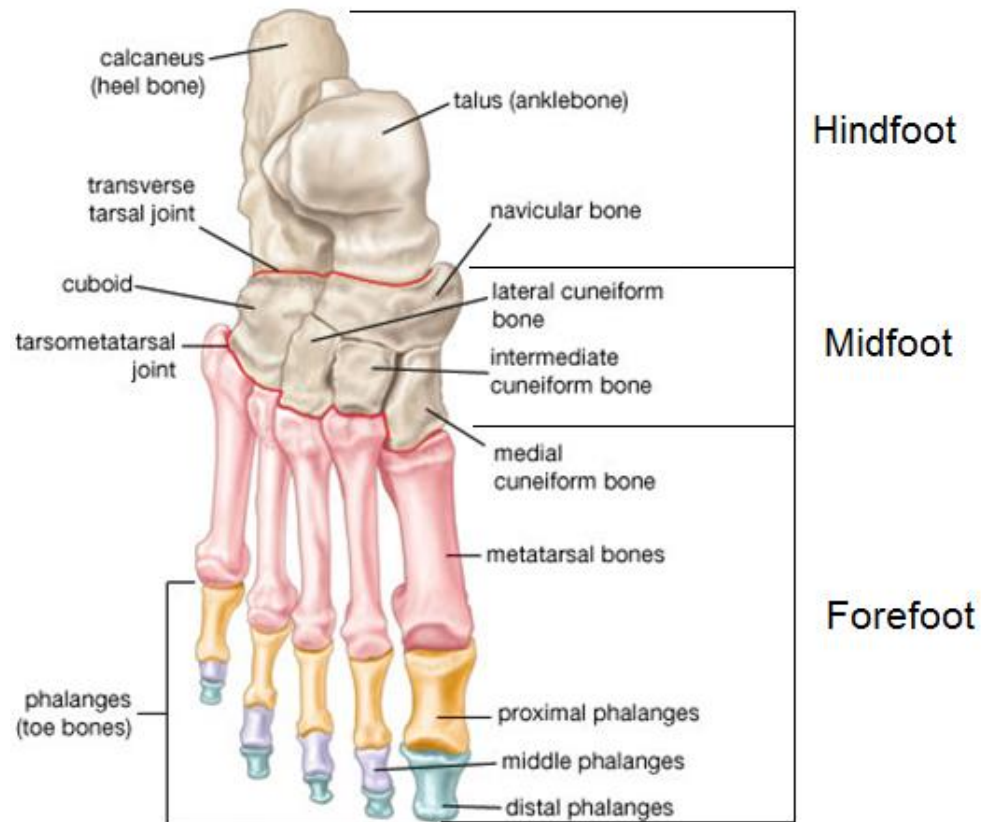


**Figure 1.3: Foot and Ankle Anatomy**

A superior view of the bones of the foot. The hindfoot is composed of the talus and calcaneus and is the primary load path through the foot and ankle. The midfoot is made up of the cuboid, navicular and cuneiform bones and transmit load from the forefoot to the ankle. The metatarsals and phalanges are the bones of the forefoot and are a secondary load path through the foot. Adapted from (Maxwell, 1878).

and plate-shaped structures known as trabeculae. The existence of the cortical and cancellous regions allow bone to maximize its strength to weight ratio. Bone marrow is found in the spaces formed by the trabecular network as well as in the center of long bones.

Wolff's law states that the structure of bone will adapt to the loads under which it is placed (Cowin, 1986). As a result, osteons align themselves with the long axis of long bones (such as the tibia) in order to resist axial loading. Furthermore, in irregular bones such as the calcaneus and talus, the trabecular network is aligned with the primary loading paths through the bones (von Meyer, 2011). The result of this adaptation of bone is that it is an inhomogeneous and anisotropic material (Martin et al., 1998). While the stress-strain curve for bone is non-linear, its behaviour is most similar to that of an elastic-plastic material, and it can be represented by a piecewise linear stress-strain curve with an easily identifiable elastic modulus, yield stress, plastic modulus and ultimate stress (Burstein et al., 1976) (Figure 1.4). It should also be noted that bone properties vary depending on what type of loading is applied (*i.e.* compressive, tensile or shear).

Bone also exhibits viscoelastic properties. Experimental compressive testing has found that the modulus and strength of cortical bone is proportional to the strain rate of the applied loading to the power of 0.06 (Carter and Hayes, 1977). As loading is applied at higher strain rates, the bone becomes stiffer (elastic modulus increases) and the yield and ultimate stress values increase. However, bone becomes more brittle at higher strain rates, meaning the ultimate strain and the area under the stress- strain curve decreases.

The marrow in trabecular bone was found to affect the properties of the bone only at strain rates higher than  $10 \text{ s}^{-1}$  (Carter and Hayes, 1977). Quasi-static is the term used

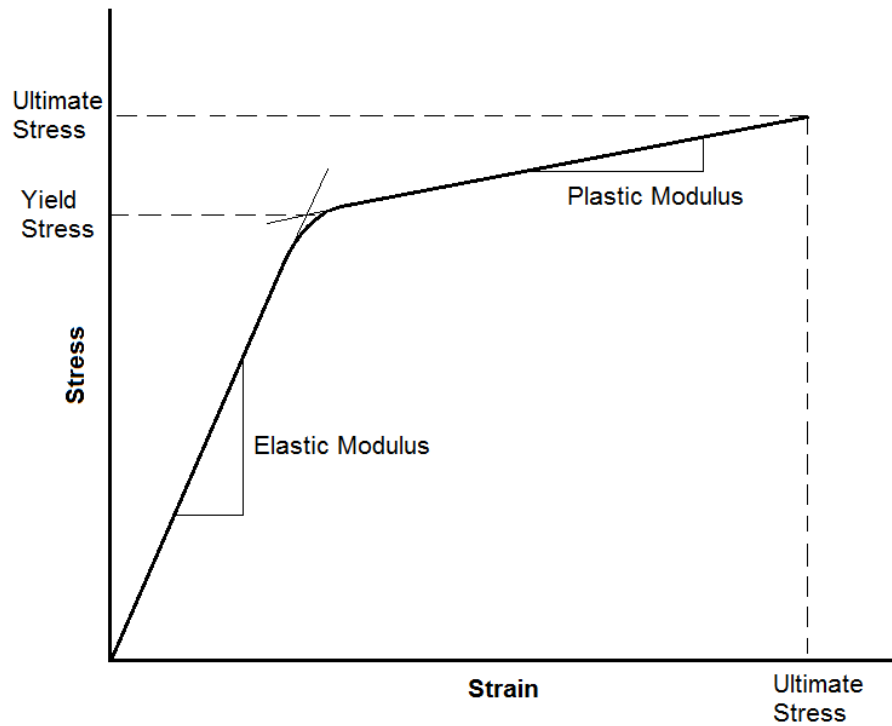


**Figure 1.4: A Typical Stress-Strain Curve for Bone**

Bone can be represented as an elastic-plastic material. It has a linear elastic region with a specific elastic modulus and a plastic region represented by a plastic modulus. Beyond the yield stress, permanent (plastic) deformation occurs, and at levels exceeding the ultimate stress and strain, the material experiences fracture.

for when loads are applied at strain rates sufficiently low that dynamic effects can be neglected. The generally accepted strain rate range for loading to be considered quasi-static is on the order of  $0.01\text{-}0.001\text{ s}^{-1}$  (Shunmugasamy et al., 2010).

Bone properties also tend to degrade with age, with elastic modulus and ultimate strength having been found to decrease by 2-5% per decade after the age of around 40 (Burstein et al., 1976, Modlesky and Lewis, 2002). The mechanical properties of both cortical and trabecular bone reported in the literature have been found to vary greatly depending on the age and gender of the bone samples tested, as well as the location of the body from which the bone was taken and the experimental testing method used (Goldstein, 1987, Reilly and Burstein, 1974).

#### **1.4 MECHANISMS OF FOOT AND ANKLE INJURY**

Due to the complexity of the foot and ankle, countless mechanisms of injury in this region are possible. Calcaneal fractures account for about 2% of all fractures and can be classified as either intra-articular or extra-articular (Daftary et al., 2005). Three quarters of all calcaneal fractures are intra-articular, meaning they occur within a calcaneal joint (Daftary et al., 2005). These fractures are typically caused by axial loading, and while the exact mechanism of fracture and number of fragments produced can vary, a shear fracture is usually formed in the sagittal plane (Carr et al., 1989). Furthermore, the anterolateral process of the talus tends to get wedged into the angle of Gissane of the calcaneus (Figure 1.5a), causing a secondary compression fracture line that runs in the coronal plane (Carr et al., 1989). The remaining quarter of calcaneal fractures are extra-articular, meaning they

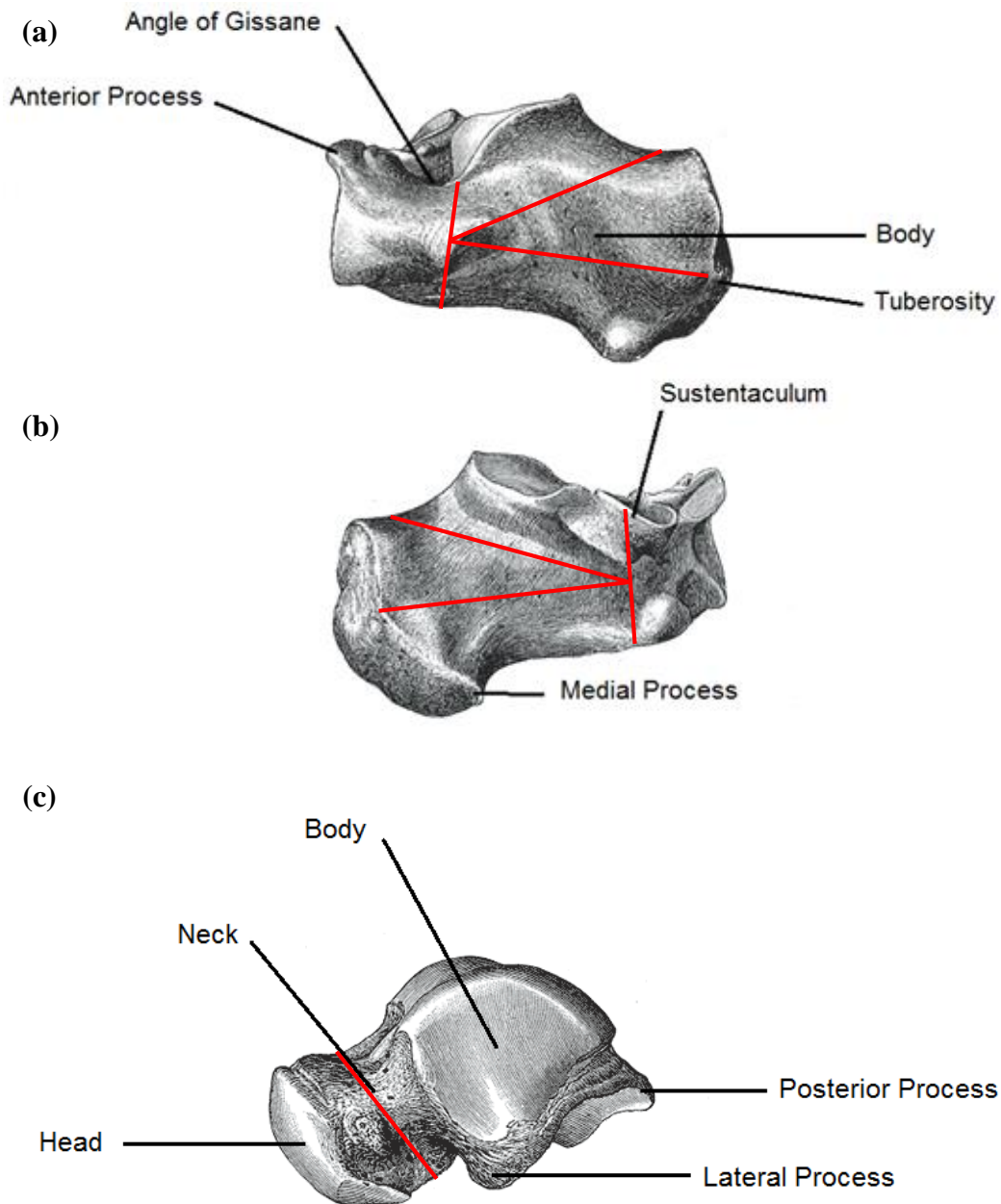


**Figure 1.5: Anatomy of the Calcaneus and Talus**

(a) Lateral view of the left calcaneus, (b) medial view of the left calcaneus and (c) lateral view of the left talus. The locations indicated on these anatomical drawings are some of the more common fracture sites on the bones of the hindfoot. Typical fracture lines (Daftary et al., 2005, Daniels and Smith, 1993) are indicated in red. Adapted from (Gray, 2009).

are situated outside the calcaneal joints (Daftary et al., 2005). Fractures of the anterior process (Figure 1.5a) have been found to occur when increased tension is placed on the bifurcate ligament (which inserts at the anterior process) during forced inversion (Fitzgibbons et al., 2001). Extreme dorsiflexion and forced eversion of the forefoot while the calcaneus is stationary have also been found to cause fractures of the anterior process (Trnka et al., 1998). Fractures of the body of the calcaneus (Figure 1.5a) are typically caused by the same mechanisms as intra-articular fractures (Daftary et al., 2005), and axial loading and inversion have been implicated in causing fractures of the sustentaculum (Figure 1.5b) (Essex-Lopresti, 1952). The medial process of the calcaneus (Figure 1.5b) has been found to fracture following a fall from a height with the foot in an everted position (Daftary et al., 2005). Finally, fractures of the calcaneal tuberosity (Figure 1.5a) are typically caused by avulsion of the Achilles tendon from its bony insertion point (Kathol et al., 1991).

Talar fractures have similar rates of incidence as calcaneal fractures. One study looking at the experience of two Level 1 trauma centers in the United States found that talar fractures accounted for 1.68% of all trauma cases over a 5 year period (Elgafy et al., 2000). Fractures of the talar neck (Figure 1.5c) are the most common, accounting for about 50% of all talar fractures (Daniels and Smith, 1993, Smith and Ziran, 1999). Historically, talar neck fractures have been theorized to occur due to a combination of axial compression and excessive dorsiflexion (Daniels and Smith, 1993). However, Peterson was only able to induce talar neck fractures in cadaveric feet by placing the ankle in a neutral position and compressing the calcaneus against the talus (1976). Talar neck fractures were

generated by applying a dorsally-directed force to the plantar surface of the foot just distal to the talus. In this case, the talus acted as a cantilever between the tibia and the plantar surface of the foot (Daniels and Smith, 1993). Excessive inversion of the ankle can also lead to talar neck fractures due to contact between the talar neck and the medial malleolus of the tibia (Sanders and Lindvall, 1999). Talar body (Figure 1.5c) fractures account for 13 to 23 % of talar fractures, and are typically caused by axial compression, trapping the talar body between the calcaneus and tibia (Smith and Ziran, 1999). Excessive plantarflexion has been implicated in causing fracture of the posterior process (Figure 1.5c) by having the posterior tubercle come into contact with the tibial plafond (Smith and Ziran, 1999). Finally, fracture of the lateral process (Figure 1.5c) has been noted to occur due to combined inversion and dorsiflexion of the ankle (Smith and Ziran, 1999)

Ankle fractures involving the distal tibia and fibula are categorized according to the Weber (Hughes et al., 1979) and Lauge-Hansen (Lauge-Hansen, 1950) classifications of ankle fracture. Lauge-Hansen cites three primary mechanisms of tibio-fibular fracture at the ankle: inversion, which occurs infrequently (Gardner et al., 2006), combined inversion and external rotation, and combined eversion and external rotation (Lauge-Hansen, 1950). Combined inversion and external rotation accounts for 40-70% of all ankle fractures, making it the most common ankle fracture mechanism (Okanobo et al., 2012). The second most prevalent fracture mechanism is eversion and external rotation, accounting for about 20% of all ankle fractures (Gardner et al., 2006). Another important type of ankle fracture to note is the Pilon fracture, which accounts for less than 1% of all lower extremity fractures (Helfet et al., 1994). These fractures are commonly caused by high-energy impact of the

talus with the tibia, causing the distal tibia to fracture. These fractures are some of most challenging for surgeons to fix and are associated with an extremely high incidence of complications, including infection, surgical malalignment and arthritis (Helfet et al., 1994).

A study by Manoli et al. examined the level of impairment an individual will suffer for different types of ankle skeletal damage (1997). It was found that pilon fractures were the most severe types of ankle injury and resulted in the greatest impairment. Ruptures of the talus and calcaneus bones of the ankle caused the second highest level of long-term deficiency.

Various types of midfoot and forefoot fractures have also been reported in the literature. The navicular is the most commonly fractured midfoot bone, and fractures of the cuboid and cuneiforms have also been shown to occur (Lee and Donatto, 1999). A Lisfranc fracture occurs when a dislocation occurs between the metatarsal bones and the cuboid and cuneiform (tarsus) bones (Rammelt et al., 2008). These injuries are typically caused by direct crushing of the affected area, falls from a height or high-energy vehicular crashes (Vuori and Aro, 1993). Different types of metatarsal and phalangeal fractures have also been reported (Otte et al., 1992). Most of these injuries do not require surgical intervention (Lee and Donatto, 1999) and typically result in lower morbidity than fractures of the hindfoot.

## **1.5 EXPERIMENTAL INJURY ASSESSMENT OF THE LOWER LEG**

Historically, injury prediction and assessment of the lower leg and ankle has been performed using studies on cadaveric lower legs (*e.g.* Yoganandan et al., 1996).

### 1.5.1 INJURY ASSESSMENT IN THE NEUTRAL POSTURE

The majority of previous studies examining the injury tolerance of the lower leg have been performed with the ankle in a neutral position, and the most widely referenced study of this type was conducted by Yoganandan (1996, 1997). In this experiment, cadaveric lower legs were potted at the knee, ballasted to a 16 kg mass, and attached to a mini-sled that rode along a linear rail and bearing system. The sole of the foot was impacted with a 24 kg pendulum at velocities ranging between 2.2 and 7.6 m/s. Forces were measured using a load cell and accelerometer attached to the pendulum, and a second load cell proximal to the potting fixture. Of the destructive tests, forces at the proximal tibia ranged from 8.3 to 11.4 kN. Fractures were observed in the distal tibia and calcaneus, and often propagated into the articular surfaces.

A study by Seipel (2001) attempted to quantify the tolerance of the calcaneus to axial impact using Yoganandan's experimental apparatus (1997). Twenty-two full lower legs were subjected to axial impacts representative of car crashes with pendulum velocities between 2.2 and 6.7 m/s. Using a regression analysis, it was found that the probability of a calcaneal fracture was 25% at 4 kN and 50% at 5.5 kN.

A study by Funk (2002a) expanded upon Yoganandan's work by applying pre-tension representative of bracing prior to a vehicular impact to the Achilles tendons of cadaveric lower leg specimens. The legs were impacted by a piston at 5 m/s and forces were measured with load cells at the foot plate and in the tibia. Calcaneal fractures were most common, but tibial pilon fractures were also observed, especially in cases with Achilles tension applied. The probability of injury was estimated using a regression

analysis based on the force applied and the subject's gender, age, body weight, and Achilles tension. The 50% risk of injury for a 50<sup>th</sup> percentile male was a tibial force of 8.3 kN.

#### 1.5.2 INJURY ASSESSMENT WITH VARIATION IN POSTURE

Studies performed by Begeman (1990, 1993) attempted to quantify the injury tolerance of the ankle under dynamic dorsiflexion, inversion and eversion. Cadaveric lower legs were potted at the proximal end and the ankle was placed in a neutral position. The ankle was then struck by a pneumatically-actuated impactor in such a way as to produce the desired direction of ankle rotation. Forces were measured by a load cell at the footplate and a triaxial load cell at the proximal tibia. In the dorsiflexion case, the axial loads ranged from 1.1 to 5 kN and the dorsiflexion angle ranged from 25° to 75°. In the case of inversion/eversion, the axial loads ranged from 0.27 to 1.3 kN and the angles ranged from 30° to 85°. It was found that the ankle angle, rather than the force, was the greatest predictor of ankle injury: no injuries were sustained above 45° of dorsiflexion and 60° of inversion/eversion. The types of injuries that were observed were malleolar fractures and talar and calcaneal ligamentous avulsions. However, the loads applied during these studies were relatively low, especially for the inversion/eversion study, and the injury mechanisms may be different at higher loads. A different effect might also be observed when the ankle assumes a particular starting posture as opposed to it being moved due to the force of the impact. A similar study by Rudd (2004) examining dorsiflexion found that a dorsiflexion angle of 51° corresponded to a 50% risk of injury.

A study by Funk (2002b) attempted to assess the injury tolerance of the ankle to forced inversion and eversion, which is a commonly-reported mechanism of injury during vehicular impacts. This type of dynamic loading was applied to three sets of cadaveric lower legs: one in the neutral posture with no preload applied, one in the neutral posture with a 2 kN preload and one in 30° of dorsiflexion and a 2 kN preload. Fractures of the articular surfaces and lateral process of the talus, malleolar fractures, and ligament tears were the injury mechanisms observed. For the neutral posture with no preload, the injury threshold was 38° and 28° in inversion and eversion, respectively. For the neutral posture with preload, the injury threshold was at 40° and 41°. For dorsiflexion with preload, the injury threshold was at 33° and 40°. In a follow-up study (Funk et al., 2003), fractures of the lateral process of the talus (or snowboarder's talus fractures) were experimentally produced in cadaveric specimens by generating forced eversion in dorsiflexed and axially loaded lower legs.

## **1.6 FINITE ELEMENT ANALYSIS**

One drawback with experimental testing is that it can be expensive, especially if many samples are tested. Due to natural anatomical variation among specimens, wide variations in response are often noted. Furthermore, only a few parameters and loading conditions can be examined for any given experimental model during destructive testing. Finally, instrumentation of the specimen can be problematic, especially when cadaveric specimens are used. Numerical modeling circumvents these issues by allowing a model to be subjected to a wide variety of loading conditions with measurements of stress, strain,

displacement and more taken at any location in the model. Furthermore, the model can be reused *ad infinitum*.

Finite element analysis (FEA) is often used in the automotive and defense industries to assess injury risk (*e.g.* Sapuan et al., 2006). By allowing one to analyze the stress distribution in complex geometry, FEA is ideal for modeling bone's biomechanical response to loading. This is done by dividing complex geometry into smaller, simple shapes, known as elements, which are joined together at specific points known as nodes. Each element is assigned a stiffness, and the overall sum of the elements is called the mesh (Figure 1.6). Boundary conditions and loads are applied, and stress and strain throughout the model are computed. The two types of element shapes that are typically used in FEA are hexahedrals and tetrahedrals. Hexahedrals have been shown to be more computationally accurate than tetrahedrals, especially during dynamic simulations (Untaroiu et al., 2005). However, fitting hexahedrals to curved geometry can prove to be challenging and time consuming. Tetrahedrals, on the other hand, can be easily conformed to curved surfaces, and commercial software that will automatically generate a tetrahedral mesh is available. That being said, meshes created manually typically are of higher quality than those that are automatically generated (Valle and Ray, 2005). Tetrahedrals and hexahedrals are known as solid (3D) elements, and a two-dimensional analogue is available for each of these shapes (triangles and quadrilaterals) known as shell elements. Shell elements are appropriate to model structures when one dimension is much smaller than the other two and the change in the analyzed feature in the thinner dimension can be neglected. While shell elements are less computationally-intensive than solids, solids are more often

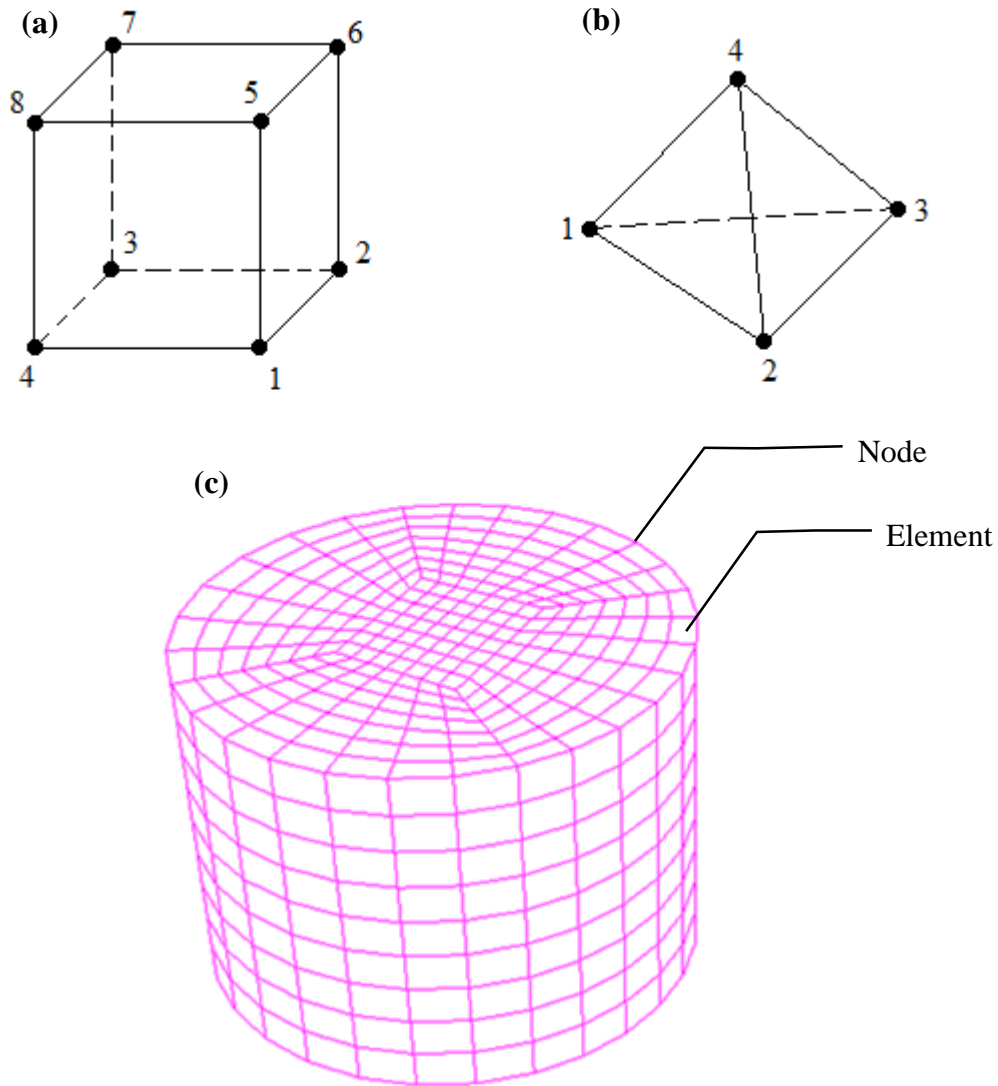


**Figure 1.6: Types of Elements**

(a) Hexahedral and (b) tetrahedral elements are the two types of solid elements used in FE modeling. Nodes are indicated with numbered dots. The overall continuum of elements connected by shared nodes is known as the (c) mesh.

used in FEA, especially when the stress field for the geometry being analyzed is unknown. 1D bar elements also exist that connect two nodes and act as a spring.

Mesh quality is typically assessed by calculating the Jacobian, aspect ratio and orthogonality of each element (Knupp, 2000). The Jacobian provides a measure of the deviation of each element from the “ideal” element. A Jacobian of one is a perfect cube, while a Jacobian below one indicates that the element is distorted, with the difference between the actual Jacobian value and one indicating the severity of the distortion. In the case of negative Jacobians, at least two element surfaces have passed through one another, and any finite element solver attempting to solve a model that includes this element will return an error.

Aspect ratio is the ratio between the shortest and longest sides of an element. An aspect ratio of one is ideal as it indicates that all sides of the element are the same length. Elements with one side much longer than the others may produce inaccurate results.

Orthogonality is a measure of the deviation of the interior angles of a hexahedral element from  $90^\circ$ . The closer the interior angles are to  $90^\circ$ , the more cube-like the element is, and the more accurate its response will be.

Biomechanical FEA modeling generally follows a set method that tends to be fairly time-consuming. The process usually begins with acquiring the 3D surface geometry upon which the mesh will be based. In the case of bones this generally comes from Computed Tomography (CT) scans and for soft tissues such as ligaments or cartilage, this geometry is derived from Magnetic Resonance Imaging (MRI). The advantage of these methods is that they are non-invasive and the resolution of modern scanners is quite high (sub 1 mm

slices), which gives accurate geometrical information. Some orthopaedic studies use grayscale values from scans in order to apply inhomogenous material properties to the model (Rho et al., 1995). However, for general dynamic studies, bone is usually separated into cancellous and cortical regions (and sometimes marrow) (*e.g.* Iwamoto et al., 2005), with each region being assigned bulk material properties.

FEA has some inherent disadvantages. Due to the numerical nature of FEA, the solution is always approximate. Only as the number of elements used tends towards infinity does the solution equal the analogous analytical solution. Convergence studies can be performed to assess how many elements are required (*e.g.* Eberlein et al., 2004). Furthermore, the solution is affected by the element shape. FEA is also computationally intensive: as the number of elements increases, the computational time increases and simulations can sometimes take hours or even days depending on the computer hardware used and the problem solved. Assigning boundary conditions and loads analogous to those experienced in real life can be challenging. Numerical modeling of contact between surfaces (for example at joints), as well as friction is another major challenge when using FEA (Laursen, 2002).

## **1.7 PREVIOUS FINITE ELEMENT SIMULATIONS OF THE FOOT AND ANKLE**

### **1.7.1 TANNOUS AND BANDAK, 1996, 2001**

The first finite element model that included all the bones of the foot and ankle up to the knee, as well as the plantar soft tissues and major ankle ligaments, was constructed by Tannous (1996). Bandak (2001) later improved the model by matching the bone

geometry to CT scans of a lower leg. Deformable solid hexagonal elements were used to model the fibula, tibia, calcaneus, talus and plantar soft tissue, and a finer solid hexahedral mesh was used at the areas of contact between hindfoot bones. The friction coefficient between bone surfaces was chosen to be similar to that between surfaces covered in hyaline cartilage (0.02). The cortical and cancellous regions of the hindfoot bones were assigned homogenous, isotropic, linear elastic properties from the literature (Cowin, 1989, Carter and Hayes, 1977), and the bones of the midfoot and forefoot were modeled as one fused rigid body. Nine ligaments were modeled in total using shell elements, with linear elastic properties assigned based on force-displacement data from tensile tests (*e.g.* Siegler et al., 1988). The soft tissue under the foot was also modeled as linear elastic. The entire model was composed of 16596 elements, 33% of which were rigid bodies. Mesh quality was assessed, although the specific quality criteria that were used were not disclosed.

The model was validated by comparison with Yoganandan's axial impact tests (1997), based on force-time and acceleration-time histories at the impactor and knee. At low velocities, the simulated and experimental force-time histories matched well. The forces were overestimated by the simulation at higher velocities, but the load curve durations and shapes were in good agreement.

#### 1.7.2 IWAMOTO ET AL., 2005

Iwamoto (2005) constructed a model of the lower leg and foot, terminating at the knee, based on CT data scaled to the size and weight of a 50<sup>th</sup> percentile male. For the fibula, calcaneus and talus, isotropic elastic-viscoplastic materials were assigned (Yamada

and Evans, 1970). The cortical and trabecular regions of these bones were modeled using shell and solid elements, respectively. Specific moduli were assigned to the calcaneus and talus based on values taken from a previous finite element study by Beaugonin et al. (1997). The forefoot and midfoot bones were modeled as isotropic linear elastic, and it was not explicitly stated how these bones were connected to one another and to the hindfoot. A viscoelastic, anisotropic material model that was dependent on the type of loading applied was assigned to the cortical and cancellous regions of the tibia. The authors reported that it accurately described directional loading, strain rate effects and damage evolution. Seven ankle ligaments were modeled using shell elements, and were assigned linear elastic properties from the literature (Corazza et al., 2003). The plantar soft tissues were assigned linear elastic material properties that were the same as flesh. The author did not divulge the number of elements in the model or any methods used to assess element quality.

The model was validated against both Yoganandan's axial impact data (1996) and a second study by Kitagawa (1998), in which the forefoot was impacted by an 18 kg pendulum at 3.5 m/s while a constant Achilles tension of 1 kN was applied. Force-time histories were compared between the simulation and experiment at the impactor and the proximal tibia, along with fracture locations. In comparison with Kitagawa's study, the shapes of the force-time curves did not match perfectly, although the first peak of tibial force agreed well, as did the durations of the load curves. The location and severity of a pilon fracture in the model also matched the experimental data. In comparison with Yoganandan's study, the peak force, shape, and duration of the simulation agreed well with the experiment at high velocities. The model slightly overestimated the peak force at lower

velocities, even though the load curve shapes and durations still agreed well. The model also predicted calcaneal and pilon fractures observed experimentally at the highest velocity impact.

### 1.7.3 SHIN ET AL., 2012

A study by Shin (2012) used CT data from a 50<sup>th</sup> percentile male to construct a finite element model of the leg and foot, ending at the knee. The tibia, fibula, talus and calcaneus were assigned homogenous, isotropic, elastic-plastic properties from the literature (*e.g.* Burstein et al., 1976). The material properties of the calcaneus and talus were estimated, since little data on this topic were found in the literature. Midfoot and forefoot bones were modeled as rigid bodies and were connected to one other and to the hindfoot via ligaments and contact surfaces. Most of the cortical and trabecular bone was composed of solid hexahedral elements. The cortical bone of the epiphyseal regions of the long bones and the talus and calcaneus were modeled with shell elements. Twenty-five hindfoot and forefoot ligaments were modeled as 1D bar elements with properties based on non-linear tensile force-displacement relationships by Funk (2000) and Hall (1998). It was noted that the material properties of the midfoot ligaments are lacking in the literature, and they were assumed to be similar to those of the anterior-talofibular ligament, scaled by cross-sectional area. An unspecified number of ligaments among the metatarsals and cuneiforms were modeled as 1D bar elements with linear force-displacement relationships (*e.g.* Solan et al., 2001). Heel pad properties were assigned based on a hyperelastic rubber model from the literature (Erdemir et al., 2006). The total number of elements in this model

was 44548, and the quality of the mesh was assessed by measuring the Jacobian and the degree of warpage of the elements. Warpage is defined as the amount by which an element face deviates from being planar. Only a small percentage of elements failed to meet the specified targets for element quality ( $>0.5$  Jacobian,  $<20^\circ$  warpage).

The model was first validated by a set of low-energy forefoot pendulum impact tests at 6 m/s on cadaveric specimens and human volunteers. The simulation was compared to the acceleration-time history corridor recorded by an accelerometer attached to the pendulum, and the simulation response fell within the corridor. The model was then validated against quasi-static internal and external rotation data. The foot of the model was rigidly connected to a footplate that was rotated at  $10^\circ/\text{s}$  to a final angle of  $\pm 20^\circ$ . The response of the model was compared to moment-angle corridors generated from the experimental test, and the model's response in both rotation directions was within the appropriate corridors. Next, the model was validated in dorsiflexion based on experimental testing performed by Rudd (2004). Brake pedal loading was applied to head of the first metatarsal at speeds of 6 m/s. The moment-angle curve of the ankle was compared between the simulation and experiment, demonstrating good agreement. The model also predicted failure of the posterior talotibial ligament and a malleolar fracture, the most common ankle failure mechanisms reported during experimental testing. Finally, the model was compared to experimental tests on cadaveric legs in a combined loading configuration consisting of  $10^\circ$  dorsiflexion, 2 kN of axial compression and  $20^\circ/\text{s}$  of external rotation. The moment-external rotation angle response of the model was within the corresponding experimental

corridor. The model accurately predicted the moment and rotation angle at failure, as well as failure of the talofibular ligament.

A follow up to Shin's 2012 paper details comparison of the model with more experimental tests (2013). The model was first compared to the force-time history of the distal tibia during axial impacts on cadaveric lower legs by Funk (2002a). A good agreement was found between the experimental tests and simulation in terms of peak force and load curve duration and shape. The location of calcaneal fractures observed during testing were also predicted by the model. The model was then validated in inversion and eversion against more experimental tests by Funk (2002b), with and without a 2 kN preload. The foot of the model was rigidly connected to a footplate that was rotated in both inversion and eversion until failure occurred, with the center of rotation of the ankle estimated based on FE simulations. Moment-angle curves generated from the model fell within the experimental corridor. For both the preloaded and non-preloaded cases, the model accurately predicted ligament failure that was observed experimentally in both inversion and eversion, as well as the failure moment and angle. In addition, for the 2 kN preload, the model accurately predicted tibial plafond fractures under eversion and malleolar fractures under inversion.

#### 1.7.4 DONG ET AL., 2013

In a study by Dong (2013), a full body finite element model, representing the size of a 50<sup>th</sup> percentile male, was constructed for the purpose of simulating the high velocity, strain rate sensitive impacts associated with IED blasts. In the lower leg the tibia, fibula,

calcaneus and talus were modeled using a linear elastic-plastic material with properties from the literature (*e.g.* Gomez and Nahum, 2002). Strain rate effects were implemented for cortical bone of the tibia using the “Cowper-Symonds” formulation in order to simulate IED blasts, and were neglected for cortical bone of the calcaneus and talus as well as for trabecular bone. The plantar soft tissue was modeled using a hyperelastic and viscoelastic material. While no specifics were given about the modeling of ligaments and their properties, by inspection of the model, a reasonable number of foot and ankle ligaments seem to be present (at least 35 or more), and were modeled using a combination of bar elements and shells. The one region where ankle ligaments appear to be lacking is at the hindfoot. The bones of the foot and ankle appear to be discrete and allowed to move relative to each other via contact surfaces. The entire model was composed of 354,603 hexahedral elements with an average mesh size of 3 mm, but with no assessment of mesh quality declared. This model was previously designed to simulate aortic injury during car crashes, and as a result the geometry of the foot, ankle and lower leg bones appears to be somewhat over-simplified.

The model was first validated based on experimental tests by McKay and Bir (2009), in which cadaveric legs, instrumented at the mid-tibia with a triaxial load cell, were impacted by a 36.7 kg mass at speeds of 7.2, 9.9, and 11.6 m/s. The simulation response was compared to tibial force-time corridors for these speeds. At the lowest speed, the load-time response of the tibia matched the experimental results well, but at the higher speeds no experimental force-time corridors were defined due to large variations in response. As a result, the simulation was compared with the general trends of the individual test trials.

The simulations were within the range of the test trials for the most part, especially during the first force peak, and the locations of calcaneal fractures observed at these speeds in experimental testing were similar to those observed in the model. The model was further validated by comparison with as-of-yet unpublished impact tests applied to the lower legs and pelvises of full cadavers up to 20 m/s. Lower tibial and calcaneal fractures observed experimentally were reproduced in the model. Accelerometers attached to the upper tibia of the cadavers were used as a basis of comparison of acceleration-time data, and peak acceleration values and the overall curve pattern matched well.

## **1.8 CRITIQUE OF PREVIOUS FINITE ELEMENT MODELS OF THE LOWER LIMB**

Over the last 20 years, injury-predicting finite element models of the lower limb have become increasingly complex and accurate. However, the models summarized in Section 1.7 still exhibit some weaknesses and simplifications. Model geometry was often based upon scaled (Iwamoto et al., 2005) or simplified (Dong et al., 2013) CT data. The more realistic the geometry, the more accurate the response should be. The model created by Dong (2013) had the finest mesh, with an average element size of 3 mm. This was still fairly coarse, as the finer anatomical features of the leg (especially of the hindfoot bones) were not accurately recreated. As a result, stress distribution, failure and contact with adjacent bones may not be representative. Furthermore, most studies do not make any mention of testing for element quality, and those that do rarely supply any metrics regarding the number of elements in the model that met specific quality thresholds. The more recent studies use mostly hexahedral elements and quadrilateral shells (Iwamoto et

al., 2005, Dong et al., 2013), which have been shown to exhibit the most accurate response, especially in dynamic simulations (Untaroiu et al., 2005). However, there is still occasional use of other element shapes (Shin et al., 2012).

Material property data for the calcaneus and talus bones are limited in the literature and the aforementioned studies made educated guesses about what properties to assign.

Very few finite element models have examined the effect of ankle posture on fracture tolerance, despite the fact that this has proven to be a predictor of injury risk in tests on cadaveric lower limbs (Klopp et al., 1997). The main limitation with current tests involving altered ankle postures (*e.g.* Shin et al., 2012) is that the bone positions in these postures were estimated. The sole of the foot was rigidly fixed to the footplate and the footplate was moved into varying degrees of inversion/eversion and dorsiflexion. The ankle bone positions that resulted were not validated and are not necessarily indicative of the actual positions these bones would adopt in the natural ankle.

Another important factor when examining ankle posture is the ligaments connecting the discrete bones of the foot. While the most recent studies model over 30-40 ligaments (Shin et al., 2012, Dong et al., 2013), many more ligaments are present in this region that contribute to controlling the overall motion of the foot and ankle. Linear elastic properties are often assigned (*e.g.* Iwamoto et al., 2005), even though ligaments have been shown to exhibit non-linear force-displacement responses (Funk et al., 2000).

Finally, earlier models tended to assign linear elastic flesh-like material to the soft tissues on the plantar surface of the foot (*e.g.* Bandak et al., 2001), but the more recent models use a hyperelastic material for this region (*e.g.* Shin et al., 2012).

## **1.9 OVERVIEW OF VALIDATION METHODS FOR LOWER LIMB MODELS**

As was seen in Section 1.7, the most common method of validation for lower limb models is comparison with biofidelity corridors yielded from experimental data. Biofidelity corridors represent the average response of a set of test data, with the minimum and maximum boundary of the corridor defined as one standard deviation from the average. In the case of axial impact tests (*e.g.* Yoganandan et al., 1996), force-time and acceleration-time corridors were acquired from load cells and/or accelerometers attached to the impactor and/or proximal tibia. Occasionally, load cells or accelerometers are placed within the tibia (*e.g.* Dong et al., 2013). In the case of experimental tests involving ankle movement, a moment-angle curve can be generated. The moment is based on the product of the applied force causing the rotation and the estimated center of rotation of the ankle joint. The angle is usually measured by high-speed photography (Funk et al., 2002b). When the simulation result is compared to the experimental result, the simulated curve ideally fits within the biofidelity corridor.

Failure locations are often used as a secondary method of model validation. The location and severity of bony fractures, and sometimes ligament failure (*e.g.* Shin et al., 2012) predicted by the model are compared with the most common fractures and ligament failures that were observed during experimental testing. This type of validation gives an idea of how useful the model is for injury prediction.

Although less common, strain gauges have also been used to validate finite element models (*e.g.* Gray et al., 2008). In this case, experimental tests are performed on cadaveric material with strain gauges attached to regions of interest on the bones. The bone geometry

is then usually used as the basis of a finite element model (via CT scanning). The same loading conditions are applied to the model as were applied during experimental testing, and the strains at the gauge locations are compared between the experimental and simulated tests. This method of validation is usually performed on isolated bones, such as the tibia and femur, and the quality of the validation is assessed by plotting the experimental and simulated strains against each other and calculating the coefficient of determination (otherwise known as the  $R^2$  value). For previous studies in which FE models of isolated bones with inhomogeneous material properties were tested under quasi-static conditions, the coefficient of determination has ranged between 0.89 (Grassi et al., 2013) and 0.96 (Trabelsi et al., 2009). Conversely, for dynamic studies with homogenous material properties, greater strain deviations of up to 70% have been noted between the experiment and simulation (Burkhart et al., 2014, Quenneville and Dunning, 2011), even though overall force and fracture prediction were accurate. While biofidelity corridors assess the overall response of the model, this type of validation gives an indication of the accuracy of each individual bone's response to loading.

## **1.10 STRAIN GAUGES**

Strain gauges are used to measure the deformation of a structure in response to loading. The gauges are typically affixed to the surface of interest using a strong adhesive, such as cyanoacrylate. The gauge must adhere to the surface uniformly and securely in order to yield accurate strain measurements. The gauges themselves are essentially a wire twisted into a pattern reminiscent of the heating element in a stove and sandwiched between

two layers of insulation. When loading is applied to the structure, the surface at the gauge location is deformed, causing the foil structure to also deform. This changes the resistance of the wire proportionally to the exerted strain. The ends of the sensing wire are attached to insulated lead wires that connect to a data acquisition system (DAQ). The DAQ supplies power to the gauge and measures the change in resistance in response to loading.

Strain gauges are useful for measuring local strain values, which is adequate when the critical failure locations on a structure are known or can be estimated. However, the state of strain throughout an object can only be measured using more complex methods, such as digital speckle pattern interferometry (*e.g.* Yang et al., 2007). Other drawbacks of strain gauges are that the area to which they are to be attached must be readily accessible, and the lead wires and gauges themselves tend to be fragile. Furthermore, strain gauges have an averaging effect. As a result, at regions of high curvature with large strain gradients and areas of stress concentration, the strain readings may underestimate the actual value if the gauge is too large relative to the curvature (Intertechnology, 2013).

Strain gauges are linear, which means that they can only measure strain along their longitudinal direction. In order to measure the two plane strains and shear strain present at a location on the surface of a structure, three strain gauges can be combined to form a rosette. The strains from the three gauges can then be used to calculate the 2D state of strain (the principal strains and their orientations) (Beckwith et al., 2007).

## **1.11 STUDY RATIONALE AND OVERVIEW**

Ankle orientation has been shown to be a strong indicator of fracture risk during in-vehicle impacts (Klopp et al., 1997). However, the majority of previous experimental and numerical studies have been performed with the ankle in a neutral posture, and this may lead to an underestimation of the fracture tolerance of the foot/ankle complex. In order to examine and quantify this effect, a finite element model of the lower limb that is capable of being placed into a variety of validated postures will be constructed. Previous finite element models of the lower limb often position the bones of the foot and ankle by rotating a footplate to which the sole of the foot was attached (e.g. Shin et al., 2012). However, there is no way of knowing that the final bone positions that result from this rotation are true to the natural response of the ankle. Any inaccuracy in positioning may lead to error in how the load is transferred through the lower leg when the ankle posture is altered, particularly at the hindfoot.

In order to quantify this, the hindfoot bones of a cadaveric leg were instrumented with strain gauges, and subjected to sub-failure loads while CT scans were taken in a variety of ankle postures (Chapter 2). A finite element model of the lower limb was then constructed from these scans and evaluated based on several mesh quality criteria (Chapter 3). The posture of the ankle model was varied and the resulting bone positions and strains were compared with those from the experimental tests. The fracture tolerance of the lower leg was then predicted based on the maximum strains observed in the model and the critical strain values for cortical and cancellous bone from the literature (Chapter 4). Finally, conclusions, limitations and future directions were discussed (Chapter 5). The overall goal

of this project was to develop an enhanced FE model that can be used for future injury prediction studies. The results from this study will be useful in determining injury limits of the ankle, for developing postural guidelines to minimize injury, and for numerically evaluating new protective designs.

### **1.12 OBJECTIVES AND HYPOTHESES**

The objectives of this thesis are:

1. To develop a CT-compatible testing apparatus that allows the angle of the ankle of a cadaveric leg to be adjusted independently in three dimensions and the resulting bone positions to be measured, while also recording ankle strains in response to sub-failure loading applied during imaging.
2. a) To develop a finite element model based on CT scans of the cadaveric lower leg, and compare its response with the experimental strain and bone position data.  
b) To use the model to predict the fracture threshold and location in all tested ankle postures and to determine which posture is the most vulnerable to injury.

The corresponding hypotheses are:

1. CT scans taken of the ankle will demonstrate that ankle motion is a complicated combination of motions at various joints of the hind-foot, and strains measured in this region as posture is adjusted will demonstrate a relationship between ankle posture and load path.

2. a) The finite element model of the cadaveric leg developed herein will be reasonably in line with the experimental tests in terms of the strain distribution and the bone positions in all of the tested ankle postures.
- b) The model will be able to predict injury in altered postures, and will demonstrate that non-neutral ankle posture could reduce the fracture threshold of the lower leg and alter the predicted fracture location.

### 1.13 REFERENCES

- BANDAK, F., TANNOUS, R. & TORIDIS, T. 2001. On the development of an osseoligamentous finite element model of the human ankle joint. *International journal of solids and structures*, 38, 1681-1697.
- BEAUGONIN, M., HAUG, E. & CESARI, D. Improvement of numerical ankle/foot model: modeling of deformable bone Proceedings: Stapp Car Crash Conference, 1997. Society of Automotive Engineers SAE (Technical Paper 973328), 225-237
- BECKWITH, T. G., MARANGONI, R. D. & LIENHARD, J. H. 2007. *Mechanical measurements*, Pearson Prentice Hall.
- BEGEMAN, P., BALAKRISHNAN, P., LEVINE, R. & KING, A. 1993. Dynamic human ankle response to inversion and eversion. SAE Technical Paper 933115.
- BEGEMAN, P. C. & PRASAD, P. 1990. Human ankle impact response in dorsiflexion. SAE Technical Paper 902308.
- BURKHART, T. A., QUENNEVILLE, C. E., DUNNING, C. E. & ANDREWS, D. M. 2014. Development and validation of a distal radius finite element model to simulate impact loading indicative of a forward fall. *Proceedings of the Institution of Mechanical Engineers, Part H: Journal of engineering in medicine*, 0954411914522781.
- BURSTEIN, A. H., REILLY, D. T. & MARTENS, M. 1976. Aging of bone tissue: mechanical properties. *The Journal of Bone & Joint Surgery*, 58, 82-86.
- CARR, J. B., HAMILTON, J. J. & BEAR, L. S. 1989. Experimental intra-articular calcaneal fractures: anatomic basis for a new classification. *Foot & Ankle International*, 10, 81-87.
- CARTER, D. R. & HAYES, W. C. 1977. The compressive behavior of bone as a two-phase porous structure. *The Journal of Bone & Joint Surgery*, 59, 954-962.
- CASTILLO, R. C., MACKENZIE, E. J., WEGENER, S. T. & BOSSE, M. J. 2006. Prevalence of chronic pain seven years following limb threatening lower extremity trauma. *Pain*, 124, 321-329.

- CORAZZA, F., O'CONNOR, J., LEARDINI, A. & CASTELLI, V. P. 2003. Ligament fibre recruitment and forces for the anterior drawer test at the human ankle joint. *Journal of biomechanics*, 36, 363-372.
- COWIN, S. 1986. Wolff's law of trabecular architecture at remodeling equilibrium. *Journal of biomechanical engineering*, 108, 83-88.
- COWIN, S. C. 1989. *The mechanical properties of cortical bone tissue*, CRC Press, Boca Raton, FL.
- DAFTARY, A., HAIMS, A. H. & BAUMGAERTNER, M. R. 2005. Fractures of the Calcaneus: A Review with Emphasis on CT 1. *Radiographics*, 25, 1215-1226.
- DANIELS, T. R. & SMITH, J. W. 1993. Talar neck fractures. *Foot & Ankle International*, 14, 225-234.
- DONG, L., ZHU, F., JIN, X., SURESH, M., JIANG, B., SEVAGAN, G., CAI, Y., LI, G. & YANG, K. H. 2013. Blast effect on the lower extremities and its mitigation: A computational study. *Journal of the Mechanical Behavior of Biomedical Materials*, 28, 111-124.
- EBERLEIN, R., HOLZAPFEL, G. A. & FRÖHLICH, M. 2004. Multi-segment FEA of the human lumbar spine including the heterogeneity of the annulus fibrosus. *Computational mechanics*, 34, 147-163.
- ELGAFY, H., EBRAHEIM, N. A., TILE, M., STEPHEN, D. & KASE, J. 2000. Fractures of the talus: experience of two level 1 trauma centers. *Foot & Ankle International*, 21, 1023-1029.
- ERDEMIR, A., VIVEIROS, M. L., ULBRECHT, J. S. & CAVANAGH, P. R. 2006. An inverse finite-element model of heel-pad indentation. *Journal of biomechanics*, 39, 1279-1286.
- ESSEX-LOPRESTI, P. 1952. The mechanism, reduction technique, and results in fractures of the os calcis. *British Journal of Surgery*, 39, 395-419.
- FITZGIBBONS, T., MCMULLEN, S. & MORMINO, M. 2001. Fractures and dislocations of the calcaneus. *Rockwood and Green's Fractures in Adults*, ed, 5, 2131-2179.
- FUNK, J., HALL, G., CRANDALL, J. & PILKEY, W. 2000. Linear and quasi-linear viscoelastic characterization of ankle ligaments. *Journal of biomechanical engineering*, 122, 15-22.
- FUNK, J. R., CRANDALL, J. R., TOURET, L. J., MACMAHON, C. B., BASS, C. R., PATRIE, J. T., KHAEWPOONG, N. & EPPINGER, R. H. 2002a. The axial injury tolerance of the human foot/ankle complex and the effect of Achilles tension. *Journal of biomechanical engineering*, 124, 750-757.
- FUNK, J. R., SRINIVASAN, S. C. & CRANDALL, J. R. 2003. Snowboarder's talus fractures experimentally produced by eversion and dorsiflexion. *The American journal of sports medicine*, 31, 921-928.
- FUNK, J. R., SRINIVASAN, S. C., CRANDALL, J. R., KHAEWPOONG, N., EPPINGER, R. H., JAFFREDO, A. S., POTIER, P. & PETIT, P. Y. 2002b. The effects of axial preload and dorsiflexion on the tolerance of the ankle/subtalar joint to dynamic inversion and eversion. SAE Technical Paper 2002-22-0013.
- GARDNER, M. J., DEMETRAKOPOULOS, D., BRIGGS, S. M., HELFET, D. L. & LORICH, D. G. 2006. The ability of the Lauge-Hansen classification to predict

- ligament injury and mechanism in ankle fractures: an MRI study. *Journal of orthopaedic trauma*, 20, 267-272.
- GOLDSTEIN, S. A. 1987. The mechanical properties of trabecular bone: dependence on anatomic location and function. *Journal of biomechanics*, 20, 1055-1061.
- GOMEZ, M. A. & NAHUM, A. M. 2002. Biomechanics of bone. *Accidental injury*. Springer.
- GRASSI, L., VÄÄNÄNEN, S. P., AMIN YAVARI, S., WEINANS, H., JURVELIN, J. S., ZADPOOR, A. A. & ISAKSSON, H. 2013. Experimental validation of finite element model for proximal composite femur using optical measurements. *Journal of the Mechanical Behavior of Biomedical Materials*, 21, 86-94.
- GRAY, H. 2009. *Gray's Anatomy: With original illustrations by Henry Carter*, Arcturus Publishing.
- GRAY, H. A., TADDEI, F., ZAVATSKY, A. B., CRISTOFOLINI, L. & GILL, H. S. 2008. Experimental validation of a finite element model of a human cadaveric tibia. *Journal of biomechanical engineering*, 130, 031016.
- HADDOCK, N. T., WAPNER, K. & LEVIN, L. S. 2013. Vascular bone transfer options in the foot and ankle: a retrospective review and update on strategies. *Plastic and reconstructive surgery*, 132, 685-693.
- HALL, G. W. 1998. *Biomechanical Characterization and Multibody Modeling of the Human Lower Extremity*. University of Virginia.
- HELFET, D. L., KOVAL, K., PAPPAS, J., SANDERS, R. W. & DIPASQUALE, T. 1994. Intraarticular" pilon" fracture of the tibia. *Clinical orthopaedics and related research*, 298, 221-228.
- HUGHES, J., WEBER, H., WILLENEGGER, H. & KUNER, E. 1979. Evaluation of ankle fractures: non-operative and operative treatment. *Clinical orthopaedics and related research*, 138, 111-119.
- HUTTON, W. & DHANENDRAN, M. 1979. A study of the distribution of load under the normal foot during walking. *International orthopaedics*, 3, 153-157.
- INTERTECHNOLOGY 2013. Strain Gage Selection: Criteria, Procedures, Recommendations.
- IWAMOTO, M., MIKI, K. & TANAKA, E. 2005. Ankle skeletal injury predictions using anisotropic inelastic constitutive model of cortical bone taking into account damage evolution. *Stapp car crash journal*, 49, 133.
- KATHOL, M., EL-KHOURY, G., MOORE, T. & MARSH, J. 1991. Calcaneal insufficiency avulsion fractures in patients with diabetes mellitus. *Radiology*, 180, 725-729.
- KITAGAWA, Y., ICHIKAWA, H., KING, A. I. & LEVINE, R. S. 1998. A severe ankle and foot injury in frontal crashes and its mechanism. SAE Technical Paper 983145.
- KLOPP, G., CRANDALL, J., HALL, G., PILKEY, W., HURWITZ, S. & KUPPA, S. Mechanisms of injury and injury criteria for the human foot and ankle in dynamic axial impacts to the foot. Proceedings of the 1997 International IRCOBI Conference on the Biomechanics of Impact, 1997.
- KNUPP, P. M. 2000. Achieving finite element mesh quality via optimization of the Jacobian matrix norm and associated quantities. Part I—a framework for surface

- mesh optimization. *International Journal for Numerical Methods in Engineering*, 48, 401-420.
- LAUGE-HANSEN, N. 1950. Fractures of the ankle: II. Combined experimental-surgical and experimental-roentgenologic investigations. *Archives of Surgery*, 60, 957-985.
- LAURSEN, T. A. 2002. *Computational contact and impact mechanics: fundamentals of modeling interfacial phenomena in nonlinear finite element analysis*, Springer Science & Business Media.
- LEE, E. W. & DONATTO, K. C. 1999. Fractures of the midfoot and forefoot. *Current Opinion in Orthopaedics*, 10, 224-230.
- LUNDBERG, A., GOLDIE, I., KALIN, B. & SELVIK, G. 1989. Kinematics of the ankle/foot complex: plantarflexion and dorsiflexion. *Foot & Ankle International*, 9, 194-200.
- MACKENZIE, E. J., CASTILLO, R. C., JONES, A. S., BOSSE, M. J., KELLAM, J. F., POLLAK, A. N., WEBB, L. X., SWIONTKOWSKI, M. F., SMITH, D. G. & SANDERS, R. W. 2007. Health-care costs associated with amputation or reconstruction of a limb-threatening injury. *The Journal of Bone & Joint Surgery*, 89, 1685-1692.
- MANOLI, A., PRASAD, P. & LEVINE, R. S. 1997. Foot and ankle severity scale (FASS). *Foot & ankle international*, 18, 598-602.
- MARTIN, R., BURR, D. & SHARKEY, N. 1998. Skeletal tissue mechanics. *Editions Springer*.
- MAXWELL, J. C. 1878. *Encyclopedia Britannica*. Samuel L. Hall, New York, NY.
- MCCARTHY, M. L., MACKENZIE, E. J., EDWIN, D., BOSSE, M. J., CASTILLO, R. C., STARR, A., KELLAM, J. F., BURGESS, A. R., WEBB, L. X. & SWIONTKOWSKI, M. F. 2003. Psychological distress associated with severe lower-limb injury. *The Journal of Bone & Joint Surgery*, 85, 1689-1697.
- MCKAY, B. J. & BIR, C. A. 2009. Lower extremity injury criteria for evaluating military vehicle occupant injury in underbelly blast events. *Stapp car crash journal*, 53, 229.
- MODLESKY, C. M. & LEWIS, R. D. 2002. Does exercise during growth have a long-term effect on bone health? *Exercise and sport sciences reviews*, 30, 171-176.
- MORRIS, A., THOMAS, P., TAYLOR, A. M. & WALLACE, W. A. Mechanisms of Fractures in Ankle and Hind-Foot Injuries to Front Seat Car Occupants: An In-Depth Accident Data Analysis. Proceedings of the 41st Stapp Car Crash Conference, November 13-14, 1997, Orlando, Florida, USA (Sae Technical Paper 973328), 1997.
- NOE, D., VOTO, S., HOFFMANN, M., ASKEW, M. & GRADISAR, I. 1993. Role of the calcaneal heel pad and polymeric shock absorbers in attenuation of heel strike impact. *Journal of biomedical engineering*, 15, 23-26.
- OKANOBO, H., KHURANA, B., SHEEHAN, S., DURAN-MENDICUTI, A., ARIANJAM, A. & LEDBETTER, S. 2012. Simplified diagnostic algorithm for Lauge-Hansen classification of ankle injuries. *Radiographics*, 32, E71-E84.
- OTTE, D., VON RHEINBABEN, H. & ZWIPP, H. 1992. Biomechanics of injuries to the foot and ankle joint of car drivers and improvements for an optimal car floor development. SAE Technical Paper 922514.

- PETERSON, L., ROMANUS, B. & DAHLBERG, E. 1976. Fracture of the collum tali— an experimental study. *Journal of biomechanics*, 9, 277-279.
- QUENNEVILLE, C. E. & DUNNING, C. E. 2011. Development of a finite element model of the tibia for short-duration high-force axial impact loading. *Computer methods in biomechanics and biomedical engineering*, 14, 205-212.
- RAMASAMY, A., HARRISSON, S. E., CLASPER, J. C. & STEWART, M. P. 2008. Injuries from roadside improvised explosive devices. *The Journal of Trauma and Acute Care Surgery*, 65, 910-914.
- RAMASAMY, A., MASOUIROS, S. D., NEWELL, N., HILL, A. M., PROUD, W. G., BROWN, K. A., BULL, A. M. & CLASPER, J. C. 2011. In-vehicle extremity injuries from improvised explosive devices: current and future foci. *Philosophical Transactions of the Royal Society B: Biological Sciences*, 366, 160-170.
- RAMASAMY, M. A., HILL, C. A. M., MASOUIROS, S., GIBB, L.-C. I., PHILLIP, L.-C. R., BULL, A. M. & CLASPER, C. J. C. 2013. Outcomes of IED Foot and Ankle Blast Injuries. *The Journal of Bone & Joint Surgery*, 95, e25 1-7.
- RAMMELT, S., SCHNEIDERS, W., SCHIKORE, H., HOLCH, M., HEINECK, J. & ZWIPP, H. 2008. Primary open reduction and fixation compared with delayed corrective arthrodesis in the treatment of tarsometatarsal (Lisfranc) fracture dislocation. *Journal of Bone & Joint Surgery, British Volume*, 90, 1499-1506.
- REILLY, D. T. & BURSTEIN, A. H. 1974. The mechanical properties of cortical bone. *The Journal of Bone & Joint Surgery*, 56, 1001-1022.
- RHO, J., HOBATHO, M. & ASHMAN, R. 1995. Relations of mechanical properties to density and CT numbers in human bone. *Medical engineering & physics*, 17, 347-355.
- RUDD, R., CRANDALL, J., MILLINGTON, S., HURWITZ, S. & HÖGLUND, N. 2004. Injury tolerance and response of the ankle joint in dynamic dorsiflexion. *Stapp car crash journal*, 48, 1.
- SANDERS, R. & LINDVALL, E. 1999. Fractures and fracture-dislocations of the talus. *Surgery of the Foot and Ankle, ed*, 7, 1465-1518.
- SAPUAN, S., OSMAN, M. & NUKMAN, Y. 2006. State of the art of the concurrent engineering technique in the automotive industry. *Journal of Engineering Design*, 17, 143-157.
- SEIPEL, R. C., PINTAR, F. A., YOGANANDAN, N. & BOYNTON, M. D. 2001. Biomechanics of calcaneal fractures: a model for the motor vehicle. *Clinical orthopaedics and related research*, 388, 218-224.
- SHIN, J. & UNTAROIU, C. D. 2013. Biomechanical and Injury Response of Human Foot and Ankle Under Complex Loading. *Journal of Biomechanical Engineering*, 135, 101008-101008.
- SHIN, J., YUE, N. & UNTAROIU, C. D. 2012. A finite element model of the foot and ankle for automotive impact applications. *Annals of biomedical engineering*, 40, 2519-2531.
- SHUNMUGASAMY, V. C., GUPTA, N. & COELHO, P. G. 2010. High strain rate response of rabbit femur bones. *Journal of biomechanics*, 43, 3044-3050.

- SIEGLER, S., BLOCK, J. & SCHNECK, C. D. 1988. The Mechanical Characteristics of the Collateral Ligaments of the Human Ankle Joint\*. *Foot & Ankle International*, 8, 234-242.
- SMITH, P. N. & ZIRAN, B. H. 1999. Fractures of the talus. *Operative techniques in orthopaedics*, 9, 229-238.
- SOLAN, M. C., MOORMAN, C. T., MIYAMOTO, R. G., JASPER, L. E. & BELKOFF, S. M. 2001. Ligamentous restraints of the second tarsometatarsal joint: a biomechanical evaluation. *Foot & Ankle International*, 22, 637-641.
- TAKEBE, K., NAKAGAWA, A., MINAMI, H., KANAZAWA, H. & HIROHATA, K. 1984. Role of the Fibula in Weight-bearing. *Clinical orthopaedics and related research*, 184, 289-292.
- TANNOUS, R. E., BANDAK, F. A., TORIDIS, T. G. & EPPINGER, R. H. 1996. A three-dimensional finite element model of the human ankle: development and preliminary application to axial impulsive loading. SAE Technical Paper 962427.
- TRABELSI, N., YOSIBASH, Z. & MILGROM, C. 2009. Validation of subject-specific automated p-FE analysis of the proximal femur. *Journal of Biomechanics*, 42, 234-241.
- TRNKA, H.-J., ZETTL, R. & RITSCHL, P. 1998. Fracture of the anterior superior process of the calcaneus: an often misdiagnosed fracture. *Archives of orthopaedic and trauma surgery*, 117, 300-302.
- TROY, K. L. & GRABINER, M. D. 2007. Off-axis loads cause failure of the distal radius at lower magnitudes than axial loads: a finite element analysis. *Journal of biomechanics*, 40, 1670-1675.
- UNTAROIU, C., DARVISH, K., CRANDALL, J., DENG, B. & WANG, J.-T. 2005. A finite element model of the lower limb for simulating pedestrian impacts. *Stapp car crash journal*, 49, 157.
- VALLE, L. & RAY, M. 2005. Development and validation of a 50th percentile male human femur: Attachment A. *National Highway Traffic Safety Administration, Worcester, MA: Worcester Polytechnic Institute*.
- VON MEYER, G. H. 2011. The Classic: The Architecture of the Trabecular Bone (Tenth Contribution on the Mechanics of the Human Skeletal Framework). *Clinical Orthopaedics and Related Research®*, 469, 3079-3084.
- VUORI, J.-P. & ARO, H. T. 1993. LISFRANC JOINT INJURIES. TRAUMA MECHANISMS AND ASSOCIATED INJURIES. *Journal of Trauma and Acute Care Surgery*, 35, 40-45.
- YAMADA, H. & EVANS, F. G. 1970. *Strength of biological materials*, Williams & Wilkins Baltimore.
- YANG, L., ZHANG, P., LIU, S., SAMALA, P. R., SU, M. & YOKOTA, H. 2007. Measurement of Strain Distributions in Mouse Femora with 3D-Digital Speckle Pattern Interferometry. *Optics and lasers in engineering*, 45, 843-851.
- YOGANANDAN, N., PINTAR, F., KUMARESAN, S. & BOYNTON, M. 1997. Axial impact biomechanics of the human foot-ankle complex. *Journal of biomechanical engineering*, 119, 433-437.

YOGANANDAN, N., PINTAR, F. A., BOYNTON, M., BEGEMAN, P., PRASAD, P., KUPPA, S. M., MORGAN, R. M. & EPPINGER, R. H. 1996. Dynamic axial tolerance of the human foot-ankle complex. SAE Technical Paper 962426.

---

## Chapter 2 – Cadaveric Testing

---

### 2.1 INTRODUCTION

The ankle is an intricate mechanism with many degrees of freedom provided by multiple joints. Interactions between the fibula, tibia, talus and calcaneus play an important role in some of the most common ankle fractures (*e.g.* Lauge-Hansen, 1950), but few known studies have examined how the bones of the hindfoot move relative to one another when loads are applied and ankle posture is adjusted (Lundberg, 1988, Siegler et al., 1988). These postural changes may also have an effect on the load path through the foot/ankle complex, potentially reducing the fracture threshold and altering the fracture location. The majority of previous studies examining the injury tolerance of the lower leg and ankle have been performed with the ankle in a neutral posture (*e.g.* Yoganandan et al., 1997). The studies that have looked at the effect of ankle posture on the injury tolerance of the lower leg typically test in a limited number of positions (*e.g.* Rudd et al., 2004), making it difficult to obtain a sense of which postures are the most resilient, and what types of injuries are most commonly observed in which positions. Furthermore, the outcomes of these studies are usually moment-angle curves (*e.g.* Funk et al., 2002b) that give an overall response of the foot/ankle complex to rotation, but provide little information on the stresses in the individual bones.

The purpose of this study was to quantify the change in the positions and rotations of the bones of the foot/ankle complex, relative to the neutral posture, in a variety of positions that the ankle frequently assumes during injurious events and in which fractures

are commonly reported, using a cadaveric lower leg. The ankle postures were also chosen to be representative of the full range of motion of the ankle. The change in load path through this region in response to variation in ankle posture was also studied by measuring surface strains on the hindfoot bones in response to sub-failure loading at each chosen posture. This positional and strain data will be used to evaluate the response of the finite element model of the foot and ankle discussed in Chapter 4.

## **2.2 METHODS**

### **2.2.1 SPECIMEN PREPARATION – DISSECTION**

A fresh-frozen male cadaveric left lower leg (age 46, sectioned at the tibial plateau) was dissected to allow for the placement of seven strain gauges, the locations of which are described in Section 2.2.3. The leg was removed from the freezer and allowed to thaw at room temperature for nine hours. A quarter-circular incision was made on the medial side (Figure 2.1a) and the fascia and fat directly beneath the skin were cut with a scalpel. The incision was spread with forceps to reveal the medial malleolus, and the medial surface of the calcaneus bone was revealed by cutting through and spreading a superficial layer of flesh. At bone surfaces where gauges were to be placed, the periosteum was removed using a scalpel followed by sandpaper when this layer became sufficiently thin. In order to access the talar neck, the tibionavicular and anterior tibiotalar portions of the deltoid ligament were spread apart. Using a pair of forceps to hold the incision open and another pair as a lever to pull the skin, fascia, ligaments and tendons away from the bottom of the foot, the plantar surface was revealed.

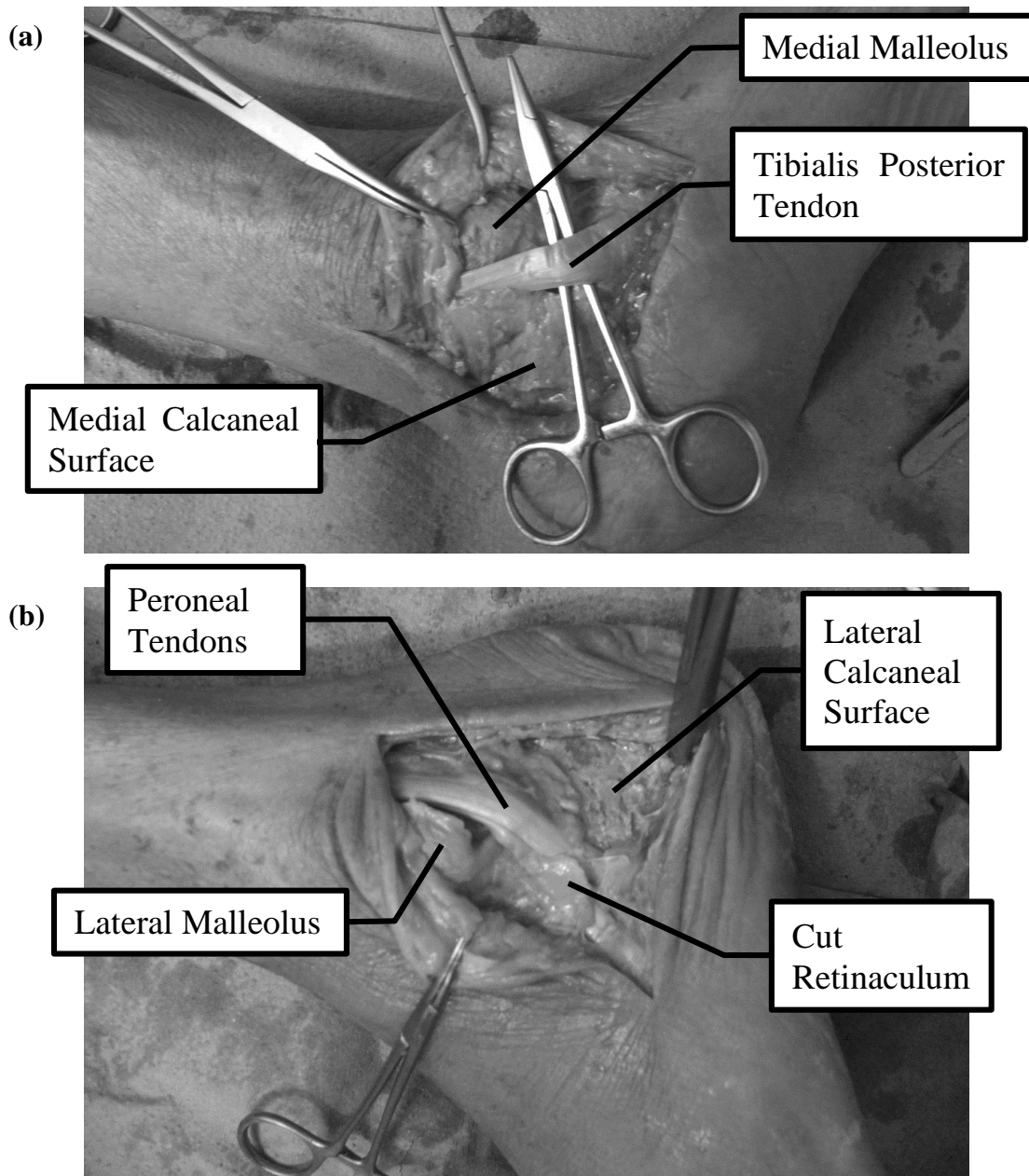


**Figure 2.1: Accessing the Medial and Lateral Ankle Compartments**

The medial compartment of the ankle (a) was exposed by spreading a semi-circular incision with forceps and cutting the fascia and fat directly beneath the skin. This allowed for access to the medial malleolus of the tibia, the medial and plantar calcaneal surfaces, and the medial talar neck. The tibialis posterior tendon is indicated as a reference for location. The lateral compartment of the ankle (b) was exposed in the same way as the medial side, enabling access to the lateral malleolus of the fibula, the lateral calcaneal surface, and the talar sulcus. The peroneal retinaculum had to be sacrificed to access the talar sulcus and its remains are shown. The peroneal tendons are also indicated as a reference for location.

A quarter-circular incision was made on the lateral side (Figure 2.1b), and using a similar procedure to the medial side, the soft tissues were resected using scalpel and forceps to reveal the lateral malleolus of the fibula and the lateral calcaneal surface. In order to access the talar sulcus, the inferior peroneal retinaculum had to be sacrificed, and a small amount of flesh and fascia were removed using scissors and a scalpel. The total amount of flesh removed throughout the entire specimen preparation process was minimal (on the order of about 1-2 cm<sup>3</sup> of volume). Finally, in order to create room to place a strain gauge in the arch of the talar sulcus, the interosseous ligament was sacrificed. Apart from those mentioned above, no visible damage was observed to any other load-bearing soft tissues on the medial and lateral sides of the foot. Both incisions were sutured, and a space was left in each incision for the wires to pass through.

## 2.2.2 SPECIMEN PREPARATION – STRAIN GAUGE SELECTION

It was important to select strain gauges suitable for mounting on the surfaces of the talus and calcaneus bones, where curvature is often substantial. Under load, large strain gradients may be generated at these regions of curvature, and as a result, the gauge length should be no more than one tenth of the radius of curvature of the surface upon which it is applied in order to get a proper reading of the local stresses and not an average over a large region (Intertechnology, 2013). The locations of gauge placement (described in Section 2.2.3), were identified on a hard foam skeletal model of a 50<sup>th</sup> percentile male lower limb, and the curvature was estimated by drawing contour lines at these locations and measuring the resulting radii. The smallest radius of curvature was estimated to be 1 cm, meaning

that gauge lengths of 1 mm or less had to be used. One millimeter strain gauges are the smallest size that are readily available and relatively inexpensive, and so stacked 0°-45°-90° rosettes of this gauge length were selected (I274-UFRA-1-23-3L, Hoskin Scientific Ltd., Burlington, ON). Rosettes were selected due to the complex state of strain throughout these bones, the principal direction of which was not known. The curvature values at the actual gauge locations after installation were subsequently measured on the Computed Tomography (CT) scans (Appendix B).

### 2.2.3 SPECIMEN PREPARATION – STRAIN GAUGE PLACEMENT

The seven strain gauge rosettes were placed on the bones of the foot and ankle complex to record strains in response to quasi-static axial loading. These gauges were placed on the apex of the medial malleolus of the tibia (1), on the apex of the lateral malleolus of the fibula (2), on the plantar (3), medial (4) and lateral (5) surfaces of the calcaneus, on the medial side of the talar neck (6) and on the talus at the apex of the sulcus tali (7). Tibial, fibular and calcaneal gauge positions are shown in Figures 2.2 - 2.4, representing the medial, lateral, and dorsal sides of the foot/ankle complex, respectively, and talar strain gauges are shown in Figure 2.5. The strain gauge rosettes were attached to the bones using the protocol described in Appendix C.

The strain locations were chosen to be easily accessible from the incisions made on the lateral and medial sides of the specimen, as this would minimize dissection, and in particular the removal of soft tissues such as ligaments and tendons. This was true for all gauges except for those on the lateral talus (3) and plantar calcaneus (7), which required

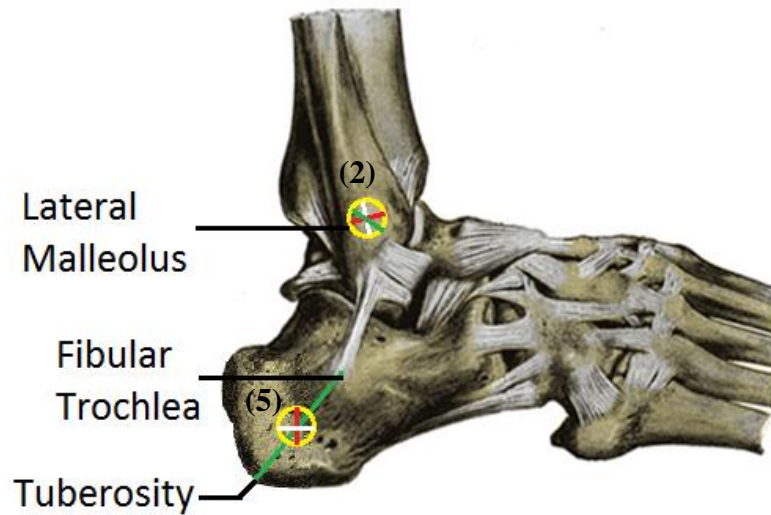


**Figure 2.2: Strain Gauge Locations on the Lateral Side of the Foot**

A strain gauge was placed on the lateral malleolus of the fibula (2), as well as the lateral calcaneal surface (5) midway between the tuberosity and the fibular trochlea. Rosettes are indicated with yellow circles, and red, white and green lines show the intended orientations of the gauges. Adapted from (Gray, 2009).

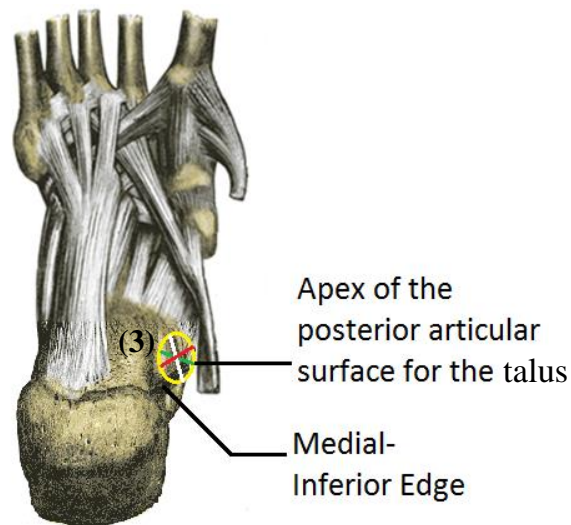


**Figure 2.3: Strain Gauge Locations on the Plantar Surface of the Foot**

A strain gauge was placed on the plantar surface of the calcaneus (3) along the medial inferior edge. Rosettes are indicated with yellow circles, and red, white and green lines show the intended orientations of the gauges. Adapted from (Gray, 2009).

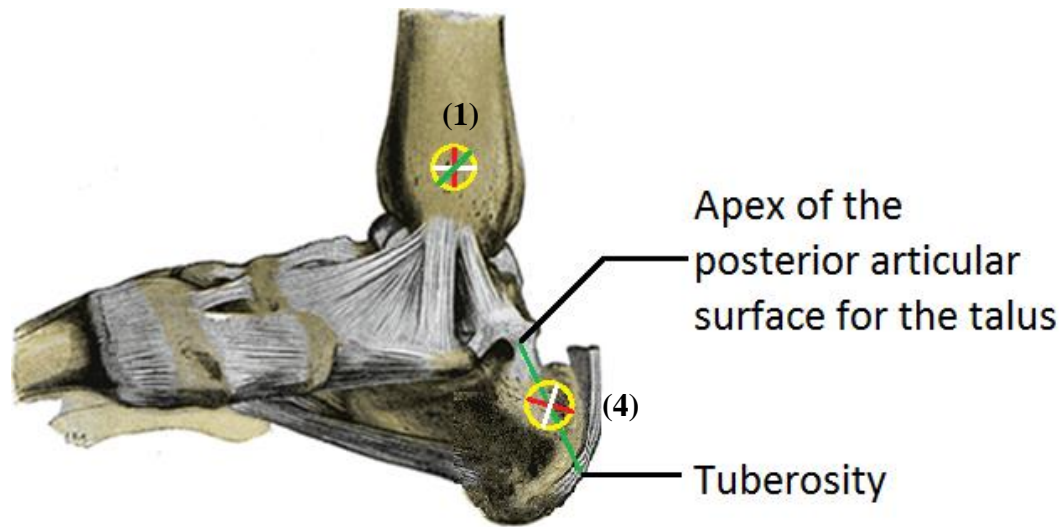


**Figure 2.4: Strain Gauge Locations on the Medial Side of the Foot**

A strain gauge was placed on the medial malleolus of the tibia (1), as well as the medial calcaneal surface (4) midway between the apex of the posterior articular surface for the talus and the tuberosity. Rosettes are indicated with yellow circles, and red, white and green lines show the intended orientations of the gauges. Adapted from (Gray, 2009).

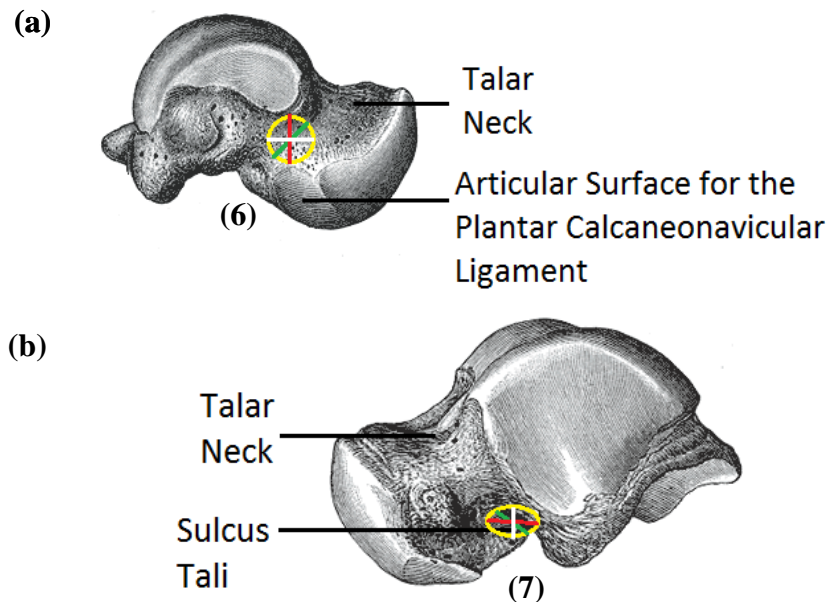


**Figure 2.5: Talar Strain Gauge Locations**

On the medial side of the talus (a), a strain gauge was attached to the talar neck (6). On the lateral side of the talus (b), a strain gauge was attached to the talar sulcus (7). Rosettes are indicated with yellow circles, and red, white and green lines show the intended orientations of the gauges. Adapted from (Gray, 2009).

more substantial dissection. Gauges were also positioned at locations that would not come into contact with other bones as the posture of the ankle was altered, in order to minimize the risk of damage to the gauges, which was a concern mostly for the talar gauges. Where possible, the locations coincided with, or were located close to, areas of particular vulnerability, such as fracture lines, as strain readings may be highest at these locations. Common fracture lines for the calcaneus are seen in Figure 2.6 (Daftary et al., 2005), with the calcaneal gauge locations indicated to give a sense of their proximity to the fracture lines. The talar gauges were both placed on the talar neck, which is the most common location for talar fracture (Metzger et al., 1999). Gauges were placed on the medial, lateral and plantar aspects of the calcaneus, and the medial and lateral aspects of the talus, in an effort to produce a picture of the overall distribution of the strain field on the entire surface of these bones.

Accurate positioning for the gauges was ensured by using a laser line intersecting anatomic landmarks that were easily palpated or identified visually. In certain cases, a set square was used to position gauges at the 90° intersection of lines emanating from anatomical landmarks. In the case of the calcaneus, the rosettes were always oriented so that the 45° gauge was aligned with the laser. In the case of the talus, the 45° gauge was always aligned with direction of the “groove” of the talar neck. CT-sensitive markers (1/8” acrylic balls) were glued on top of each strain gauge so that their locations would be more apparent on the CT scans. However, the high density of the metal in the gauges themselves proved to be sufficient to identify them.

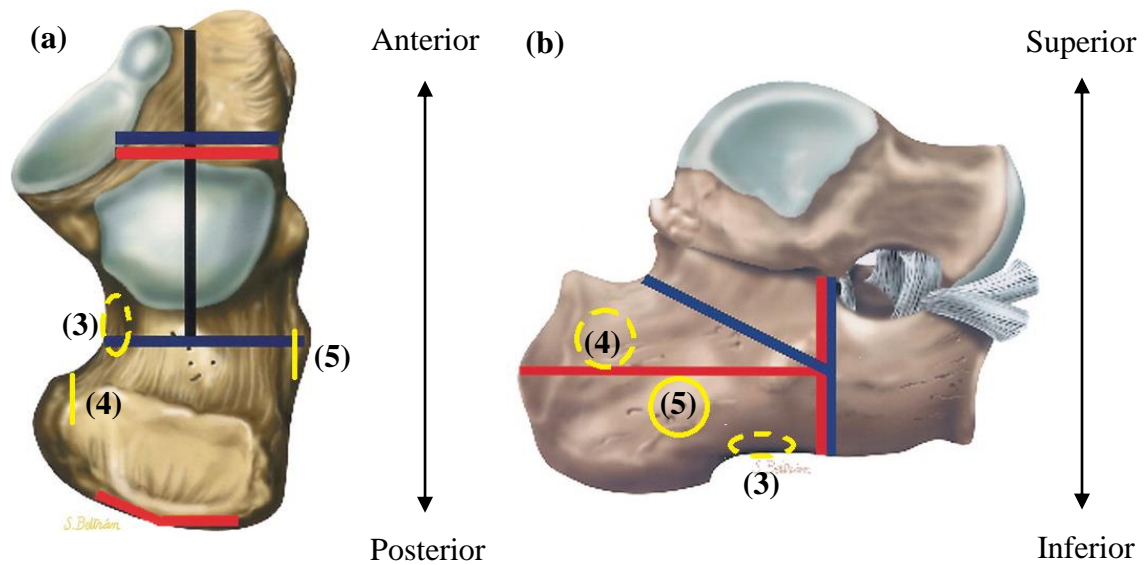


**Figure 2.6: Calcaneal Fracture Lines**

Common fracture lines of the calcaneus in the transverse plane (superior view) (a) and sagittal plane (lateral view) (b). The axes beside each figure specify the anatomical directions. Black, blue and red lines indicate shear, compression and tongue fracture lines respectively. Yellow circles indicate strain gauge locations: plantar gauge (3), medial gauge (4), lateral gauge (5). Adapted from (Daftary et al., 2005).

The lateral calcaneal gauge (5) was placed halfway between a line intersecting the posterior-most bulge of the tuberosity and the fibular trochlea (Figure 2.2). The plantar calcaneal gauge (3) was placed at the location where a 90° angle was formed between a line emanating from the apex of the posterior articular surface for the talus and the medial-inferior edge of the calcaneus, just on the plantar side of this edge (Figure 2.3). The medial calcaneal gauge (4) was placed halfway between a line drawn from the apex of the posterior articular surface for the talus to the posterior-most bulge of the tuberosity (Figure 2.4). The medial talar gauge (6) was placed on the medial neck of the talus immediately superior to the articulating surface for the plantar calcaneonavicular ligament (Figure 2.5a). The lateral talar gauge (7) was placed on the inferior surface of the talus bone at the apex of the opening to the sulcus tali (Figure 2.5b).

Finally, strain gauges were placed on the apex of both the lateral malleolus of the fibula (2) (Figure 2.2) and the medial malleolus of the tibia (1) (Figure 2.4). For the fibula, the 0° gauge was aligned with the direction of the long axis of the bone, whereas for the tibia, the 90° gauge was aligned with the direction of the long axis. These gauge orientations were chosen so that the gauge wires had the most direct path to exit through the medial and lateral incisions without having to bend or kink.

#### 2.2.4 SPECIMEN PREPARATION – POTTING PROCEDURE

Approximately 3” of soft tissues were stripped away from the proximal end of the leg in preparation for potting. The bones were then lightly sanded to remove any fat and remaining soft tissue. This was done to improve the adhesion of the dental cement, which

is the medium in which the leg was potted. In order to fit the leg into the 3.5” diameter potting fixture (Figure 2.7), a few millimeters at the lateral head of the fibula and approximately one centimeter at the medial tibial plateau had to be sawed away. No apparent damage was done to the joint connecting the two bones proximally. Potting of the bone was made easier by using a custom-designed potting apparatus that is capable of both holding the bone and adjusting its alignment by turning threaded rods. The four screw holes on the bottom of the empty potting fixture were aligned with the 4 screws on the potting apparatus.

Denstone<sup>®</sup> dental cement (Saint-Gobain NorPro, Stow, Ohio, USA) (at a mix of 30 ml water per 100 g of powder) was used as the adhesive material, and proper alignment of the leg was ensured using laser levels 90° to each other and perpendicular to the long axis of the tibia. The leg was placed in the potting fixture to a depth of 3.25”, and the threaded rods were used to adjust the position of the leg until proper alignment was achieved. In the sagittal plane, the laser was lined up with the center screws of the potting fixture and the medial malleolus (Figure 2.7a). In the frontal plane, the laser was lined up with the center screws of the potting fixture and the space between the first and second toes (Figure 2.7b). Once the alignment was achieved, the dental cement was poured into the potting fixture and allowed to cure for 15 minutes.

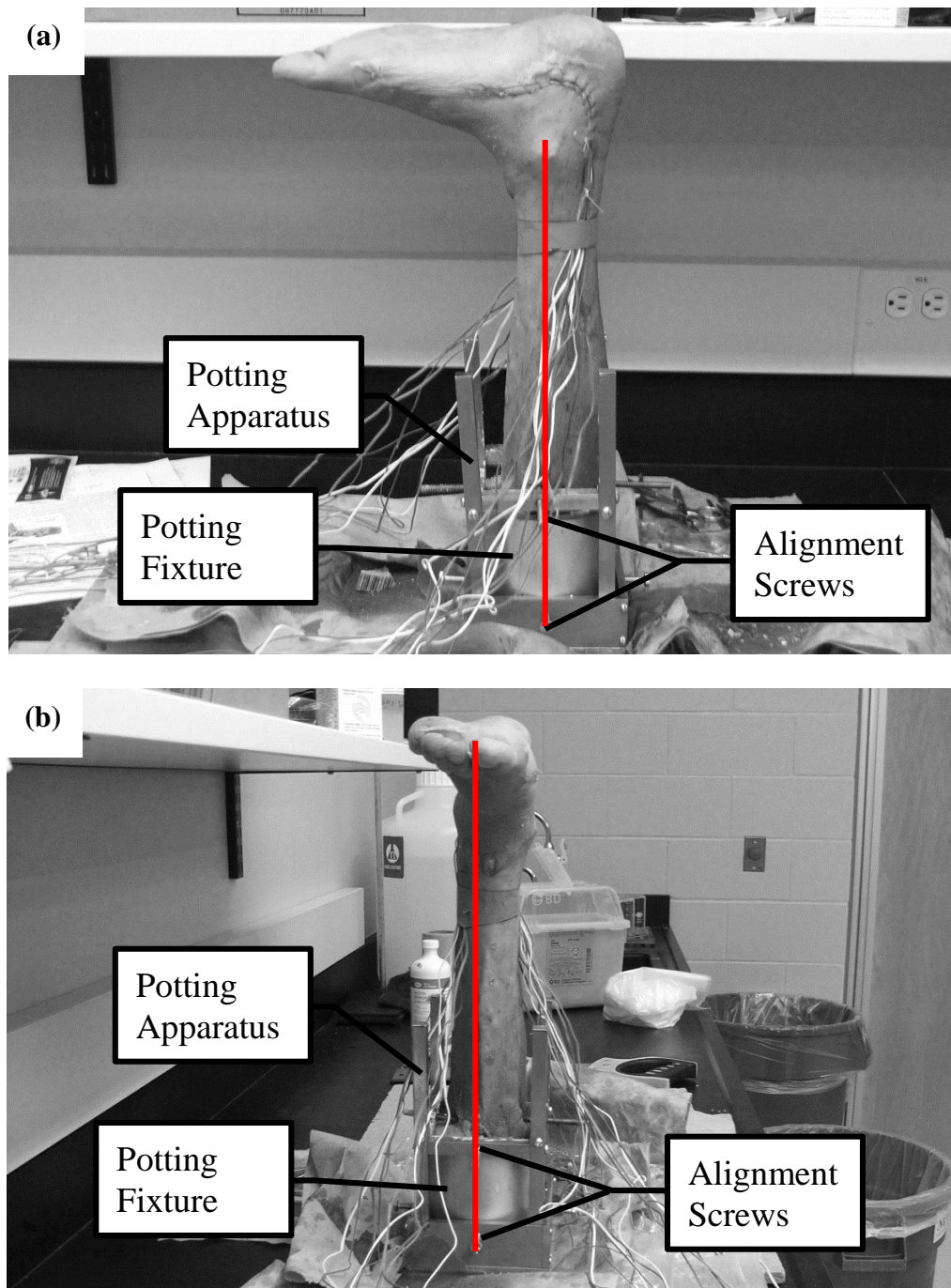


**Figure 2.7: Alignment of the Potted Leg**

In the sagittal plane (a), proper alignment of the specimen was ensured by using a laser line intersecting the two screws of the potting apparatus and the medial malleolus. In the frontal plane (b), proper alignment of the specimen was ensured by using a laser line intersecting the two screws of the potting apparatus and the space between the first and second toes. The red lines indicate laser alignment.

## 2.2.5 TEST FRAME CONSTRUCTION

### 2.2.5.1 *Design Objectives*

In order to measure the precise positions of the bones of the foot in various postures, while recording strains at the hindfoot in response to axial load, a custom-designed CT-compatible test frame was constructed. The main design objectives for this device were:

- To allow for the attachment of a variety of sizes of leg, potted at the proximal tibia, and the application of measurable and incremental static axial loads to the sole of the foot from 0 to 150 lbs (667 N).
- To incorporate a previously-constructed ankle positioner that is capable of adjusting the angle of the ankle independently in three dimensions.
- To be able to fit into the 34.5” bore of the available CT scanner (Philips Brilliance Big Bore, 120 kV, 249.48 mAs, 1 mm axial slice thickness, 0.32 mm in-plane resolution), with the specimen within the 23.6” field of view, and be devoid of any metal in areas that may potentially need to be scanned.
- To be low cost, easy to repair, and weigh less than 350 lbs total, as this is the approximate load limit of the CT scanner.
- To be able to be machined in a standard machine shop.

### 2.2.5.2 *Ankle Positioner*

A previously-constructed ankle positioner (Figure 2.8a) that is capable of adjusting the angle of the ankle independently in three dimensions was incorporated into the test frame. The foot rests against the foot plate of the ankle positioner and is secured via an

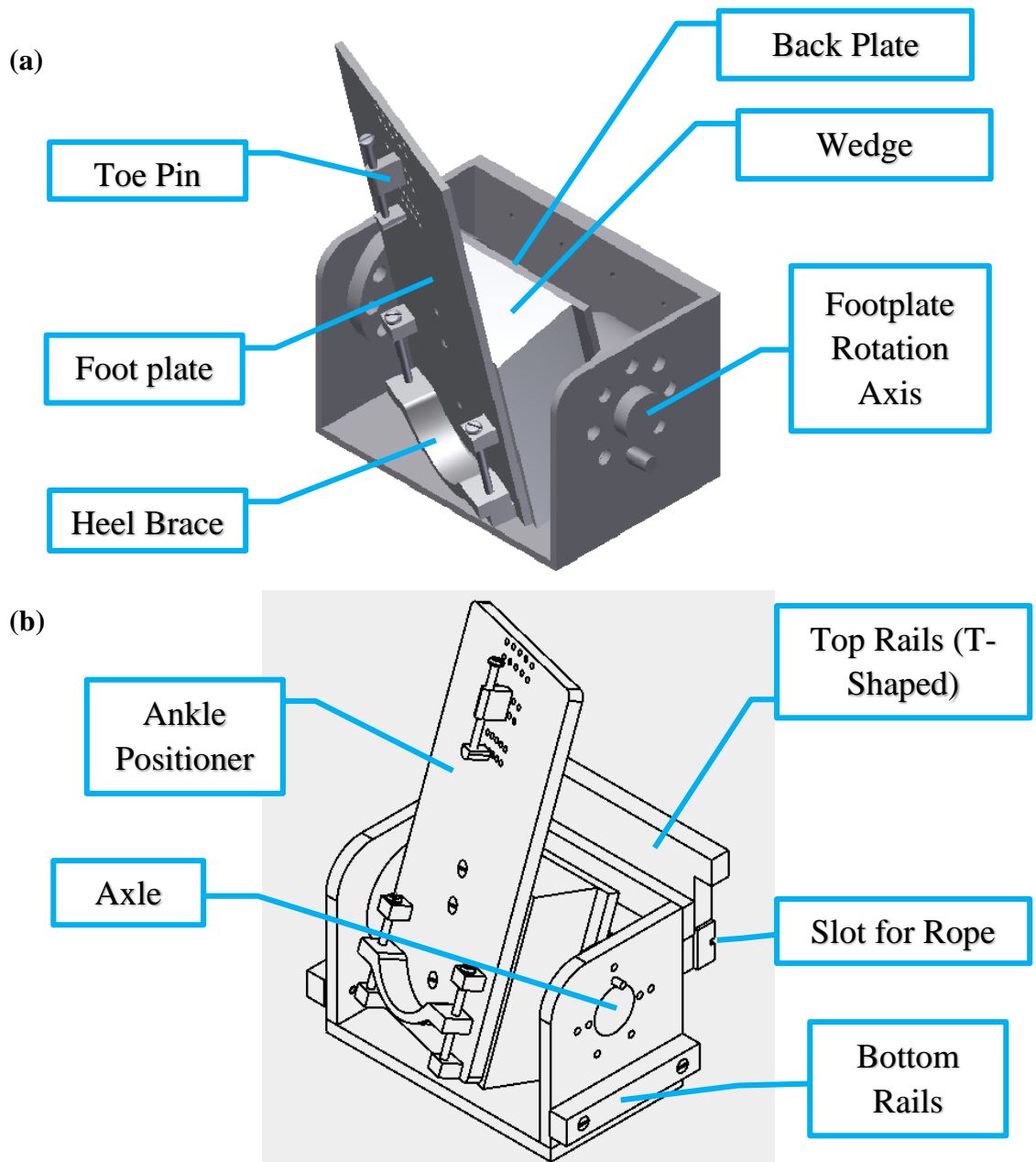


**Figure 2.8: Original and Modified Ankle Positioner**

The ankle positioner (a) can adjust the posture of the ankle independently in three dimensions via wedges (for inversion/eversion), rotation of the footplate (for dorsiflexion/plantarflexion) and toe pin position (for internal/external rotation). The foot rests against the footplate and is secured by adjusting the heel brace and the toe pin. The ankle positioner was modified (b) by attaching rails to allow it to slide freely in the slots of the top and bottom struts of the test frame. Bottom rails were attached on the sides of the bottom of the ankle positioner that span the length of the device. A t-shaped piece was attached to the back of the ankle positioner to provide the top rails.

adjustable heel brace and toe pin. Dorsiflexion and plantarflexion are controlled by rotating the footplate about the medial-lateral axis, and pins are used to select the desired angle. Inversion and eversion are controlled via wedges of various inclination, which are attached between the footplate and backplate. Internal and external rotation are controlled by the location of the toe pin, which sits between the big toe and the second toe.

### *2.2.5.3 Test Frame*

The test frame can be seen in Figure 2.9 and detailed engineering drawings of each of the components described in this section can be found in Appendix D. The test frame is essentially a crate that houses the ankle positioner and allows it to slide freely along the long axis of the test frame via slots that were machined into the top and bottom struts. The load path was kept aligned with the center axis of the leg, and the struts were made from  $\frac{3}{4}$ " acrylic so that the slots would deform minimally under load, allowing the ankle positioner to slide with minimal friction. All components that were within the CT-scanning range (at the center of the frame) were made from acrylic, a CT-compatible material. Slot lengths were chosen based on an anthropomorphic chart (TheErgonomicsCenter, 2008) that shows that the distance from the sole of the foot to the knee measures 21.7" for a 95<sup>th</sup> percentile male and 16.76" for a 10<sup>th</sup> percentile female. These measurements represent the distance between the potting fixture and the footplate, and are the largest and smallest specimens that the test frame is capable of accommodating. The depth of the ankle positioner in all postures was also accounted for when selecting the size of the frame and the length of the slots.

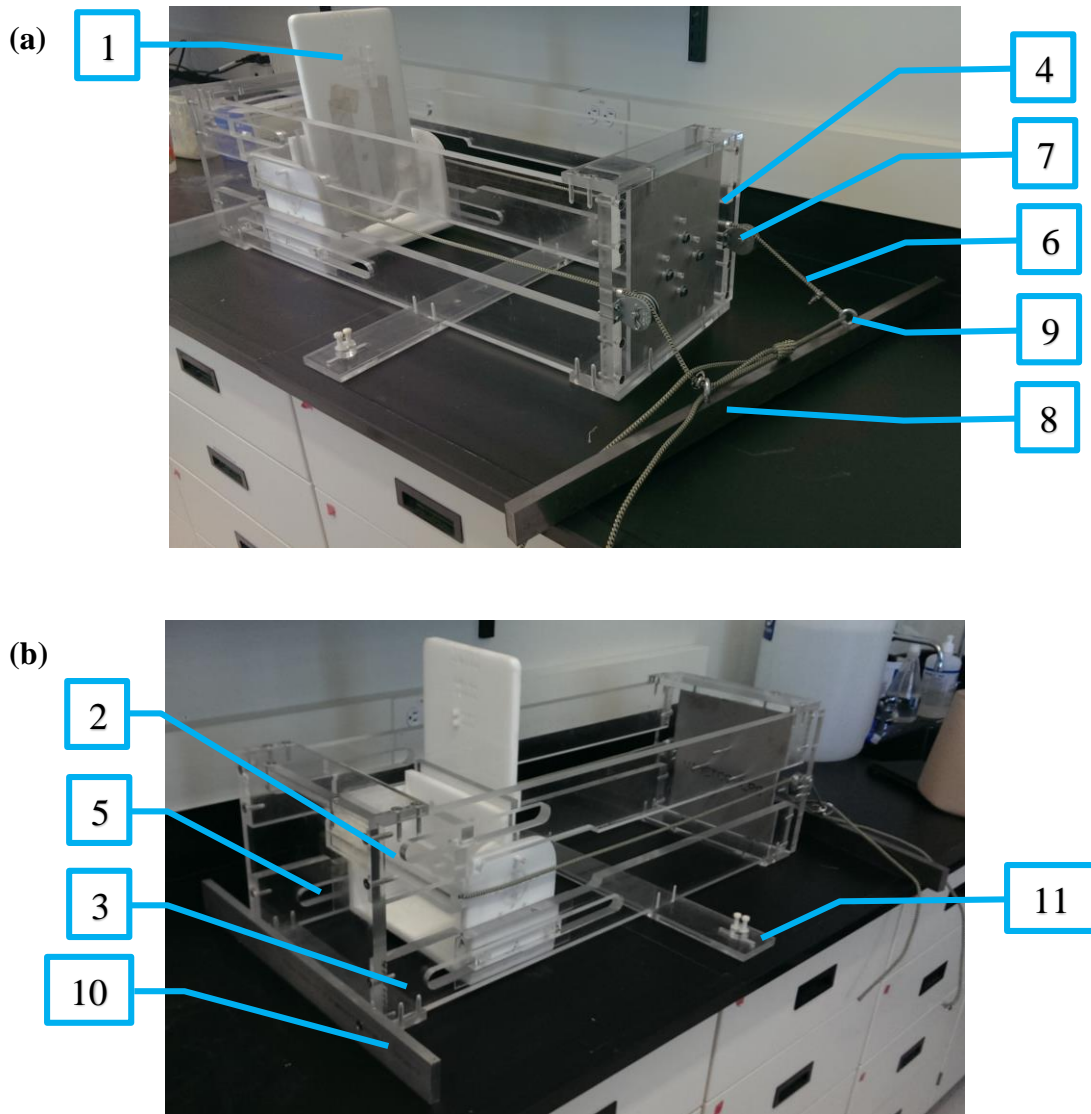


**Figure 2.9: Test Frame**

Front (a) and back (b) views of the test frame are shown. The test frame allows the ankle positioner (1) to move freely within slots in the top (2) and bottom (3) struts, and these struts meet at the front (4) and back (5) end plates. The front end plate has four screw holes that allow for attachment of the potting fixture, and another two holes on either side that allow the pulley ropes (6) to pass through. The ropes pass through the pulleys (7) that are also attached to the front plate, and allow for the application of force to the cadaveric lower leg by connecting the ankle positioner with the weight bar (8). The rope passes through eyelets (9) screwed into the weight bar and the force from the weights is balanced by fixation of the test frame to the CT bed at the clamping bar (10) via C-clamps. Slotted wings and pegs on each side (11) allow the frame to be centered in the CT scanner.

The four slotted struts that make up the sides of the test frame were attached to the front and back end plates via  $\frac{1}{4}$ " steel machine screws, and these connections were reinforced by cross-members that limit relative movement between the struts and the plates. Metal inside the range of the CT scan can cause distortion, but outside this range has no negative effects. The front and back plates were made from  $\frac{3}{4}$ " acrylic as they are some of the main structural supports of the test frame. This is especially true for the front plate, which must bear both the compressive force of the potting fixture and the leg, and the downward shear force from the hanging weights and pulleys. The potting fixture mounts to this plate via four screw holes, and another two holes are present at the sides to allow the pulley ropes to pass through. These ropes pass through the pulleys that are attached to the front plate just below these holes, and allow the test frame to apply axial force to a cadaveric leg by connecting the ankle positioner and the weight bar. When the test frame is mounted in the CT scanner, the weight bar is suspended off the cantilevered end of the bed and weights are applied. This causes the ankle positioner to apply force to the sole of the foot of the cadaveric leg that is between it and the front plate. The front plate was chosen to be slightly wider than the back plate to accommodate the pulleys.

The pulleys that were chosen are 1.5" in diameter, and were used with five millimeter nylon climbing rope. The weight bar was constructed by screwing two threaded eyelets (through which the rope would pass) into a ten lb rectangular prism of cold rolled steel, and the thickness of the bar was chosen to match the slot width of slotted weights that were available to use. The length of the bar allowed 150 lbs of weights to be suspended, based on the slot lengths. Weights of the same mass were always applied in

tandem on opposite ends of the weight bar, and were pushed up against the threaded eyelets, to ensure that the weight was evenly distributed between the two pulleys. At the locations where the rope passed through the eyelets, two clamps were attached to the rope to restrict movement of the bar and guarantee that it would remain parallel with the ground. The ultimate strength of nylon rope is 880 lbs (TheEngineeringToolbox, 2014), and due to the fact that two pulleys were used, there were two load paths through the device, meaning that each side of the rope would take 75 lbs of load. To connect two ends of the rope to form a loop, a triple fisherman's knot was chosen, as this knot has been shown to only reduce the tensile strength of rope by around 25%, whereas most other knots or mechanical rope connectors have been shown to reduce rope strength by much greater percentages (Richards, 2014). Combining this information, the safety factor on the rope, for a 150 lb total load to the leg was  $(880 * 0.75 \text{ lbs}) / 75 \text{ lbs} = 8.8$ .

The purpose of the clamping bar is to rigidly fix the entire test frame to the CT bed, limiting its motion in all directions and acting as a counterbalance for the hanging weights. This part is attached to the back plate and is made from aluminum to provide the necessary strength under bending, since it is away from the scanning region. This part is attached to the test frame in an upright position because its moment of inertia in this orientation creates the greatest bending resistance. The clamping bar is attached to the test frame via two steel  $\frac{1}{4}$ " screws that pass through the back plate and screw directly into the bottom struts.

Accurate positioning of the frame is accomplished by the wing. Slots in this component allow for adjustment of positioning pegs that fit into semi-circular holes located all along the length of the CT bed. The pegs can be tightened into place, limiting movement

of the test frame from side-to-side and front-to-back. The wing attaches to the middle of each bottom strut via acrylic screws, as this is in the field of view of the scanner.

The potting fixture has a depth of 3.25” and an inner diameter of 3.5” to serve the function of potting the proximal tibia. Threaded screw holes are present in the solid back of the fixture to allow it to connect rigidly with the front plate of the test frame.

The overall dimensions of the device are 37” x 24” x 10.75”, and its total weight is 75 lbs. When the specimen (10 lbs) and the hanging weights (150 lbs) are included, the total weight is 235 lbs, which is less than the CT scanner load limit of 350 lbs. The cross-sectional dimensions of the device (24” x 10.75”) allow it to fit within the circular bore (34.5” diameter), and the specimen is centered in this cross section, allowing it to be detected in the 23.6” field of view. All components were connected via screws, permitting the device to be easily repaired in the future, as needed.

#### *2.2.5.4 Ankle Positioner Modifications*

To adapt the ankle positioner to slide in the slots of the top and bottom struts of the test frame, top and bottom rails had to be attached (Figure 2.8b). The bottom rails were selected to be the same length as the ankle positioner itself and were attached via acrylic screws. The top rails were generated via a t-shaped component that was attached to the back of the ankle positioner also via acrylic screws. Ankle positioner machining tolerances were not very consistent, and these screw holes had to be created at a slight inclination relative to the ankle positioner so that the end result would be that the top rails fit nicely in

the slots of the top struts. A slot was also cut in the face of this t-shaped component for the rope to sit.

The ankle positioner was not initially designed to bear substantial load. The two axle shafts, which are the primary load path through the ankle positioner, were initially attached to the rest of the ankle positioner by one nylon screw each. Four extra nylon screws were inserted at each axle to improve shear strength. Furthermore, the back plate and foot plate were machined from only ½” acrylic and the back plate was made from a piece of scrap acrylic that had previously been fractured into three separate pieces and was subsequently acrylic glued back together. As a result, an extra piece of acrylic was inserted between the back plate and footplate to provide additional bending strength. The height of the rails was chosen so that the center of the test frame pot and the load path provided by the rope were aligned with the footplate rotation axis of the ankle positioner.

In inversion and eversion, medial-lateral movement of the ankle causes an offset from the long axis of the tibia of the sole of the foot. As a result, extra screw holes were created in the inversion/eversion wedges so that the footplate could compensate for this offset. Based on the ankle height of the average male and the 18° wedge angle, a set of appropriate offset holes were drilled.

#### *2.2.5.5 Finite Element Stress Analysis*

Finite element models of the test frame and ankle positioner were constructed in LS-Dyna® (LSTC, Livermore, CA, USA) to assess the overall safety factor of the device. The model of the test frame was subjected to a pressure equivalent to 150 lbs at the front

plate representing the compressive force of the specimen, and two tensile point loads of 75 lbs each at the pulleys representing the downward force of the weights. The model was cantilevered at the bottom-rear end and the front end was bounded so that it could not move up or down to represent the CT bed. The highest stress was found to be 857 psi at the pulley point loads.

The ankle positioner was represented by the axle-footplate assembly. The axles were bounded so that they could not move in the up/down or forward/backward directions. Boundaries representing the angle-selecting pegs were also included. A compressive pressure equivalent to 150 lbs was applied to the footplate and the highest stress was found to be 905 psi at the location of the pegs. The yield strength of acrylic is around 5000 psi (ASTM, 2014), making the safety factor of the device  $5000/905 = 5.5$ .

## 2.2.6 TESTING OF THE SPECIMEN

### 2.2.6.1 NEUTRAL POSTURE

Figure 2.10 shows the experimental set up. The test frame was aligned and secured to the CT bed via 5” C-clamps, and the potted specimen was attached to the test frame via screws with the foot pressed against the foot plate of the ankle positioner. The heel brace of the ankle positioner was raised until it was just pressing snugly against the heel of the foot. The toe pin was secured to the appropriate holes in the foot plate to produce a neutral posture in the foot, and was adjusted until the pin was snug against the skin between the big toe and the second toe. Neutral posture was defined as having the plantar aspect of the foot completely on the transverse plane (the vertical footplate), with the shank

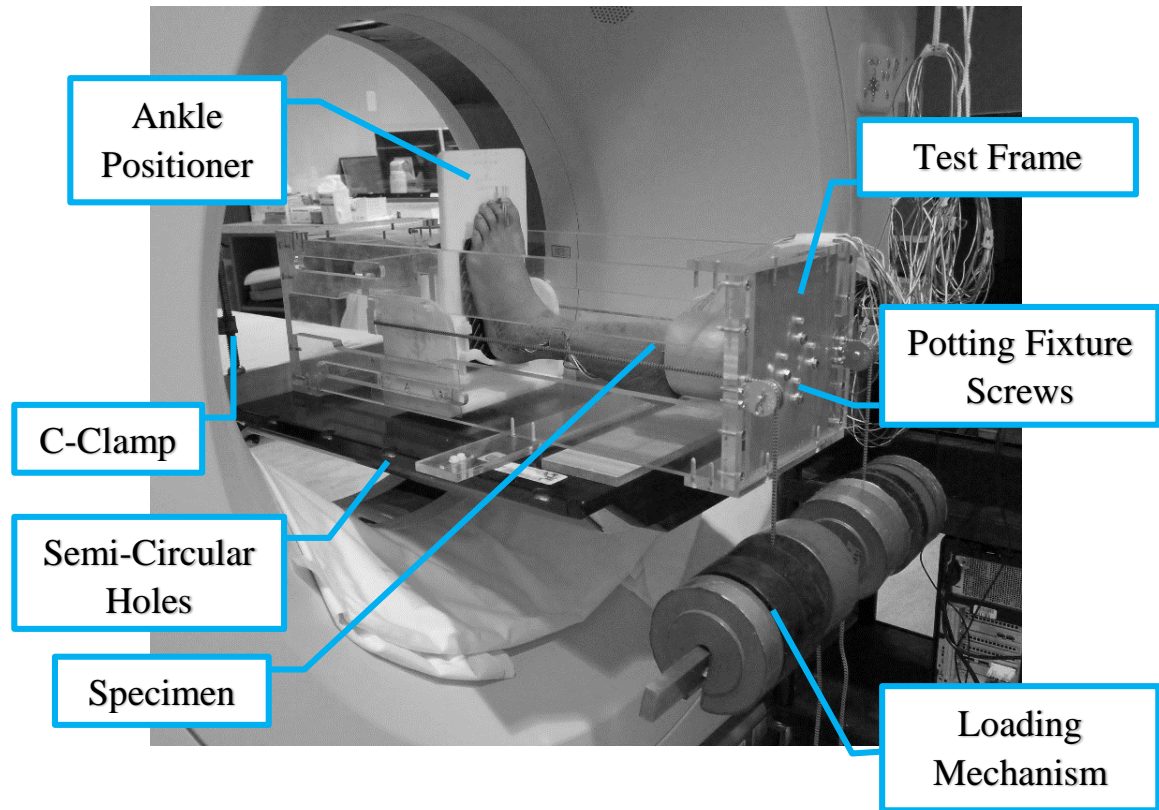


**Figure 2.10: Experimental Setup and Test Device**

The test frame used to adjust angle position and apply axial loading to a potted leg during CT scanning. The leg is attached to the test frame via four screws and the test frame is attached to the CT bed via two C-clamps.

perpendicular to this plane, and a line drawn from the back of the heel to the space between the first and second toes parallel to the sagittal plane.

Prior to beginning the testing protocol, the entire lower leg was scanned with no load applied. The full tibial and fibular geometry was acquired from this full scan, and it was also used as a starting position for the finite element model prior to load application. The rest of the scans included the entire foot but focused solely on the ankle joint, with the scanning range set to be from the bottom of the foot to the beginning of the diaphysis of the long bones to save time during the scans.

As is common procedure with mechanical testing of bones (*e.g.* Heiner and Brown, 2001), three preconditioning cycles were applied to the specimen. In these preconditioning cycles, loads were applied from 0 to 100 lbs in 20 lb increments with the ankle in the neutral posture, and strain readings were taken throughout. Strains were examined between the second and third preconditioning cycles to assess whether the specimen was adequately relaxed and ready for testing. If the strains had varied by more than 5% between these cycles, more preconditioning cycles would have been applied. One hundred lbs (67% of the maximum load) was chosen as the maximum load during the preconditioning phase in order to adequately relax the leg, but at the same time hopefully prevent damage that may occur over the course of multiple loading cycles on the same specimen.

Next, the leg was loaded from 0 to the maximum load of 150 lbs (667 N) in a neutral posture with strain gauge readings recorded throughout the loading process. First, 10 lbs was applied as the bar on which the weights were to be placed was allowed to hang freely. Next, two 40 lb increments of weights were applied, followed by three 20 lb increments.

Each load step was held for approximately ten seconds in an effort to ensure loading was applied in a step-wise fashion. A CT scan was taken at the maximum load approximately five minutes after it was reached.

At 150 lbs, strains should be below failure levels (*e.g.* Begeman and Prasad, 1990, Funk et al., 2002a, Funk et al., 2002b), but were shown in previous *in-vivo* studies to be substantial enough to generate signals in all gauges (*e.g.* Lanyon et al., 1975). 150 lbs is less than 20% of the failure loads reported in the aforementioned studies for the neutral posture and for ankle rotations within the normal physiological range of motion of the ankle joint. It was also crucial to remain well below the failure load of the test setup to ensure no damage would occur to the scanner.

In order to assess repeatability of the strain measurements and ankle bone positions, the potting fixture was unscrewed from the test frame and the specimen was removed. The potting fixture was then screwed back in and the specimen reattached. The aforementioned loading protocol was repeated three more times (for a total of four tests in the neutral posture) with the potting fixture removed and reattached between each trial. Testing in a neutral posture is important as a baseline against which to compare strain readings and bone positions with other ankle postures, and it is the posture most commonly used for developing injury criteria (*e.g.* Yoganandan et al., 1997). Furthermore, this is the most common posture in which calcaneal fractures occur (Daftary et al., 2005) and it has been shown to play a role in fractures of the body of the talus (Smith and Ziran, 1999).

#### 2.2.6.2 *NON-NEUTRAL POSTURES*

Loads were applied and CT scans were then taken for four non-neutral postures:

- 18° of inversion with 10° of external rotation
- 18° of eversion with 10° of external rotation
- 13° of dorsiflexion with 18° of inversion
- 22° of plantarflexion

At the end of all tests, the neutral posture was retested in order to quantify any degradation of the specimen that occurred over the course of testing.

The 18° inversion with 10° external rotation ankle posture was chosen since it corresponds to the most common posture in which ankle fractures occur (60% of all fractures) according to the Lauge-Hansen ankle fracture classification system (Okanobo et al., 2012, Lauge-Hansen, 1950). Furthermore, inversion of the ankle is a common mode of fracture for the talus and calcaneus bones (Daftary et al., 2005, Sneppen et al., 1977). Similarly, the 18° eversion with 10° external rotation ankle posture was chosen since this is the second most common posture in which ankle fractures occur (20% of all fractures) (Gardner et al., 2006, Lauge-Hansen, 1950). Both eversion and inversion have been previously implicated as primary fracture mechanisms for the foot and ankle during car crashes (Lestina et al., 1992, Morris et al., 1997). The 13° dorsiflexion with 18° inversion ankle posture was selected since this is a common posture for the ankle to assume during frontal vehicular collisions (Lestina et al., 1992, Morris et al., 1997). Excessive dorsiflexion has also been implicated in causing fractures of the talar neck (Daniels and Smith, 1993). The final posture, 22° of plantarflexion, was picked to evaluate the ankle in

a posture not examined in the other postures. This allowed for the ankle to be observed throughout its range of motion. Also, fractures of the posterior process of the talus have been shown to be associated with plantarflexion (Smith and Ziran, 1999). The specific dorsiflexion, inversion, eversion and external rotation angles were chosen to be at the high end of the typical range of motion of the ankle joint (Roas and Andersson, 1982, Nester et al., 2003). Beyond this limit, damage to the tibiotalar joint and ligamentous tears may occur under load (Lauge-Hansen, 1950). Since multiple tests were performed on the same specimen, accumulation of damage was a concern, and testing was targeted to be under sub-failure conditions with respect to both the loads applied and the angles of rotation. The typical range of motion in plantarflexion is much greater than for the other rotation directions, but the plantarflexion angle was chosen to be similar to the other angles in this study for comparison purposes.

#### 2.2.7 COORDINATE SYSTEM DEVELOPMENT AND DATA ANALYSIS

Taking CT scans over the full range of motion of the ankle allows for a complete picture to be developed of how the talus and calcaneus move relative to one another and to the tibia/fibula. This change in orientation of the bones can be quantified by the change in rotation angle about the x, y and z axes that are defined for the calcaneus, talus and tibia/fibula in this section, as well as the change in position of the chosen coordinate system origin for each of these bones.

The CT scans of each posture were imported into Mimics<sup>®</sup> medical imaging software (Materialise, Leuven, Belgium) and coordinate systems were developed for the

calcaneus, talus and tibiofibular complex. These coordinate systems were based on anatomic landmarks and strain gauge locations, as they were easily identified on the scans.

This study has made use of a modified version of the International Society of Biomechanics (ISB)-recommended tibiofibular coordinate system (Wu et al., 2002) (Figure 2.11a). Since the fibula and tibia were potted together in this study, the relative movement between these two bones was considered to be negligible, and they were assumed to be rigidly connected. One previous study showed that during a rotation of the ankle from 50° plantarflexion to 30° dorsiflexion, the relative translation between the fibula and tibia was at most 1.25 mm (Huber et al., 2012). The coordinate system was formed by the apexes of the medial malleolus (Point A) and lateral malleolus (Point B) as well as the anterior/superior aspect of the fibular notch of the tibia (Point C). The x-y-z coordinates for these points were acquired from the CT scans and the vectors  $\overrightarrow{AB}$  and  $(A + 0.8*\overrightarrow{AB})C$  were calculated. Vector  $(A + 0.8*\overrightarrow{AB})C$  is the vector that originates at 80% of the distance between points A and B, and points towards point C. Vector  $(A + 0.8*\overrightarrow{AB})C$  is roughly aligned with the cranial-caudal axis and was normalized as unit vector  $\hat{x}$ . The cross product of vectors  $\overrightarrow{AB}$  and  $\hat{x}$  is roughly aligned with the anterior-posterior axis of the tibia and was normalized as unit vector  $\hat{y}$ . Finally, the cross product between vectors  $\hat{x}$  and  $\hat{y}$  yielded the normalized vector  $\hat{z}$  that is roughly aligned with the medial-lateral direction. The midpoint between the medial malleolus and lateral malleolus was taken to be the origin of the coordinate system.

No standard coordinate systems were found in the literature for the calcaneus or talus, so custom coordinate systems were developed for these bones, with the axes aligned

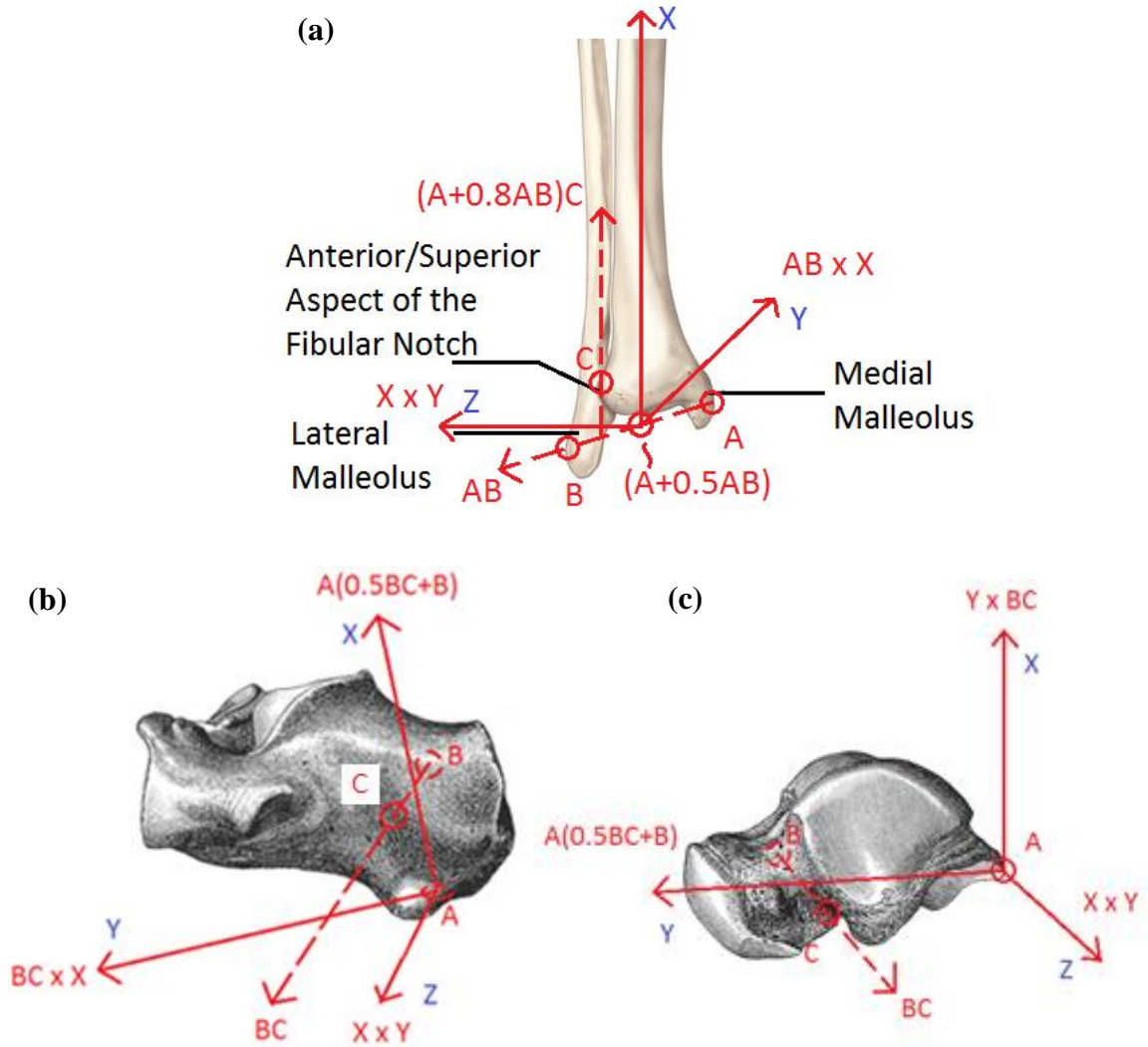


**Figure 2.11: Bone Coordinate Systems**

Coordinate systems were developed for the tibiofibular complex (a), calcaneus (b), and talus (c), based on strain gauge locations and anatomic landmarks (indicated with red circles) that were identified on the CT scans. For each coordinate system, the points, vectors and cross-products were picked so that the final axes were aligned as closely as possible with anatomical axes. Blue letters indicate the final x-y-z axes. Adapted from (Gray, 2009, Maxwell, 1878, Wu et al., 2002).

as best as possible with anatomical directions. The coordinate system for the calcaneus was formed using three non-collinear points: the notch between the medial and lateral processes (point A), the medial strain gauge (point B) and the lateral strain gauge (point C) (Figure 2.11b). The x-y-z coordinates for these points were acquired from the CT scans and vectors  $BC$  and  $A(0.5BC + B)$  were calculated. Vector  $A(0.5BC + B)$  is the vector that originates from A, and points towards the midpoint between B and C, and is roughly aligned with the cranial-caudal axis of the calcaneus (then normalized as unit vector  $\hat{x}$ ). The cross product of vectors  $BC$  and  $\hat{x}$  is roughly aligned with the anterior-posterior axis of the calcaneus (normalized as unit vector  $\hat{y}$ ). Finally, the cross product of vectors  $\hat{x}$  and  $\hat{y}$  is roughly aligned with the medial-lateral axis of the calcaneus, and was normalized as unit vector  $\hat{z}$ . Point A was chosen to be the origin of the calcaneal coordinate system.

The coordinate system for the talus was formed by the posterior tubercle (point A), the medial strain gauge (point B) and the lateral strain gauge (point C) (Figure 2.11c). The same process and vector orientations were followed as for the calcaneus, and point A was chosen to be the origin of the coordinate system.

The coordinate systems were constructed from the CT scans of each ankle posture, and the differences between the loaded neutral and repositioned postures were quantified based on the corresponding transformation matrices. Euler angles and the displacement of the chosen origin were calculated for each posture using an Euler z-y-x decomposition. To account for any slight offset in tibiofibular position between trials, all coordinate systems were subsequently adjusted so that the tibiofibular coordinate systems were aligned with the neutral tibiofibular coordinate system for all postures. Maximum principal strains and

directions of principal strain were calculated for each rosette at the peak load (Appendix E), and a one-way ANOVA was performed to examine differences between the bone strains in the neutral posture. All strains were analyzed and compared using the maximum principal strain.

## **2.3 RESULTS**

### **2.3.1 BONE POSITIONS**

The Euler angle results from the repeated neutral trials are shown in Table 2.1a. The rotations and displacements of the bones relative to the tibia were very consistent, with standard deviations on average 9% of the mean. This indicates that the repeatability of the tests was high. This table also shows the displacements and rotations for the hindfoot bones relative to the tibia for the final trial in the neutral posture (after all other tests). All values were within one standard deviation of the pre-test magnitudes, except for the z-rotation of the calcaneus, which was within two standard deviations. The maximum Euler angles and displacements that were observed and the corresponding ankle positions are summarized in Table 2.2, and the complete table of Euler angles and displacements for every posture relative to the neutral posture is provided in Appendix F.

Rotations experienced by the hindfoot bones as the posture of the ankle was adjusted were calculated about the individual bones' coordinate systems. For angles of plantarflexion and dorsiflexion, the calcaneus and talus appear to rotate together for the full range of motion about the z-axis (the axis that is the most closely aligned with the plantarflexion/dorsiflexion motion). For 22° of plantarflexion, the talus and calcaneus both

**Table 2.1: Repeatability of Neutral Posture and Comparison with the Final Trial**

The “pre” trials are presented as the mean (standard deviation) (a) calcaneus and talus bone rotations and displacements relative to the tibia and (b) maximum principal strain readings at all gauge locations, based on the four neutral trials performed at the beginning of testing. The “post” trial was performed at the end of testing. Tests where the “post” trial was within one standard deviation of the “pre” trials are in black, within two standard deviations are indicated in red, and greater than two standard deviations are indicated in blue.

(a)	Calcaneus		Talus	
	Pre	Post	Pre	Post
<b>Displacement (mm)</b>	73.5 (0.7)	73.3	25.4 (0.5)	25.4
<b>Z-Rotation (°)</b>	<b>-7.5 (0.7)</b>	<b>-6.1</b>	-9.7 (1.1)	-9.2
<b>Y-Rotation (°)</b>	13.3 (2.3)	14.5	-8.1 (1.9)	-6.2
<b>X-Rotation (°)</b>	-13.6 (0.7)	-13.0	-16.7 (0.5)	-16.2

(b)

Gauge Location	Gauge Reading ( $\mu\epsilon$ )	
	Pre	Post
<b>Tibia</b>	60.6 (47.1)	15.6
<b>Fibula</b>	214.0 (66.2)	216.4
<b>Plantar Calcaneus</b>	<b>191.7 (42.8)</b>	<b>110.0</b>
<b>Medial Calcaneus</b>	<b>103.2 (51.1)</b>	<b>169.3</b>
<b>Lateral Calcaneus</b>	281.1 (31.3)	279.9
<b>Medial Talar Neck</b>	<b>332.6 (24.4)</b>	<b>467.2</b>
<b>Talar Sulcus</b>	236.2 (47.9)	275.6

**Table 2.2: Maximum Euler Angles and Displacements of the Chosen Origin**

The largest rotations and displacements for the calcaneus and talus occurred during plantarflexion and dorsiflexion, respectively.

	Calcaneus	Talus
<b>Max Angle</b>	20° in plantarflexion about Z	21.3° in inversion-dorsiflexion about Z
<b>Max Displacement</b>	24.3 mm in plantarflexion	10.5 mm in inversion-dorsiflexion

rotated nearly this full amount ( $20.8^\circ$  and  $20^\circ$  respectively). For  $13^\circ$  of dorsiflexion (combined with inversion), the calcaneus rotated the full amount about the z-axis ( $14.5^\circ$ ), but the talus rotated about 50% further ( $21.3^\circ$ ).

For angles of inversion and eversion, only the calcaneus rotated noticeably about the y-axis (the axis most closely aligned with the inversion/eversion motion). For  $18^\circ$  of inversion (coupled with  $13^\circ$  of dorsiflexion), the calcaneus only rotated about 60% of the inversion value ( $10.3^\circ$ ). In this case, the talus actually went through an eversion of  $7.7^\circ$ , meaning it rotated in the opposite direction to the calcaneus. For  $18^\circ$  of inversion (coupled with  $10^\circ$  of external rotation) the calcaneus only rotated about 60% of this value once again ( $11^\circ$ ). Talus rotation was negligible about the y-axis in this case. For  $18^\circ$  of eversion (coupled with  $10^\circ$  of external rotation), the calcaneus only rotated about 37% of this eversion value ( $6.7^\circ$ ), with talus rotation being negligible once again.

Ten degrees of external rotation of the ankle, when coupled with  $18^\circ$  of inversion, caused the calcaneus and talus to rotate by  $3.1^\circ$  and  $8.7^\circ$  respectively about the x-axis (the axis that is the most closely aligned with external/internal rotation). However, for  $10^\circ$  of external rotation coupled with  $18^\circ$  of eversion, the calcaneus rotated this full amount about the x-axis ( $9.8^\circ$ ) but the talus only rotated by  $3.2^\circ$ .

### 2.3.2 STRAINS

The difference between the strain readings in the second and third preconditioning cycles was 4.87% or less for six of seven gauges. For the tibial gauge, this difference was 15%, but the strain readings were relatively low compared with the other gauges, and close

to the noise floor potentially causing greater variation in readings. In light of this, the specimen was considered to be adequately relaxed and ready for testing.

The strain results from the repeated neutral trials are shown in Table 2.1b. The standard deviations were small relative to peak physiological bone strains (maximum of only 66.2  $\mu\epsilon$ ), and the largest strains were observed at the medial talar neck, while the smallest strains were observed at the tibia. With regards to strain readings taken at the final trial in the neutral posture, most readings were within one standard deviation of the pre-test values. Strains at the plantar calcaneus and medial calcaneus were within two standard deviations, and strains at the medial talar neck were greater than those observed in the initial tests by several standard deviations.

Six out of seven strain gauges exhibited a linear response to loading in the pre ( $R^2 = 0.92-0.98$ ) and post ( $R^2 = 0.94-0.99$ ) neutral trials. A more non-linear response was observed at the medial malleolus of the tibia ( $R^2$  Pre = 0.42,  $R^2$  Post = 0.59).

Both first and second principal strains were calculated from the gauge readings, and the maximum of the absolute value of the two are presented in Figure 2.12. At the neutral posture (Figure 2.12a), strains were lowest in the tibia (60.6  $\mu\epsilon$ ), and highest at the medial talar neck (333  $\mu\epsilon$ ), representing 550% of the tibia value. Furthermore, the readings at several gauges were relatively similar, with the strains at the fibula, plantar calcaneus, and talar sulcus determined to be statistically equivalent by a one-way ANOVA ( $p = 0.22 - 0.61$ ). The average standard deviation for the gauge readings in the neutral posture was 44.4  $\mu\epsilon$ .

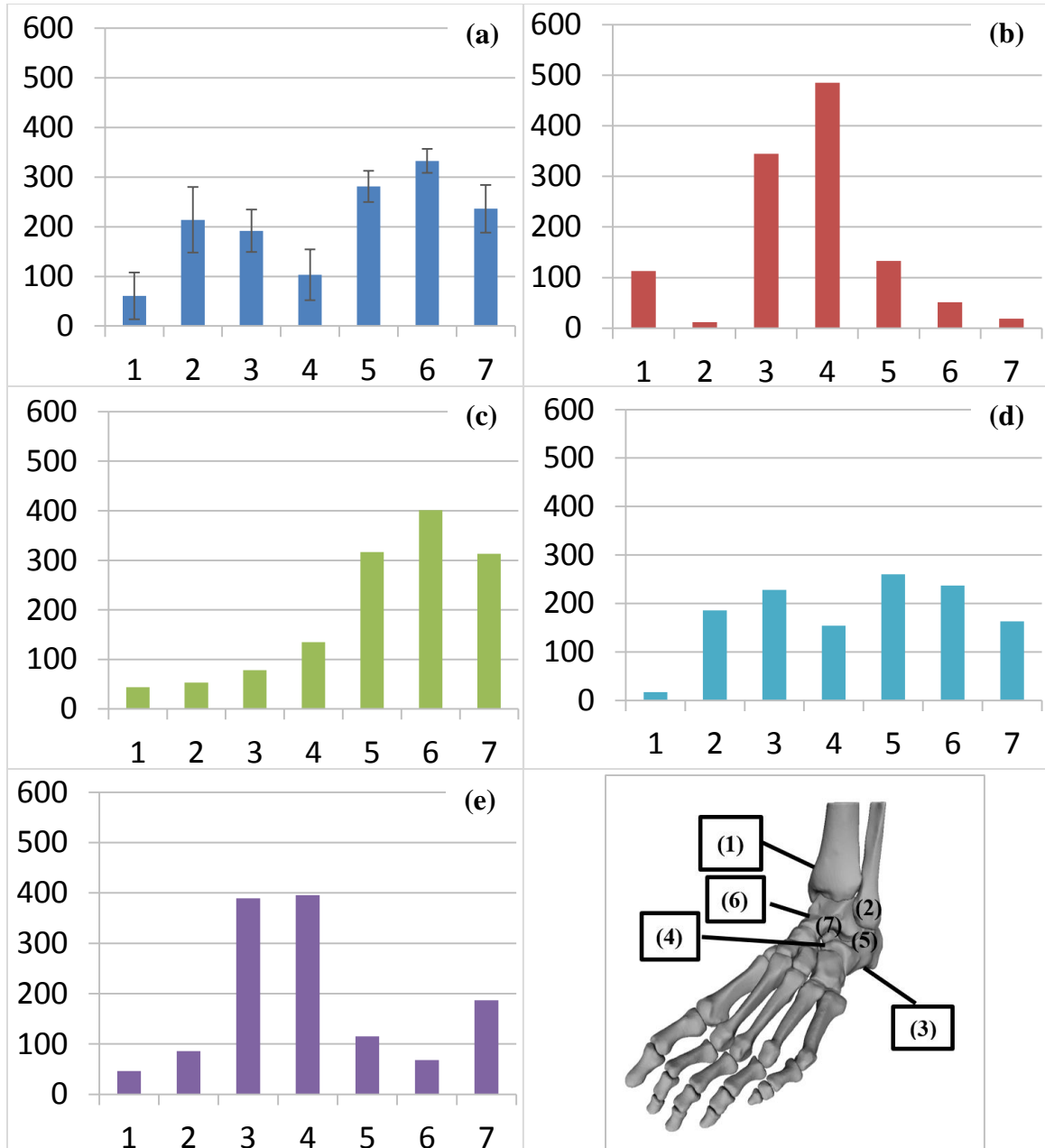


**Figure 2.12: Strain Readings at Each Position for the Tested Postures**

Peak strains (in  $\mu\epsilon$ ) at 150 lbs are presented for each of the tested postures: neutral (a), inversion-external rotation (INV-ER) (b), eversion-external rotation (EV-ER) (c), plantarflexion (PF) (d), and dorsiflexion-inversion (DF-INV) (e). For the neutral posture, peak strains were averaged over the various trials and standard deviations are presented as error bars. The numbers correspond to the following strain gauge locations: tibia (1), fibula (2), plantar calcaneus (3), medial calcaneus (4), lateral calcaneus (5), medial talar neck (6), and talar sulcus (7).

The strains at each gauge in the neutral posture were on average 67% of the maximum value recorded in any posture, with only the fibular gauge giving the maximum reading in neutral. This indicates that strains in the neutral posture were moderate relative to the other postures.

In the inversion with external rotation posture (Figure 2.12b), the medial and plantar calcaneal gauges exhibited the highest strain values. In fact, the highest strain value observed during this entire study was recorded by the medial calcaneal gauge in this posture (485  $\mu\epsilon$ ). While still relatively low, the tibia exhibited its highest recorded strain value in this posture as well (113  $\mu\epsilon$ ). Loads on the talar neck and fibula were the lowest in this posture compared with the four other postures.

In the eversion and external rotation posture (Figure 2.12c), the lateral calcaneus (317  $\mu\epsilon$ ), medial talar neck (401  $\mu\epsilon$ ) and talar sulcus (313  $\mu\epsilon$ ) all exhibited relatively high max principal strains. Low strains were observed on the plantar and medial surfaces of the calcaneus, as well as the tibia.

In the plantarflexion posture (Figure 2.12d), the strain distribution was similar to that of the neutral posture, with the strains recorded on the tibia, fibula and calcaneus all being within one standard deviation of the strains observed in the neutral posture. The one difference was that strains on the talar neck were lower than those observed in the neutral posture.

In the dorsiflexion and inversion posture (Figure 2.12e), relatively high strains were observed on the plantar (389  $\mu\epsilon$ ) and medial (396  $\mu\epsilon$ ) calcaneal surfaces, as well as

moderate strains on the talar sulcus ( $187 \mu\epsilon$ ). Strains on the tibia, fibula and medial talar neck were low.

Across all postures the fibula, and especially the tibia, seemed to exhibit consistently low strain values. The strains at the tibia and fibula were on average 14.2% and 34.6% of the maximum strain recorded across all postures. Conversely, the calcaneus and talus bones both exhibited relatively high strains depending on the posture being tested.

## **2.4 DISCUSSION**

To our knowledge, this study presents the most extensive analysis of how the positions of the bones of the ankle vary with posture. The most relevant postures for ankle injury were examined, and coordinate systems developed for the hindfoot bones allowed for the mechanisms of the talo-crural and talo-calcaneal joints to be quantitatively investigated. Furthermore, strain gauges attached to the bones of the hindfoot allowed for the observation of how the load path is altered through the ankle as posture is adjusted. Gauges were applied to a nearly intact specimen in difficult-to-access locations, allowing strain to be recorded at multiple positions on each hindfoot bone.

The neutral posture demonstrated good repeatability of bone positions, as the standard deviations for the positions of the talus and calcaneus were small relative to their means for the four neutral trials. Most values for the final neutral trial were within one standard deviation of the four neutral trials, indicating that no substantial damage occurred throughout the course of testing. The positional standard deviations were so small that the one value that was outside the standard deviation differed from the mean by only  $1.4^\circ$ , and

may be more the result of landmark identification errors on the CT scans than damage accumulation.

For the strains recorded over the four neutral trials, the standard deviations were relatively small; however, for locations with small means the standard deviations therefore represent large percentage variations. This is likely due to the fact that in order to conform to the irregular geometry of the ankle bones, gauges of very small gauge length (1 mm) had to be used. Strain gauges of gauge length less than 3 mm have been known to exhibit less stable behaviour (Intertechnology, 2013). This may also be due to the low sub-failure loading that was applied. At higher loads, the bones may have been forced back into the same positions more consistently based on their geometry, causing the load paths and strain readings to be more repeatable. Additionally, removing and reattaching the specimen between each trial introduced larger error than would have been observed in a pure measurement repeatability study, since the specimen had to be realigned at the footplate by eye each time. Overall, for the two primary bones of interest in this study (the talus and calcaneus) the strain variation was considered to be acceptable. Most values for the final neutral trial were within one standard deviation of the four neutral trials, indicating that no substantial damage occurred throughout the course of testing. The one difference was that strains at the medial talar neck were greater than those observed in the initial tests by six standard deviations. However, the standard deviation for this gauge is quite small (24.4  $\mu\epsilon$ ) relative to the others. While there is the possibility that some micro damage did occur at the talar neck over the course of testing, all strain values were less than 3% of critical strain values for cortical bone published in the literature (Burstein et al., 1976).

Six out of seven strain gauges exhibited a linear response to loading in both the pre and post neutral trials, suggesting that gauges were properly attached and strain was being measured accurately. Only the medial malleolar gauge of the tibia did not exhibit a linear strain response under load. This was also the only gauge where readings varied by more than 5% during the preconditioning phase. This is most likely due to the fact that the consistently lowest strains in this study were recorded at this gauge and readings were close to the noise floor. Gauge damage is another possibility. This also may have contributed to the large percent standard deviation of measurements at this gauge.

The talocrural joint's main purpose seems to be to accomplish dorsiflexion and plantarflexion of the ankle. As a result, the calcaneus and talus both moved relatively freely for these types of rotations. In both of these rotation directions, the calcaneus rotation mostly matched the footplate rotation, as the calcaneus is the main point of contact with the footplate. Any slight variations may be a product of heel pad compression and metatarsal positioning. For the dorsiflexion-inversion posture, the talo-calcaneal joint also seemed to play a role, as there was considerable motion at this joint as the talus rotated beyond the dorsiflexion angle of the footplate and the calcaneus. This may have been a result of the inversion posture the dorsiflexion was coupled with, and the hindfoot bone positions should be acquired in the future with the ankle in pure dorsiflexion to investigate whether the talus and calcaneus rotate together for the full range of motion as they did in pure plantarflexion.

In inversion and eversion, only the calcaneus contributed to the motion. This indicates that these types of rotations are controlled by the talo-calcaneal joint, and the talo-

crural joint contributes negligibly. The results also seem to indicate that the range of motion at the ankle in inversion ( $10.3^{\circ}$ - $11^{\circ}$ ) is greater than that in eversion ( $6.7^{\circ}$ ), which contradicts previous studies that have found that the ankle has about equal range of motion in both directions (Roaas and Andersson, 1982, Funk et al., 2002b). It is possible that the particular specimen used in this test simply had poor range of motion in the eversion direction. The other possibility is that due to the complex mechanism of the ankle, the external rotations coupled with these postures had a greater limiting effect in eversion than inversion, and in the future, the hindfoot bone positions should be acquired at these pure rotations to investigate this.

In both cases, the calcaneus did not rotate to the full inversion or eversion angle. By inspection of the CT scans, the rest of the movement seems to be accomplished mostly by the forefoot. The lower range of motion in the eversion/inversion directions may suggest that injury risk may be heightened in this posture. Figure 2.13 shows CT images comparing the talo-calcaneal joint in the neutral and eversion-external rotation positions. This image shows that the talo-calcaneal joint has been completely compressed and cannot move any further. The joint is now rigid, and this rigidity may contribute to a possible higher risk of injury elsewhere in the ankle, such as the lower tibia or fibula.

Such behaviour has been observed previously in the Lauge-Hansen classification of ankle fracture (Lauge-Hansen, 1950), which is used in clinical practice to categorize ankle fractures based on the foot position and the force applied. Furthermore, 75% of calcaneal fractures can be attributed to axial loading when the anterolateral process of the talus is wedged into the angle of Gissane of the calcaneus (Carr et al., 1989), as was

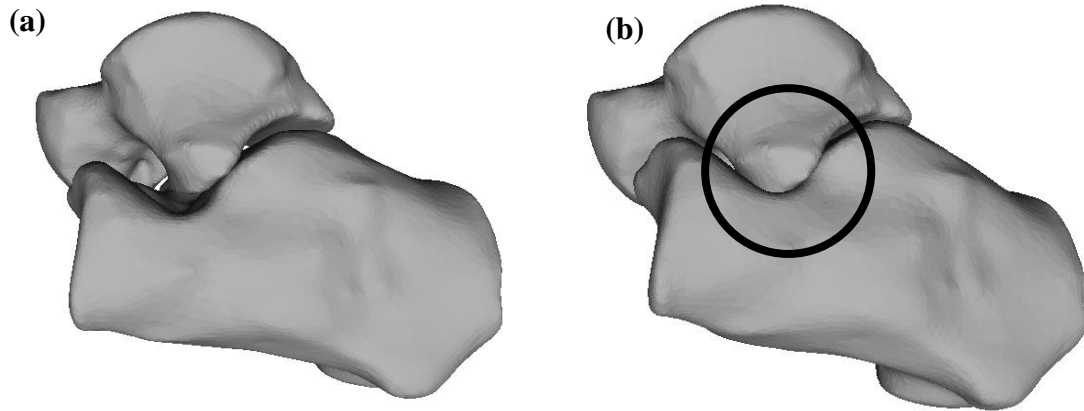


**Figure 2.13: The Lateral Aspect of the Talo-Calcaneal Joint**

Comparison of the talo-calcaneal joint for the neutral **(a)** and inversion/external rotation **(b)** postures show that the anterolateral process of the talus is being wedged into the angle of Gissane of the calcaneus. This area is circled in black.

observed here. Similarly, axial loading and inversion have been implicated in causing fractures of the sustentaculum, located on the opposite side of the calcaneus to the angle of Gissane (Essex-Lopresti, 1952). While no strain gauge was specifically placed on the sustentaculum, the medial calcaneal gauge recorded some of the highest strains observed in this study in the two postures that involved inversion.

External and internal rotations of the ankle are the least investigated and most poorly understood ankle rotations in the literature, and several other joints of the foot and ankle have also been implicated in contributing to this motion (Lundberg, 1989). The results of this study showed that the talus and calcaneus both contribute to this motion, but the relative level of involvement of each bone changes depending on what other rotations are involved.

The lowest strain values were consistently observed in the tibia and fibula. This may indicate that studies that have looked at the fracture tolerance of the tibia alone may be underestimating the absolute fracture threshold of the entire lower limb (*e.g.* Mo et al., 2012).

In the neutral posture, strains recorded at the fibula, plantar calcaneus, medial talar neck and talar sulcus were all very similar. Previous studies attempting to discern the mechanisms of fracture of the ankle found that the same loading conditions often produce a wide variety of fractures throughout this region (*e.g.* McKay and Bir, 2009). This uniformity of strains may be a contributing factor to these findings. Inversion and external rotation generated the highest tibial strains, as well as high strains at the plantar calcaneal gauge (located medially) and medial calcaneal gauge. This seems to indicate that the

principal loading is through the medial compartment of the foot and ankle in this case. Talar neck strains were low, and inspection of the CT scans seems to indicate that the neck is oriented away from the talocrural joint in this posture. Thus, it is possible that the body of the talus takes the majority of loading in this case.

Eversion and external rotation generated high strains in the lateral calcaneal gauge, as well the talus. This seems to indicate that the principal loading is through the lateral compartment of the foot and ankle in this case. Inspection of the CT scans shows that the talus is oriented about midway between the anterior and medial anatomical axes in this posture. Furthermore, the 10° of external rotation only caused the talus to rotate by 3.2° in this direction. As a result, it is possible that pressure was applied to the talar head by the talo-navicular joint, attempting to move the talus into a greater degree of external rotation. However, the high degree of eversion may have locked the talus and calcaneus together (as seen in Figure 2.13), causing torque to be applied about the talar neck. Talar neck fractures have only been consistently induced experimentally when the calcaneus was compressed against the talus, eliminating any ankle motion (Peterson et al., 1976). Another possibility is that the talar head is being impinged by the medial malleolus of the tibia due to the external rotation, also generating torque about the neck. While historically talar neck fractures were thought to be caused by hyperdorsiflexion (Adelaar, 1989), forcing the talar head against the anterior tibia and acting as a wedged fulcrum, this has been disputed in recent years (Daniels and Smith, 1993). The current philosophy is that talar neck fractures are caused by either a dorsally directed force on a braced foot and ankle (Peterson et al., 1976), or by inversion, causing impingement of the talar head by the medial malleolus

(Sneppen and Buhl, 1974). The results from the present study do not agree with the previous studies in terms of the postures that are often implicated in causing talar neck fractures, but the mechanisms that are described by these studies may also be occurring during combined eversion and external rotation, causing the elevated neck strains that have been observed herein.

Dorsiflexion and inversion generated a similar strain pattern to inversion and external rotation, suggesting that the primary load path is through the medial compartment of the leg once again. The one difference is that higher strains were observed in this posture at the talar sulcus. This may be a result of the dorsiflexion, which has been implicated in causing talar neck fractures (Smith and Ziran, 1999). Furthermore, in a study looking at mechanisms of fractures in ankle injuries to front seat car occupants, combined dorsiflexion and inversion was associated with the highest incidence of talar neck fracture out of all common ankle postures during vehicular collision (Morris et al., 1997). However, these strains are still much lower than those observed at the talar neck during eversion and external rotation.

The strains during plantarflexion were less than or equal to those at the neutral posture for all strain gauge positions. This is consistent with previous research that has indicated that plantarflexion is not often implicated in causing ankle fractures (Smith and Ziran, 1999, Daftary et al., 2005, Lauge-Hansen, 1950).

The main limitation with this study is that only one specimen was used and repeatability was not assessed for the altered postures. Due to biological variability among people, the positional data acquired may therefore not be applicable to the population at

large. The interosseous ligament, which may play an important role in ankle stability (Hoefnagels et al., 2007), had to be sacrificed during the dissection process. That being said, in general, gauges were installed with very minimal damage to the soft tissues of the foot, with more than one gauge being placed on each bone. There may have been some measurement error in the reading of the strain gauge and anatomic landmark locations from the CT scans during the construction of the coordinate systems in each posture. Steps were taken to minimize these errors, including having one author conduct all identifications in a single sitting.

Strain gauges were not necessarily located at positions of maximum strain, but their locations were selected to be close to known fracture lines. Unfortunately, many fractures of the hindfoot bones have been shown to originate at the articular surfaces, and propagate into these bones along these fracture lines (Daftary et al., 2005, Smith and Ziran, 1999). No gauges could be placed at the articular surfaces due to the presence of other bones. This was an especially challenging constraint for gauge application at the talus, since this bone is bounded on all sides by other bones and ligaments.

At the calcaneus, the three gauges were all placed closer to the posterior end of the calcaneus since there is a large concentration of ligaments near the anterior end. The presence of these ligaments would complicate the dissection and likely alter the mechanics of the foot if removed. At the talus, the two gauges were both placed closer to the anterior end since the entire body of the talus articulates with the tibia. As a result, the strain distributions were limited in their locations of evaluation.

With respect to the plantar calcaneal gauge, it would have been more ideal to place this gauge in the center of the plantar surface of the calcaneus where it could intersect common shear and compression fracture lines (Figure 2.6) (Daftary et al., 2005), but the presence of numerous plantar ligaments and tendons limited access to this surface of the bone. Therefore, the selected position was chosen as a compromise to minimize damage to the soft tissues of the foot. By inspection of the CT scans of the cadaveric lower leg, it was found that the plantar gauge, instead of being placed on the relatively flat plantar aspect of the calcaneus, was instead positioned a few millimeters too far medially. This positioning error was due to the fact that the gauge was attached via the medial incision. It was originally theorized that accessing this location from the medial incision was ideal as a whole new plantar incision did not need to be created, saving time during the dissection and maintaining the structural integrity of the soft tissues of the foot. However, in reality, accessing this location from the medial incision severely limited visibility and space, since the plantar soft tissues of the foot could only be pulled away just enough from the plantar calcaneus to create a small opening for gauge attachment. The outcome of this minor positioning error was that the gauge was placed at the highly curved transition region between the medial and plantar surfaces. Based on the CT scans, the radius of curvature at this transition region was found to be around 0.65 cm (Appendix B), meaning that the gauge length was no longer much smaller than the radius of curvature. The result of this may be an averaging effect that would cause the plantar calcaneal gauge readings to be underestimated. Future attempts to place gauges on the plantar aspect of the calcaneus

should investigate the possibility of creating a plantar incision in order to improve access and visibility.

There are countless combinations of ankle positions and rotation angles that are possible, but this study only focused on five. The chosen postures were selected due to their prevalence in injurious events and because, in many cases, they represented the ends of the range of motion of the ankle. As a result, the effects of altering ankle posture would be more easily observed in these positions. Furthermore, the number of postures tested had to be limited due to time constraints for the CT scans and the critical thaw time of the cadaveric leg (approximately 24h (*e.g.* Funk et al., 2003)). Repeatability of the non-neutral postures could also not be assessed due to these time constraints. While beyond the scope of this study, in the future it would be of value to examine the various ankle motions in isolation.

The results from this study have verified the hypothesis that ankle motion is a complicated combination of motions at various joints of the hind-foot. The strains measured in this region as posture was adjusted also demonstrated a relationship between ankle posture and load path. The large rotations, displacements and strain variations for the ankle bones in the postures that were tested emphasize the need for the construction of a finite element model of the ankle that accounts for this variation in posture, as well as for experimentally-determined injury criteria to test these vulnerable postures.

The displacements and rotations of the bones of the hind foot appear to affect the load pathway of the foot/ankle complex under axial loading, potentially reducing the fracture threshold and changing the location of fracture.

## 2.5 REFERENCES

- ADELAAR, R. S. 1989. The treatment of complex fractures of the talus. *The Orthopedic clinics of North America*, 20, 691-707.
- ASTM. 2014. *Standard Test Method for Tensile Properties of Plastics Active Standard ASTM D638* [Online]. ASTM: ASTM. Available: <http://www.astm.org/Standards/D638.htm> [Accessed September 20th 2014].
- BEGEMAN, P. C. & PRASAD, P. 1990. Human ankle impact response in dorsiflexion. SAE Technical Paper 902308.
- BURSTEIN, A. H., REILLY, D. T. & MARTENS, M. 1976. Aging of bone tissue: mechanical properties. *The Journal of Bone & Joint Surgery*, 58, 82-86.
- CARR, J. B., HAMILTON, J. J. & BEAR, L. S. 1989. Experimental intra-articular calcaneal fractures: anatomic basis for a new classification. *Foot & Ankle International*, 10, 81-87.
- DAFTARY, A., HAIMS, A. H. & BAUMGAERTNER, M. R. 2005. Fractures of the Calcaneus: A Review with Emphasis on CT 1. *Radiographics*, 25, 1215-1226.
- DANIELS, T. R. & SMITH, J. W. 1993. Talar neck fractures. *Foot & Ankle International*, 14, 225-234.
- ESSEX-LOPRESTI, P. 1952. The mechanism, reduction technique, and results in fractures of the os calcis. *British Journal of Surgery*, 39, 395-419.
- FUNK, J. R., CRANDALL, J. R., TOURET, L. J., MACMAHON, C. B., BASS, C. R., PATRIE, J. T., KHAEWPOONG, N. & EPPINGER, R. H. 2002a. The axial injury tolerance of the human foot/ankle complex and the effect of Achilles tension. *Journal of biomechanical engineering*, 124, 750-757.
- FUNK, J. R., SRINIVASAN, S. C. & CRANDALL, J. R. 2003. Snowboarder's talus fractures experimentally produced by eversion and dorsiflexion. *The American journal of sports medicine*, 31, 921-928.
- FUNK, J. R., SRINIVASAN, S. C., CRANDALL, J. R., KHAEWPOONG, N., EPPINGER, R. H., JAFFREDO, A. S., POTIER, P. & PETIT, P. Y. 2002b. The effects of axial preload and dorsiflexion on the tolerance of the ankle/subtalar joint to dynamic inversion and eversion. SAE Technical Paper 2002-22-0013.
- GARDNER, M. J., DEMETRAKOPOULOS, D., BRIGGS, S. M., HELFET, D. L. & LORICH, D. G. 2006. The ability of the Lauge-Hansen classification to predict ligament injury and mechanism in ankle fractures: an MRI study. *Journal of orthopaedic trauma*, 20, 267-272.
- GRAY, H. 2009. *Gray's Anatomy: With original illustrations by Henry Carter*, Arcturus Publishing.
- HEINER, A. D. & BROWN, T. D. 2001. Structural properties of a new design of composite replicate femurs and tibias. *Journal of Biomechanics*, 34, 773-781.
- HOEFNAGELS, E. M., WAITES, M. D., WING, I. D., BELKOFF, S. M. & SWIERSTRA, B. A. 2007. Biomechanical comparison of the interosseous tibiofibular ligament and the anterior tibiofibular ligament. *Foot & ankle international*, 28, 602-604.

- HUBER, T., SCHMOELZ, W. & BÖLDERL, A. 2012. Motion of the fibula relative to the tibia and its alterations with syndesmosis screws: A cadaver study. *Foot and Ankle Surgery*, 18, 203-209.
- INTERTECHNOLOGY 2013. Strain Gage Selection: Criteria, Procedures, Recommendations.
- LANYON, L., HAMPSON, W., GOODSHIP, A. & SHAH, J. 1975. Bone deformation recorded in vivo from strain gauges attached to the human tibial shaft. *Acta Orthopaedica*, 46, 256-268.
- LAUGE-HANSEN, N. 1950. Fractures of the ankle: II. Combined experimental-surgical and experimental-roentgenologic investigations. *Archives of Surgery*, 60, 957-985.
- LESTINA, D. C., KUHLMANN, T. P., KEATS, T. E. & ALLEY, R. M. 1992. Mechanisms of fracture in ankle and foot injuries to drivers in motor vehicle crashes. SAE Technical Paper 922515.
- LUNDBERG, A. 1988. Kinematics of the ankle and foot. In vivo roentgen stereophotogrammetry. *Acta orthopaedica Scandinavica. Supplementum*, 233, 1-24.
- LUNDBERG, A. 1989. Kinematics of the ankle and foot: in vivo roentgen stereophotogrammetry. *Acta Orthopaedica*, 60, 1-26.
- MAXWELL, J. C. 1878. Encyclopedia Britannica. Samuel L. Hall, New York, NY.
- MCKAY, B. J. & BIR, C. A. 2009. Lower extremity injury criteria for evaluating military vehicle occupant injury in underbelly blast events. *Stapp car crash journal*, 53, 229.
- METZGER, M. J., LEVIN, J. S. & CLANCY, J. T. 1999. Talar neck fractures and rates of avascular necrosis. *The Journal of Foot and Ankle Surgery*, 38, 154-162.
- MO, F., ARNOUX, P. J., JURE, J. J. & MASSON, C. 2012. Injury tolerance of tibia for the car-pedestrian impact. *Accident Analysis & Prevention*, 46, 18-25.
- MORRIS, A., THOMAS, P., TAYLOR, A. M. & WALLACE, W. A. Mechanisms of Fractures in Ankle and Hind-Foot Injuries to Front Seat Car Occupants: An In-Depth Accident Data Analysis. Proceedings of the 41st Stapp Car Crash Conference, November 13-14, 1997, Orlando, Florida, USA (Sae Technical Paper 973328), 1997.
- NESTER, C. J., FINDLOW, A. F., BOWKER, P. & BOWDEN, P. D. 2003. Transverse plane motion at the ankle joint. *Foot & ankle international*, 24, 164-168.
- OKANOBO, H., KHURANA, B., SHEEHAN, S., DURAN-MENDICUTI, A., ARIANJAM, A. & LEDBETTER, S. 2012. Simplified diagnostic algorithm for Lauge-Hansen classification of ankle injuries. *Radiographics*, 32, E71-E84.
- PETERSON, L., ROMANUS, B. & DAHLBERG, E. 1976. Fracture of the collum tali—an experimental study. *Journal of biomechanics*, 9, 277-279.
- RICHARDS, D. 2014. *Cordage Institute Tests* [Online]. Professional Association of Climbing Instructors Pty. Ltd.: Professional Association of Climbing Instructors Pty. Ltd. Available: [http://www.paci.com.au/downloads\\_public/knots/03\\_Cordage\\_Institute\\_Tests.pdf](http://www.paci.com.au/downloads_public/knots/03_Cordage_Institute_Tests.pdf) [Accessed September 20th 2014].
- ROAAS, A. & ANDERSSON, G. B. 1982. Normal range of motion of the hip, knee and ankle joints in male subjects, 30-40 years of age. *Acta Orthopaedica*, 53, 205-208.

- RUDD, R., CRANDALL, J., MILLINGTON, S., HURWITZ, S. & HÖGLUND, N. 2004. Injury tolerance and response of the ankle joint in dynamic dorsiflexion. *Stapp car crash journal*, 48, 1.
- SIEGLER, S., CHEN, J. & SCHNECK, C. 1988. The three-dimensional kinematics and flexibility characteristics of the human ankle and subtalar joints—Part I: Kinematics. *Journal of biomechanical engineering*, 110, 364-373.
- SMITH, P. N. & ZIRAN, B. H. 1999. Fractures of the talus. *Operative techniques in orthopaedics*, 9, 229-238.
- SNEPPEN, O. & BUHL, O. 1974. Fracture of the talus. A study of its genesis and morphology based upon cases with associated ankle fracture. *Acta orthopaedica Scandinavica*, 45, 307.
- SNEPPEN, O., CHRISTENSEN, S. B., KROGSØE, O. & LORENTZEN, J. 1977. Fracture of the body of the talus. *Acta Orthopaedica*, 48, 317-324.
- THEENGINEERINGTOOLBOX. 2014. *Nylon Rope Strength* [Online]. The Engineering Toolbox. Available: [http://www.engineeringtoolbox.com/nylon-rope-strength-d\\_1513.html](http://www.engineeringtoolbox.com/nylon-rope-strength-d_1513.html) [Accessed September 5th 2015].
- THEERGONOMICSCENTER. 2008. *Anthropometric Detailed Data Tables* [Online]. The Ergonomics Center of North Carolina. Available: <http://www.theergonomicscenter.com/graphics/Workstation%20Design/Tables.pdf> [Accessed March 3rd 2014].
- WU, G., SIEGLER, S., ALLARD, P., KIRTLEY, C., LEARDINI, A., ROSENBAUM, D., WHITTLE, M., D'LIMA, D. D., CRISTOFOLINI, L., WITTE, H., SCHMID, O. & STOKES, I. 2002. ISB recommendation on definitions of joint coordinate system of various joints for the reporting of human joint motion—part I: ankle, hip, and spine. *Journal of Biomechanics*, 35, 543-548.
- YOGANANDAN, N., PINTAR, F., KUMARESAN, S. & BOYNTON, M. 1997. Axial impact biomechanics of the human foot-ankle complex. *Journal of biomechanical engineering*, 119, 433-437.

---

## **CHAPTER 3 – Finite Element Model Development**

---

### **3.1 INTRODUCTION**

Finite element (FE) modeling is often used in the automotive and defense industries to assess injury risk (*e.g.* Sapuan et al., 2006), and several injury-predicting lower leg and ankle models have been previously constructed (*e.g.* Shin et al., 2012, Iwamoto et al., 2005). These models are usually based on scaled (*e.g.* Iwamoto et al., 2005) or simplified (*e.g.* Dong et al., 2013) geometry and have relatively coarse meshes (3 mm or larger average element size). Furthermore, many ligaments are often missing that play a role in the load transfer between bones and control the relative positions of these bones when foot and ankle posture is altered (*e.g.* Shin et al., 2012). These ligaments are also often assigned unrealistic linear elastic properties (*e.g.* Iwamoto et al., 2005). Finally, the complex geometry of bones often leads to elements with high degrees of distortion, and distorted elements can cause poor model accuracy (Valle and Ray, 2005). In spite of this, most of the aforementioned studies make little or no mention of testing for element quality, and those that do rarely report on the number of elements in their model that fall below an acceptable quality.

This purpose of this study was to construct a finite element model of the lower limb from the computed tomography (CT) scans of the foot and ankle discussed in Chapter 2, with special attention given to the geometric accuracy and mesh quality of the talus and calcaneus bones. It was also an objective of this work to construct finer meshes of these bones than have been seen in previous lower leg models, and to model a large number of

ligaments throughout the foot and ankle. Examination of the model response is discussed in Chapter 4, and is based on comparison with the experimental strain and positional data acquired as part of the study in Chapter 2.

## **3.2 METHODS**

### **3.2.1 ACQUISITION OF MODEL GEOMETRY**

The CT scan images of the leg and ankle in the neutral, unloaded posture were imported into Mimics<sup>®</sup> medical imaging software (Materialise, Leuven, Belgium) (Figure 3.1) for the purpose of creating 3D STL models of the anatomy to then be used to generate an FE mesh. A mask was applied to the scan in order to threshold the bones of the foot according to the Hounsfield Units (HU) of each voxel. Two different thresholds were applied: one to identify regions of cortical bone (HU between 226 and 3071), and another to identify the plantar soft tissue (HU between -200 and 225). Cancellous bone was identified by filling the regions of the bone that were not included in the cortical threshold.

The bones of the hindfoot were the focus of the model since they are the primary load path through this region (Hutton and Dhanendran, 1979) and the most debilitating ankle injuries are experienced by these bones (Manoli et al., 1997). To ensure biofidelic modeling of the hindfoot bones, they were separated into distinct cortical and cancellous regions. The calcaneus and talus required significant manipulation of the initial cortical threshold, since the transition between the cortical and cancellous bone is not clearly defined in these bones (Figure 3.2a) and it is difficult to distinguish between the two regions. The cortical regions of these bones were also very thin, and so were not identified

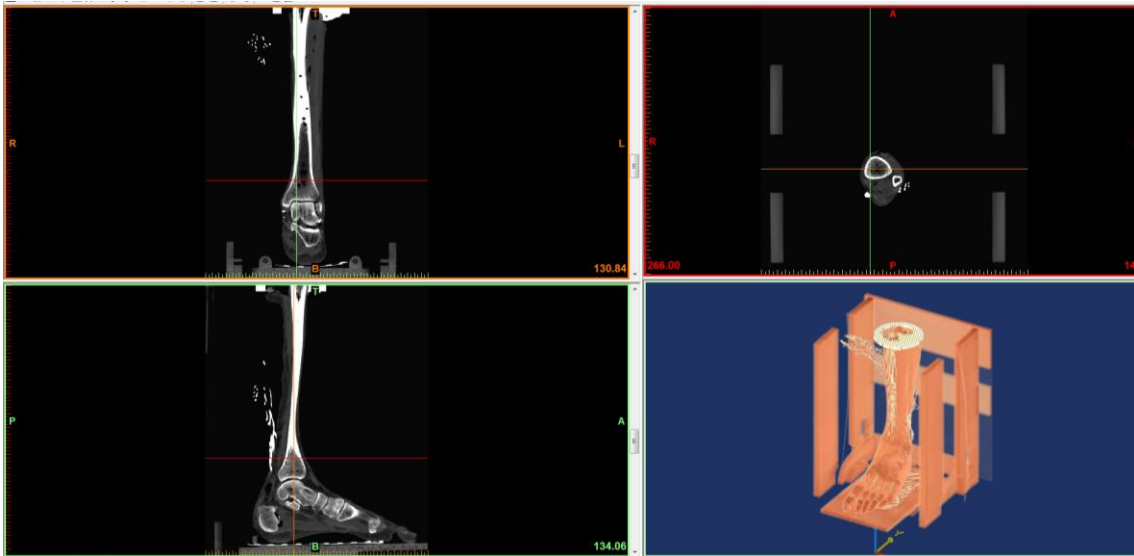


**Figure 3.1: CT Scan of the Lower Leg and Ankle**

The CT scan of the specimen in the neutral, unloaded posture was imported into Mimics<sup>®</sup> medical imaging software. This allowed the bones and soft tissues of the specimen to be viewed in three different planes: frontal (top left), transverse (top right) and sagittal (bottom left). The scans could also be viewed and manipulated in 3D in the bottom right frame. Importing the scans into Mimics<sup>®</sup> allowed the cortical bones and plantar soft tissue of the specimen to be isolated based on Hounsfield Units.

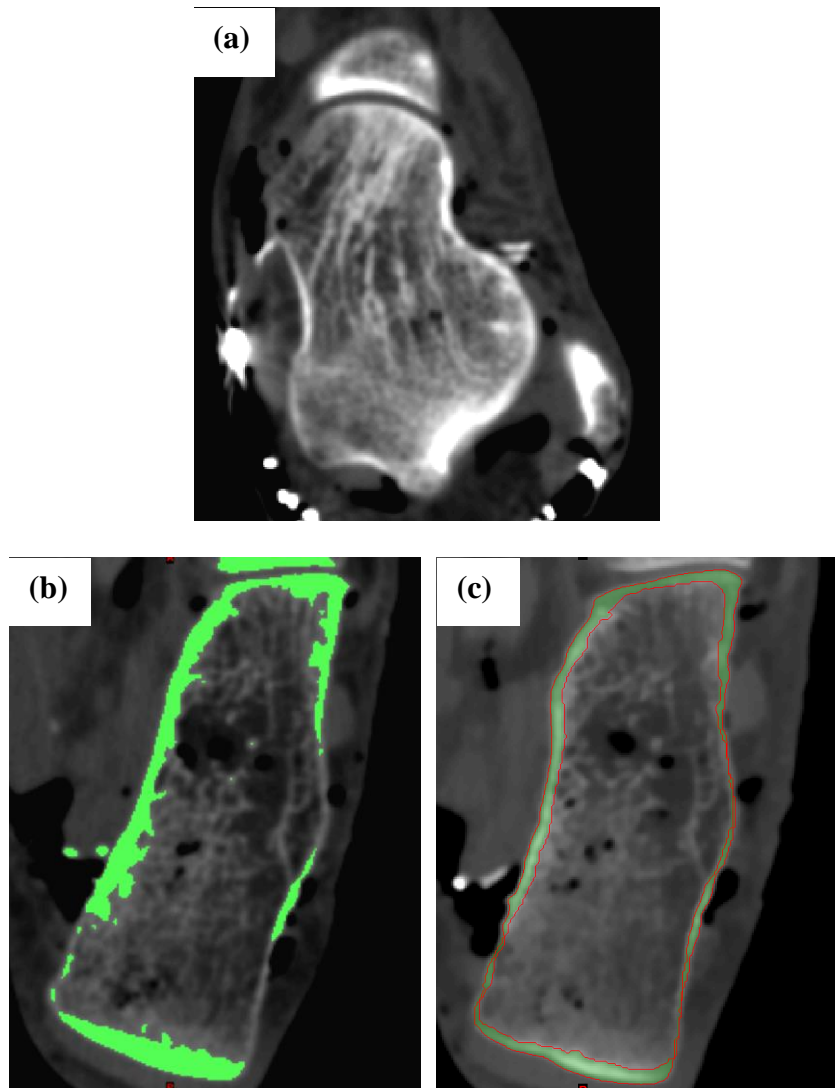


**Figure 3.2: Hindfoot Bone Thresholding Challenges and Polylines**

A CT scan slice of the talus (a) demonstrates how it and the calcaneus have a gradual transition from cortical to cancellous regions, making thresholding of these bone regions challenging. The large bright spots around the bone silhouette in this image are strain gauge wires. A CT scan slice of the calcaneus with the initial cortical thresholding applied (bright green) (b) shows that the cortical layer that is present is often very thin, and as a result, this initial thresholding left large gaps that had to be filled in manually. Once the gaps have been filled (c), and a continuous cortical mask (green) has been created, polylines (red) were generated from the mask to identify the contours of the cortical region.

very well by the Hounsfield Unit thresholding. At the lateral calcaneus in particular, the cortical region was so thin that the initial threshold left large gaps that had to be filled in manually (Figure 3.2b). Furthermore, at several locations, the thin cortical layer, combined with the relatively low-resolution one millimeter CT scans slices (0.32 mm in-plane resolution), caused cortical layer gaps to appear between subsequent slices that also needed to be filled in manually. Finally, parts of the high density metal strain gauges and strain gauge wires were included in the threshold and the corresponding voxels had to be manually removed. Once the cortical outer layer was defined for these bones, the hollow centers were filled with a second mask representing the cancellous region.

The bones of the shank were also thresholded for inclusion in the model. The difficulties encountered during thresholding the talus and calcaneus also applied to the fibular epiphysis, and the outer cortical layer was filled by a second mask representing the cancellous bone. This region extended proximally until the cancellous bone began to thin out and only covered about one-half of the area within the cortical shell of the medullary canal (as observed on the axial CT slices). Inspection of the CT scans at the diaphysis showed very little cancellous bone and the mask was just as left as a hollow cortical cylinder. The cortical region of the fibular diaphysis was very clearly defined and required little to no manipulation of the initial cortical threshold.

A previously-constructed and validated tibial model was used *in lieu* of the specimen's original tibial geometry (Quenneville and Dunning, 2011), and this is discussed further in Section 3.2.3. The original tibial geometry still needed to be acquired so that the position of the previously-constructed tibia could be matched to the original tibia's position

as closely as possible using registration software. As a result, the tibia from the CT scans was represented using only one region, without separation of cortical and cancellous bone.

The midfoot and forefoot bones were to be modeled as rigid bodies, so they were represented by single regions with no separation of cortical and cancellous bone. Modeling these bones as rigid is common practice in previous FE models of the lower leg (*e.g.* Shin et al., 2012), and was deemed to be an acceptable simplification since the hindfoot bones are the primary focus of this model, and are the primary load path through the foot and ankle (Hutton and Dhanendran, 1979). Using the initial cortical bone threshold as a starting point, holes in the mask were filled in manually and extraneous voxels were removed. Once the outer cortical surface of each bone was complete, the remaining interior was filled in to form one region. Due to the very narrow gaps between many of the bones in the midfoot and forefoot, the spaces between these bones were sometimes included in the threshold, and these gaps had to be manually defined by removing voxels slice by slice until all bones were separate. A criterion was established such that a gap of at least one voxel had to be present among all bones.

The region of plantar soft tissue was chosen to extend from the sole of the foot to the inferior surface of each of the forefoot and midfoot bones, forming a footpad. In the anterior-posterior direction, this pad was terminated just before the phalanges. At the heel, the pad entirely surrounded the lower half of the calcaneus and wrapped around the sides and back of this bone at the posterior aspect (Figure 3.3). Only a minimal number of voxels had to be filled in and removed on each scan slice so that a single heel and foot pad region could be generated from the initial thresholding.



**Figure 3.3: 3D Geometry of the Foot Bones and Soft Plantar Tissues**

3D solids representing the smoothed 26 forefoot bones, the tibia, fibula and the soft plantar tissues were generated from the polylines, and the geometry was output as STL files. The plantar soft tissue (the heel/foot pad) extends superiorly from the sole of the foot to where the forefoot/midfoot bones begin. At the hindfoot, this pad wraps around the sides and back of the calcaneus.

Polylines were automatically generated bounding each of the previously masked regions (Figure 3.2c) and 3D models of these regions were then created from the polylines (Figure 3.3). Several iterations of smoothing and triangle reduction were applied to the newly-generated 3D models. This is an important step for the meshing process since irregular geometry, such as in the bones of the hindfoot, makes meshing challenging, often resulting in overly small or distorted elements in these regions. The 3D models were then exported as STL files, which represent geometry as a 3D surface composed of many small triangles.

In order to compare the strains measured experimentally to those acquired from the finite element model in response to the same loading conditions and ankle postures, the positions of the strain gauges were identified on the CT scans. First, a 3D model of the foot was created based on the initial thresholding for cortical bone, and the locations where the three strain gauge wires converged at each rosette were selected. On the axial slices corresponding to each of these selected locations, bright voxels were observed, indicating high-density metallic regions (Figure 3.4). Cartesian coordinates of the highest density (brightest) voxel at each strain gauge location were recorded.

### 3.2.2 MESH GENERATION

#### 3.2.2.1 MESHING TECHNIQUES

The STL geometry of the hindfoot bones and the heel/foot pad was imported into TrueGrid<sup>®</sup> mesh generator (XYZ Scientific Inc., Livermore, CA, USA), software that allows the user to manually generate hexahedral meshes. This is done by first creating

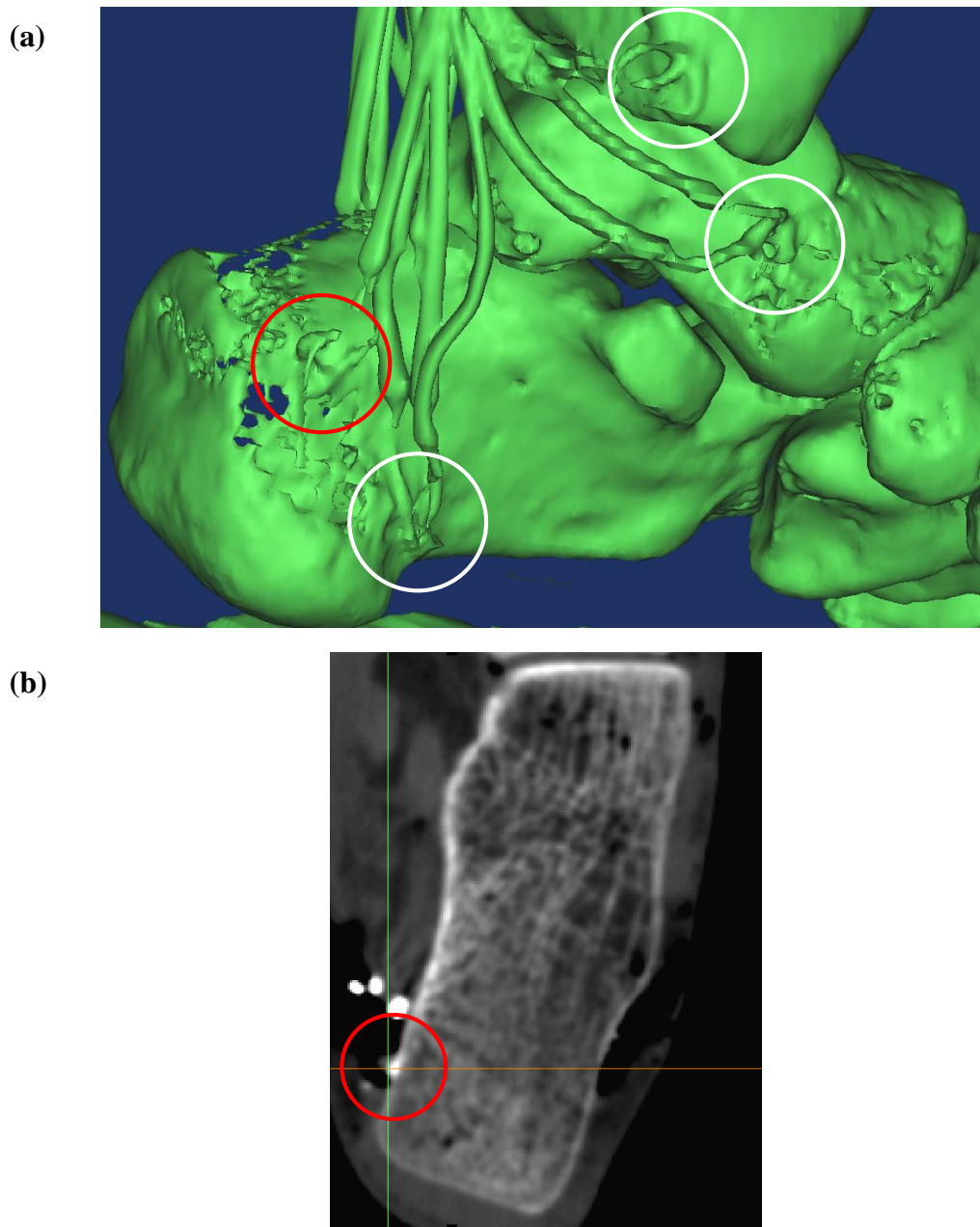


**Figure 3.4: Strain Gauge Location Identification**

Locations of strain gauges were identified as where three rosette wires converge on a model of the foot generated from the initial cortical threshold (a). The highest density voxel was then picked on a corresponding transverse CT scan slice (b) as the strain gauge location. The white circles indicate strain gauge locations and the red circle indicates the same strain gauge location in both the 3D model and the transverse slice.

blocks that are positioned and manipulated in 3D to match the imported geometry as well as possible. Each block is composed of a specified number of hexahedral elements connected by nodes, and the overall mesh can be composed of many blocks, depending on its complexity, which are separated by partitions. Once the blocks have been positioned correctly, the outer surfaces of these blocks are projected onto the surface of the imported geometry, and the end result is a mesh whose outer surface conforms to the shape of the imported geometry. As long as only minor gaps or imperfections are present in the imported geometry, this projection method usually works well. If the geometry is more complex, revisions may need to be made to the initial block structure of the mesh to allow it to conform better to the geometry. When creating meshes of complex geometry with regions of high curvature, as is often the case with bones, choosing an appropriate initial block structure is especially important. The TrueGrid<sup>®</sup> environment can be seen in Figure 3.5, with the computational view on the right showing the block structure, and the physical view on the left showing the corresponding element positions and shapes.

When dealing with areas of high curvature, the best way to generate a high quality mesh is to make an initial block structure that uses the butterfly technique. Figure 3.6a shows the result of attempting to use a single block to mesh a region with a circular cross-section. While the elements in the center of the cross-section are of good quality, near the edge of the circle some elements are nearly triangular, meaning that the mesh is not orthogonal at these locations but nearly parallel. These elements are of poor quality, may give inaccurate results, and are prone to causing simulations in which they are included to fail. A preferable alternative is to use a butterfly (Figure 3.6b), which is a cross is formed

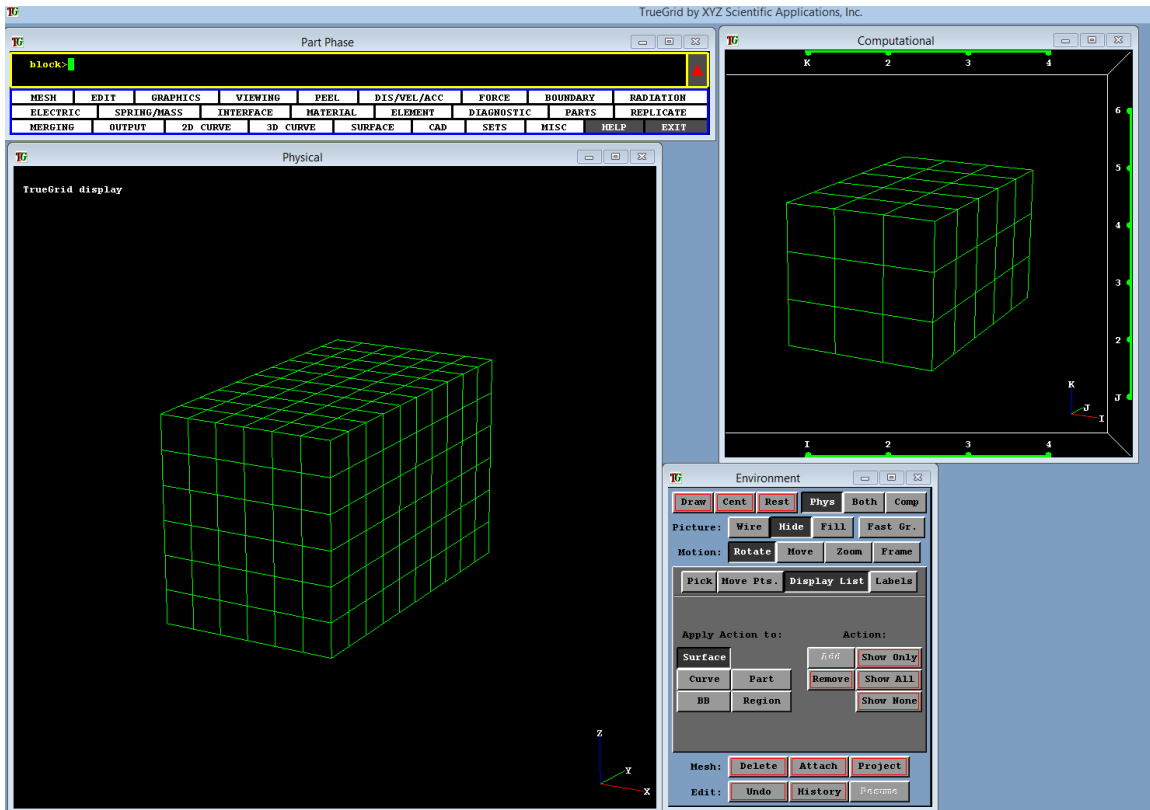


**Figure 3.5: TrueGrid® Environment**

The block structure of the mesh is created in the computational view (top right) and the blocks can be manipulated by selecting edges, faces, and corners in this view. The actual positions of the corresponding elements and nodes are shown in the physical view (bottom left). The other two panels in the top left and bottom right allow for commands to be input to manipulate the mesh.

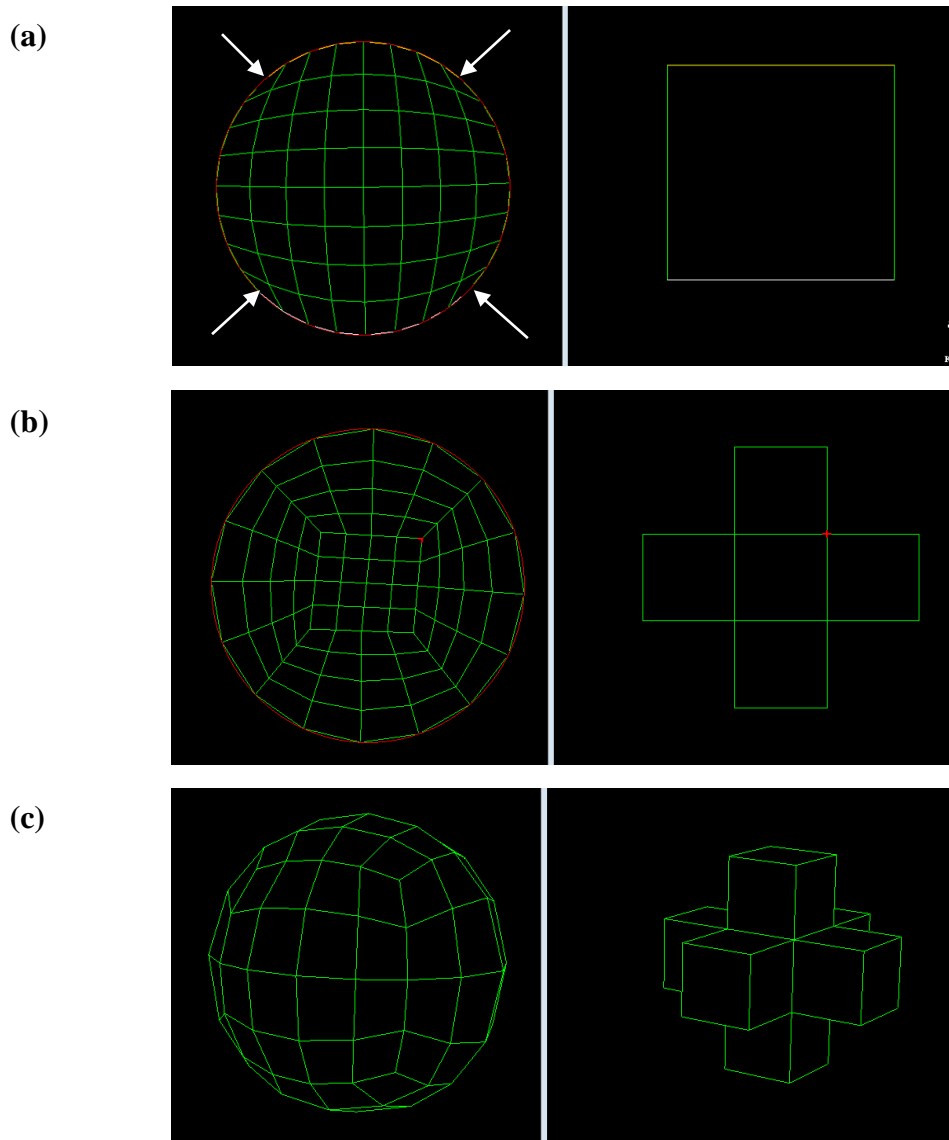


**Figure 3.6: The Butterfly Technique**

When a single hexahedral block is used to conform to a circular cross-section (physical view on the left, computational view on the right) (a), highly distorted, nearly triangular elements result at the edges. These elements are indicated by arrows. By forming a cross with five blocks, known as a butterfly, a nearly orthogonal mesh can be generated for the same cross-section (b). By forming a 3D butterfly with nine blocks, this effect can be extrapolated to 3D to generate an orthogonal mesh of a sphere (c).

by five blocks. The corners of the four exterior blocks are moved to be at 45° angles, causing the edges of neighbouring blocks to meet. These faces are connected together with the TrueGrid® block boundary command, and the elements are now orthogonal to the circular cross-section. Extrapolating this technique to 3D can aid in generating orthogonal spherical meshes (Figure 3.6c).

### 3.2.2.2 MESHING OF THE TALUS AND CALCANEUS

The cortical bone of the talus and calcaneus is very thin, and based on the CT scans of the specimen is less than one millimeter thick at certain locations, such as the lateral calcaneus. As a result, meshing separate cortical and cancellous regions for these bones using solid elements would prove to be very difficult as elements at the cortical region would have to be extremely tiny to have acceptable aspect ratios. Achieving acceptable Jacobians and interior angle deviations in the cortical regions would also be difficult due to the highly curved and complex geometry on the outside of these bones. Furthermore, the exact transition between these two regions was difficult to estimate from the CT scans. As a result, the outer surfaces of the calcaneus and talus were each meshed as one solid representing the cancellous region, with shell elements connected to these surfaces representing the cortical bone. This method of representing the cortical bone of the hindfoot has been done in previous FE models of the lower leg with good results (*e.g.* Shin et al., 2012).

The talus and calcaneus both have a shape similar to a kinked egg. For the talus, the kink is at the talar sulcus, and for the calcaneus, this kink is at the angle of Gissane. As

a result, a similar initial block topography was chosen for both bones, with half spherical 3D butterflies at the ends of the bone and several segments of 2D cylindrical butterflies in the middle. At the kinked regions, the cylindrical butterfly segments were divided into even more blocks so that the mesh could be easily manipulated to conform to the severe curvature. The meshes were projected onto the imported surfaces and the corners of the blocks at the cross sections of each butterfly were manually manipulated until no elements appeared to be overly distorted. For the calcaneus, the sustentaculum is a significant protuberance, and was meshed by attaching a spherical 3D butterfly to the side of the existing mesh. Algorithms were applied to the volumes of the meshes that uniformly smoothed the elements. This was especially important to improve the quality of elements at the kinked areas where the curvature was excessive. The relative spacing of elements along edges of blocks and the positions of the corners of blocks were also adjusted to improve mesh quality. A layer of shell elements defined as a separate part was then applied to the outside of the existing volume mesh, and a merge tolerance (0.001 mm) was applied between the parts to eliminate duplicate nodes. The number of elements in each block was chosen to create a relatively fine mesh that would closely represent the irregular geometry of the bones and approximately match the element size of the previously-meshed tibia. The meshes of the calcaneus and talus and their corresponding block structures can be seen in Figure 3.7.

The Mimics<sup>®</sup> analysis module was used to create a map of the overall distance between the cortical and cancellous surfaces of the calcaneus and talus from the CT scan, in order to determine the thicknesses that would be applied to the cortical shell elements.

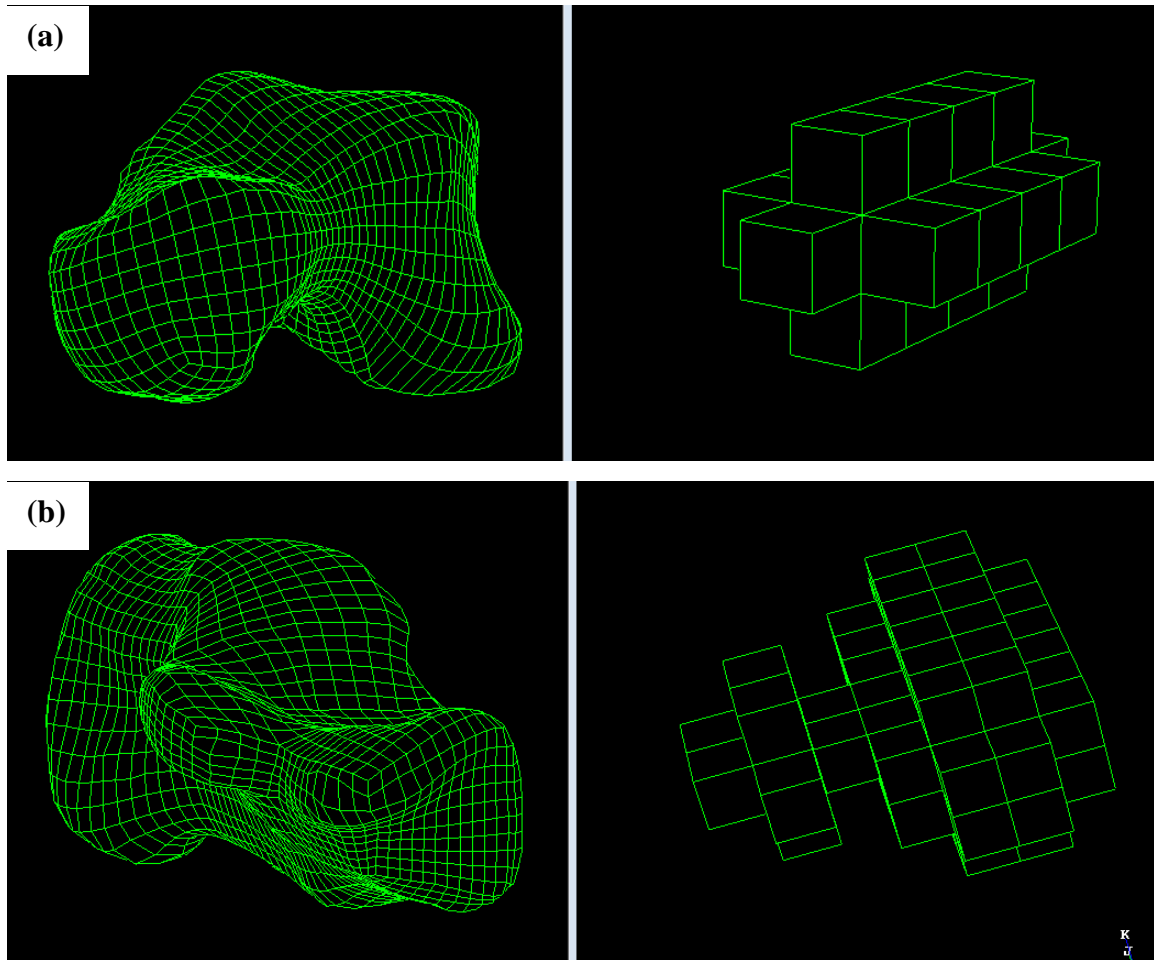


**Figure 3.7: Meshes of the Talus and Calcaneus**

The talus (a) and calcaneus (b) meshes were created by projecting blocks composed of 3D hexahedral elements onto imported 3D surfaces. The block structures in the computational view for each mesh are on the right.

### 3.2.2.3 MESHING OF THE FIBULA

The fibula was meshed along the entire length of the CT scan up to the potting fixture, ending 67 mm below the proximal end of the previously constructed tibia. The cortical and cancellous bone were represented as two different solid mesh regions. In this case, shells were not used to represent the cortical bone of the fibula since the epiphysis had a mostly thicker cortical shell than the talus and calcaneus, and the cortical bone at the diaphysis was very thick. Also, the outer surface geometry was less complex, making it easier to meet the mesh quality criteria using solid hexahedral elements. The STL files of the outer surfaces of these regions were imported into TrueGrid<sup>®</sup>, and the distal epiphysis of the bone was meshed first, as this was the area of greatest interest. A block structure with butterflies corresponding to a cylinder capped by a half-sphere was created. The outer surfaces of this block structure were projected onto the surface defining the transition from cancellous to cortical, and by using the same techniques described in Section 3.2.2.2, the mesh was manipulated to improve mesh quality. The cancellous mesh can be seen in Figure 3.8a. Block boundaries were generated on the outer surfaces of the mesh and a new part was created to represent the cortical layer. The block structure of this part was the same as for the cancellous region, except the blocks in the center were deleted so that this part could surround the cancellous region. This part was attached to the block boundaries of the cancellous surface on the inside and was projected onto the outer cortical STL surface on the outside. Due to the small thickness of the cortical layer, a single element depth was used. Block boundaries were defined at the proximal end of this part, and once the minimum element quality criteria was achieved through mesh manipulation, a third part

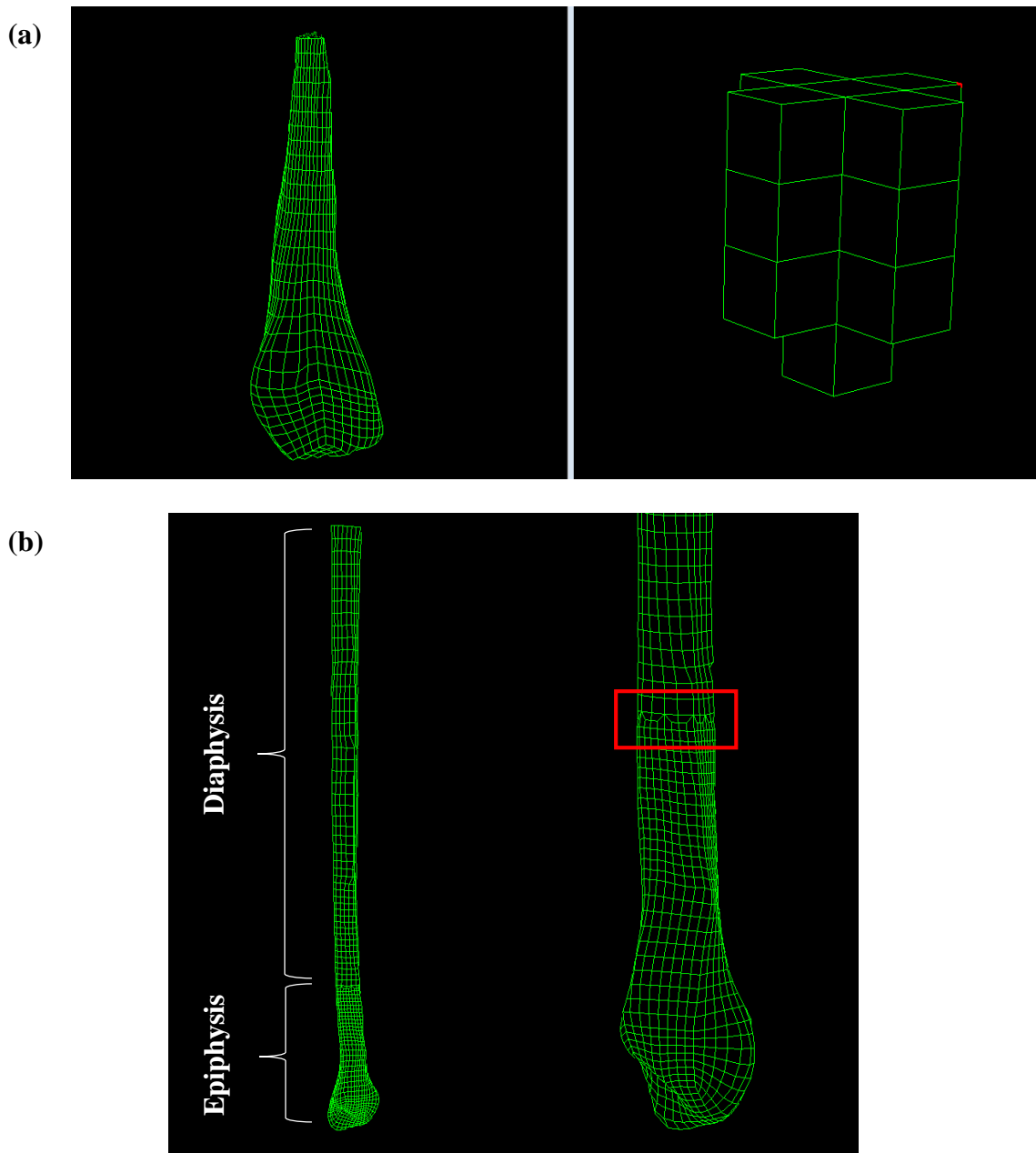


**Figure 3.8: Fibula Mesh**

The fibula was meshed in three separate parts: the inner cancellous epiphysis (a), the cortical epiphysis and the cortical diaphysis (b). The block structure in the computational view of the cancellous part is shown to the right of the physical view, and the block structure of the cortical region is similar, except the center blocks were removed to provide room for the cancellous region. The number of elements in the diaphysis was reduced by a factor of two relative to the epiphysis via a transition region (highlighted in red), in order to improve the aspect ratios of the elements.

was created for the diaphysis. This part was attached to the newly created block boundary distally, and was projected onto the inner and outer cortical STL surfaces elsewhere. The block structure was that of a hollow cylinder (butterflies with the center block removed). Due to the narrowing of the bone's geometry, a transition zone was defined between the epiphysis and diaphysis to reduce the number of elements by a factor two in each of the directions along the transverse plane. This improved the aspect ratios of the elements along the diaphysis, as many elements were being fit through the relatively narrow cortical region. Duplicate nodes were eliminated between the parts and the final fibula mesh is shown in Figure 3.8b.

#### *3.2.2.4 MESHING OF THE HEEL/FOOT PAD*

At the posterior heelpad, the geometry had been defined to wrap around the sides and back of the calcaneus, and so the mesh of this component used the pre-existing calcaneus mesh as a starting point. Block boundaries were defined on the outer surfaces of the calcaneus, and blocks were attached to these boundaries to form the heel pad. The block structure in this region was that of a hollow hemisphere, the outer surface of which was projected onto the outer surface of the imported heel pad STL. Moving anteriorly from the back of the heel, the hemisphere was transitioned into a hemi-cylinder, and this block structure was maintained all the way along the length of the footpad. At the front of the footpad, another hemispherical butterfly was created to end the mesh. The outer surfaces of the mesh were projected onto the footpad STL surfaces, and the mesh was adjusted to improve mesh quality. The heel and footpads were separated into two distinct

parts at the anterior aspect of the calcaneus, and the final mesh of this region is shown in Figure 3.9.

#### *3.2.2.5 MESH QUALITY EVALUATION*

The quality of the elements in each hexahedral mesh created with TrueGrid® was assessed based on three diagnostic techniques: the Jacobian, the orthogonality and the aspect ratio. It should be noted that the cortical shell layers on the surface of the talus and calcaneus were included in the mesh evaluation of those bones.

The Jacobian is a measure of an element's deviation from an ideally shaped element, which has a Jacobian of one. If the Jacobian is negative, this indicates that two surfaces of the element have passed through one other, and if this occurs during analysis, a negative volume error will be returned. The greater the Jacobian values of the elements in a mesh, the less likely that negative volumes will result during analysis. The criterion for Jacobian in this study was that no element should have a Jacobian lower than 0.25, and that the mean Jacobian value of all elements be greater than 0.7 (Untaroiu et al., 2005a).

Orthogonality is a measure of the deviation of the interior angles of the elements from 90°. Elements that have large angle deviations may deform unrealistically under load, and the goal for this mesh quality criterion was to avoid angular deviations greater than 70° (Burkhart et al., 2013), with as many angles as close to 0° as possible.

The final diagnostic technique that was used to assess element quality was the aspect ratio, which is the ratio of the longest to the shortest sides of an element. The most numerically accurate solution is obtained when the edges of all elements are equal in

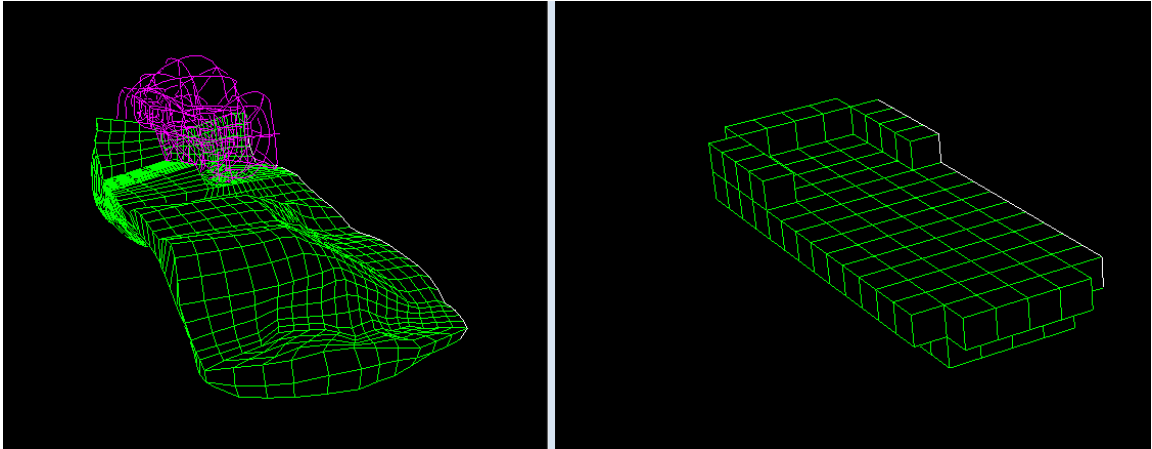


**Figure 3.9: Heel/Foot Pad Mesh**

The inner surface of the heel pad was meshed based on the outer surface of the calcaneus, as seen in purple in the physical view on the left. The computational view showing the block structure is on the right.

length and their aspect ratios are equal to one. The goal for this criterion was to have mean element aspect ratios for all meshes between one and two (Burkhart et al., 2013), with no elements exceeding an aspect ratio of ten (Untaroiu et al., 2005a).

#### *3.2.2.6 MESHING OF THE MIDFOOT/FOREFOOT BONES*

The 24 forefoot and midfoot bone STL files were imported into the meshing component of the Mimics<sup>®</sup> software, 3-Matic<sup>®</sup> (Materialise, Leuven, Belgium) and were automatically meshed using tetrahedral elements. The solid element type and the element quality for these bones was unimportant since they were later defined as rigid bodies, and would not undergo any deformation. The element size of the meshes of these bones was chosen to avoid contact instabilities, and this is discussed further in Section 3.2.4.2.

#### 3.2.3 TIBIAL ALIGNMENT

A previously-validated tibia mesh (Quenneville and Dunning, 2011) was used in this model of the foot and ankle instead of the tibial geometry acquired from the CT scans of the specimen. The reasons for this were two-fold. Firstly, the previously-constructed tibia model was rigorously validated against a battery of validation metrics, including strain gauges and biofidelity corridors over a range of impact speeds. It also adhered to the same quality criteria implemented in the current study. Secondly, meshing is an involved and complicated process, and by not having to mesh the tibia, more time could be afforded to improving the hindfoot bones of the model that were the focus of this study. The extremely thin epiphyseal cortical layer was also meshed with solid elements, which is extremely

difficult to do with acceptable mesh quality. It should also be noted that the tibia model was built from a subject representing the average male population in height, age, weight and fracture force, and so would be appropriate for a general injury-predicting model.

The STL files of the two different tibias were both imported into Mimics<sup>®</sup> so that they could be compared, and the previously-meshed tibia could be aligned with the foot and ankle from the specimen used in this study.

First, the previously-validated tibia's geometry was aligned with the specimen's tibial geometry using global registration algorithms. No rotation was allowed about the medial-lateral and anterior-posterior axes, as both tibias had been previously aligned with the cranial-caudal axis, and this alignment needed to be maintained as a reference for the relative hindfoot bone rotations. Particular attention was given to matching the curvature of the distal articular surface, as well as alignment of the medial malleolus and the fibular notch. Once the tibias had been aligned, the Cartesian coordinates of three identical arbitrary points were recorded on the tibia's initial position and its registered position in order to be able to transform the initial position of the mesh to the registered position during importation to the final model. The resulting alignment of the bones can be seen in Figure 3.10. The relative distance between the two tibias along their lengths was compared using the Mimics<sup>®</sup> analysis module, as were their surface areas and volumes, in order to evaluate the use of the previously validated tibia instead of the specimen's tibia.

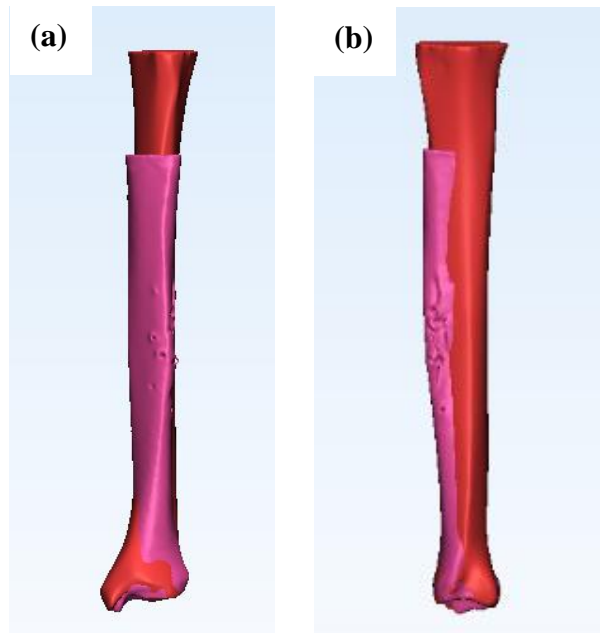


**Figure 3.10: Alignment of the Two Tibial Geometries**

Anterior (a) and lateral (b) views of the tibial alignment are shown. The geometry of the previously-validated tibial mesh is in red, and the specimen's tibial geometry is in pink. The previously-validated tibial mesh geometry was registered to the specimen's tibial geometry while maintaining its cranial-caudal alignment.

### 3.2.4 FINITE ELEMENT MODEL SETUP

#### *3.2.4.1 SOFTWARE OVERVIEW*

The 28 bone meshes and the heel/foot pad mesh were all imported into LS-PrePost<sup>®</sup>, a component of the LS-Dyna<sup>®</sup> (LSTC, Livermore, CA, USA) finite element analysis software that allows for pre- and post- processing of the model. LS-PrePost<sup>®</sup> allows the user to apply boundary conditions, define contact between parts, and assign material properties. The two solid hexahedral element formulations used in this study were the standard constant stress solid (ELFORM 1), with a single point of integration, and the fully integrated quadratic 8 node element with nodal rotations (ELFORM 3), which has eight integration points. The greater the number of integration points, the greater the accuracy of the solution, but the higher the computational cost. Tetrahedrals, shells and 1-D bar elements were assigned standard element formulations with one point of integration.

#### *3.2.4.2 BOUNDARY CONDITIONS AND CONTACT*

A footplate mesh was created in LS-PrePost<sup>®</sup> to represent the footplate of the ankle positioner. This footplate was modeled as a rectangular prism, one element thick, composed of hexahedral elements. Only a single element thickness was used to reduce computation time, since this mesh was assigned rigid body properties. The footplate was positioned to cover the entire sole of the foot, and by using automatic contact detection, this part was moved superiorly until it was just touching the sole of the foot, without any initial penetrations. Having no initial nodal penetrations is important for defining contact between objects since if nodes pass through a neighbouring contact surface, contact

instabilities can result. If initial nodal penetrations between contact surfaces are not manually eliminated by repositioning the objects, LS-Dyna® will move the offending nodes prior to computation, altering the geometry of the parts. Due to CT resolution limitations making it difficult to define the exact separation between different structures in the foot, some initial nodal penetrations were present between the midfoot/forefoot bones and the foot pad. These initial penetrations were eliminated by moving the forefoot and midfoot bones away from the footpad where necessary with automatic contact detection. Metatarsal 5 had to be moved the farthest distance of 1.4 mm, and all other bones were moved less than 1 mm. These distances were considered to be negligible, as when load was applied to the bottom of the foot the soft footpad would deform, hopefully allowing the forefoot bones to return to their original positions.

The footplate was constrained to move only in the superior direction, and a linear load curve ramp from 0 to 150 lbs was applied to the center of the footplate, followed by a brief 25 ms period where the maximum load was held constant. These conditions corresponded to the footplate boundaries and forces that were applied experimentally. The time over which the force was applied was selected to maintain quasi-static strain rates in the bones (see Section 4.3.2). The nodes at the proximal end of the tibia and fibula were fixed in translation and rotation, corresponding to the conditions imposed on the proximal end of the leg experimentally by potting.

Contact surfaces were defined between any bones that may come into contact, as well as the calcaneus and the heel pad, the forefoot/midfoot bones and the footpad, and the heel/foot pad and the footplate. For the talus and calcaneus, the contact surfaces were

defined to be very large to cover any locations that might come into contact when ankle posture is adjusted. The coefficient of friction among bones was chosen to be 0.01, which is the same as between surfaces covered in articular cartilage (Hills and Butler, 1984). As a layer of rubber was present on the footplate during the experiment to reduce the potential for slipping of the foot, the coefficient of friction between the heel/foot pad and the footplate was chosen to be 0.9, which is the same as that between skin and rubber (Seo and Armstrong, 2009). Finally, in the natural foot, the bones are connected to the plantar soft tissues, so a coefficient of friction of 1 was chosen between the heel/foot pad and the bones to reduce relative movement among these parts.

According to the LS-Dyna<sup>®</sup> documentation, a rigid part should have a finer mesh than any deformable body with which it may come into contact to avoid contact instabilities. As a result, the navicular and cuboid bones had a fine mesh with element sides of around 1.5 mm in length, since they come into contact with the talus and calcaneus, which have element sides at most 3 mm in length. Likewise, the forefoot bones were assigned a finer mesh than the footpad, and the footplate a finer mesh than the foot and heel pads.

The phalanges are mainly important for assessment of gait (Leardini et al., 2007), which is beyond the scope of the current model, with the heads of the metatarsals being the primary point of load transfer with the ground in the forefoot. As a result, the phalanges were rigidly connected to the heads of the metatarsals, and no contact was defined between these bones and any other parts of the model.

### 3.2.4.3 BONE MATERIAL PROPERTY ASSIGNMENT

The cortical and cancellous bone were modeled as elastic-plastic materials (MAT\_24), with all properties assigned to be the same as those used in the previously-validated FE model of the tibia (Quenneville and Dunning, 2011). It was assumed that if the entire model was from the same individual, then all cortical and cancellous bone should have similar properties, and so the cortical and cancellous bone of the calcaneus, talus, fibula and tibia were all assigned the same density (cortical =  $1850 \text{ kg/m}^3$ , cancellous =  $1000 \text{ kg/m}^3$ ), elastic modulus (cortical = 22.5 GPa, cancellous = 0.4 GPa), yield stress (cortical = 0.125 GPa, cancellous = 0.01 GPa), tangent modulus (cortical = 1.5 GPa, cancellous = 0.05 GPa), Poisson's ratio (0.3), and Cowper-Symonds strain rate coefficients ( $C = 360.7$ ,  $P = 4.605$ ). A sensitivity study was later performed (discussed in Chapter 4), to fine tune some of the properties to best match the strains measured on the bones experimentally, as these properties may vary greatly depending on the person.

The rigid body midfoot and forefoot bones were assigned the same elastic modulus as cortical bone for contact calculation purposes, and the density of these bones was chosen to be the average of the densities of cortical and cancellous bone, as they were represented by one part where these two types of bone were combined.

Hexahedral elements of bone were set to ELFORM 1 and the shell elements of the cortical bone of the talus and calcaneus were set to the equivalent standard formulation for shell elements. The thicknesses of the shell elements were defined to be the same everywhere except for two thinner regions (see Section 3.3.3), and the contact surfaces for these shells were set to be on the outer surface of the bones to which they were connected.

#### 3.2.4.4 LIGAMENT POSITIONING AND MATERIAL PROPERTY ASSIGNMENT

In conjunction with the contact surfaces, ligaments control bone-to-bone interactions and relative motion throughout the FE model of the foot and ankle. Sixty-seven ligaments were modeled as 1D bar elements with a single point of integration (springs), and were attached to the bones via surface nodes. The ligament attachment sites on each bone were identified based on ligamentous dissections of the foot and ankle documented in anatomical textbooks and journal papers (Golanó et al., 2010, Rohen et al., 1992), as well as illustrations of this anatomical region (Gray, 2009). In order to minimize personal bias in the selection of ligament insertion locations, four researchers were each given a copy of the FE model of the foot, and independently picked nodes that they considered to be the closest to each actual ligament insertion location, in reference to the aforementioned anatomical texts. The Cartesian coordinates of all nodes that were picked for each insertion location were averaged, and the node closest to the resulting average position was selected as the final ligament insertion node.

Material properties for eight of the ligaments that involve the tibia and fibula were based on non-linear force-strain equations from the literature (Funk et al., 2000). The elastic response function is of the form  $T(\epsilon) = a(e^{b\epsilon} - 1)$ , and values of  $a$  and  $b$  for each ligament were based on the curve fit data provided in Table 3.1. When applying these non-linear force-strain relations to the ligaments in the FE model, the strain values were converted to displacement based on the initial length of each ligament calculated from the ligament insertion coordinates. The ninth ligament involving the tibia and fibula, the

**Table 3.1: Tibia and Fibula Ligament Properties**

Ligament properties for eight ligaments that connect the tibia and fibula with the bones of the foot and ankle are expressed as curve fit data (a and b) for an elastic force-strain response function (Funk et al., 2000). The stiffness k of the tibionavicular ligament is also provided (Siegler et al., 1988).

<b>Ligament</b>	<b>a (N)</b>	<b>b</b>
Anterior Talofibular	7.18	12.50
Anterior Tibiofibular	5.52	22.63
Anterior Tibiotalar	2.06	20.11
Calcaneofibular	0.20	49.63
Posterior Talofibular	0.14	44.35
Posterior Tibiofibular	6.87	20.07
Posterior Tibiotalar	1.34	28.65
Tibiocalcaneal	0.51	45.99
Tibionavicular	k = 39.1 N/mm	

tibionavicular ligament, was modeled as a linear spring with a stiffness value taken from the literature (Siegler et al., 1988).

Material data is severely lacking in the literature for midfoot ligaments and hindfoot ligaments connecting the talus and calcaneus. Good results have been achieved in a previous FE study by assuming these ligament material properties to be the same as those for the anterior-talofibular ligament, scaled by the ratio between their respective cross-sectional areas (Shin et al., 2012). Cross sectional areas of the midfoot ligaments and anterior-talofibular ligament have been reported by Imhauser (2004), Mkandawire (2001, 2005) and Shin (2012). The anterior-talofibular ligament has a cross-sectional area of 63 mm<sup>2</sup> (Mkandawire et al., 2005), and the cross-sectional areas and area ratios for the midfoot ligaments are provided in Table 3.2.

Forefoot ligaments were modeled as linear springs with stiffness values taken from the literature (Hofstede et al., 1999, Kitaoka et al., 1994, Kura et al., 2001, Solan et al., 2001). In the absence of material property data, a previous study assumed the ligaments in this region to have the same properties as the dorsal intermetatarsal ligament (Shin et al., 2012). The stiffness of the long plantar ligament was calculated based on an elastic modulus value for this ligament used in a previous FE model (Cheung et al., 2006), as well as its area (Mkandawire et al., 2001) and length, calculated from its insertion points in the current FE model. Properties for these ligaments are provided in Table 3.3.

**Table 3.2: Calcaneus, Talus and Midfoot Bone Ligament Properties**

Properties for the calcaneal, talar and midfoot bone ligaments were assumed to be the same as the anterior-talofibular ligament, scaled by their relative cross-sectional areas. The anterior-talofibular ligament has a cross-sectional area of 62.85 mm (Mkandawire et al., 2005) and areas for all other ligaments were provided by Imhauser (2004), Mkandawire (2001, 2005) and Shin (2012). For ligaments involving the cuneiform bones, Lat, Int and Med refer to the lateral, intermediate and medial cuneiforms, respectively.

<b>Ligament</b>	<b>Area (mm<sup>2</sup>)</b>	<b>Area Ratio</b>	<b>Reference</b>
Anterior Talocalcaneal	14.4	0.229	Imhauser (2004)
Posterior Talocalcaneal	14.96	0.238	Mkandawire (2001)
Lateral Talocalcaneal	6.84	0.109	Mkandawire (2001)
Medial Talocalcaneal	14.91	0.237	Mkandawire (2001)
Interosseous Talocalcaneal	72.80	1.158	Imhauser (2004)
Dorsal Talonavicular	35.15	0.559	Mkandawire (2001)
Interosseous Calcaneocuboid	72.80	1.158	Imhauser (2004)
Plantar Calcaneocuboid	98.70	1.570	Shin (2012)
Calcaneonavicular	9.23	0.147	Mkandawire (2001)
Plantar Calcaneonavicular	161.00	2.560	Mkandawire (2005)
Dorsal cuboideonavicular	13.10	0.208	Mkandawire (2001)
Plantar Cuboideonavicular	27.80	0.442	Shin (2012)
Interosseous Cuboideonavicular	14.01	0.223	Mkandawire (2001)
Plantar Cuneonavicular (Med)	12.59	0.200	Mkandawire (2001)
Plantar Cuneonavicular (Int)	8.10	0.129	Mkandawire (2001)
Plantar Cuneonavicular (Lat)	7.12	0.113	Mkandawire (2001)
Dorsal Cuneonavicular 1 (Med)	6.46	0.103	Mkandawire (2001)
Dorsal Cuneonavicular 2 (Int)	10.33	0.164	Mkandawire (2001)
Dorsal Cuneonavicular 3 (Lat)	11.61	0.185	Mkandawire (2001)
Dorsal Cuneocuboid	7.52	0.120	Mkandawire (2001)
Plantar Cuneocuboid	13.80	0.219	Mkandawire (2001)
Dorsal Intercuneiform (Lat to Int)	13.80	0.220	Shin (2012)
Dorsal Intercuneiform (Int to Med)	13.80	0.220	Shin (2012)
Plantar Intercuneiform (Lat to Int)	13.80	0.220	Shin (2012)
Plantar Intercuneiform (Int to Med)	13.80	0.220	Shin (2012)
Interosseous Intercuneiform (Lat to Int)	121.07	1.925	Mkandawire (2005)
Interosseous Intercuneiform (Int to Med)	121.07	1.925	Mkandawire (2005)

**Table 3.3: Forefoot Ligament Properties**

Linear elastic stiffness values reported in the literature for the forefoot ligaments are provided (Hofstede et al., 1999, Kitaoka et al., 1994, Kura et al., 2001, Solan et al., 2001). Since many ligaments share the same name in this part of the foot, the insertion points of each ligament are given, with Meta referring to a metatarsal, and Med, Int and Lat referring to medial, intermediate and lateral for the cuneiforms.

<b>Ligament</b>	<b>Insertion Points</b>	<b>Stiffness k (N/mm)</b>	<b>Reference</b>
Dorsal Tarsometatarsal	Meta1 / Med Cuneiform	115.0	Solan (2001)
	Meta2 / Med Cuneiform	115.0	Solan (2001)
	Meta2 / Int Cuneiform	115.0	Solan (2001)
	Meta2 / Lat Cuneiform	115.0	Solan (2001)
	Meta3 / Lat Cuneiform	115.0	Solan (2001)
	Meta4 / Lat Cuneiform	115.0	Solan (2001)
	Meta4 / Cuboid	115.0	Solan (2001)
	Meta5 / Cuboid	115.0	Solan (2001)
Plantar Tarsometatarsal	Meta1 / Med Cuneiform	90.0	Solan (2001)
	Meta2 / Med Cuneiform	90.0	Solan (2001)
	Meta3 / Med Cuneiform	90.0	Solan (2001)
	Meta4 / Cuboid	90.0	Solan (2001)
	Meta5 / Cuboid	90.0	Solan (2001)
Interosseous Tarsometatarsal	Meta2 / Med Cuneiform	189.7	Kura (2001)
	Meta2 / Lat Cuneiform	189.7	Kura (2001)
	Meta3 / Lat Cuneiform	189.7	Kura (2001)
Dorsal Intermetatarsal	Meta1 / Meta2	125.0	Hofstede (1999)
	Meta2 / Meta3	125.0	Hofstede (1999)
	Meta3 / Meta4	125.0	Hofstede (1999)
	Meta4 / Meta5	125.0	Hofstede (1999)
Plantar Intermetatarsal	Meta1 / Meta2	125.0	Hofstede (1999)
	Meta2 / Meta3	125.0	Hofstede (1999)
	Meta3 / Meta4	125.0	Hofstede (1999)
	Meta4 / Meta5	125.0	Hofstede (1999)
Plantar Fascia	Meta1 / Calcaneus	203.3	Kitaoka (1994)
	Meta2 / Calcaneus	203.3	Kitaoka (1994)
	Meta3 / Calcaneus	203.3	Kitaoka (1994)
	Meta4 / Calcaneus	203.3	Kitaoka (1994)
	Meta5 / Calcaneus	203.3	Kitaoka (1994)
Long Plantar Ligament		75.9	Cheung (2006)

#### *3.2.4.5 FOOT/HEEL PAD MATERIAL PROPERTY ASSIGNMENT*

Properties for the foot and heel pad were taken from a study by Erdemir et al. (2006), in which an inverse finite element model was used to estimate the mechanical properties of the heel pad, based on experimental heel pad indentation tests. The heel pad was assigned a first order hyperelastic Ogden rubber material model (MAT\_77) with the parameters  $\mu = 4.82$  kPa and  $\alpha = 6.82$ . Due to an absence of material data in the literature for the foot pad, this region was assumed to have the same properties as the heel pad. For soft materials that undergo large deformations, such as for the foot/heel pad, using elements with ELFORM 1 causes significant hourglassing of the mesh. This is a non-physical effect that manifests itself by elements assuming a “zig- zag” or hourglass pattern under load, causing the solution to be numerically inaccurate. Instead, for these parts, the more computationally expensive ELFORM 3 was applied, which does not suffer from this effect.

### **3.3 RESULTS**

#### **3.3.1 MESH STATISTICS AND EVALUATION**

The talus was composed of 20000 hexahedral elements and 1640 shell elements, while the calcaneus was composed of 31876 hexahedral elements and 2314 shell elements. Both bones had maximum element sizes on the outer surface of around 3 mm. The fibula was composed of 13024 solid elements with maximum element sizes at the surface of the epiphysis and diaphysis of 2.9 and 4.3 mm, respectively. Finally, the heel/foot pad was composed of 6538 solid elements with a maximum element size at the surface of 9.8 mm.

Table 3.4 provides a summary of the element Jacobian ranges and means for all meshes. All Jacobians in the talus, calcaneus and heel/foot pad were 0.3 or greater, but at the fibula, ten elements in the transition zone had Jacobians below 0.25. The mean Jacobians for all meshes were 0.7 or greater.

Table 3.5 provides a summary of the angle deviation ranges and means for all meshes. Completely eliminating angle deviations above  $70^\circ$  was not possible, but all meshes had a minimal number of elements with angular deviations above this value (0.35% or less), and the mean deviation in all cases was  $0^\circ$ . In the calcaneus, the elements with significant angle deviations were all located around the boundary between the body and the sustentaculum (Figure 3.11a), and in the fibula, these elements were concentrated in the transition region and the epiphysis (Figure 3.11b). In the talus and heel/foot pad, only a few of these deviated elements were present, and they were not concentrated at any region in particular (Figure 3.11c and d).

Table 3.6 provides a summary of the aspect ratio ranges and means for all meshes. The mean aspect ratio for all meshes was less than two, and the maximum aspect ratio for the talus, calcaneus and heel/foot pad was below ten. The maximum aspect ratio for the fibula was 17.48, with 4.11% of all fibular elements between ten and this maximum value. The elements with aspect ratios greater than ten in the fibula were concentrated in the cancellous section of the bone just before the transition region. Information on the quality of the previously validated tibial mesh is provided in Appendix G.

**Table 3.4: Jacobian Ranges and Means**

All meshes met the minimum Jacobian criterion of 0.25 except for the fibula that contained ten elements below this value at the transition region. The mean Jacobians were 0.7 or greater.

Mesh	Range of Jacobians	Percentage of Elements with Jacobian <0.25	Mean Jacobian
Talus	0.30 to 3.80	0	0.80
Calcaneus	0.33 to 5.21	0	0.75
Fibula	0.17 to 10.4	0.08%	0.80
Heel/Foot Pad	0.32 to 2.75	0	0.70

**Table 3.5: Angular Deviation Range and Mean**

Completely eliminating angular deviations was not possible, but the number of elements above the threshold of  $70^\circ$  was minimal for all meshes. The mean angle of deviation for each mesh was  $0^\circ$ .

Mesh	Range of Angle Deviations	Percentage of Elements with Deviations > $ 70^\circ $	Mean Angle of Deviation
Talus	$-67.8^\circ$ to $74.3^\circ$	0.03%	$0^\circ$
Calcaneus	$-77.9^\circ$ to $83.5^\circ$	0.07%	$0^\circ$
Fibula	$-75.9^\circ$ to $81.6^\circ$	0.35%	$0^\circ$
Heel/Foot Pad	$-66.8^\circ$ to $75.5^\circ$	0.05%	$0^\circ$

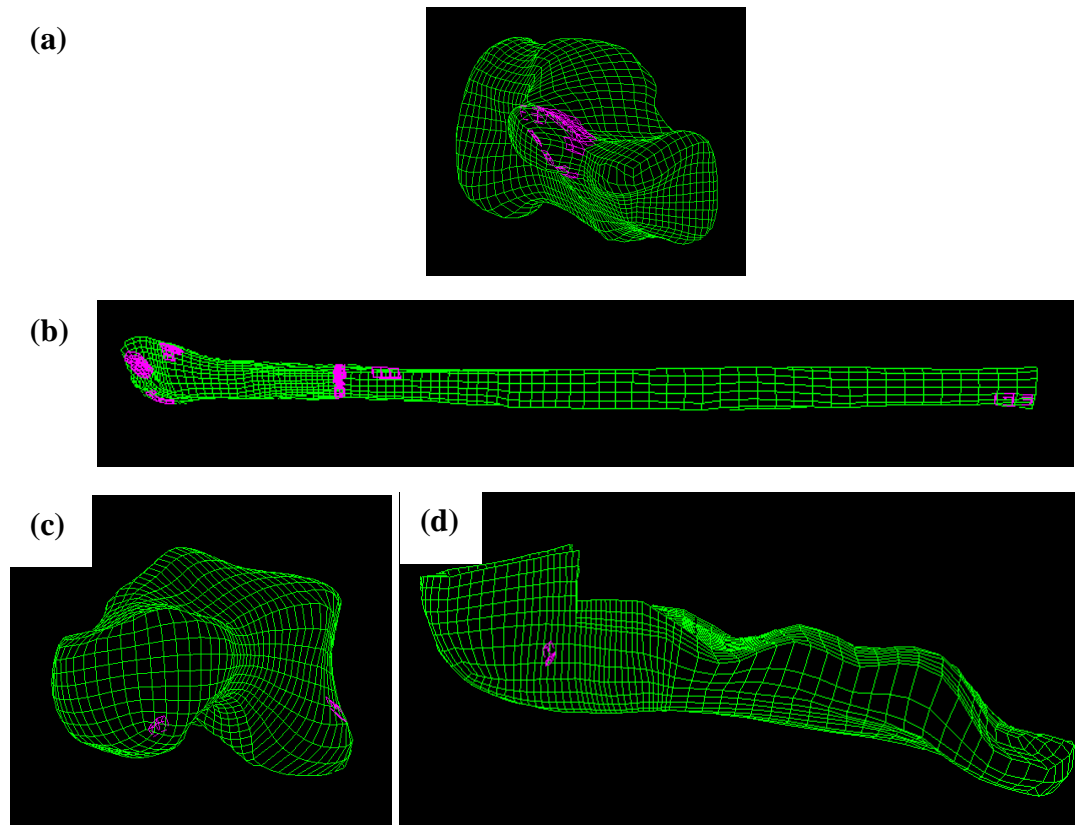


**Figure 3.11: Elements with Large Angular Deviations**

Locations with angular deviations greater than  $70^\circ$  are shown in pink. In the calcaneus (a), these elements are located between the sustentaculum and the body. Of all the hexahedral meshes, the fibula (b) had the greatest percentage of these elements relative to the total number of elements in the mesh, and they are located at the epiphysis and the transition region. The talus (c), and heel/foot pad (d) had a minimal number of these elements.

**Table 3.6: Aspect Ratio Range and Mean**

For the talus, calcaneus and heel/foot pad, all aspect ratios were below 10. However, for the fibula, elements with aspect ratios up to 17.48 were present in the mesh, and these elements accounted for 4.11% of all fibular elements. The mean aspect ratio for all meshes was between 1 and 2.

Mesh	Range of Aspect Ratios	Percentage of Elements with Aspect Ratios > 10	Mean Aspect Ratio
Talus	1.02 to 7.70	0	1.6
Calcaneus	1.00 to 8.59	0	1.6
Fibula	1.06 to 17.48	4.11%	1.5
Heel/Foot Pad	1.20 to 8.34	0	1.9

### 3.3.2 TIBIAL ALIGNMENT

A map of the overall distance between the previously-validated tibial geometry and the specimen's tibia can be seen in Figure 3.12. The maximum distance was found to be 10.8 mm at the diaphysis and only 3.5 mm at the medial malleolus of the epiphysis.

The two tibias were both potted to different depths and CT scanned over different distances during testing, and so the proximal end of the previously-validated tibial geometry was removed so that the two tibias were the same length. This was done to be able to compare their relative volume and surface area, which were measured using Mimics®. The surface area and volume of the previously-validated tibial geometry were 31753 mm<sup>2</sup> and 212538 mm<sup>3</sup>, whereas the same measurements for the specimen's tibia were 33443 mm<sup>2</sup> and 187050 mm<sup>3</sup>. This yielded a percent difference in surface area of 5.2% and a percent difference in volume of 12.8%.

### 3.3.3 SHELL THICKNESS

The average cortical region thicknesses for the talus and calcaneus were found to be fairly consistent throughout both bones (Figure 3.13), with a thickness of 2.74 mm for the talus and 2.68 mm for the calcaneus. The cortical shell element thicknesses were set to be these constant values throughout both bones, except for a thinner lateral calcaneal region that was assigned a cortical thickness of 1.25 mm based on the distance map.

### 3.3.4 FINAL LOWER LEG MODEL

The complete lower leg model can be seen in Figure 3.14.

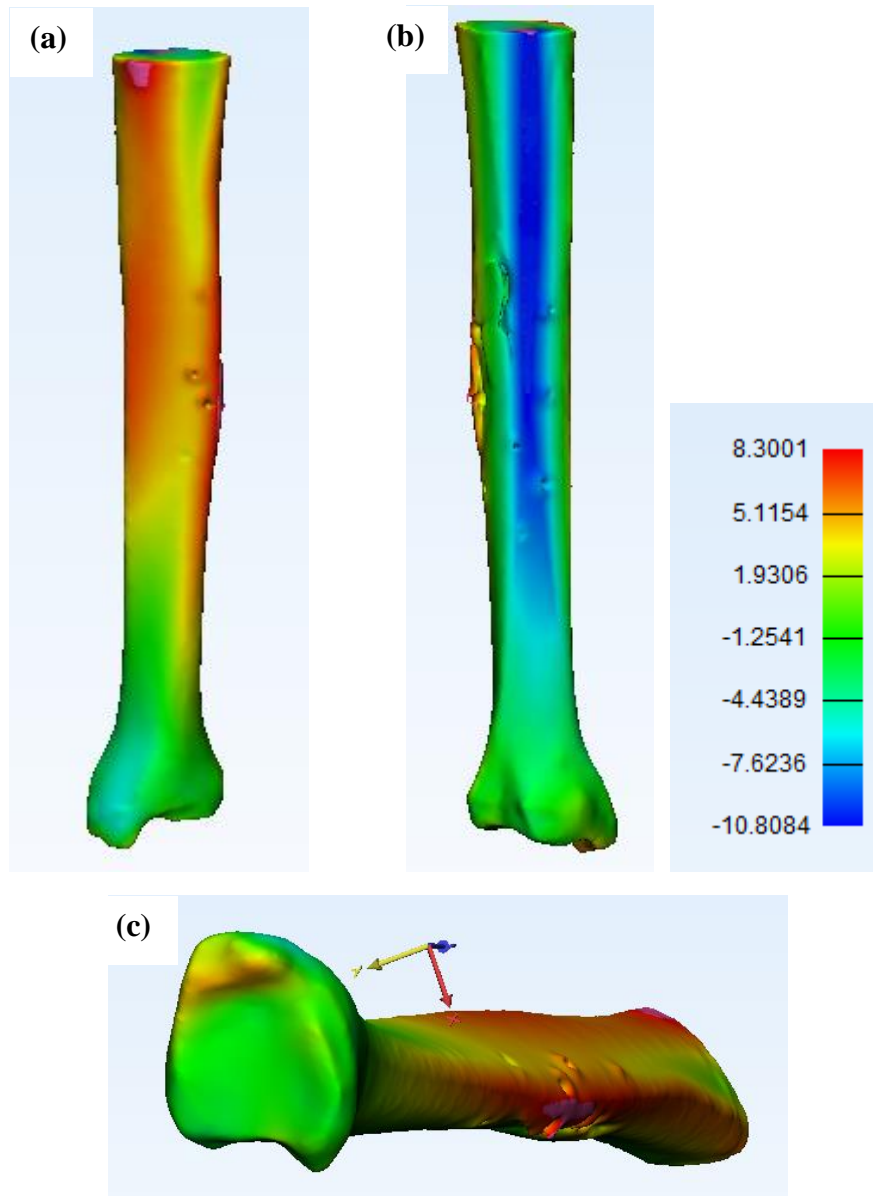


**Figure 3.12: Distance Map Between the Two Tibias**

Anterior-medial (a), posterior-lateral (b) and inferior (c) views of a contour map of the distance between the two tibias is shown (scale in mm). For the purpose of simplicity, only the geometry of the previously-validated tibial model is displayed. On the medial side of the diaphysis, the maximum distance between the tibias was 8.3 mm, whereas on the lateral side, the maximum distance was 10.8 mm. At the epiphysis, the maximum distance was 3.5 mm at the medial malleolus.

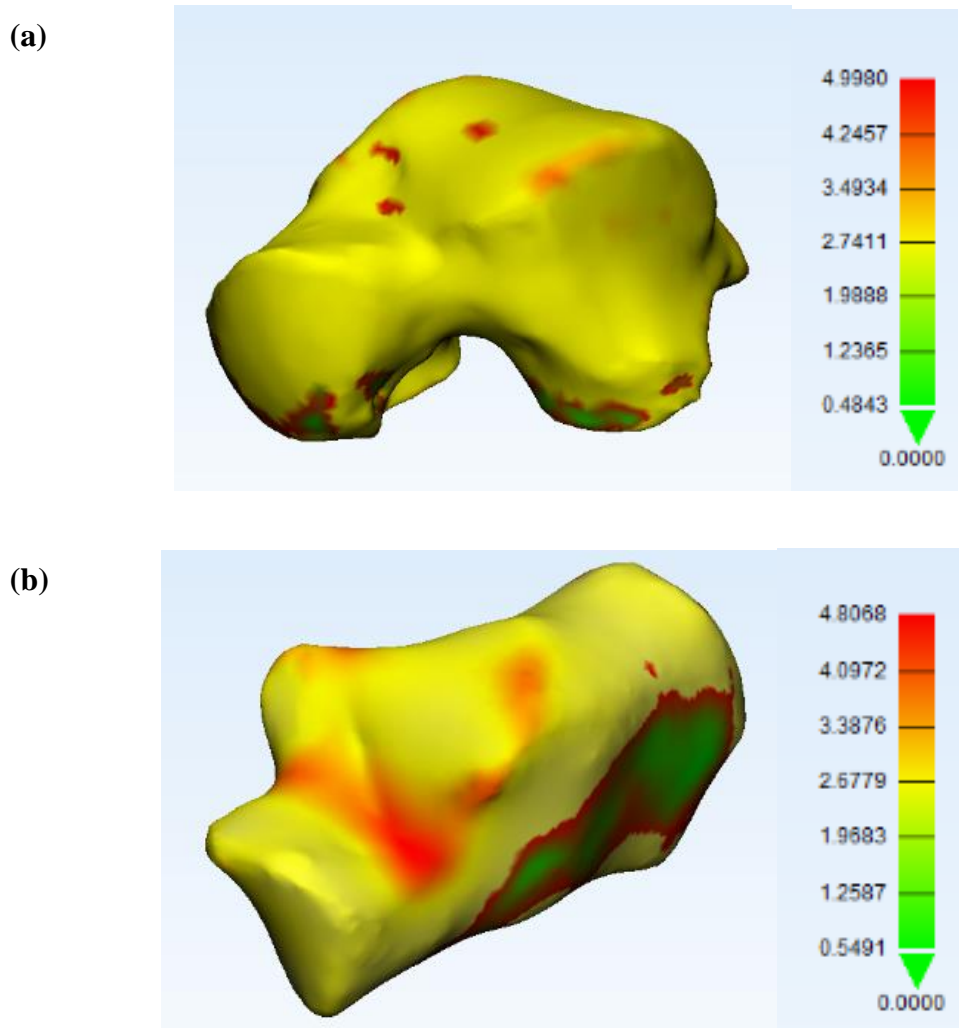


**Figure 3.13: Talus and Calcaneus Shell Thicknesses**

A distance map was generated between the cortical and cancellous regions of the talus (a) and calcaneus (b) (scale in mm). A relatively consistent thickness was observed of around 2.74 mm for the talus and 2.68 mm for the calcaneus. The lateral calcaneus had a thinner cortical shell, at around 1.25 mm.



**Figure 3.14: Complete Lower Leg Model**

The final lower leg model is composed of 28 bones, with contact surfaces defined among them, that are interconnected by 67 ligaments. The heel/foot pad underneath the foot is also represented, as is the footplate of the ankle positioner.

### 3.4 DISCUSSION

This study presents the most complex FE model of the lower leg and ankle constructed to date. Twenty-eight discrete bones were modeled to a high degree of geometric accuracy, based on CT scans. The meshes of these bones are also very fine relative to those seen in previous studies (*e.g.* Dong et al., 2013), with the largest surface element size on the hindfoot bones in this study (3 mm) corresponding to the smallest average element size seen previously. The hindfoot bones had discrete cancellous and cortical regions that were assigned elastic-plastic material properties, and an unprecedented sixty-seven ligaments were included, thirty-five of which were assigned non-linear force-displacement relationships. The foot/heel pad was modeled based on the actual geometry of this region acquired from the CT scans of the specimen, and was assigned a hyperplastic material that had been previously shown to accurately model the response of this region under load. The model was also set up with boundary conditions and loads analogous to those experienced during experimental testing.

Unlike in many previous models, special attention was given to the quality of the elements in the deformable meshes, with the rigorous element quality criteria being nearly fully met. The mean Jacobians, aspect ratios and angular deviations for all meshes met the desired criteria, indicating that in general, elements were of good quality. The elements of the talus, calcaneus and foot/heel pad were all above the Jacobian threshold and below the aspect ratio limit. Furthermore, only a very small number of elements in these meshes had excessive angular deviations (0.07% of elements or fewer). It was impossible to completely eliminate elements with large angular deviations, but steps were taken to

minimize them as much as possible. The fibula had very few elements below the Jacobian threshold (0.08% of all elements in the mesh), and angular deviations in the fibula were also very good, with a minimum of elements exceeding the threshold value (0.35% of all elements in the mesh). The one criterion where improvement could be made is for the aspect ratios of the fibula. The limited number of poor elements was deemed acceptable as the hindfoot bones were the primary focus of the model, not the shank, and the fibula has an overall minor contribution to the load path through the ankle, accounting for only 6.4% of the load through this region (Takebe et al., 1984). That being said, the fibula could be improved in the future by using an even finer mesh, or selecting the transition region to be located more distally, positioned right as the epiphysis begins to taper.

One of the main limitations with this study is that a tibial geometry other than the specimen's tibia was used. With expected interpersonal anatomical variability in mind, the maximum distances between the two tibias as well as their comparable surface areas and volumes were deemed to be acceptable for using the previously validated tibia *in lieu* of the specimen's tibia. Furthermore, the benefits of the tibia being previously validated and saving duplicate effort of remeshing were considered to outweigh the potential limitations, especially in light of the fact that the very thin epiphyseal cortical bone had been meshed using solid elements. Due to a natural difference in curvature between the two bones, the largest positional difference was observed at the diaphysis. This may have been a function of the two different tibias being potted and aligned by two different investigators. If a full global registration had been performed between the two bones with the cranial-caudal alignment allowed to vary, a much closer alignment would have been obtained. However,

maintaining the alignment in which the previously-constructed tibia had been validated was important to ensure the accuracy of its mechanical response.

The distal articular surfaces of the tibias matched up well, with a minimal difference throughout this region. The medial malleolus protruded 3.5 mm further than the specimen's malleolus for the previously-validated tibia model. This will be addressed further in Chapter 4. Furthermore, while meeting the mesh quality requirements for the fibula was difficult, with the worst quality elements in the whole model in this bone, meeting these requirements during meshing of the tibia would have been even more problematic since its geometry is even more complex.

With a few exceptions, the cortical shells of the talus and calcaneus were assigned uniform thicknesses. This was deemed acceptable, as the distance map between the cortical and cancellous regions indicated that the thickness was relatively constant throughout these bones. Modeling regional variation in cortical shell thicknesses was beyond the scope of this study, but could be implemented in the future. Another alternative would be to use an even finer mesh, and model the cortical region with solid elements. Shells were appropriate for use in the cortical bone of the talus and calcaneus since it is a situation in which the two planar dimensions of the cortical surface layer are much larger than its thickness, and the deformation across the direction of shell thickness should be negligible due to the reinforcement provided by the cancellous region.

Bone was modeled as isotropic and homogenous with properties taken from previous studies, which is the current standard in dynamic, injury-predicting FE modeling (*e.g.* Shin et al., 2012). Using this approximation has yielded good results for these types

of models of long bones such as the femur (Untaroiu et al., 2005a), tibia (Quenneville and Dunning, 2011) and radius (Burkhart et al., 2014). However, the loading through the calcaneus and talus is more complex due to their connections with multiple load paths through the hindfoot and forefoot. As a result, due to Wolff's law, the density and properties of these bones vary throughout (von Meyer, 2011), and this is exemplified by the large variation in greyscale values that can be observed in the axial slice of the talus in Figure 3.2a. While beyond the scope of the current study, more effort should be made in the future to implement regional material variations in these bones to obtain an accurate numerical solution. Some effort was made to optimize the properties to the specific specimen used in this study, and this is discussed in Chapter 4.

The ligaments were modeled as 1D springs, whereas in reality, ligaments in the ankle are more like 2D sheets. Implementing realistic ligament geometry is beyond the scope of this study, and is challenging in general since overall ligament responses from tension tests are available (*e.g.* Funk et al., 2000), but there is a lack of information about the material properties of ligaments to assign to an FE mesh (Weiss and Gardiner, 2001). Finding the range of each insertion site on each bone would also be a huge undertaking. 2D or 3D FE modeling of ligaments is typically only recommended if the study is specifically focused on ligament biomechanics, or the interaction of the ligaments with the surrounding tissues (Weiss et al., 2005, Galbusera et al., 2014). No properties for the midfoot and forefoot ligaments are available in the literature, and so their properties were obtained by scaling currently known ligament properties based on cross-sectional area. This has been done in previous FE models of the lower limb (Shin et al., 2012), and until

more material data are available, this is the only viable option for modeling these ligaments. Furthermore, no pretension was applied to the ligaments, as no values are available in the literature for the amount of tension naturally present in the ligaments of the foot. The Achilles tendon was also omitted as no tension was applied to it during experimental testing on the lower leg specimen. Achilles tension increases the joint forces experienced at the ankle, and experimental tests in which Achilles tension was applied (*e.g.* Funk et al., 2002) exhibited a greater incidence of tibial fracture and a reduced likelihood of calcaneal fracture when compared with experiments in which this force was neglected.

The only location where flesh was modeled was at the foot/heel pad. In this study testing was only performed under quasi-static compressive conditions, and flesh has been shown to only play a significant energy-absorbing role in the biomechanical response of the lower leg under dynamic impacts (Untaroiu et al., 2005b). Likewise, viscoelastic properties were omitted from the soft tissues in general, but were implemented for bone. If this model is to be used for dynamic impacts in the future, its properties will need to be updated to respond more realistically under these conditions.

Including cartilage was beyond the scope of this model, and instead, small gaps were present between bones, with the friction factor between them chosen to be the same as between surfaces covered in articular cartilage. This is the current standard in FE models of the ankle (*e.g.* Shin et al., 2012) and will likely lead to slightly greater compressions during simulations. However, with limited information available about cartilage thickness in these joints, it was omitted and could be examined in future studies.

Finally, modeling the midfoot and forefoot bones as deformable was also beyond the scope of this study, with previous FE models of the foot and ankle often assigning rigid properties to these bones (*e.g.* Shin et al., 2012). The hindfoot is the primary load path through the foot and ankle (Hutton and Dhanendran, 1979) and was therefore the focus of this study. The geometric accuracy of the bones in this area was still high, and these bones could be made to be deformable in the future to investigate injuries to this region.

For the purposes of this study, these bones were modeled as one region, the density of which was equal to the average of cortical and trabecular bone densities. While this approach does not necessarily yield the most accurate inertial response for these bones since there may not be equal quantities of cortical and cancellous bone present, the types of simulations that were performed with this model were quasi-static, with minimal inertial effects. The inaccuracy of the inertial properties of these bones is also minor considering that the flesh of the foot was neglected, except on the plantar aspect.

This model of the foot and ankle will be used in Chapter 4 to simulate the quasi-static tests that were conducted experimentally (Chapter 2). The ankle model will be moved into the same postures that were produced experimentally, with the same load applied, and the resulting bone positions and strains will be compared to those observed during the experiment. This will allow the model to be validated, and assess its use as a tool for injury prediction in a wide range of postures.

### **3.5 REFERENCES**

BURKHART, T. A., ANDREWS, D. M. & DUNNING, C. E. 2013. Finite element modeling mesh quality, energy balance and validation methods: A review with

- recommendations associated with the modeling of bone tissue. *Journal of biomechanics*, 46, 1477-1488.
- BURKHART, T. A., QUENNEVILLE, C. E., DUNNING, C. E. & ANDREWS, D. M. 2014. Development and validation of a distal radius finite element model to simulate impact loading indicative of a forward fall. *Proceedings of the Institution of Mechanical Engineers, Part H: Journal of engineering in medicine*, 0954411914522781.
- CHEUNG, J. T.-M., AN, K.-N. & ZHANG, M. 2006. Consequences of partial and total plantar fascia release: a finite element study. *Foot & ankle international*, 27, 125-132.
- DONG, L., ZHU, F., JIN, X., SURESH, M., JIANG, B., SEVAGAN, G., CAI, Y., LI, G. & YANG, K. H. 2013. Blast effect on the lower extremities and its mitigation: A computational study. *Journal of the Mechanical Behavior of Biomedical Materials*, 28, 111-124.
- ERDEMIR, A., VIVEIROS, M. L., ULBRECHT, J. S. & CAVANAGH, P. R. 2006. An inverse finite-element model of heel-pad indentation. *Journal of biomechanics*, 39, 1279-1286.
- FUNK, J., HALL, G., CRANDALL, J. & PILKEY, W. 2000. Linear and quasi-linear viscoelastic characterization of ankle ligaments. *Journal of biomechanical engineering*, 122, 15-22.
- FUNK, J. R., CRANDALL, J. R., TOURET, L. J., MACMAHON, C. B., BASS, C. R., PATRIE, J. T., KHAEWPOONG, N. & EPPINGER, R. H. 2002. The axial injury tolerance of the human foot/ankle complex and the effect of Achilles tension. *Journal of biomechanical engineering*, 124, 750-757.
- GALBUSERA, F., FREUTEL, M., DÜRSELEN, L., D'AIUTO, M., CROCE, D., VILLA, T., SANSONE, V. & INNOCENTI, B. 2014. Material models and properties in the finite element analysis of knee ligaments: a literature review. *Frontiers in bioengineering and biotechnology*, 2.
- GOLANÓ, P., VEGA, J., DE LEEUW, P. A. J., MALAGELADA, F., MANZANARES, M. C., GÖTZENS, V. & VAN DIJK, C. N. 2010. Anatomy of the ankle ligaments: a pictorial essay. *Knee Surgery, Sports Traumatology, Arthroscopy*, 18, 557-569.
- GRAY, H. 2009. *Gray's Anatomy: With original illustrations by Henry Carter*, Arcturus Publishing.
- HILLS, B. A. & BUTLER, B. D. 1984. Surfactants identified in synovial fluid and their ability to act as boundary lubricants. *Annals of the Rheumatic Diseases*, 43, 641-648.
- HOFSTEDDE, D. J., RITT, M. J. & BOS, K. E. 1999. Tarsal autografts for reconstruction of the scapholunate interosseous ligament: a biomechanical study. *The Journal of hand surgery*, 24, 968-976.
- IMHAUSER, C. W. 2004. *The development and evaluation of a 3-dimensional, image-based, patient-specific, dynamic model of the hindfoot*. Drexel University.
- IWAMOTO, M., MIKI, K. & TANAKA, E. 2005. Ankle skeletal injury predictions using anisotropic inelastic constitutive model of cortical bone taking into account damage evolution. *Stapp car crash journal*, 49, 133.

- KITAOKA, H. B., LUO, Z. P., GROWNEY, E. S., BERGLUND, L. J. & AN, K.-N. 1994. Material properties of the plantar aponeurosis. *Foot & Ankle International*, 15, 557-560.
- KURA, H., LUO, Z.-P., KITAOKA, H. B., SMUTZ, W. P. & AN, K.-N. 2001. Mechanical behavior of the Lisfranc and dorsal cuneometatarsal ligaments: in vitro biomechanical study. *Journal of orthopaedic trauma*, 15, 107-110.
- LEARDINI, A., BENEDETTI, M., BERTI, L., BETTINELLI, D., NATIVO, R. & GIANNINI, S. 2007. Rear-foot, mid-foot and fore-foot motion during the stance phase of gait. *Gait & posture*, 25, 453-462.
- MANOLI, A., PRASAD, P. & LEVINE, R. S. 1997. Foot and ankle severity scale (FASS). *Foot & ankle international*, 18, 598-602.
- MKANDAWIRE, C., LEDOUX, W., SANGEORZAN, B. & CHING, R. Hierarchical cluster analysis of area and length of foot and ankle ligaments. Proceedings of the 25th Annual Meeting of the American Society of Biomechanics, 2001. 8-11.
- MKANDAWIRE, C., LEDOUX, W. R., SANGEORZAN, B. J. & CHING, R. P. 2005. Foot and ankle ligament morphometry. *Journal of rehabilitation research and development*, 42, 809.
- QUENNEVILLE, C. E. & DUNNING, C. E. 2011. Development of a finite element model of the tibia for short-duration high-force axial impact loading. *Computer methods in biomechanics and biomedical engineering*, 14, 205-212.
- ROHEN, J., YOKOCHI, C. & LUTJEN-DRECOLL, E. 1992. Color Atlas of Anatomy: Aphotographic Study of the Human Body. *New York: Igaku-Shoin*.
- SAPUAN, S., OSMAN, M. & NUKMAN, Y. 2006. State of the art of the concurrent engineering technique in the automotive industry. *Journal of Engineering Design*, 17, 143-157.
- SEO, N. J. & ARMSTRONG, T. J. 2009. Friction coefficients in a longitudinal direction between the finger pad and selected materials for different normal forces and curvatures. *Ergonomics*, 52, 609-616.
- SHIN, J., YUE, N. & UNTAROIU, C. D. 2012. A finite element model of the foot and ankle for automotive impact applications. *Annals of biomedical engineering*, 40, 2519-2531.
- SIEGLER, S., CHEN, J. & SCHNECK, C. 1988. The three-dimensional kinematics and flexibility characteristics of the human ankle and subtalar joints—Part I: Kinematics. *Journal of biomechanical engineering*, 110, 364-373.
- SOLAN, M. C., MOORMAN, C. T., MIYAMOTO, R. G., JASPER, L. E. & BELKOFF, S. M. 2001. Ligamentous restraints of the second tarsometatarsal joint: a biomechanical evaluation. *Foot & Ankle International*, 22, 637-641.
- TAKEBE, K., NAKAGAWA, A., MINAMI, H., KANAZAWA, H. & HIROHATA, K. 1984. Role of the Fibula in Weight-bearing. *Clinical orthopaedics and related research*, 184, 289-292.
- UNTAROIU, C., DARVISH, K., CRANDALL, J., DENG, B. & JENNE-TAI, W. 2005a. A finite element model of the lower limb for simulating pedestrian impacts. *Stapp car crash journal*, 49, 157.

- UNTAROIU, C., DARVISH, K., CRANDALL, J., DENG, B. & WANG, J.-T. Characterization of the lower limb soft tissues in pedestrian finite element models. 19th International technical conference on the Enhanced Safety of Vehicles, 2005b. 124-131.
- VALLE, L. & RAY, M. 2005. Development and validation of a 50th percentile male human femur: Attachment A. *National Highway Traffic Safety Administration, Worcester, MA: Worcester Polytechnic Institute.*
- VON MEYER, G. H. 2011. The Classic: The Architecture of the Trabecular Bone (Tenth Contribution on the Mechanics of the Human Skeletal Framework). *Clinical Orthopaedics and Related Research®*, 469, 3079-3084.
- WEISS, J. A. & GARDINER, J. C. 2001. Computational modeling of ligament mechanics. *Critical Reviews™ in Biomedical Engineering*, 29.
- WEISS, J. A., GARDINER, J. C., ELLIS, B. J., LUJAN, T. J. & PHATAK, N. S. 2005. Three-dimensional finite element modeling of ligaments: technical aspects. *Medical engineering & physics*, 27, 845-861.

---

## **CHAPTER 4 – Model Verification and Injury Prediction**

---

### **4.1 INTRODUCTION**

In academia, cadaveric testing is often performed to evaluate injury limits and new protective systems, while industry makes use of surrogates, such as anthropomorphic test devices (ATDs) or finite element models (FEMs). While cadaveric testing may provide the most accurate response, it does have some inherent disadvantages, including high costs, and natural anatomic variation among specimens. Instrumentation can be problematic, and only a minimal number of parameters and loading conditions can be investigated for each specimen due to damage accumulation. Finite element (FE) modeling circumvents these issues by allowing for a reusable model that can be subjected to a wide variety of loading conditions with measurement of stress and strain at any location. Also, once constructed, FE models are relatively inexpensive to run.

FE models need to be compared with experimental data to ensure the accuracy of their responses. The most commonly accepted method of validation for lower leg dynamic FE models is comparison of the overall force-time or acceleration-time response of the model at the impactor or at the proximal tibia, with a range of responses known as biofidelity corridors generated from cadaveric specimens in analogous experimental tests (*e.g.* Iwamoto et al., 2005). This verifies that the appropriate “global” model response falls within the range of responses that can be expected, but does not ensure that the individual components of the model, such as bones or ligaments, are exhibiting accurate behaviour. Correct response of the individual model components is important, since the interactions

between these components are what lead to potential failure in the lower leg and ankle. If the separate parts are not exhibiting accurate behaviour, the failure location and load may not be correctly predicted by the model, even if the overall force-time response falls within the appropriate corridor.

Another issue with previous FE models of the lower limb is that validation is usually performed only with the ankle in a neutral posture (*e.g.* Dong et al., 2013), and while the overall response of the model may be accurate for this one posture, there is no guarantee that the same will be true for any other posture the ankle may assume. Examination of the response of lower limb FE models in a variety of ankle postures is important for injury prediction studies, as this variation in posture may alter the fracture threshold and location throughout this region (Klopp et al., 1997). When comparisons have been made with experimental data as ankle posture is varied (Shin et al., 2012, 2013), the sole of the foot was rigidly fixed to a footplate that was rotated about an approximate center of rotation of the ankle joint, and the ankle bone positions that resulted were not necessarily indicative of the actual positions these bones would adopt in the natural ankle.

The overall purpose of this study was to compare the response of the FE model of the foot and ankle constructed in Chapter 3 against strain and positional data acquired during testing on the cadaveric specimen upon which the model was based (Chapter 2). Three main goals comprised this purpose: to tune the material properties of the model, to investigate each bone's response to loading and posture, and to predict the loads that would cause failure in each posture.

## **4.2 METHODS**

### **4.2.1 TUNING OF MATERIAL PROPERTIES**

Tuning of the model began with the properties of the heel/foot pad. This region was initially assigned the average hyperelastic properties from Erdemir et al. (2006). A force ramp was applied from 0 to 667 N in 125 ms and then held at the maximum load for 25 ms. Based on these results, a further two runs were performed with the properties at 75% and 100% of their maximum values within the normal physiological range. The compression was measured and compared in both the simulation and Computed Tomography (CT) scans in the loaded neutral posture in eight locations: underneath each metatarsal head, and at the plantar calcaneus at both the medial process and immediately below the angle of Gissane. These points were chosen as they are the primary points of contact with the footplate, and hence, the main loading paths into the foot. The difference between the simulation and experiment at all eight locations was summed to yield a total error at the three levels of heel pad stiffness.

Using the properties that resulted in the closest heel/foot pad compression to that of the experimental tests, the bone properties were tuned by increasing and decreasing the elastic moduli (cortical: 18 – 24.75 GPa, step size: 2.25 GPa; cancellous: 0.32 – 0.44 GPa, step size: 0.4 GPa) within their normal physiological ranges over the course of four tests. The properties that minimized the total error between the model and the experimental strains were selected.

#### 4.2.2 INVESTIGATION OF FRICTION FACTOR SENSITIVITY

As previously discussed in Section 3.2.4.2, the friction factor between bones was set to be 0.01 based on experimental tests on cartilaginous friction from the literature (Hills and Butler, 1984). In order to determine how sensitive the model was to changes in friction factor, a simulation was performed with the optimized model in the neutral posture with the friction factor set to be 0.02, the value used in the model by Bandak et al. (2001). The Euler angles and displacements of the chosen origins of the talus and calcaneus were calculated relative to the tibiofibular coordinate system at the end of the period in which the maximum force was held, and were compared for simulations in which the friction factor was set to 0.01 and 0.02.

#### 4.2.3 VERIFICATION OF QUASI-STATIC STRAIN RATES

Experimental testing was performed under quasi-static conditions. However, due to the complexity of the model and the fact that LS-Dyna<sup>®</sup> is a dynamic program intended for short duration simulations, if the simulated footplate force were applied as it was in the experiment, the simulation would require an inordinate amount of time to complete. Therefore, for the aforementioned runs, the loading rate was determined by taking the maximum strain measured experimentally and calculating the time that would result in a quasi-static strain rate ( $0.01 - 0.001 \text{ s}^{-1}$  (Shunmugasamy et al., 2010)). In order to verify that the strain rates in the model were, in fact, quasi-static, the maximum strain rates that were induced in the hindfoot bones of the model were calculated. Due to the fact that ligaments were represented by 1D bar elements in this model, concentrated point loading

was observed in the bones at the ligament insertion points, artificially increasing the strains at these isolated locations. Therefore, ligament connection nodes and the adjacent elements were excluded from the maximum strain measurements. A run was then performed with twice the force ramp-up time, and both the maximum strains in each bone and the strains at the gauge locations were compared between the “short” and “long” runs to determine the effect of loading speed/strain rate on the strains induced in the bones.

#### 4.2.4 SIMULATION WITH ORIGINAL TIBIAL GEOMETRY

At the distal articular surface, the biggest difference between the specimen’s original tibia and the previously-validated tibia was the geometry of the medial malleolus. While in general the articular surfaces of the two tibias matched up very well, this anatomical feature protruded 3.5 mm farther medially on the previously-validated tibia, potentially imposing less restriction on the movement of the talar head and neck. This is important since talar neck fractures may be caused by impingement of the talar neck by the medial malleolus (Sneppen and Buhl, 1974). In order to determine how talar neck strains may be affected by the geometry of the medial malleolus, the original tibia was auto-meshed with tetrahedral elements using Mimics 3-Matic<sup>®</sup> and assigned rigid body properties. It was then imported into LS-Dyna<sup>®</sup> and incorporated into the foot and ankle model, including ligament attachments. The modified model was similarly loaded, and the strain results at the talus were compared with those in the original model.

#### 4.2.5 ADJUSTMENT OF ANKLE POSTURE

In order to produce the same ankle postures in the model that were generated experimentally, the axes of rotation of the ankle in the different directions were determined from the CT scans. The center of rotation in plantarflexion/dorsiflexion was determined by picking the same points on the bottom of the calcaneus and first metatarsal in both the neutral and plantarflexion CT scans. Lines were generated in each posture from the two points, and the center of rotation was found by determining the intersection of the perpendicular bisectors of these two lines. The center of rotation in inversion/eversion was determined using the same technique with the two points measured on the footplate in the neutral and inversion/external rotation postures. The rotation axis in internal/external rotation could not be determined from the CT scans since no two points on the foot remained in line throughout this motion. As a result, this rotation axis was estimated to be where the normal from the footplate intersected the midpoint between the two malleoli.

The final position of the footplate in each posture was determined based on these centers of rotation. Four runs of the model were then performed in which the heel/foot pad was rigidly connected to the footplate and the footplate was moved from the neutral posture to each of the final positions corresponding to the experimentally-tested ankle postures. This is how ankle posture has been altered for the few FE models that have examined this effect (*e.g.* Shin et al., 2012). During these rotations, the calcaneus and the forefoot and midfoot bones were fixed to the heel/foot pad to force them to move with the footplate, but were released once the final position was achieved.

For the inversion-external rotation and eversion-external rotation runs, the rotations took place over 100 ms. For the runs involving plantarflexion and dorsiflexion, the rotation time was doubled since the bones of the forefoot were a greater distance from the axis of rotation, causing the bones of the foot to bounce excessively if the rotation occurred too quickly. The plantarflexion run was performed at both 100 and 200 ms of rotation to quantify this effect. After the rotation, the footplate was held in place for 25 ms to allow the bones to ‘settle’ into place. The same loading ramp used in the neutral posture was then applied to the foot in the adjusted posture. In order to stop the foot from moving during the initial stages of loading due to residual inertial effects from the footplate rotation, the tie between the plantar surface of the foot and the footplate was maintained until 30% of the maximum force had been applied. The tie between the bones and the heel/foot pad was then removed at 40% of the maximum load. As in the neutral posture runs, once the maximum load was reached, it was held for a brief period of time.

#### 4.2.6 COMPARISON OF SIMULATION AND EXPERIMENT

For the optimized model run in the neutral posture, the Euler angles and displacements of the chosen origins of the talus and calcaneus were calculated relative to the tibiofibular coordinate system. For the four simulations in which ankle posture was altered, the rotations and displacements of the calcaneus and talus after loading were calculated relative to the loaded neutral posture. These calculations were performed at the end of the period in which the maximum force was held, and the results were compared with the analogous experimental results. The numerical strain gauge values were averaged

over the last 10 ms of constant force application and were also compared with the experimental strains.

Since the previously-validated tibia had been used in the model instead of the original tibial geometry, the tibiofibular coordinate system was altered slightly by selecting the nodes on the previously-validated tibia in closest proximity to the anatomic landmarks used to construct the tibiofibular coordinate system originally. The Euler angle rotations and displacement of the origin of the original and modified tibiofibular coordinate systems were compared to determine if they were within the normal variation for this coordinate system measured experimentally.

Since no coordinate systems had been developed for the midfoot and forefoot bones, the distances between these bones in the simulation and experiment were compared. The first step towards doing this was to acquire sets of 3D STL files of these bones at each tested posture, and in order to avoid having to create their geometry from scratch in each posture, global registration was used in Mimics<sup>®</sup> to move the STL files of the bones in the neutral posture to their corresponding locations in the CT scans of each of the adjusted postures (within a positioning error of 0.1 mm). The bones of the midfoot and forefoot at each adjusted posture were then exported as separate sets of STL files.

STL files of the midfoot and forefoot bones in each adjusted posture from the simulations were exported from LS-Dyna<sup>®</sup>, and were superimposed against the STL files of their respective experimental positions in Mimics<sup>®</sup>. The Analysis module was then used to compare the distances between the bones from the experiment and simulation.

#### 4.2.7 INJURY PREDICTION

The maximum strains in every bone were measured from the simulations, and the force that would cause fracture in each posture was predicted based on a linear extrapolation of the force-strain response up to the critical strain thresholds for cortical and cancellous bone reported in the literature (0.016 and 0.134, respectively) (Burstein et al., 1976, Linde et al., 1989). Once again, ligament connection nodes and the adjacent elements were excluded from these maximum strain measurements.

### 4.3 RESULTS

#### 4.3.1 TUNING OF MATERIAL PROPERTIES

The overall summed errors in heel/foot pad thicknesses measured at the maximum load in the simulation as the hyperelastic material property parameters of this region ( $\mu, \alpha$ ) were adjusted are provided in Figure 4.1.

The final result of this tuning was that the maximum (stiffest) properties within the normal physiological range ( $\mu=24.72$  kPa,  $\alpha= 8.39$ ) (Erdemir et al., 2006) yielded the closest match to the thicknesses measured from the CT scans in the loaded neutral posture. The heel/foot pad thicknesses at the eight investigated locations are compared between the simulation and experiment for the properties that minimized the total error in Figure 4.2. The poorest match was at the lateral head of metatarsal 1, with an error of 75% in thickness. All other metatarsal heads, including the medial head of metatarsal 1, had much smaller errors from 3.7 – 25.1%. At the calcaneus, the medial process had the largest thickness error of 34.5%, but underneath the angle of Gissane matched very well (error of 3.7%).

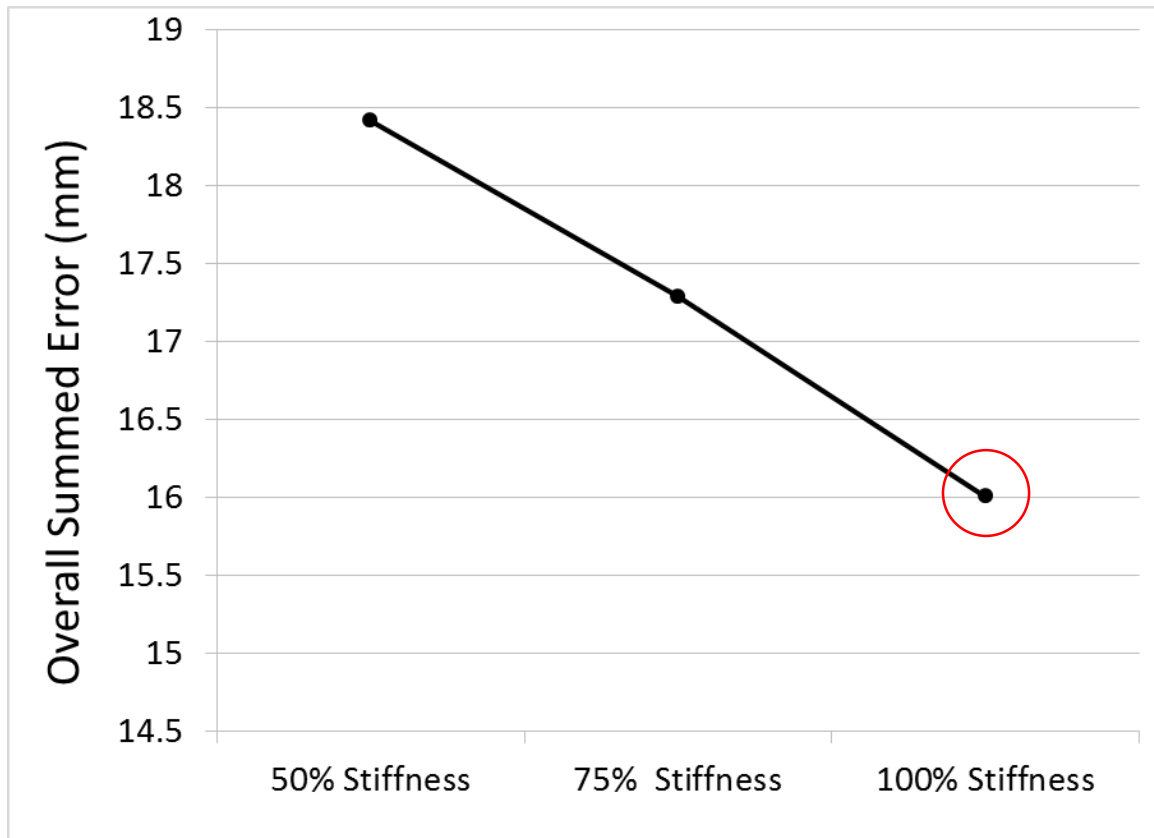


**Figure 4.1: Overall Summed Error Between Experimental and Simulated Heel/Foot Pad Thickness in the Neutral Posture at Maximum Load as Properties are Varied**

The overall summed error between the experimental and simulated heel/foot pad thickness in the neutral posture at 150 lbs of load are provided for three different levels of heel pad stiffness. 100% stiffness corresponds to the properties within the normal physiological range that yield the stiffest response. The total error was summed from the individual errors at eight locations on the plantar surface of the foot. The red circle indicates the stiffness level (100%) that minimized the error between the simulation and experiment.

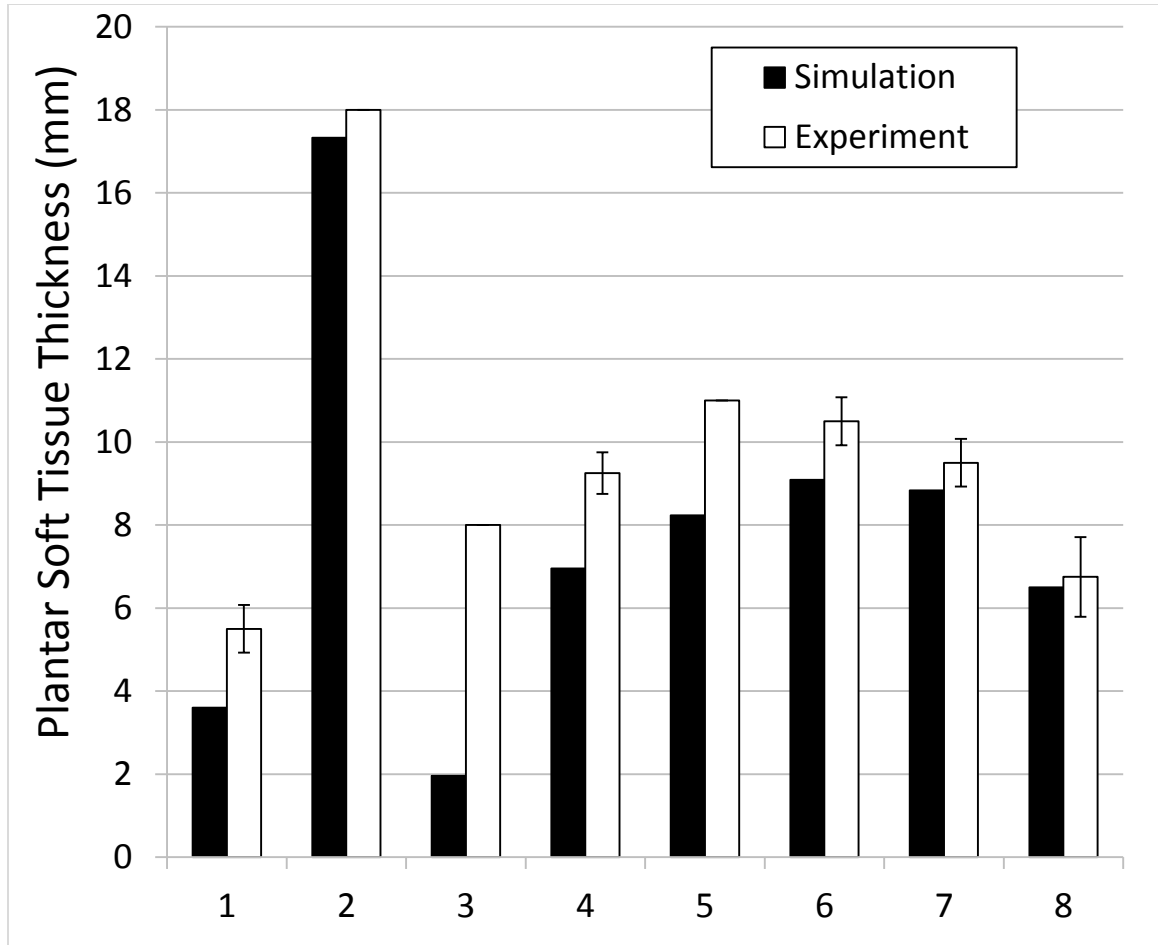


**Figure 4.2: Simulated and Experimental Heel/Foot Pad Thickness in the Neutral Posture at Maximum Load**

The thicknesses of the heel/foot pad under 150 lbs of load are provided at eight locations for both the experiment and for the simulation that minimized the overall summed error. The overall summed error was minimized for the properties within the normal physiological range that generated the maximum stiffness (100%). The numbers correspond to the following heel/foot pad locations: medial process of the calcaneus (1), plantar surface of the calcaneus immediately below the angle of Gissane (2), medial head of metatarsal 1 (3), lateral head of metatarsal 1 (4), head of metatarsal 2 (5), head of metatarsal 3 (6), head of metatarsal 4 (7), head of metatarsal 5 (8). No error bars are present for the experimental results at locations (2), (3) and (5) since the same thickness value was measured at these locations for all repeated trials.

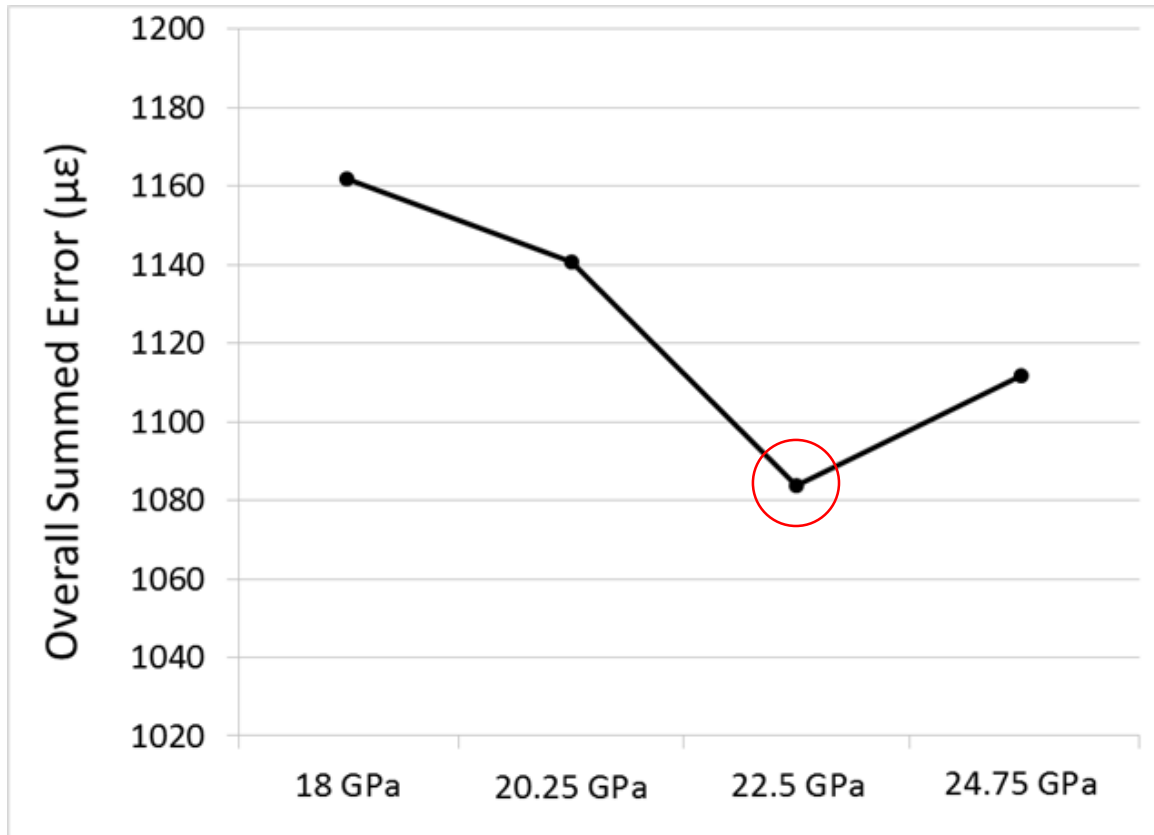
The effect of the adjustment of the material properties of cortical and trabecular bone on the total summed error between the simulation and experiment at the seven gauge locations is provided in Figure 4.3. This error was minimized when the elastic moduli of cortical bone and trabecular bone were selected to be 22.5 GPa and 0.4 GPa, respectively.

#### 4.3.2 INVESTIGATION OF FRICTION FACTOR SENSITIVITY

The Euler angles and displacements of the chosen origins of the talus and calcaneus, relative to the tibiofibular coordinate system, are compared between the simulations with friction factors set to 0.01 and 0.02 in Figure 4.4. The maximum difference between simulations was observed in the z-rotation of the talus, and was less than 5%.

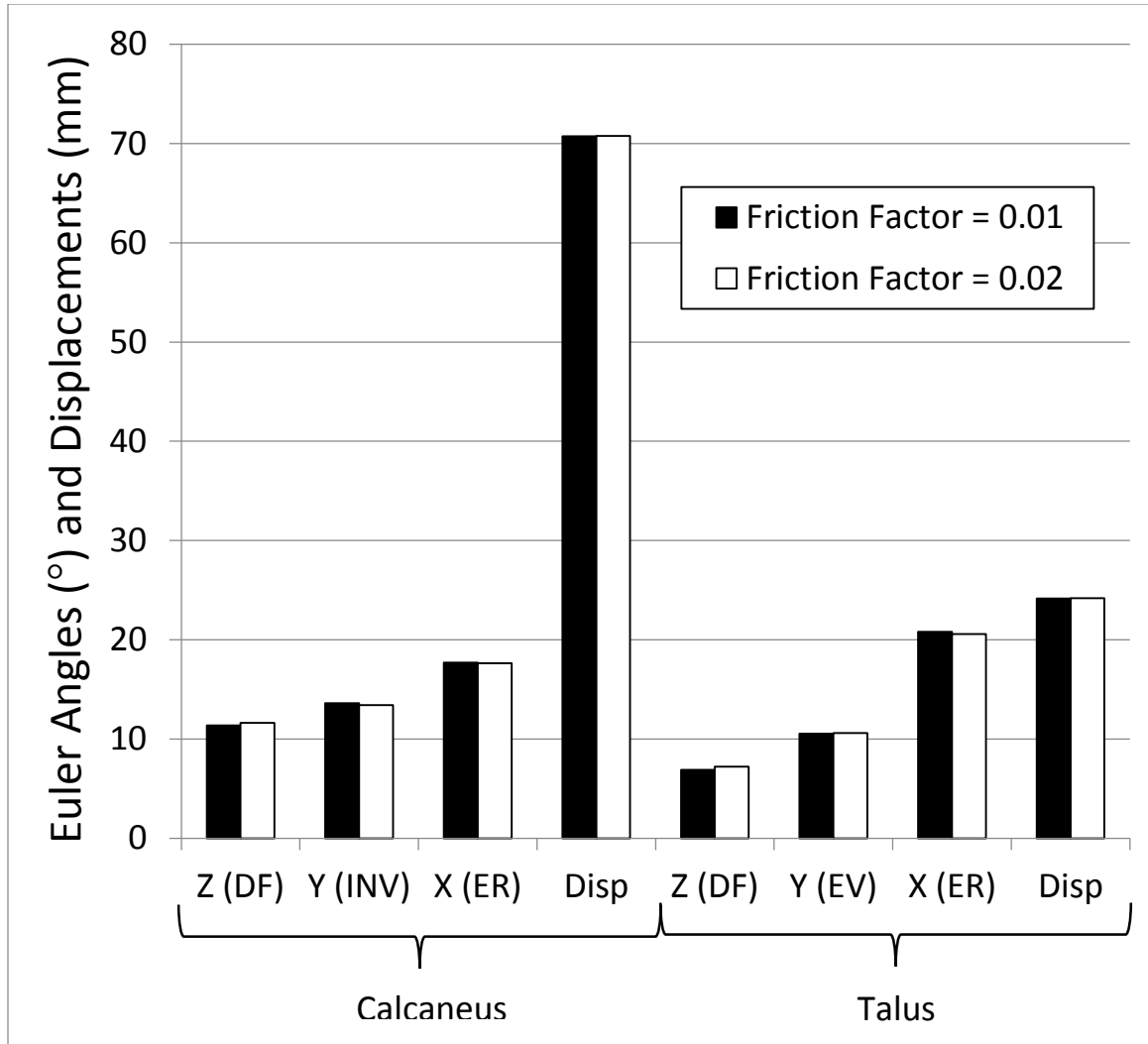
#### 4.3.3 VERIFICATION OF QUASI-STATIC STRAIN RATES

Table 4.1 provides the maximum strain in each bone for the simulations with short (125 ms) and long (250 ms) force ramp-up times. The difference between the strains were calculated, and the strain rate in each case was determined by dividing the strain over the force ramp-up time. At the locations of maximum strain in each bone, the corresponding strain rates for the short force ramp-up run were usually within the quasi-static range or just above the upper limit of  $0.01 \text{ s}^{-1}$ . Only in two instances did the strain rate exceed the upper limit by a factor of two or more. For the “long” simulation, all but three values were within the quasi-static range, and those three values were just above the upper limit. The strain rates at all gauge locations were within the quasi-static range for both long and short runs ( $0.006 \text{ s}^{-1}$  or less), and strains changed by less than 6% from short to long runs.



**Figure 4.3: Overall Summed Error Between Experimental and Simulated Strains in the Neutral Posture as Bone Elastic Modulus is Varied**

The overall summed error in strains between the experiment and simulation in the neutral posture are provided for different values of cortical bone elastic modulus. The elastic modulus of trabecular bone was varied as well, and for cortical elastic moduli of 18, 20.25, 22.5 and 24.75 GPa, the cancellous elastic moduli were set to be 0.32, 0.36, 0.4 and 0.44 GPa, respectively. The total error was summed from the individual errors at the seven strain gauge locations. The red circle indicates the bone properties (cortical = 22.5 GPa, trabecular = 0.4 GPa) that minimized the error between the simulation and experiment.



**Figure 4.4: Comparison of Euler Angles and Displacements at the Neutral Posture for the Calcaneus and Talus as Friction Factor is Adjusted**

The Euler angles and displacements of the chosen origins of the talus and calcaneus relative to the tibiofibular coordinate system in the neutral posture are provided for simulations where the friction factor was set to 0.01 and 0.02. All values were measured at 150 lbs of footplate compression. z, y and x represent the Euler angle rotations about those axes, and “Disp” abbreviates the displacement of the origin. For the calcaneus, the origin is at the calcaneal notch, and for the talus, the origin is at the posterior tubercle. All rotation values in the figure were changed to be positive for the sake of readability. The z-rotations are all in dorsiflexion (DF), while the x-rotations are in external rotation (ER). The y-rotations of the calcaneus and talus are in eversion (EV) and inversion (INV), respectively. The maximum difference between the two simulations was less than 5%.

**Table 4.1: Maximum Strains and Strain Rates in Each Bone for Short and Long Runs**

The maximum strains and strain rates for the short (125 ms load ramp-up) and long (250 ms load ramp-up) runs are provided for the cortical and cancellous regions of each bone. The percent difference between the strains or each run was calculated, and the strain rates were calculated by dividing the strain by the load ramp-up time. Simulations where the strain rate exceeded  $0.02 \text{ s}^{-1}$  are highlighted in yellow.

<b>Bone</b>	<b>Short Strain</b>	<b>Long Strain</b>	<b>% Difference</b>	<b>Short Strain Rate (<math>\text{s}^{-1}</math>)</b>	<b>Long Strain Rate (<math>\text{s}^{-1}</math>)</b>
<b>Cortical Calcaneus</b>	0.00165	0.00163	1.2%	0.013	0.007
<b>Cancellous Calcaneus</b>	0.00303	0.00286	5.7%	0.024	0.011
<b>Cortical Talus</b>	0.00175	0.00175	0.0%	0.014	0.007
<b>Cancellous Talus</b>	0.00239	0.00254	6.0%	0.019	0.010
<b>Cortical Fibula</b>	0.00103	0.00083	21.3%	0.008	0.003
<b>Cancellous Fibula</b>	0.00207	0.00163	23.7%	0.017	0.007
<b>Cortical Tibia</b>	0.00116	0.00094	21.0%	0.009	0.004
<b>Cancellous Tibia</b>	0.00349	0.00355	1.8%	0.028	0.014

#### 4.3.4 EFFECT OF ORIGINAL TIBIAL GEOMETRY

The strains at the two talar gauge locations, as well as the maximum strain anywhere in the talus were determined for both the run with the rigid mesh of the specimen's original tibia and the run with the previously-validated tibia mesh (Figure 4.5). For the run with the specimen's tibia, the strain at the medial talar neck gauge location increased from 128 to 175  $\mu\epsilon$  while the strain at the talar sulcus gauge location (located laterally), decreased from 245 to 80  $\mu\epsilon$ . With the specimen's tibia, both of these strain readings underestimated the strains measured experimentally at the same locations, while with the previously-validated tibia, the strains at the talar sulcus matched well with the experiment. The maximum strain in the talus, located at the center of the talar sulcus increased slightly (by 5.5%) for the run with the original tibial geometry (was not measured experimentally).

#### 4.3.5 NEUTRAL POSTURE

The Euler angles and displacements of the chosen origins of the talus and calcaneus, relative to the tibiofibular coordinate system, are compared between the FE simulation and the experiment in the loaded neutral posture in Figure 4.6. The results matched well, with maximum rotation and displacement differences between the simulation and experiment of 4.1° and 2.8 mm. The simulation slightly overestimated the dorsiflexion of the calcaneus and underestimated the dorsiflexion of the talus, while overestimating the inversion of the talus. External rotation was also slightly overestimated and the displacements were slightly overestimated for both bones.

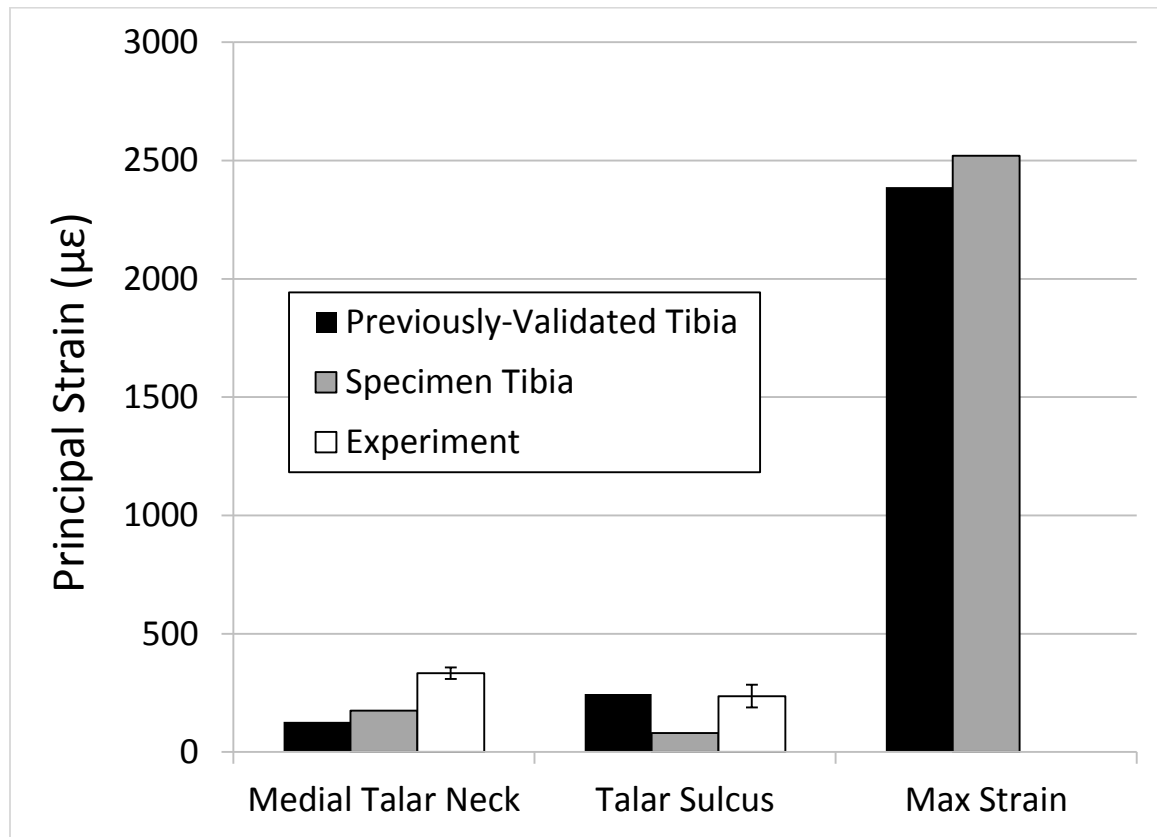


**Figure 4.5: Comparison of Talar Strains in the Neutral Posture for the Specimen’s Original Tibial Geometry and the Previously Validated Tibia**

The strains at the two talar gauge locations as well as the maximum talar strain are provided for the simulation in the neutral posture with the specimen’s original tibial geometry, and with the previously-validated tibia. The values are also compared with the experimental gauge readings (maximum strain in the talus unknown for experimental condition).

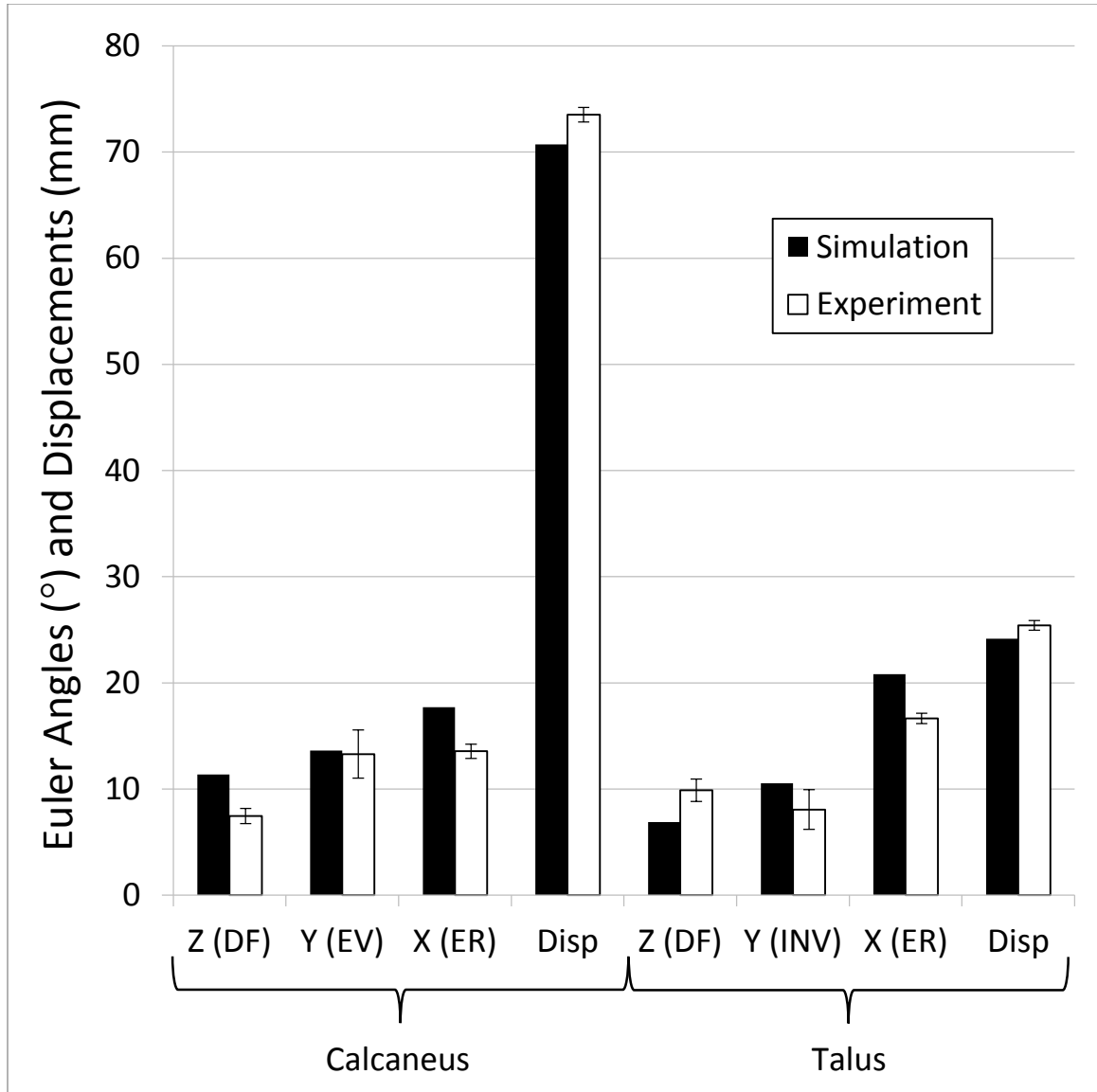


**Figure 4.6: Comparison of Experimental and Simulated Euler Angles and Displacements at the Neutral Posture for the Calcaneus and Talus**

The Euler angles and displacements of the chosen origins of the talus and calcaneus relative to the tibiofibular coordinate system in the neutral posture are provided for both the FE simulation and experiment. All values were measured at 150 lbs of footplate compression. z, y and x represent the Euler angle rotations about those axes, and “Disp” abbreviates the displacement of the origin. For the calcaneus, the origin is at the calcaneal notch, and for the talus, the origin is at the posterior tubercle. All rotation values in the figure were changed to be positive for the sake of readability. The z-rotations are all in dorsiflexion (DF), while the x-rotations are in external rotation (ER). The y-rotations of the calcaneus and talus are in eversion (EV) and inversion (INV), respectively.

The comparison of strain between the FE simulation and the experiment in the loaded neutral posture is provided in Figure 4.7. The simulation values at the tibia, lateral calcaneus and talar sulcus all were within two standard deviations (SDs) of the experimental results. The simulation underestimated the strains at the fibula and overestimated the strains at the medial calcaneus by three SDs. Strains were underestimated by nine SDs at the medial talar neck, and overestimated by 13 SDs at the plantar calcaneus.

Repeated trials could not be performed during experimental testing in the altered postures, and so the average standard deviation of strain from the neutral trials ( $44.4 \mu\epsilon$ ) was used as a baseline to evaluate how well the strains matched at these postures. Two standard deviations was selected to be the acceptable difference between strains in the simulation and experiment. The average standard deviations of the Euler angles and displacements in the neutral posture were extremely small ( $1.2^\circ$  and  $0.6 \text{ mm}$ ), and so differences of less than  $5^\circ$  and  $3 \text{ mm}$  between the simulation and experiment were considered to be acceptable.

#### 4.3.6 INVERSION–EXTERNAL ROTATION

The Euler angles and displacements of the chosen origins of the talus and calcaneus, relative to the neutral posture, are compared between the FE simulation and the experiment for inversion-external rotation in Figure 4.8. External rotation of the calcaneus, and the inversion and displacement of the talus matched the experimental results well. Dorsiflexion of the calcaneus was overestimated by just over  $5^\circ$ , and the inversion and

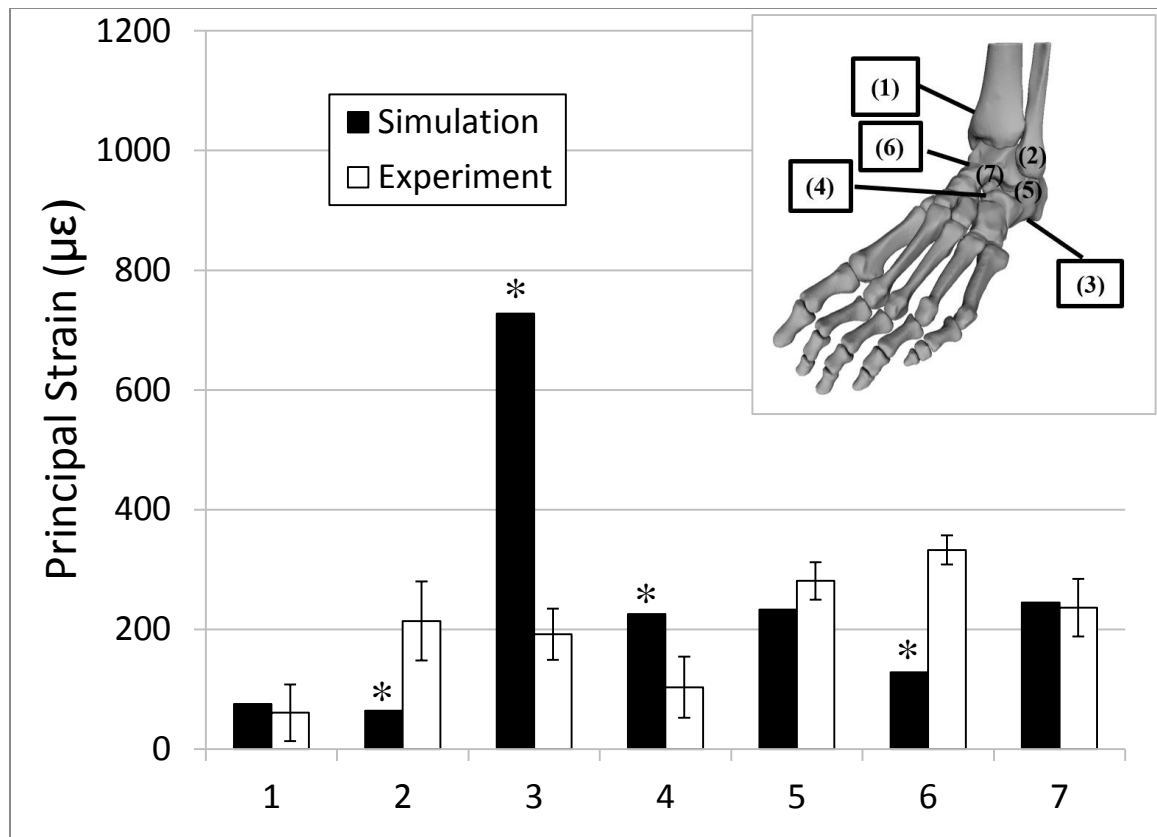


**Figure 4.7: Comparison of Experimental and Simulated Strains at the Neutral Posture**

The strains in the neutral posture at 150 lbs of footplate compression are compared at the seven strain gauge locations between the FE simulation and the experiment. The numbers correspond to the following strain gauge locations: tibia (1), fibula (2), plantar calcaneus (3), medial calcaneus (4), lateral calcaneus (5), medial talar neck (6), and talar sulcus (7). Stars indicate values that are not within two standard deviations of the experiment.

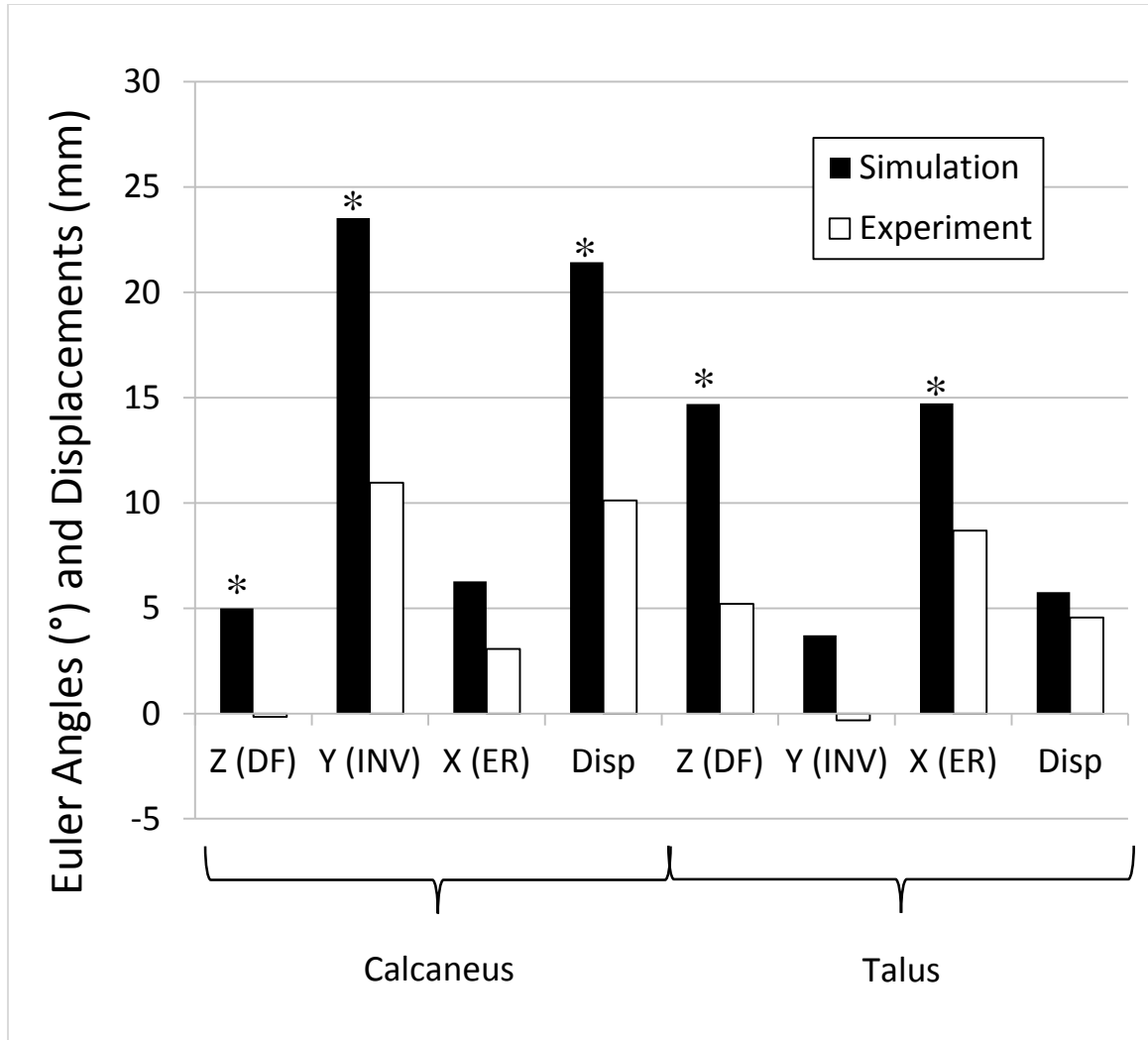


**Figure 4.8: Comparison of Experimental and Simulated Euler Angles and Displacements in Inversion-External Rotation for the Calcaneus and Talus**

The Euler angles and displacements of the chosen origins of the talus and calcaneus relative to the neutral posture are provided for both the FE simulation and experiment. z, y and x represent the Euler angle rotations about those axes, and “Disp” abbreviates the displacement of the origin. For the calcaneus, the origin is at the calcaneal notch, and for the talus, the origin is at the posterior tubercle. The positive z, y and x rotations indicate dorsiflexion (DF), inversion (INV) and external rotation (ER), respectively. Stars indicate that differences between the simulation and experiment are not within 5° or 3 mm.

displacement of this bone were overestimated as well by 13°, and 11 mm. Dorsiflexion and external rotation of the talus were likewise overestimated by 9° and 6°.

The comparison of strain between the FE simulation and the experiment in the inversion-external rotation posture is provided in Figure 4.9. Strains at the fibula, lateral calcaneus and medial talar neck were within two average neutral SDs (89  $\mu\epsilon$ ). The readings at the tibia and medial calcaneus were within three SDs, while the talar sulcus strain was within four SDs. Much greater error was observed at the plantar calcaneus, with an overestimation in strain by 18 SDs.

#### 4.3.7 EVERSION–EXTERNAL ROTATION

The Euler angles and displacements of the chosen origins of the talus and calcaneus, relative to the neutral posture, are compared between the FE simulation and the experiment for eversion-external rotation in Figure 4.10. Dorsiflexion of the calcaneus, and eversion of the calcaneus and talus were all overestimated by 7°. Displacement of the calcaneus was also overestimated by 4 mm.

The comparison of strain between the FE simulation and the experiment in the eversion-external rotation posture is provided in Figure 4.11. The strains at the tibia, fibula, medial calcaneus and talar sulcus matched well, and were within two average neutral SDs (89  $\mu\epsilon$ ). The strains at the lateral calcaneus were overestimated by four SDs, while strains at the medial talar neck were underestimated by six SDs. Finally, the largest error was observed at the plantar calcaneus, with an overestimation of strain by nine SDs.

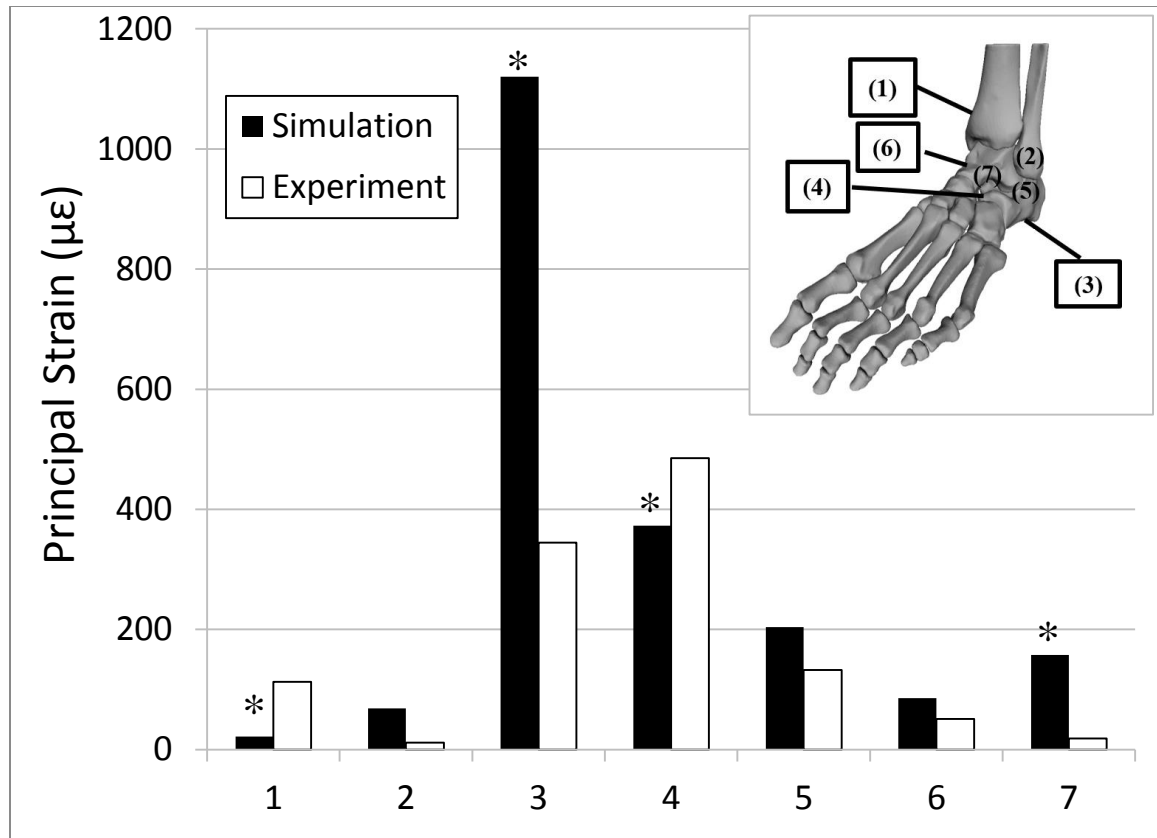


**Figure 4.9: Comparison of Experimental and Simulated Strains at the Inversion-External Rotation Posture**

The strains in the inversion-external rotation posture at 150 lbs of footplate compression are compared at the seven strain gauge locations between the FE simulation and the experiment. The numbers correspond to the following strain gauge locations: tibia (1), fibula (2), plantar calcaneus (3), medial calcaneus (4), lateral calcaneus (5), medial talar neck (6), and talar sulcus (7). Stars indicate values that are not within two neutral average standard deviations (89 µε) of the experiment.

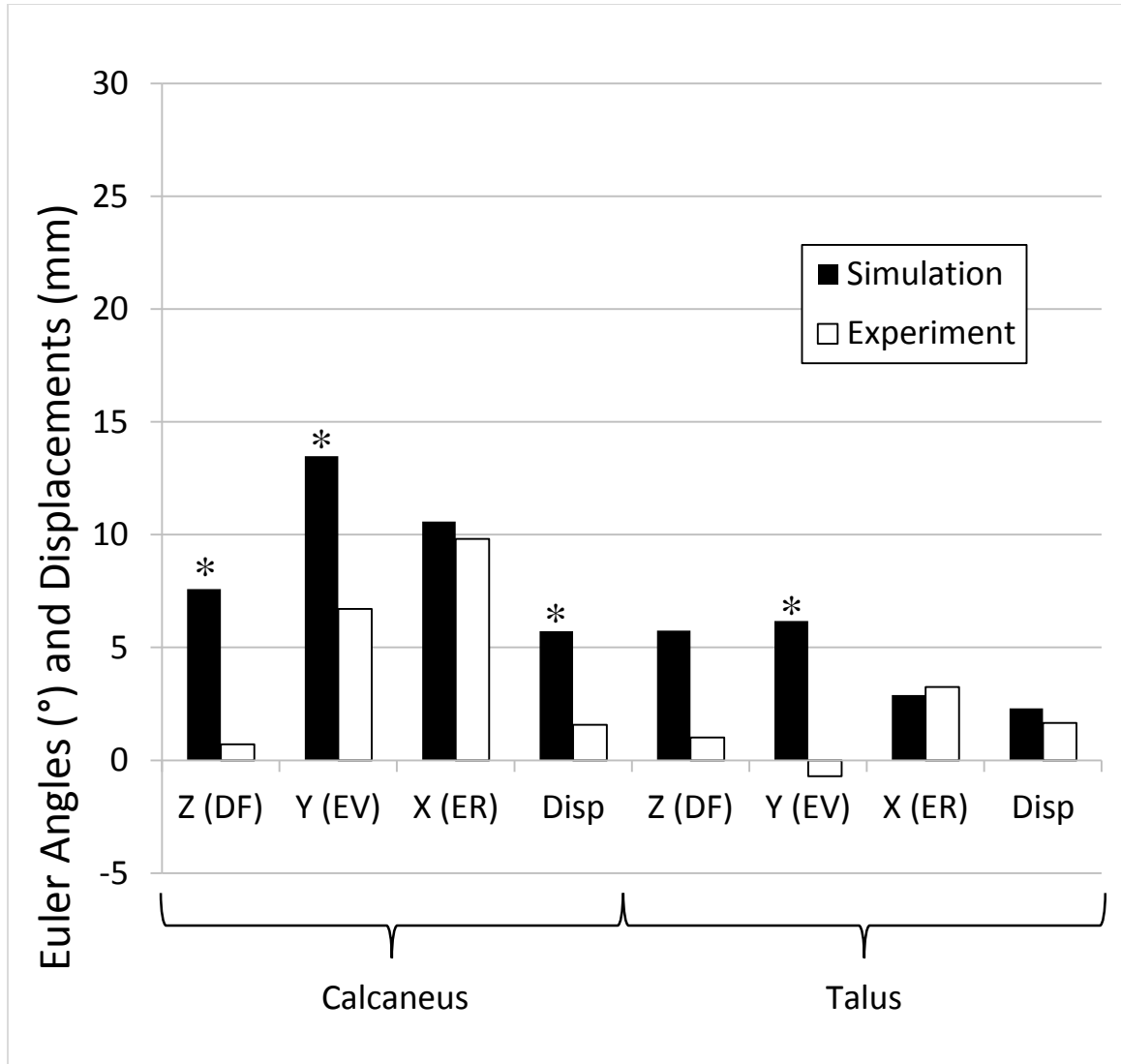


**Figure 4.10: Comparison of Experimental and Simulated Euler Angles and Displacements in Eversion-External Rotation for the Calcaneus and Talus**

The Euler angles and displacements of the chosen origins of the talus and calcaneus relative to the neutral posture are provided for both the FE simulation and experiment. z, y and x represent the Euler angle rotations about those axes, and “Disp” abbreviates the displacement of the origin. For the calcaneus, the origin is at the calcaneal notch, and for the talus, the origin is at the posterior tubercle. The positive z, y and x rotations indicate dorsiflexion (DF), eversion (EV) and external rotation (ER), respectively. Stars indicate that differences between the simulation and experiment are not within 5° or 3 mm.

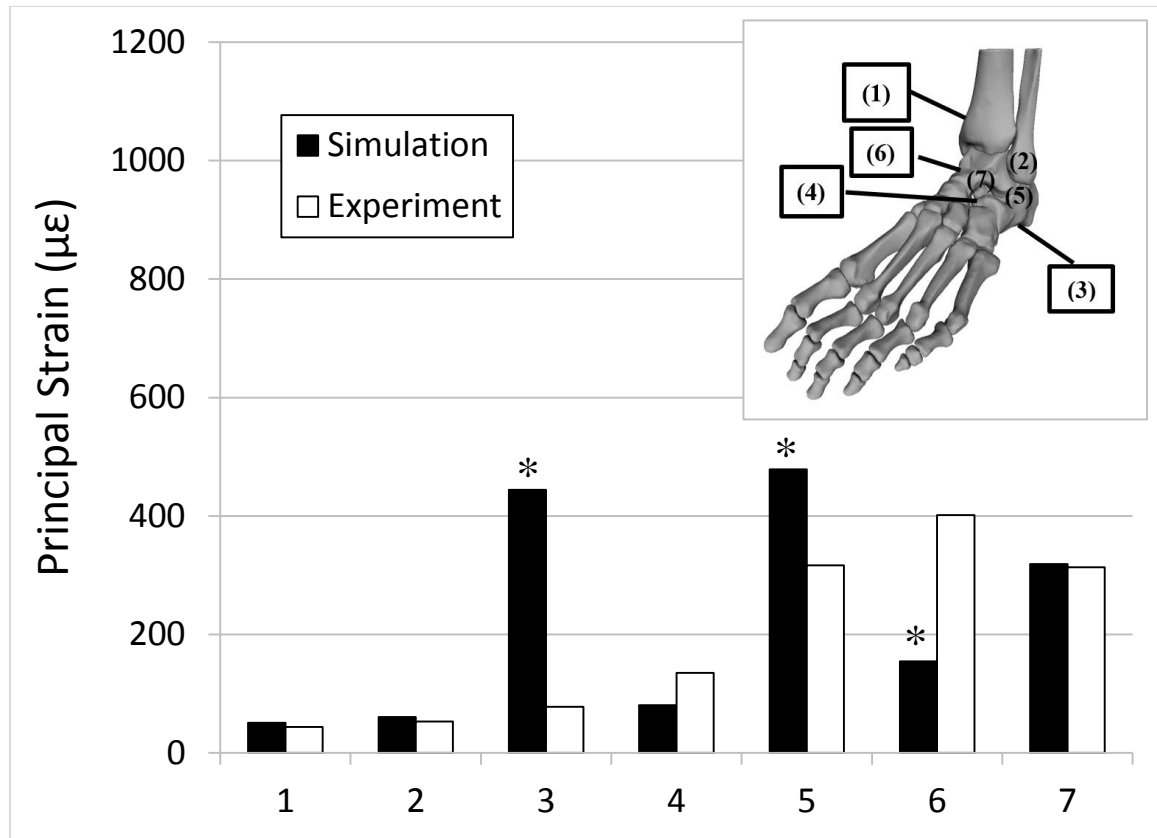


**Figure 4.11: Comparison of Experimental and Simulated Strains at the Eversion-External Rotation Posture**

The strains in the eversion-external rotation posture at 150 lbs of footplate compression are compared at the seven strain gauge locations between the FE simulation and the experiment. The numbers correspond to the following strain gauge locations: tibia (1), fibula (2), plantar calcaneus (3), medial calcaneus (4), lateral calcaneus (5), medial talar neck (6), and talar sulcus (7). Stars indicate values that are not within two neutral average standard deviations (89  $\mu\epsilon$ ) of the experiment.

#### 4.3.8 PLANTARFLEXION

The Euler angles and displacements of the chosen origins of the talus and calcaneus, relative to the neutral posture, are compared between the two FE simulations and the experiment for plantarflexion in Figure 4.12. The overall (summed) error in Euler angle and displacement was lower during the long simulation by a narrow margin (overall short error: 30°, 5.8 mm, and overall long error: 27°, 5.6 mm). For the short simulation, the inversion and displacement of the calcaneus were overestimated and underestimated by 11° and 3 mm, respectively, while plantarflexion of the talus was underestimated by 9°.

The comparison of strain between the FE simulation and the experiment in the plantarflexion posture is provided in Figure 4.13, and the overall (summed) error in strain was lower during the short simulation (overall short error = 446  $\mu\epsilon$ , and overall long error = 633  $\mu\epsilon$ ). For this simulation, the strains at the tibia, medial calcaneus, lateral calcaneus and talar sulcus were within two average neutral SDs (89  $\mu\epsilon$ ). The strain readings at the fibula, plantar calcaneus and medial talar neck were within three SDs.

#### 4.3.9 DORSIFLEXION-INVERSION

The Euler angles and displacements of the chosen origins of the talus and calcaneus, relative to the neutral posture, are compared between the simulation and experiment in Figure 4.14. The dorsiflexion of both the calcaneus and talus were overestimated in the simulation by 6° and 7°, respectively. Inversion and displacement of the calcaneus were also overestimated by 7° and 8 mm. Finally, the external rotation of both bones was overestimated in the simulation by 9° for the calcaneus and by 7° for the talus.

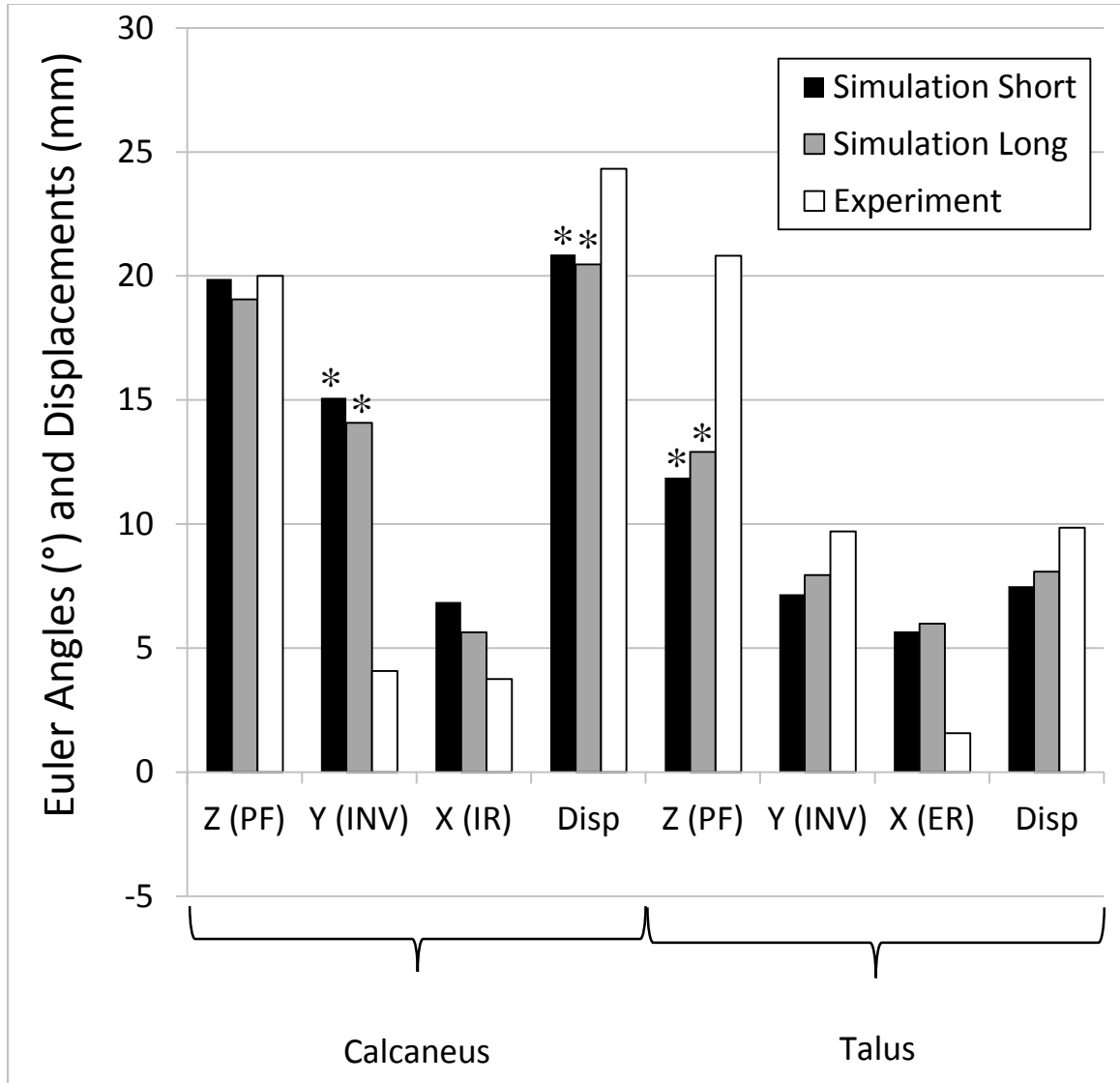


**Figure 4.12: Comparison of Experimental and Simulated Euler Angles and Displacements in Plantarflexion for the Calcaneus and Talus**

The Euler angles and displacements of the chosen origins of the talus and calcaneus relative to the neutral posture are provided for both the FE simulation and experiment. Two different simulations are compared in which the rotation of the foot occurred over 100 ms (short simulation) and 200 ms (long simulation). z, y and x represent the Euler angle rotations about those axes, and “Disp” abbreviates the displacement of the origin. For the calcaneus, the origin is at the calcaneal notch, and for the talus, the origin is at the posterior tubercle. The z and y rotations indicate plantarflexion (PF) and inversion (INV), while the x rotations for the calcaneus and talus indicate internal rotation (IR) and external rotation (ER), respectively. Stars indicate that differences between the simulation and experiment are not within 5° or 3 mm.

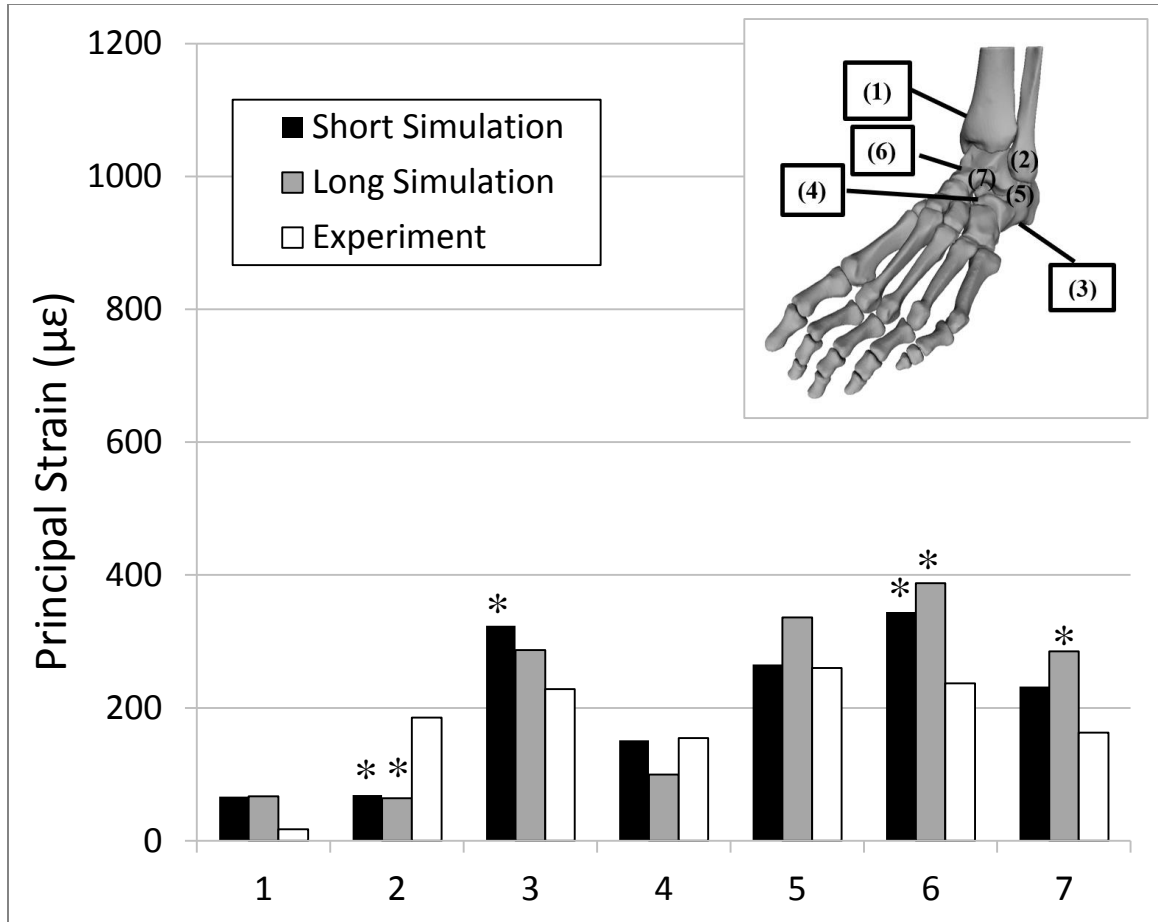


**Figure 4.13: Comparison of Experimental and Simulated Strains at the Plantarflexion Posture**

The strains in the plantarflexion posture at 150 lbs of footplate compression are compared at the seven strain gauge locations between the FE simulation and the experiment. Two different simulations are compared in which the rotation of the foot occurred over 100 ms (short simulation) and 200 ms (long simulation). The numbers correspond to the following strain gauge locations: tibia (1), fibula (2), plantar calcaneus (3), medial calcaneus (4), lateral calcaneus (5), medial talar neck (6), and talar sulcus (7). Stars indicate values that are not within two neutral average standard deviations (89  $\mu\epsilon$ ) of the experiment.

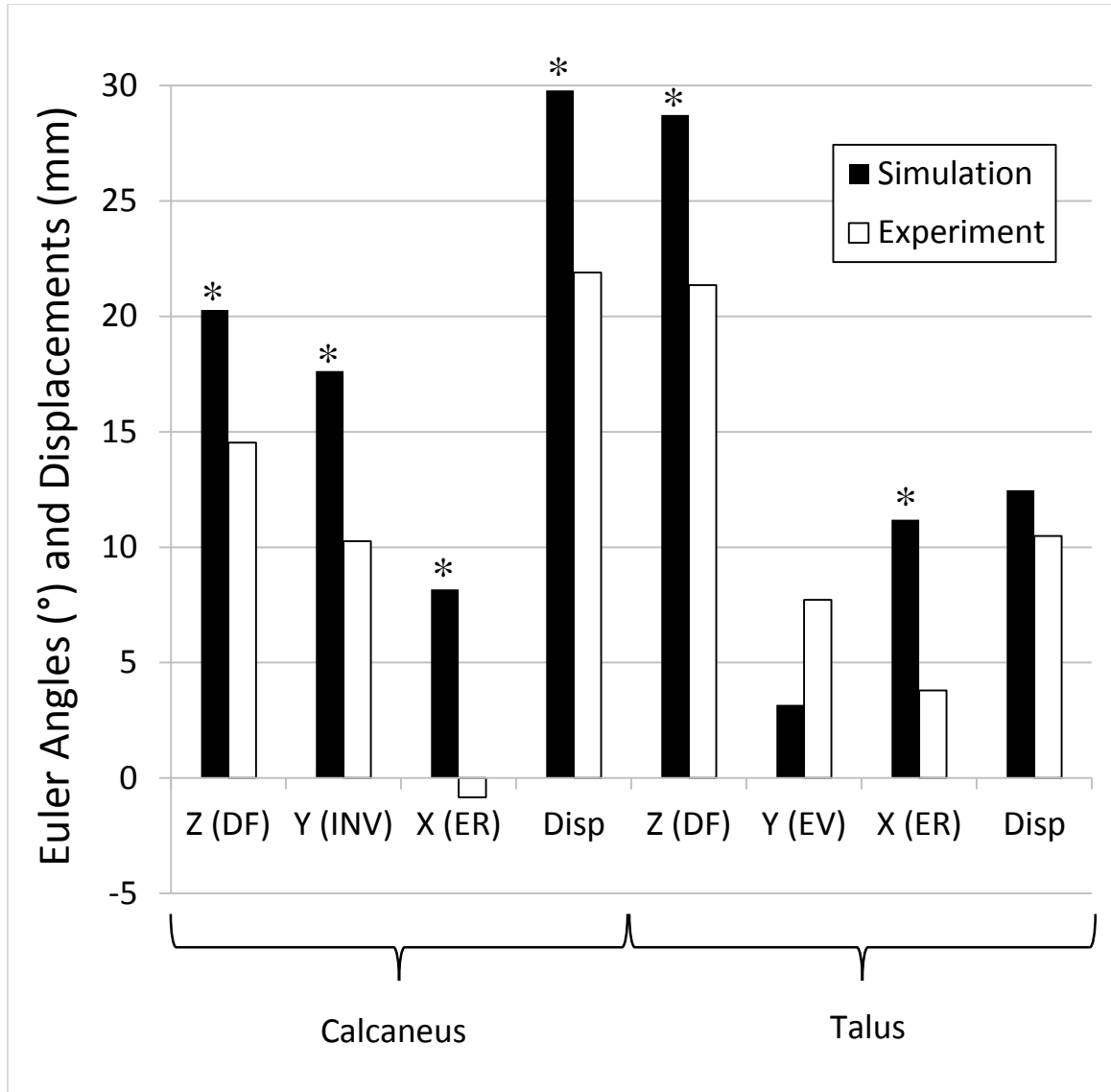


**Figure 4.14: Comparison of Experimental and Simulated Euler Angles and Displacements in Dorsiflexion-Inversion for the Calcaneus and Talus**

The Euler angles and displacements of the chosen origins of the talus and calcaneus relative to the neutral posture are provided for both the FE simulation and experiment. z, y and x represent the Euler angle rotations about those axes, and “Disp” abbreviates the displacement of the origin. For the calcaneus, the origin is at the calcaneal notch, and for the talus, the origin is at the posterior tubercle. The positive z and x rotations indicate dorsiflexion (DF), and external rotation (ER). For the calcaneus and talus, the positive y rotation indicates inversion (INV) and eversion (EV), respectively. Stars indicate that differences between the simulation and experiment are not within 5° or 3 mm.

The comparison of strain between the FE simulation and the experiment in the dorsiflexion-inversion posture is provided in Figure 4.15. The strains at the tibia, fibula, medial calcaneus and lateral calcaneus matched well, and were within two average neutral SDs ( $89 \mu\epsilon$ ). The strains at the medial talar neck and talar sulcus were overestimated by three and five SDs, while the strains at the plantar calcaneus were overestimated substantially by 18 SDs.

#### 4.3.10 MIDFOOT/FOREFOOT BONE POSITIONS

The maximum distances between the experimental and simulated midfoot/forefoot bone positions at each posture under load are provided in Table 4.2, and varied between 3.9 and 17.0 mm. While the maximum distance for each bone fluctuated depending on its rotation, the midfoot and forefoot bones as a whole in the simulation were always offset in the same direction relative to the experiment at each posture. The minimum distance in each case was 0, as during the simulation no bone was displaced so far from the experiment that there was no overlap with its experimental position. With the exception of the neutral case, the smallest maximum distance between bones was observed at the first metatarsal for each ankle posture (4.5-10.0 mm). In the neutral case, this was at the medial cuneiform (3.9 mm), followed by the first metatarsal (4.7 mm). The largest distance was observed at the fifth metatarsal in all postures (10.3-17.0 mm) except inversion-external rotation, where it was at the navicular and lateral cuneiform (9.9 mm). The smallest average maximum distance between bones was 6.5 mm in the neutral posture, while the largest was 13.5 mm

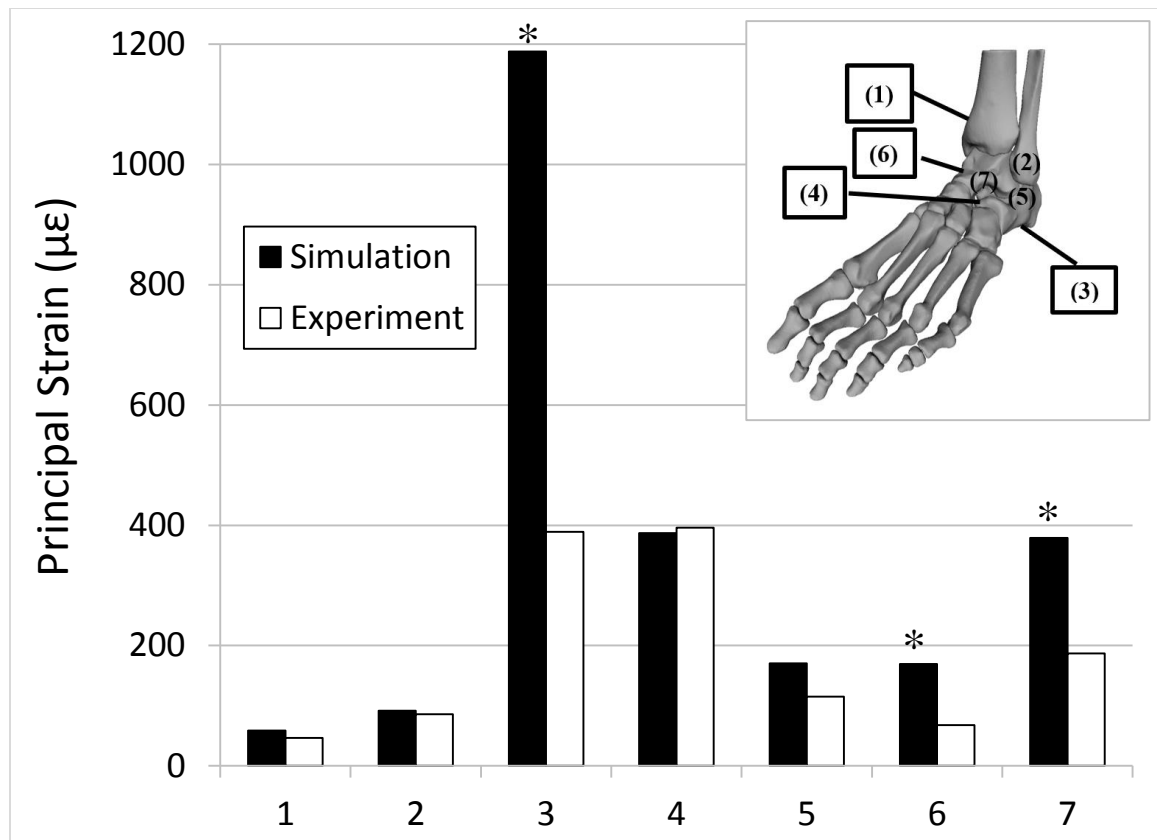


**Figure 4.15: Comparison of Experimental and Simulated Strains at the Dorsiflexion-Inversion Posture**

The strains in the dorsiflexion-inversion posture at 150 lbs of footplate compression are compared at the seven strain gauge locations between the FE simulation and the experiment. The numbers correspond to the following strain gauge locations: tibia (1), fibula (2), plantar calcaneus (3), medial calcaneus (4), lateral calcaneus (5), medial talar neck (6), and talar sulcus (7). Stars indicate values that are not within two neutral average standard deviations (89 µε) of the experiment.

**Table 4.2: Maximum Distances between Simulated and Experimental Forefoot and Midfoot Bones at Each Ankle Posture**

The maximum distance between each forefoot/midfoot bone at each posture is provided, as well as the average maximum distance for each posture: Inversion-External Rotation (INV-ER), Eversion-External Rotation (EV-ER), Plantarflexion (PF) and Dorsiflexion-Inversion (DF-INV). All numbers are in units of millimeters (mm). Mcune, Icune, Lcune and Meta indicate the medial cuneiform, intermediate cuneiform, lateral cuneiform and metatarsal, respectively.

	<b>Neutral</b>	<b>INV-ER</b>	<b>EV-ER</b>	<b>PF</b>	<b>DF-INV</b>
<b>Cuboid</b>	6.3	8.9	12.2	14.1	8.1
<b>Navicular</b>	9.4	9.9	15.6	16.0	7.7
<b>Mcune</b>	3.9	7.5	10.4	12.0	9.2
<b>Icune</b>	5.7	8.6	12.6	12.6	9.5
<b>Lcune</b>	6.2	9.9	12.8	14.1	10.7
<b>Meta1</b>	4.7	4.5	7.8	10.0	6.4
<b>Meta2</b>	4.7	6.5	11.8	13.8	7.8
<b>Meta3</b>	6.3	7.5	13.5	13.7	8.6
<b>Meta4</b>	7.7	8.7	14.6	14.4	13
<b>Meta5</b>	10.3	9.2	17.0	14.7	15.8
<b>Average:</b>	<b>6.5</b>	<b>8.1</b>	<b>12.8</b>	<b>13.5</b>	<b>9.7</b>

in plantarflexion. The distance contour plot of bone distance in the neutral posture is provided in Figure 4.16.

#### 4.3.11 INJURY PREDICTION

The predicted failure loads in kN for the calcaneus, talus, tibia and fibula across all postures are presented in Figure 4.17. In each case, the fracture threshold was predicted for both the cortical and cancellous regions, and the lowest values are provided. The neutral posture exhibited the highest failure loads in all bones (meaning the lowest risk of fracture in this posture), and the greatest vulnerability to fracture in all bones except for the calcaneus was predicted to occur in the dorsiflexion-inversion posture. The lowest failure loads across all postures were always observed at the talus and calcaneus, and the lowest fracture threshold in all bones across all postures was 0.66 kN at the talus in the dorsiflexion-inversion posture. The lowest fracture threshold for the calcaneus was 2.7 kN in the inversion-external rotation posture.

The locations of maximum strain in the hindfoot for all postures are described in Table 4.3, and contour plots of maximum strain for each posture are provided in Figure 4.18. In the tibia, this location was typically at the distal articular surface. The one exception was in dorsiflexion-inversion, when it was located at the distal anterior surface, just superior to the articular surface. In the talus and calcaneus, the maximum strain was medial at the sustentaculum during inversion-external rotation, and lateral at the angle of Gissane during eversion-external rotation. In dorsiflexion-inversion, the maximum talar strain was at the upper articular surface near the neck, and the maximum calcaneal strain

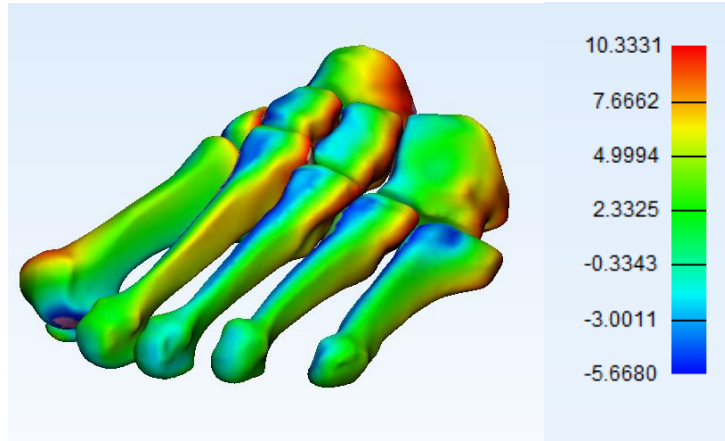


**Figure 4.16: Contour Plot of Bone Distance in the Neutral Posture**

The experimental bone positions in the loaded neutral posture are shown, and the contour map displays how far away the simulated bone positions were from their experimental counterparts. The plot is in units of millimeters (mm).

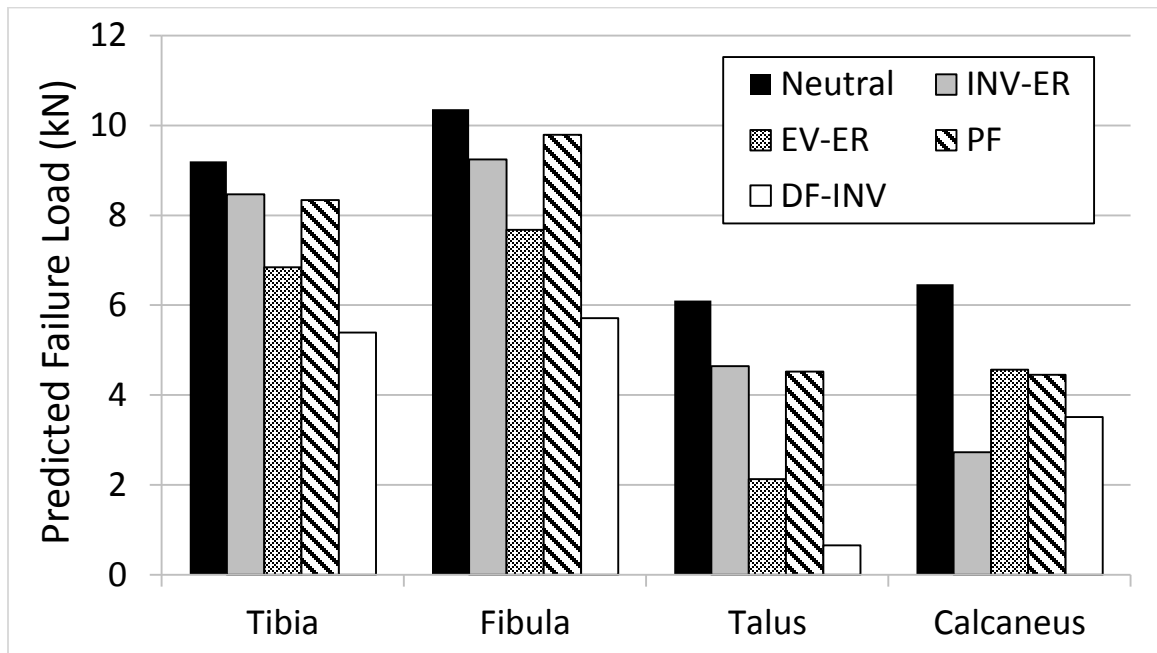


**Figure 4.17: Predicted Failure Load in the Hindfoot for all Tested Postures**

The footplate loads that would cause failure in the tibia, fibula, talus and calcaneus were predicted based on the maximum strains measured in these bones at a footplate load of 150 lbs and the critical strain values for cortical and cancellous bone. The lowest failure load was predicted to be 0.66 kN, causing failure of the talus in the dorsiflexion-inversion posture. INV-ER, EV-ER, PF and DF-INV denote the inversion-external rotation, eversion-external rotation, plantarflexion and dorsiflexion-inversion postures, respectively.

**Table 4.3: Maximum Strain Locations in the Hindfoot for all Tested Postures**

The locations of maximum strain at the tibia, fibula, talus and calcaneus for all five postures are provided and the locations with the lowest fracture tolerance in each posture are highlighted. Elements near ligament attachment nodes were excluded. INV-ER, EV-ER, PF and DF-INV denote the inversion-external rotation, eversion-external rotation, plantarflexion and dorsiflexion-inversion postures, respectively.

	<b>Maximum Strain Location</b>			
	<b>Tibia</b>	<b>Fibula</b>	<b>Talus</b>	<b>Calcaneus</b>
<b>Neutral</b>	Articular Surface	Outer Epiphyseal Surface	Articular Surface with the Sustentaculum	Articular Surface with Talus
<b>INV-ER</b>	Articular Surface	Potting Fixture Attachment	Medial-Inferior Talar Neck	Upper Surface of Sustentaculum
<b>EV-ER</b>	Articular Surface	Potting Fixture Attachment	Lateral Process	Angle of Gisanne
<b>PF</b>	Articular Surface	Outer Epiphyseal Surface	Talar Sulcus	Upper Surface of Sustentaculum
<b>DF-INV</b>	Distal/Anterior Tibia above Articular Surface	Potting Fixture Attachment	Upper Articular Surface, Near the Neck	Upper Surface of Sustentaculum

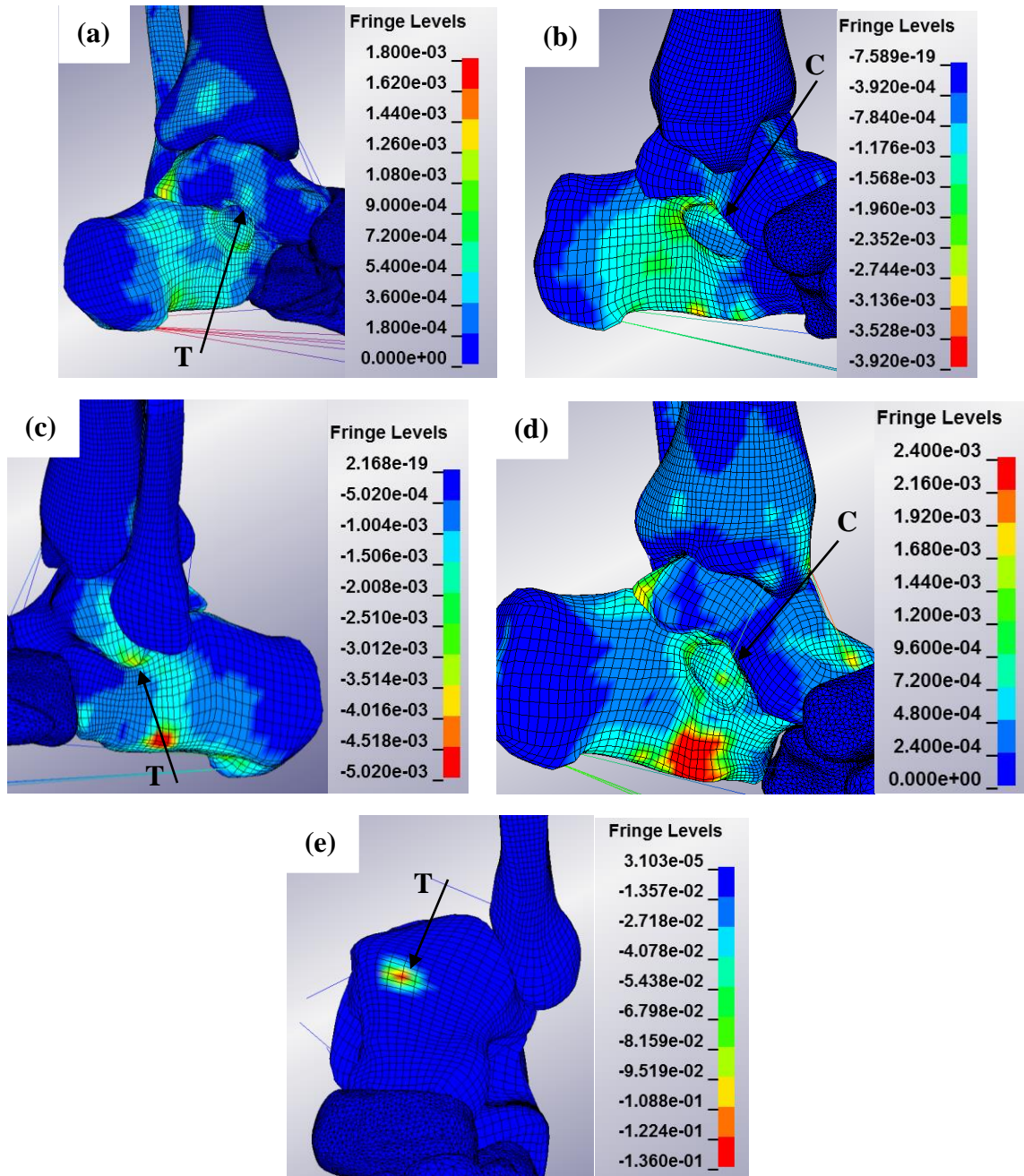


**Figure 4.18: Contour Plots of Maximum Strain in Each Posture**

The locations of maximum strain for the neutral (a), inversion-external rotation (b), eversion-external rotation (c), plantarflexion (d) and dorsiflexion-inversion (e) postures are indicated by arrows. The letter “T” or “C” next to each arrow indicates if the maximum strain location is in the talus or calcaneus, respectively. Elements near ligament insertion sites were excluded from being chosen as locations of maximum strain due to point loading effects.

was at the sustentaculum. The failure locations in all bones were similar for the neutral and plantarflexion postures.

#### **4.4 DISCUSSION**

This study presents the only known investigation of the accuracy of bone positions and strains as ankle posture is adjusted and load is applied in an FE model of the foot and ankle. Bone rotations, positions and strains were compared with experimental tests at five different postures that have been previously implicated in causing fractures of the hindfoot bones. Across all postures, the simulated strains matched the experimental strains reasonably well at most locations, and no known studies have before attempted to validate the strains at the component level of the individual ankle bones, in the neutral posture or otherwise.

The hindfoot bone positions and rotations matched the experimental results very well at the neutral posture, and while there were some discrepancies in the other postures, some of the most important features of the behaviour of the talo-crural and talo-calcaneal joints were captured by the model. This is especially notable in light of the fact that the change in bone positions in response to adjustment in ankle posture was controlled almost entirely by the articular surfaces between the bones and ligaments connecting them. The positions of the midfoot and forefoot bones were also compared between the experiment and simulation. While there were a few differences in the positions of these bones, their

simulated positions in response to ankle posture adjustment and load application matched the experimental tests reasonably well.

The bone positions, rotations and strains were only compared to repeated trials using one specimen. If more specimens had been tested, due to natural anatomical variation it is extremely likely that all of the outcomes would have fallen within the natural range found in the population. As such, this study constitutes an extremely thorough and critical evaluation of the model.

Unlike in previous studies where properties were assigned only based on literature values, or values used in other FE studies, attempts were made to tune the material properties of the heel pad and bone within their natural range until the error between the experiment and the simulation was minimized. A strain rate assessment was also performed to ensure that strains in the simulation were within, or close to, the quasi-static range, to best reflect the experimental loading conditions.

The fracture tolerance of the lower leg was predicted in every bone at each posture, and the critical load level at the neutral, inversion and eversion postures was similar to the values reported in the literature (Yoganandan et al., 1996, Funk et al., 2002a, Seipel et al., 2001, Begeman et al., 1993). Furthermore, the locations of highest strain at each posture matched locations where fractures have been noted to occur at those same postures during experimental testing (Essex-Lopresti, 1952, Sanders and Lindvall, 1999, Funk et al., 2003, Smith and Ziran, 1999). This suggests that the model in the current study may be capable of accurately predicting both fracture load and fracture location.

#### 4.4.1 HEEL PAD PROPERTIES

The minimum overall error in heel/foot pad thickness under 150 lbs of compression was achieved at the maximum stiffness within the natural physiological range reported by Erdemir et al. (2006). Through examination of the total thickness error as a function of heel/foot pad stiffness, we found that if the stiffness of this region were increased beyond the reported physiological range, the total error could be minimized further. However, without justification by new experimental data, the properties were maintained within the range reported in the literature. Wrapping the soft tissues around the entire foot might also provide the necessary reinforcement to achieve a better match between simulated and experimental heel/foot pad compression. This effect may also be why the medial head of metatarsal 1 kept sliding and rotating through the simulations.

The large deviations observed at the medial process of the calcaneus, and especially at the medial head of metatarsal 1, may also be due to the presence of distorted elements at these locations causing the deformation to be unrealistic. While all elements in the heel/foot pad met the specific quality criteria outlined in Chapter 3, deformation in this region is much more severe than at any other location in the model due to its soft properties. Over the course of the simulation, the elements in the heel/foot pad became increasingly distorted, potentially leading to increasing model inaccuracy.

The resolution of the CT scanner in the axial direction, which is the direction in which the heel/foot pad thickness was measured, was only 1 mm, limiting the precision of

these measurements and potentially contributing to the discrepancies in the results. Some of these errors may also be a result of the fact that Erdemir assumed the heel pad to abide by an Ogden rubber model, which may not properly represent the exact response of the soft plantar tissues of the foot under compressive load. A different material model may be better suited to describe the mechanical behaviour of this anatomy. Furthermore, in this study, the foot pad was assumed to have the same hyperelastic properties as the heel pad, but the properties that were applied had only been measured at the heel, and a different natural response may be found at the fore- and mid-foot. Recent FE studies have assumed flesh at all locations except the heel (Shin et al., 2012), or flesh everywhere (Dong et al., 2013), to abide by a Mooney-Rivlin hyperelastic material model, with specific parameters acquired from compression tests on rectangular samples of flesh taken from the thigh (Untaroiu et al., 2005). In the current study, it was assumed that due to their proximity, the response of the foot pad would be more similar to the heel pad than flesh acquired from the thigh, which is why the same properties were assigned to both regions. More work needs to be done in the future to characterize the properties of soft tissues, specifically those of the plantar surface of the foot.

#### 4.4.2 BONE PROPERTIES

The cortical and trabecular elastic moduli that were found to minimize the overall error between simulated and experimental strains were 22.5 GPa and 0.4 GPa, respectively. The cortical and trabecular elastic moduli were adjusted in the same direction in each run, and it is possible that the total error could be minimized further by performing additional

runs in which these properties are altered separately. Furthermore, only the elastic moduli were altered in these material property adjustment runs, and modifying other parameters, such as the plastic modulus, yield stress, or Poisson's ratio may also have an effect on the total error. However, since the loading was largely within the elastic region in all simulations, this is unlikely to have a major impact on the results. Limitations in the modeling of the hindfoot bones, such as using isotropic and homogenous material properties, no doubt also contributed to this error.

#### 4.4.3 FRICTION FACTOR SENSITIVITY

The rotations and displacements of the calcaneus and talus did not vary substantially as the friction factor was doubled from 0.01 to 0.02, suggesting that the model is not very sensitive to this parameter. Since the friction factor did not markedly affect the results, the chosen friction factor of 0.01 was deemed to be acceptable for use in the model, and was used for all simulations in which ankle posture was altered.

#### 4.4.4 STRAIN RATES

In most cases, the maximum strain rates in all bones at a loading time of 125 ms were within the quasi-static range, or just above the upper limit of  $0.01 \text{ s}^{-1}$ . Only in a few cases (the cancellous calcaneus and tibia), was this upper limit exceeded by a factor of two to three. The upper limit was only exceeded by this larger margin at localized regions in the cancellous bone, and the cortical layers at the same locations were within the quasi-static range, or very close to the upper strain rate limit. These small, isolated spots of

elevated strain (and strain rate), were typically within articular surfaces between the hindfoot bones, and may be caused by neglecting cartilage in the model. This lack of cartilage causes the stress to be unevenly distributed over the joint/contact surface due to slight differences in mating bone surface geometry, yielding an unrealistic stress distribution at the joints. Apart from these isolated locations of high strain and strain rate, the rest of the bones were within the quasi-static range.

Almost all strain rates in the run with the longer loading time were within the quasi-static range, or just above the upper limit. The locations of maximum strain in the bones were the same for both loading times, and except for three regions, all values for the long and short runs had a difference of 6.01% or less. The strain readings with the largest differences between the long and short runs were at the cortical fibula (21.32%), cancellous fibula (23.74%), and cortical tibia (20.99%). The values at the cortical tibia and fibula were within the quasi-static strain rate range, even for the short run, and the cancellous fibula was just above the upper limit, suggesting that these differences are more a result of minor bone positioning variations caused by the differing load speed, than strain rate effects.

The similarity in the majority of the strain readings between the short and long runs suggests that strain rate effects are minimal at the chosen loading speed of 125 ms. While some isolated locations were above the quasi-static strain rate range at the faster 125 ms loading speed, and this is a limitation of the current study, the longer loading time would not be worth the increased run time. The fact that the maximum force was held at the end

of the loading ramp for a brief period of time also ensures that the bones were allowed to settle into position and the strain rate approached zero during the constant-force period.

It should be noted that the method used to calculate strain rate in the present study has inherent errors. While dividing the maximum strains by the total duration of force application gives an overall “average” measure of the strain rate, there may be non-linear instantaneous strain increases or decreases that were introduced as the bones shifted due to load application. These effects were not taken into account by the strain rate calculations.

#### 4.4.5 ORIGINAL TIBIAL GEOMETRY

For the simulation in the neutral posture using a rigid tetrahedral mesh of the specimen’s original tibial geometry, the strain at the medial talar neck gauge location increased in comparison with the previously-validated tibia. By visual inspection at the maximum load, the talar neck did impinge against the medial malleolus (Figure 4.19) – an effect that did not occur in the simulation using the previously-validated tibia. While only the neutral posture was tested using the specimen’s original tibial geometry, this effect may be more pronounced in other ankle postures such as inversion, potentially causing failure of the talar neck as predicted by Sneppen and Buhl (1974). Furthermore, while the simulated and experimental strains agreed well for the gauge on the talar sulcus using the previously-validated tibia, the simulated strain at this location decreased substantially when the specimen’s original tibial geometry was used. This large difference may be a result of assigning rigid body properties to the tibia, eliminating any minor deflection that occurs at the distal tibial epiphysis, and altering the load path through the talus. The

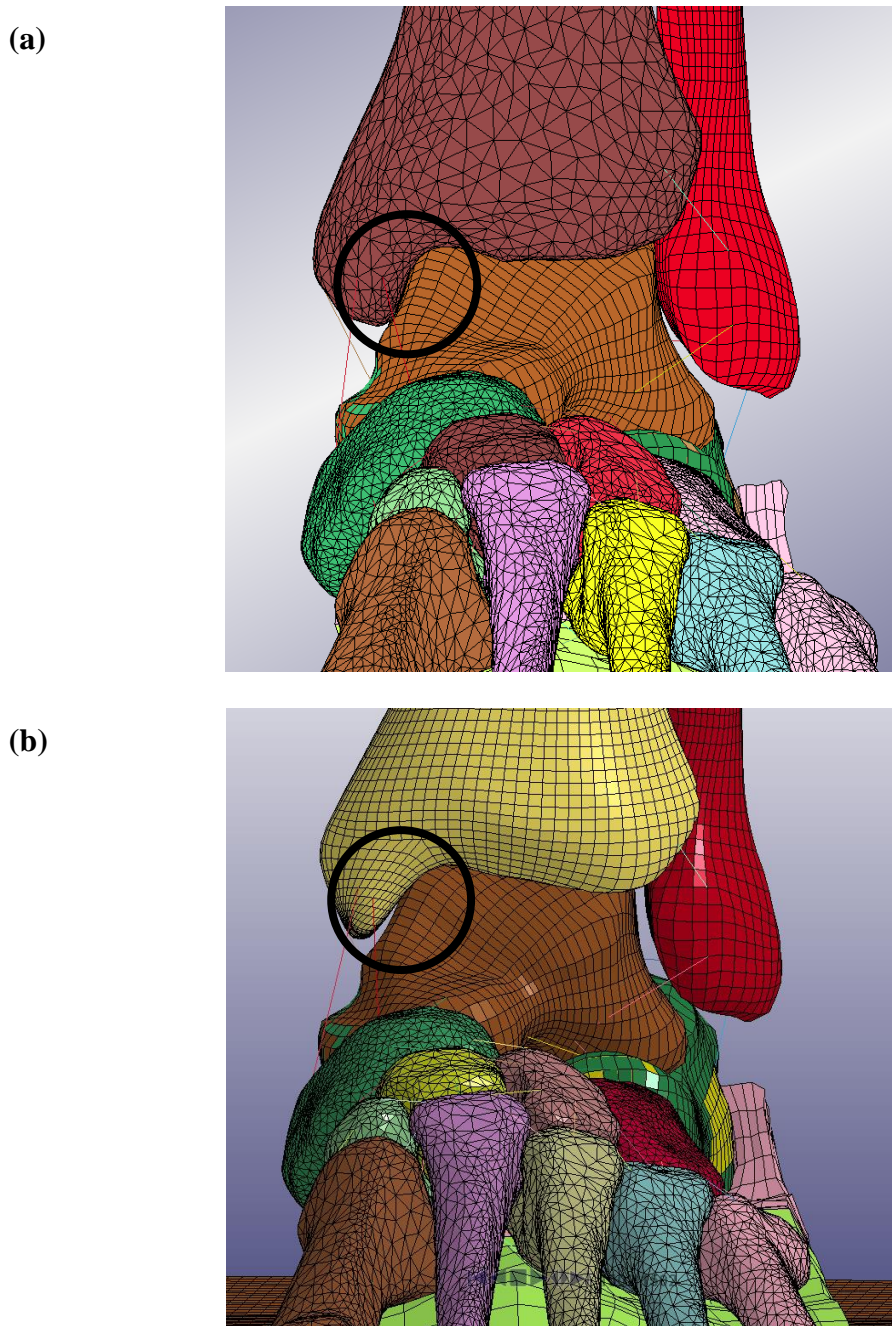


**Figure 4.19: Anterior View of the Ankle in the Neutral Posture**

When the model of the foot and ankle with the specimen's original tibia **(a)** was loaded to 150 lbs in the neutral posture, the talar neck impinged on the medial malleolus of the tibia. This area is circled in black. The model with the previously-validated tibia **(b)** loaded to 150 lbs in the neutral posture exhibits a noticeable gap between the tibia and talar neck (also circled in black).

maximum strain, located at the center of the talar sulcus, remained fairly consistent between the two simulations. Overall, the total error in strain readings at the gauge locations was minimized when using the previously-validated tibia, suggesting that this tibia is acceptable for use in the model. If the specimen's original tibia was used after being segmented into cortical and cancellous regions and assigned deformable bone properties, the overall model response may be improved even further.

#### 4.4.6 GENERAL MODEL EVALUATION

The greatest source of error in the rotations and displacements of the hindfoot bones may have been a result of the simplifications made in the modeling of the ligaments. In the model, ligaments were idealized as 1D bars instead of 2D sheets, and by having only one ligament attachment node on each bone instead of having attachment occur over a range of nodes, there is less of a restriction imposed on the movement of each bone. In particular, rotation is free to occur about a ligament attached at one node, whereas a range of ligament attachment nodes would restrict this motion. Accurate ligament force-displacement curves are also lacking in the literature, especially for the ligaments connecting the bones of the midfoot and forefoot.

Ligaments were also not pre-tensioned in the model in any way, and this is most likely one of the largest sources of error in bone positioning, particularly for the simulations in which ankle posture was altered. A lack of ligament pretension, combined with the small gaps between the bones due to the lack of cartilage, causes much less restriction to be imposed on the movement and rotation of all the bones of the foot in every direction

when compared with the actual foot and ankle. Implementing ligament pretension, or preloading of any kind, in FE models is difficult, as a specific “preload” period would need to be implemented in which the ligaments become tensed prior to beginning the actual test. Furthermore, there is no information in the literature on realistic amounts of ligament pretension to apply. The result of these limitations is that no known FE models of the foot and ankle to date have imposed ligament pretension, and this is one of the major improvements that need to be made to such models in the future.

Other factors that may have contributed to the rotation and displacement errors were the coefficient of friction chosen between the bones, the absence of cartilage, and the compliance of the heel pad. Furthermore, the medial malleolus protrudes more medially in the previously-validated tibia than in the specimen’s original tibia, potentially imposing less of a restriction on the talus, particularly about the inversion/eversion axis of rotation.

The relatively fast speed at which the rotation of the ankle took place caused some bouncing of the bones that may have also contributed to the positioning errors. This effect was more severe in plantarflexion and dorsiflexion, as the bones of the foot had the greatest distance offset from the center of rotation in these postures. An attempt was made to mitigate this bouncing by having a rest period after the rotation to lessen any residual inertial effects, and the effect of rotation speed on bone positions and strain was assessed by performing two different simulations in the plantarflexion posture in which the rotations took place over 100 and 200 ms. For the slow run at 200 ms, less of a bouncing effect was observed, and the results show that in general, the bone rotations more closely matched the experimental results at this slower rotation speed. If the speed were reduced even more,

the bone rotation results may be further improved. However, a slower rotation speed was not used in the current study, as the run with a 200 ms rotation time required approximately 60 hours to complete.

It is also interesting to note that these minor positional changes in the bones between the long and short runs caused fairly substantial changes to the strains measured at the talar and calcaneal gauge locations. The maximum difference between the long and short runs was  $71 \mu\epsilon$  (or 1.6 average neutral standard deviations), and the short run exhibited a closer match with the experimental strains. The differences in bone rotations and positions between the simulations and experiments seem to contribute to the strain errors by altering the load path through the bones of the ankle from the experimental trials.

In each posture the simulated strains matched up well with the experimental strains (within two average neutral SDs) for at least three or four gauge locations, and there are several general sources of error introduced by modeling simplifications that may have contributed to the discrepancies that were observed at the other locations. Comparing the model's response within two SDs of the response of one specimen constitutes quite a small difference, and is a relatively strict evaluation metric. In comparison with the SDs of the entire population, the model's response is possibly quite reasonable.

One of the main sources of error was the use of homogeneous material properties throughout these bones. While the material properties in the diaphyseal regions of the long bones seem to be fairly consistent due to the thick cortical shell and relative lack of trabecular bone, they may vary much more at regions with a thinner cortical shell and a greater concentration of trabecular bone, such as at the epiphysis. The calcaneus and talus

bones also have this type of structure, and by inspection of the CT scans, there was substantial variation in cortical and trabecular density (brightness) throughout these bones, while the density in the diaphysis of the fibula and tibia appeared to be fairly consistent over their whole length. All strain gauges in this study were located either on the hindfoot bones or at the epiphyses of the long bones, where the material properties vary substantially.

The anisotropy of bone was also neglected in the model, possibly contributing to the discrepancies between simulated and experimental strains. The calcaneus and talus bones have highly anisotropic microstructures (Souzanchi et al., 2012) due to the multiple load paths passing through these bones from both the heel and the midfoot (von Meyer, 2011).

A previous study using strain gauges as a method of validation for an FE model of a radius (Burkhart et al., 2014), in which the gauges were all placed at the diaphysis/metaphysis, found strain deviations of approximately 33% between the model and experiment. Another study doing the same for the tibia (Quenneville and Dunning, 2011), found acceptable agreement for the gauges located at the diaphysis, but poor agreement at the epiphysis (deviations of up to 70%). Many strain readings from the simulations in the current study that are outside the two neutral average standard deviation range are within an error of 70% in comparison with the experiments. However, it should be noted that these studies were performed under dynamic impact conditions, which tend to result in poorer agreement in general than static testing.

#### 4.4.7 SIMILARITIES AND DIFFERENCES AMONG ALL POSTURES

Dorsiflexion of the calcaneus was overestimated in all postures except the plantarflexion posture. In the neutral posture, it was observed that the heel pad compressed more at the back of the heel in the simulation than in the experiment, while the compression at the anterior calcaneus nearly matched that in the experiment. This effect caused the calcaneus to assume a greater inclination in the neutral and dorsiflexed ankle postures. Further refinement of heel/foot pad properties is required to ensure accurate positioning of the bones of the foot under load.

The underestimation of strains in the fibula in the plantarflexion and neutral postures can be attributed to the absence of cartilage in the model. This absence of cartilage caused a gap to be present between the talus and fibula, and even at the maximum compressive footplate load, the two bones never actually came into contact. The strains observed at the fibula in these postures are therefore most likely caused only by ligament tension, the forces of which are also underestimated in the model when compared with the experiment, due to a lack of ligament pre-tension. The lack of cartilage in the model also contributed to the positioning errors in the hindfoot bones since it causes these bones to be in closer proximity under load in the simulations than in the experiments.

In all postures except neutral and plantarflexion, the calcaneal displacement was overestimated by a large margin in the simulation. The inversion or eversion of the calcaneus was likewise overestimated, and since the origin of the calcaneal coordinate system is at the calcaneal notch on the plantar surface of this bone, these greater rotations caused the resulting overestimation of displacement.

In all postures except inversion-external rotation, the simulated tibial strains were within two average neutral standard deviations of the experimental strains, and even in inversion-external rotation, the simulated tibial strain is just outside this range, at 2.1 neutral standard deviations. The match in tibial strain values at all positions further justifies the use of the previously-validated tibia instead of developing a new model using the specimen's geometry.

At the plantar calcaneus, the strains were severely overestimated by the model in all postures except for plantarflexion. This may actually be a result of error in the experimental gauge reading, as this gauge was placed at a location where the radius of curvature was less than ten times the gauge length (Appendix B). The result of this may be an averaging effect that would cause the plantar calcaneal gauge readings to be underestimated. In the model at the neutral posture, the strains varied greatly, by approximately  $825 \mu\epsilon$ , along this curved surface. Furthermore, this gauge location is very close to the ligament insertion node for the plantar fascia, and the point loading caused by these ligaments may have artificially increased the strain at the plantar calcaneal gauge location.

Despite the large differences in the specific values, the simulated and experimental strains at the plantar calcaneal gauge followed the same general trend. With the exception of the plantarflexion posture, the lowest strains at this gauge location in both the simulation and experiment were observed in eversion-external rotation and the neutral posture. Likewise, the highest strains at this gauge location in both the simulation and experiment were observed in dorsiflexion-inversion and inversion-external rotation.

The one posture in which strains at the plantar calcaneal gauge was not overestimated in the simulation was in plantarflexion. This may have been a result of the excessive inversion of the calcaneus in the simulation in this posture, causing the point of contact between the heel and the footplate to be shifted laterally, with the medially-located plantar calcaneal gauge located away from the load path. Another possibility is that in plantarflexion, more load is passing through the heel and less through the metatarsals, causing reduced tension in the plantar fascia relative to the other postures. This would reduce the point loading near the plantar calcaneal gauge, causing the strain distribution at this area to decrease to a more realistic level. The strain range along the curved surface in this case (approximately  $620 \mu\epsilon$ ) was also reduced when compared with the neutral posture.

#### 4.4.8 TALO-CRURAL AND TALO-CALCANEAL JOINT BEHAVIOUR

In the inversion-external rotation experiment, the calcaneus inverted by half of the total inversion angle and the rest of the motion was accomplished by the forefoot, while in the simulation, the calcaneus inverted the full amount. This was partially a result of fixing the heel of the foot to the footplate during the inversion rotation, causing the calcaneus to follow this rotation more completely in the simulation than the experiment. In essence, this boundary condition was more severe in the simulation, while in reality the calcaneus would not be able to move this far in inversion due to the restriction imposed on it by the ligaments. The talar inversion was relatively minor in the model, which indicates that the simulation captures the experimentally-observed effect of how the talo-calcaneal joint

solely contributes to the inversion-eversion rotation of the hindfoot, and the talo-crural joint plays a negligible role.

Similarly, the eversion of the calcaneus in the model was overestimated in the eversion-external rotation posture due to the fact that the sole of the foot was rigidly connected to the footplate during the rotation. However, unlike in the inversion-external rotation posture, the calcaneus did not assume the full eversion rotation of the footplate, and stopped at about two-thirds of the complete value. While this rotation was still overestimated, this result is consistent with the experimental finding that the range of motion of the calcaneus about the inversion-external rotation axis is lower in eversion than inversion. The excessive eversion of the calcaneus might have also been, in part, due to excessive eversion of the talus by  $6^\circ$ . By inspection of the simulation, the talus slid medially within the talo-crural joint due to its larger freedom of movement in the simulation, impinging against the medial malleolus of the tibia. As the talus impinged on the medial malleolus, the curvature of the inner surface of this protrusion acted like a ramp, allowing the medial-superior aspect of the talus to travel up the ramp, and evert within the talo-crural joint. This possibly contributed to the excessive eversion of the calcaneus. The overall relative motion between the talus and calcaneus within the talo-calcaneal joint was consistent with the approximately  $7^\circ$  of eversion observed experimentally.

In the plantarflexion posture, the plantarflexion of the calcaneus agreed well with the experimental result, and this was due to the fact that the plantar surface of the foot was rigidly attached to the footplate. However, the plantarflexion of the talus was underestimated by approximately  $8^\circ$ , meaning that there was some relative motion about

the plantar/dorsiflexion axis in the talo-calcaneal joint. In the experiment, the talus and calcaneus rotated together about this axis by the same angle, and there was very little motion at this joint. While underestimated, the plantarflexion motion of the talus within the talo-crural joint was substantial in both the simulation and experiment.

In the dorsiflexion-inversion posture, the dorsiflexion of the calcaneus and talus were both overestimated by similar amounts. Despite these deviations, the model did capture how the talus dorsiflexed further than the calcaneus at this posture, and the amount by which the talar dorsiflexion exceeded the calcaneal dorsiflexion was similar in the simulation and the experiment (the relative motion at the talo-calcaneal joint about this rotation axis was consistent). Also, while overestimated, the dorsiflexion motion of the talus within the talo-crural joint was substantial in both the simulation and experiment.

Like in the inversion-external rotation posture, the inversion of the calcaneus was overestimated in dorsiflexion-inversion. In the experiment, the calcaneus inverted by half of the total footplate inversion value, while in the simulation, calcaneal inversion was 85% of the full rotation. This is still an improvement over the inversion-external rotation posture, in which the calcaneus rotated 100% of the footplate inversion value. The model still captured the behaviour of the talo-calcaneal and talo-crural joints, specifically how the talus everted slightly while the calcaneus inverted.

#### 4.4.9 MIDFOOT/FOREFOOT BONE POSITIONS

The positions of the midfoot and forefoot bones in the simulations did not deviate substantially from the experiments, with a maximum distance of only 1.7 cm. It should

also be noted that the maximum distance across all postures was generally located at metatarsal 5, which is not a bone that constitutes a major load path in the foot. Furthermore, the relative positions of the bones in the simulations seemed to match the experimental observations well, with a slight offset depending on the posture. This overall offset was most likely due to the difference in calcaneal and talar positions and rotations between the simulation and experiment, causing the midfoot and forefoot bones to shift uniformly.

The neutral posture exhibited the lowest average maximum distance, and this was no doubt due to the lack of ankle rotation in this posture prior to force application. The plantarflexion posture, which had the largest rotation value at the furthest offset from the rotation axis exhibited the highest average maximum distance. This large rotation performed over a relatively short amount of time caused vibrational motion in the forefoot and midfoot, which may have contributed to some of these discrepancies, and might be reduced if the simulation were run with a longer rotation time.

Another factor that most likely contributed to the observed deviations was the difference in heel pad compliance between the experiment and the simulation. The lack of ligament pre-tension and cartilage in the simulation, as well as the absence of flesh surrounding the bones, also played a role by imposing less of a limitation on their movement and should be added in future iterations of the model.

The smallest deviations in bone position were consistently at the first metatarsal, or in the case of the neutral posture, at the medial cuneiform, which is located immediately posterior to the first metatarsal. Conversely, the largest deviations were consistently at the fifth metatarsal. This suggests that the fifth metatarsal had an excessive amount of freedom

of movement, and by implementing the aforementioned improvements to the model, the response of this bone could be improved.

#### 4.4.10 INJURY PREDICTION

The results of the predicted failure loads of the hindfoot bones showed that the load that would cause fracture in each bone was always higher in the neutral posture than in all other tested postures. While the majority of previous cadaveric and numerical studies predicting the fracture tolerance of the lower leg have been conducted with the ankle in a neutral posture (*e.g.* Yoganandan et al., 1996, Iwamoto et al., 2005), the current results suggest that the fracture tolerance of the lower leg is overestimated in this posture. This highlights the need for more robust injury limits for the lower leg and ankle that account for the variation in ankle posture that may occur during injurious events.

The talus and calcaneus consistently exhibited the lowest predicted fracture loads across all postures, suggesting that previous studies that have looked at the fracture tolerance of the tibia alone may be underestimating the absolute fracture threshold of the entire lower limb (*e.g.* Mo et al., 2012).

The predicted fracture tolerance of the lower leg at the neutral posture was found to be 6.5 kN at the calcaneus and 9.2 kN at the tibia, which agree very well with the values reported by Yoganandan et al. (1996) (8.3-11.4 kN at the proximal tibia), Funk (2002a) (50% risk of injury = 8.3 kN at the proximal tibia) and Seipel (2001) (50% risk of injury = 5.5 kN at the calcaneus). Furthermore, the fracture locations that were observed in these previous studies were at the distal tibia and the superior articular surface of the calcaneus,

and this is consistent with the locations of maximum strain observed for those bones at the neutral posture in the current study. It should be noted that these aforementioned studies did not take Achilles tension into account, and so are suitable for comparison with the present model that also did not include this force. The inclusion of Achilles tension in the model would increase the joint forces, potentially reducing the calculated fracture tolerances. It may also change the locations of critical strain observed in the model at each posture.

The one discrepancy with the literature findings is that the lowest predicted fracture threshold in the neutral posture was predicted to occur at the talus at the contact surface with the sustentaculum of the calcaneus. Experimental testing in the neutral posture typically induces fractures at the calcaneus and distal tibia (Funk et al., 2002a).

In the inversion-external rotation posture, the lowest predicted fracture tolerance was at the sustentaculum of the calcaneus. This was the lowest fracture load for the calcaneus observed in this study, and this mechanism is consistent with previous research that has found that excessive inversion of the ankle may cause fractures of the sustentaculum (Essex-Lopresti, 1952). High strains were also observed at the talar neck in this posture, and inversion has been previously implicated in causing talar neck fracture (Sanders and Lindvall, 1999).

Eversion-external rotation generated one of the lowest fracture tolerances seen in this study at the lateral process of the talus. By inspection of the simulation, this anatomical feature was wedged into the Angle of Gissane of the calcaneus, causing high strains at this location on both bones. Eversion of the ankle has been previously implicated in causing

fracture of the lateral process of the talus, known as a “snowboarder’s fracture”, and this effect has been reproduced experimentally in cadaveric specimens (Funk et al., 2003).

The fracture thresholds for all bones except the calcaneus were the lowest in the dorsiflexion-inversion posture. In fact, the lowest failure load observed in this study was predicted to occur in this posture at the upper articular surface of the talus near the talar neck, and by inspection of the simulation, the dorsiflexion caused the talar neck to be wedged against the distal anterior tibia, generating high strains in both bones. This exact mechanism has been proposed in the literature to cause talar neck fracture in ankle postures involving dorsiflexion (Smith and Ziran, 1999). Furthermore, in a study looking at mechanisms of fractures in ankle injuries to front seat car occupants, combined dorsiflexion and inversion was associated with the highest incidence of talar neck fracture out of all common ankle postures during vehicular collision (Morris et al., 1997).

The fracture tolerance in this case was at the maximum load applied to the specimen experimentally (150 lbs, 667 N), suggesting that damage may have occurred to the specimen at the talar neck during testing. Since this location of high strain was caused by contact between the talus and the previously-validated tibia, there is a possibility that using the specimen’s original tibia in the model would have generated a slightly different response due to its geometric differences. However, around the point of contact with the talus, the geometry of the two tibias matched very well (1-2 mm difference). In Chapter 2, the strains recorded at the gauge on the medial talar neck in the final trial at the end of all tests were higher than those in the initial neutral trials by six standard deviations, also indicating the possibility of damage at this location. This posture was the second-to-last

altered posture that was tested, with the plantarflexion trial being last, meaning that the neutral, inversion-external rotation and eversion-external rotation results would not have been affected by the possible damage.

In a study by Begeman et al. (1993), fractures of the calcaneus and talus were produced in cadaveric specimens as a result of forced inversion and eversion, and the lowest predicted fracture tolerances in the current study were in the talus and calcaneus in the postures involving inversion and eversion. Begeman applied up to 1.3 kN of load and generated ligamentous avulsions in the hindfoot bones with much larger inversion and eversion angles (30 - 85°). The current study predicted fracture of the calcaneus in inversion-external rotation at 2.7 kN and failure of the talus in eversion-external rotation at 2.1 kN, which are larger than Begeman's failure load, but comparable given the different angles. The predicted fracture tolerance of the lower leg in dorsiflexion-inversion in the present model was 0.66 kN, which is in the middle of the range reported by Begeman.

According to the Lauge-Hansen classification of ankle fractures, eversion-external rotation and inversion-external rotation produce malleolar and distal epiphyseal fractures of the distal tibia and fibula (Lauge-Hansen, 1950). Malleolar fractures were also observed in previous cadaveric studies involving inversion and eversion (Funk et al., 2002b, Begeman et al., 1993). In the postures involving inversion and eversion in the current study, the highest strains in the shank were observed at the distal articular surface of the tibia and at the proximal fibula, but not at the malleoli. In the case of Lauge-Hansen ankle fractures, the external rotation angles in the current study were within the natural range of motion of the ankle joint (Nester et al., 2003), and may not have been sufficient to cause

excessive strains in the epiphyseal regions of the long bones of the lower leg. Ligaments also play a major role in the fracture mechanisms proposed by Lauge-Hansen (1950), and the lack of ligament pretension in the model may have caused strains around the malleoli to be underestimated. The previously-noted limitations with the model may have also contributed.

While the predicted bone failure loads in plantarflexion were lower than those in the neutral posture, they were still moderate compared with the postures involving inversion or eversion. This is consistent with how plantarflexion is rarely implicated in causing fractures of the ankle.

There are several limitations with the failure load prediction done in the current study. Firstly, the failure load was extrapolated based on the strains measured at relatively low footplate loads, and therefore the strains at the bones were assumed to increase linearly from this low load all the way to failure. Due to this potential non-linearity of strains, the locations of highest strain observed at the low load may not be the same at failure. In fact, since bone was assumed to be an elastic-plastic material in the current model, it is likely that a linear strain extrapolation to failure introduces inherent error in the calculations.

All tests were performed under quasi-static conditions, and dynamic testing may also alter the fracture threshold and location of the lower leg. More simulations need to be performed in the future in which the model is loaded to failure at each posture, as well as analogous experimental tests for validation.

Points of ligament attachment and the adjacent nodes were neglected from being chosen as locations of maximum strain due to concentrated point loading. While

ligamentous avulsion fractures are sometimes observed experimentally in the lower leg (*e.g.* Funk et al., 2002b), this mechanism of injury is not the most prevalent for traumatic events involving axially-directed loading. In order to accurately represent these types of injuries in an FE model, more investigation would be needed into ligament failure properties and regions of ligament attachment, which is beyond the scope of this project.

It should also be noted that the boundary conditions at the proximal shank were slightly different in the experiment and model. The previously-validated tibia was potted to a different depth than the specimen used in the current study, and as a result, there is a discrepancy in the length of the fibula and tibia in the model. In the experiment, both the tibia and fibula were bounded at the same vertical position, whereas in the model, the tibia and fibula were bounded at different vertical positions. Due to this discrepancy in boundary conditions, the response of the model's shank in bending may differ somewhat from the experiment, and this effect no doubt contributed to the finding that the fibula was most vulnerable to injury at the proximal boundary in three of the five ankle postures.

Finally, the locations of highest strain were often observed within the articular surfaces between the bones, and the lack of articular cartilage in the model may have resulted in some concentrated point loading at these surfaces, as cartilage helps distribute the load over a larger area within the joints.

Despite these limitations, the model accurately predicted the fracture loads and locations in each posture when compared with data from previous studies examining the fracture tolerance of the lower leg and ankle.

#### 4.5 REFERENCES

- BANDAK, F., TANNOUS, R. & TORIDIS, T. 2001. On the development of an osseoligamentous finite element model of the human ankle joint. *International journal of solids and structures*, 38, 1681-1697.
- BEGEMAN, P., BALAKRISHNAN, P., LEVINE, R. & KING, A. 1993. Dynamic human ankle response to inversion and eversion. SAE Technical Paper 933115.
- BURKHART, T. A., QUENNEVILLE, C. E., DUNNING, C. E. & ANDREWS, D. M. 2014. Development and validation of a distal radius finite element model to simulate impact loading indicative of a forward fall. *Proceedings of the Institution of Mechanical Engineers, Part H: Journal of engineering in medicine*, 0954411914522781.
- BURSTEIN, A. H., REILLY, D. T. & MARTENS, M. 1976. Aging of bone tissue: mechanical properties. *The Journal of Bone & Joint Surgery*, 58, 82-86.
- DONG, L., ZHU, F., JIN, X., SURESH, M., JIANG, B., SEVAGAN, G., CAI, Y., LI, G. & YANG, K. H. 2013. Blast effect on the lower extremities and its mitigation: A computational study. *Journal of the Mechanical Behavior of Biomedical Materials*, 28, 111-124.
- ERDEMIR, A., VIVEIROS, M. L., ULBRECHT, J. S. & CAVANAGH, P. R. 2006. An inverse finite-element model of heel-pad indentation. *Journal of biomechanics*, 39, 1279-1286.
- ESSEX-LOPRESTI, P. 1952. The mechanism, reduction technique, and results in fractures of the os calcis. *British Journal of Surgery*, 39, 395-419.
- FUNK, J. R., CRANDALL, J. R., TOURET, L. J., MACMAHON, C. B., BASS, C. R., PATRIE, J. T., KHAEWPOONG, N. & EPPINGER, R. H. 2002a. The axial injury tolerance of the human foot/ankle complex and the effect of Achilles tension. *Journal of biomechanical engineering*, 124, 750-757.
- FUNK, J. R., SRINIVASAN, S. C. & CRANDALL, J. R. 2003. Snowboarder's talus fractures experimentally produced by eversion and dorsiflexion. *The American journal of sports medicine*, 31, 921-928.
- FUNK, J. R., SRINIVASAN, S. C., CRANDALL, J. R., KHAEWPOONG, N., EPPINGER, R. H., JAFFREDO, A. S., POTIER, P. & PETIT, P. Y. 2002b. The effects of axial preload and dorsiflexion on the tolerance of the ankle/subtalar joint to dynamic inversion and eversion. SAE Technical Paper 2002-22-0013.
- HILLS, B. A. & BUTLER, B. D. 1984. Surfactants identified in synovial fluid and their ability to act as boundary lubricants. *Annals of the Rheumatic Diseases*, 43, 641-648.
- IWAMOTO, M., MIKI, K. & TANAKA, E. 2005. Ankle skeletal injury predictions using anisotropic inelastic constitutive model of cortical bone taking into account damage evolution. *Stapp car crash journal*, 49, 133.
- KLOPP, G., CRANDALL, J., HALL, G., PILKEY, W., HURWITZ, S. & KUPPA, S. Mechanisms of injury and injury criteria for the human foot and ankle in dynamic axial impacts to the foot. Proceedings of the 1997 International IRCOBI Conference on the Biomechanics of Impact, 1997.

- LAUGE-HANSEN, N. 1950. Fractures of the ankle: II. Combined experimental-surgical and experimental-roentgenologic investigations. *Archives of Surgery*, 60, 957-985.
- LINDE, F., HVID, I. & PONGSOIPETCH, B. 1989. Energy absorptive properties of human trabecular bone specimens during axial compression. *Journal of Orthopaedic Research*, 7, 432-439.
- MO, F., ARNOUX, P. J., JURE, J. J. & MASSON, C. 2012. Injury tolerance of tibia for the car–pedestrian impact. *Accident Analysis & Prevention*, 46, 18-25.
- MORRIS, A., THOMAS, P., TAYLOR, A. M. & WALLACE, W. A. Mechanisms of Fractures in Ankle and Hind-Foot Injuries to Front Seat Car Occupants: An In-Depth Accident Data Analysis. Proceedings of the 41st Stapp Car Crash Conference, November 13-14, 1997, Orlando, Florida, USA (Sae Technical Paper 973328), 1997.
- NESTER, C. J., FINDLOW, A. F., BOWKER, P. & BOWDEN, P. D. 2003. Transverse plane motion at the ankle joint. *Foot & ankle international*, 24, 164-168.
- QUENNEVILLE, C. E. & DUNNING, C. E. 2011. Development of a finite element model of the tibia for short-duration high-force axial impact loading. *Computer methods in biomechanics and biomedical engineering*, 14, 205-212.
- SANDERS, R. & LINDVALL, E. 1999. Fractures and fracture-dislocations of the talus. *Surgery of the Foot and Ankle, ed*, 7, 1465-1518.
- SEIPEL, R. C., PINTAR, F. A., YOGANANDAN, N. & BOYNTON, M. D. 2001. Biomechanics of calcaneal fractures: a model for the motor vehicle. *Clinical orthopaedics and related research*, 388, 218-224.
- SHIN, J. & UNTAROIU, C. D. 2013. Biomechanical and Injury Response of Human Foot and Ankle Under Complex Loading. *Journal of Biomechanical Engineering*, 135, 101008-101008.
- SHIN, J., YUE, N. & UNTAROIU, C. D. 2012. A finite element model of the foot and ankle for automotive impact applications. *Annals of biomedical engineering*, 40, 2519-2531.
- SHUNMUGASAMY, V. C., GUPTA, N. & COELHO, P. G. 2010. High strain rate response of rabbit femur bones. *Journal of biomechanics*, 43, 3044-3050.
- SMITH, P. N. & ZIRAN, B. H. 1999. Fractures of the talus. *Operative techniques in orthopaedics*, 9, 229-238.
- SNEPPEN, O. & BUHL, O. 1974. Fracture of the talus. A study of its genesis and morphology based upon cases with associated ankle fracture. *Acta orthopaedica Scandinavica*, 45, 307.
- SOUZANCHI, M. F., PALACIO-MANCHENO, P., BORISOV, Y. A., CARDOSO, L. & COWIN, S. C. 2012. Microarchitecture and bone quality in the human calcaneus: Local variations of fabric anisotropy. *Journal of Bone and Mineral Research*, 27, 2562-2572.
- UNTAROIU, C., DARVISH, K., CRANDALL, J., DENG, B. & WANG, J.-T. Characterization of the lower limb soft tissues in pedestrian finite element models. 19th International technical conference on the Enhanced Safety of Vehicles, 2005. 124-131.

VON MEYER, G. H. 2011. The Classic: The Architecture of the Trabecular Bone (Tenth Contribution on the Mechanics of the Human Skeletal Framework). *Clinical Orthopaedics and Related Research*®, 469, 3079-3084.

YOGANANDAN, N., PINTAR, F. A., BOYNTON, M., BEGEMAN, P., PRASAD, P., KUPPA, S. M., MORGAN, R. M. & EPPINGER, R. H. 1996. Dynamic axial tolerance of the human foot-ankle complex. SAE Technical Paper 962426.

---

## CHAPTER 5 – General Discussion and Conclusions

---

### 5.1 SUMMARY

The foot/ankle complex is frequently injured in a wide array of debilitating events, such as car crashes. Numerical models and experimental tests have been used to assess injury risk, but most do not account for the various postures the ankle may assume during these events. These postural changes likely affect the load pathway of the foot/ankle complex, potentially reducing the fracture threshold from that of the neutral case, and changing the location of fracture (*e.g.* Calhoun et al., 1994). The overall purpose of this study was to develop a finite element model of the foot and ankle that accounts for these positional changes and exhibits a biofidelic response.

The first step towards accomplishing this was to develop a Computed Tomography (CT)-compatible testing apparatus that could apply load while adjusting the angle of the ankle of a cadaveric lower leg in three dimensions (*i.e.*, Objective #1, Chapter 2). The hindfoot bones of the lower leg were instrumented with strain gauges, and CT scans were taken as static loading of 150 lbs was applied at five different ankle postures that have been shown to cause particular vulnerability to injury. At the neutral posture, the repeatability of bone positions was assessed and found to be high, and the gauge readings were mostly repeatable and reliable. The CT scans at the altered postures demonstrated that ankle rotation was a complex combination of motion at the talo-crural and talo-calcaneal joints, as well as the forefoot, and the individual contributions of these joints were highly dependent on the particular ankle posture being investigated. The strains recorded on the

surfaces of the hindfoot bones showed that the load path through this region changed as ankle posture was adjusted. In particular, inversion and eversion caused the load path through the bones to be located more medially and laterally, respectively (*i.e.*, Hypothesis #1 accepted).

These CT scans were then used as the basis of a Finite Element (FE) model of the lower limb (*i.e.*, Objective #2a, Chapter 3) that could serve as a useful tool for injury risk assessment. Finite element models are often used in industry to perform safety evaluations, and a lower leg model that accurately represents the response of the natural lower leg as ankle posture is adjusted would be a useful tool. Meshes of the 26 bones of the foot as well as the two bones of the shank and the soft plantar heel/foot pad, were constructed and rigorously evaluated to ensure they would provide accurate and stable responses during simulations. Sixty-seven ligaments connecting the bones were also included. Model material properties were adjusted to minimize error between the simulation and experiment, and the model response at each posture was compared with the experimental strain and positional data to evaluate the biofidelity of the model (*i.e.*, Objective #2a, Chapter 4). For the most part, the strain deviations at all postures were within the usual range reported in previous studies attempting to validate FE models of isolated bones using strain gauges, with the strains matching very well for at least a few gauge positions in each posture. The hindfoot bone displacements and rotations were likewise reasonably in line with the experimental results, with the model capturing some of the most important behavioural features of the ankle joints observed experimentally (*i.e.*, Hypothesis #2a accepted).

The fracture thresholds and locations at each posture were estimated based on the maximum strains observed in the model and the critical strain levels for cortical and cancellous bone from the literature. The failure loads and locations observed in the model at each posture were compared with findings from relevant cadaveric studies to assess the ability of the model to predict injury as ankle posture is adjusted (*i.e.*, Objective #2b, Chapter 4). The fracture tolerances were similar to those reported in the literature, and the critical locations matched up well in each posture. The model suggested that the fracture tolerance of the lower leg is the lowest in the dorsiflexion-inversion posture, and all postures in which ankle angle was adjusted exhibited a lower fracture threshold than the neutral posture (*i.e.*, Hypothesis #2b accepted).

## **5.2 STRENGTHS AND LIMITATIONS**

The strengths and limitations specific to each study were discussed in their respective chapters, but some are generally applicable to the thesis at large. A major strength of this work is the relatively large number of ankle postures that were investigated, which allowed the load path through the hindfoot and the mechanisms of the ankle joint to be investigated numerically and experimentally throughout the natural range of motion of the ankle. This is the only known study to examine the biofidelity of the individual bone positions in an FE model as ankle posture is adjusted. Furthermore, the CT-compatible test frame allowed the positions of the bones of the foot under load to be observed for the first time, to our knowledge. Another major strength of this work was that comparison with experimental results was performed via strain gauges, allowing for an assessment of

individual bone responses as loading was applied and posture was adjusted. The most commonly-accepted method of validation for FE models in the literature is using biofidelity corridors, which provide an assessment of the overall response of the model, but little information on the accuracy of the individual bone responses.

The mesh quality of the finite element model was rigorously tested to a level rarely seen in published dynamic FE studies. The model was also constructed using relatively fine meshes, which allowed for a high degree of geometric accuracy. Sixty-seven ligaments were represented in total, which is the more than any previously-published FE study of the lower leg. Furthermore, attempts were made to tune the properties of the model to best match the experimental results, which is only really possible when the model is derived from the same specimen upon which experimental testing was performed. This is rarely seen in the literature, and is a strength of the current work.

While this research addressed many of the drawbacks in the current literature pertaining to examination of lower leg response in non-neutral ankle postures, FE mesh evaluation and FE model complexity, several limitations are still present. *In-vitro* testing was used to approximate the *in-vivo* response of the lower leg, but this was necessary in order to apply strain gauges to the bones of the hindfoot, and is a standard representation used in injury biomechanics research. While this research addressed the effect of ankle posture on fracture tolerance, which is often overlooked in the literature, the loads were applied exclusively in the axial direction in both the experiment and the simulation. Off-axis loading, in the neutral or adjusted ankle posture, may alter the injury risk, and the results from the current study are only applicable to axial loading events. Furthermore,

both the experiments and simulations were performed under static loading conditions, which may underestimate the injury risk of the lower leg.

A major limitation with this study was the lack of repeated trials in the adjusted ankle postures. The bone positions and strains exhibited good repeatability at the neutral posture, and this suggests that the same would be true at the other postures. However, the only way to know for sure would be to perform a repeatability study. This would also allow the FE model bone positions and strains to be compared against a range of values instead of a single reading that may be affected by measurement noise. Along the same lines, cadaveric testing of multiple specimens all instrumented with strain gauges at the same locations would allow for the generation of strain and bone position biofidelity corridors, which would better represent natural anatomic variability. While some of the FE results did not match the experimental values, comparisons against single values are a relatively critical means of assessing the biofidelity of the model, and the error in the simulation would no doubt be lessened in comparison with biofidelity corridors.

There were several limitations inherent to the FE modeling process which may have contributed to error in the results. The material properties of bone, ligaments and plantar soft tissues were selected from previous experimental tests and FE studies, and may not represent the specific properties of the specimen used in this study. Furthermore, all tissues were modeled as isotropic and homogenous, and the bone in the epiphyseal regions of the long bones and the hindfoot is known to be inhomogenous and anisotropic. Finally, using a different tibia than the specimen's natural tibia, and neglecting ligament pretension,

cartilage and the soft tissues encapsulating the sides and top of the foot, may have allowed the bones greater freedom of movement in the model than in the natural ankle.

### **5.3 FUTURE DIRECTIONS**

In order to evaluate the fracture thresholds of the lower leg and ankle estimated in the current study, it would be beneficial to thaw the specimen that was used as the basis of the FE model and load it to failure in the posture that was deemed to cause the greatest injury risk in the simulation (dorsiflexion-inversion). The fracture load and location could then be compared between the simulation and experiment to assess the biofidelity of the model response at failure. Along the same lines, several major assumptions were made when estimating fracture threshold and location in the current study, and the model should be subjected to quasi-static loads great enough to cause strains to exceed the critical values in each posture to obtain a more accurate estimation of failure load and location.

Prior to fracturing the specimen, sub-failure dynamic impacts could also be performed to collect strain data for dynamic model evaluations. Strain-rate effects of bone, ligaments and soft tissues could be implemented in the model, and the model response could be compared against the experimental impact strains, as well as force-time biofidelity corridors under dynamic axial loading, as is common in the literature. Similarly, the response of the ankle to dynamic rotation could also be compared against angle-moment corridors from the literature. In addition to dynamics tests, off-axis loading could be examined, as these types of loading conditions may result in different loading patterns and

fracture tolerances. Anisotropic material properties would most likely need to be included in the model for an accurate response to be exhibited under such types of loading.

The greatest errors observed between experimental and simulated strains were at the plantar calcaneal gauge, and this may have been a function of the gauge being placed at a location of excessive curvature, causing an averaging effect that may have underestimated the measured strains. The specimen could be thawed, a new incision could be made on the plantar side of the foot, and a new gauge could be placed at the plantar calcaneus at a more central location where the curvature is negligible. The specimen could then be loaded again in each posture to acquire more accurate strain readings at this gauge location.

It would be valuable to repeat the experimental tests on multiple cadaveric lower leg specimens instrumented with strain gauges at the same locations as the specimen in the present study. This would allow for the generation of corridors of strain and bone rotation with which to compare FE models of the lower leg and ankle. FE models could also be built from CT scans of these other specimens to investigate the range of responses that may be exhibited by the general population (*i.e.* smaller females vs. larger males, young vs. elderly donors).

In order to improve the response of the current FE model, pretension could be applied to the ligaments to impose a greater restriction on the relative motions of the bones. The ligaments could also be modeled using shells or solids instead of bars elements. Zones of cartilage could also be included by defining 3D solids at the spaces between the bones on the CT scans. These regions could then be meshed with hexahedrals and assigned the

properties of cartilage derived from the literature. Applying inhomogeneous material properties based on Hounsfield Units from the CT scans would also most likely improve the match between the experimental and simulated strains throughout the hindfoot. Furthermore, it would also be beneficial to model the talus and calcaneus using only hexahedral elements, instead of a combination of solids and shells, to improve the numerical accuracy of the model.

The injury tolerance of the forefoot and midfoot could be evaluated by addressing the simplifications made in the modeling of this region. The bones could be modeled using hexahedral elements and defined as deformable bodies with distinct cortical and cancellous regions (or assigned inhomogeneous properties). The flesh and skin surrounding this region could also be included by acquiring the appropriate geometry from the CT scans of the lower leg, much in the same way the heel/foot pad geometry was acquired.

Finally, there is a lack of material property information in the literature for the soft tissues and bones of the foot. Non-linear force-displacement relationships are missing for the ligaments of the midfoot and forefoot, and even for many ligaments of the hindfoot. Similarly, there is an absence of information on the properties of flesh throughout the lower leg, and no information is available on the properties of the calcaneus and talus. Typically, when selecting material properties for the calcaneus and talus, educated estimations are made based on the cortical and trabecular properties of the long bones, or properties used in previous models are applied. Some basic material testing needs to be performed on these tissues to improve FE models in the future.

Once the model has been updated with refined properties and its response thoroughly verified, it could be used to evaluate safety and protective devices. Some examples include the assessment of protective footwear, the effect of sitting posture on the fracture tolerance of the leg, and the efficacy of blast-mitigating materials for use in military vehicles.

#### **5.4 SIGNIFICANCE**

This work has contributed to the understanding of the response and injury tolerance of the foot/ankle complex in non-neutral ankle postures. A number of aspects that are usually taken for granted in FE modeling of the lower limb and ankle were investigated, such as the accuracy of hindfoot bone positions as posture is adjusted, and element quality. It was also shown that postural adjustments of the ankle are more than just a straight-forward movement, but instead are a complicated combination of motions at multiple joints. The experimental and finite element techniques employed in this work could be used in future studies to assess injury risk in other parts of the body, such as the wrist. By changing the geometry and material properties of the model, it could also be used to assess how injury risk is increased for people of smaller stature or advanced age. It is anticipated that the results from this thesis will be used to develop injury limits for the ankle and postural guidelines to minimize injury. The finite element model that was the end result of this work is extremely versatile, and can be used for safety evaluations and for developing new protective devices/systems, the ultimate goal of which would be to reduce the occurrence of debilitating lower leg and ankle injuries.

## **5.5 REFERENCES**

CALHOUN, J. H., LI, F., LEDBETTER, B. R. & VIEGAS, S. F. 1994. A comprehensive study of pressure distribution in the ankle joint with inversion and eversion. *Foot & ankle international*, 15, 125-133.

## **APPENDICES**

---

## **APPENDIX A - Glossary of Medical Terms**

---

**Achilles Tendon:** A tendon connecting the posterior calcaneus to the calf muscles.

**Amputation:** The removal of an extremity of the body by trauma or surgery.

**Anterior:** Situated in the front of the body.

**Articulation:** The junction of contact between two bones.

**Biofidelity:** The quality of being lifelike in response or properties.

**Cadaveric:** Of, or pertaining to, a dead body intended for anatomical study.

**Calcaneo-cuboid joint:** The joint between the calcaneus and the cuboid.

**Calcaneus:** The bone of the foot that constitutes the heel.

**Cancellous Bone:** Light, porous bone found at the ends of long bones and the tarsals.  
Synonymous with trabecular bone.

**Cartilage:** Flexible connective tissue covering joint surfaces, which allows for low-friction motion and shock absorption.

**Coronal:** See frontal.

**Cortical Bone:** The dense outer shell of most bones. Forms the shaft of the long bones.  
Synonymous with compact bone.

**Cuboid:** A cubic tarsal bone on the lateral side of the foot, anterior to the calcaneus.

**Cuneiforms:** Three bones in the midfoot medial to the cuboid and anterior to the talus.

**Diaphysis:** The tube-like shaft of a long bone composed of cortical bone.

**Distal:** Situated away from the center of the body or the point of attachment.

**Dorsal:** The back of an organism.

**Dorsiflexion:** Lifting the toes upward.

**Epiphysis:** The end of a long bone composed of cancellous bone with a cortical shell.

**Eversion:** Movement of the sole of the foot away from the midline of the body.

**External Rotation:** Rotation of the foot about the long-axis of the tibia away from the center of the body.

**Fibula:** The smaller bone of the lower leg on the lateral side between the knee and ankle.

**Forefoot:** The anterior section of the foot composed of the metatarsals and phalanges.

**Frontal:** The plane parallel to the long axis of the body that divides the body into front and back sections.

**Hindfoot:** The posterior section of the foot composed of the calcaneus and talus.

**Inferior:** Situated below, or closer to the feet.

**Internal Rotation:** Rotation of the foot about the long-axis of the tibia towards the center of the body.

**Intramedullary Canal:** The central cavity in a bone filled with marrow.

**Inversion:** Movement of the sole of the foot towards the midline of the body.

**In-Vitro:** In an artificial environment outside a living body.

**In-Vivo:** In a living body.

**Joint:** The location at which two bones come into contact, allowing for relative motion.

**Lateral:** A position away from the midline of the body.

**Ligament:** Fibrous tissue connecting a bone to another bone.

**Lower Leg:** The section of the leg spanning between the ankle and the knee.

**Lunate:** A bone of the wrist that articulates with the radius and scaphoid bones.

**Malleolus:** Bony prominences located on each side of the ankle.

**Marrow:** The flexible tissue that fills interior bone cavities.

**Medial:** A position closer to the midline of the body.

**Metatarsals:** The five major bones of the forefoot directly anterior to the midfoot bones.

**Midfoot:** The arch of the foot, composed of the navicular, cuboid and the cuneiforms.

**Navicular:** A boat-shaped tarsal bone on the medial side of the foot, anterior to the talus.

**Neutral Foot Posture:** Having the plantar aspect of the foot completely on the transverse plane, with the shank perpendicular to this plane, and a line drawn from the back of the heel to the space between the first and second toes parallel to the sagittal plane.

**Osteon:** A cylindrical structure of which cortical bone is formed.

**Phalanges:** The digital bones of the forefoot attached to the heads of the metatarsals.

**Pilon:** Distal tibial articular surface forming the joint with the talus.

**Plantar:** Towards the bottom or sole of the foot.

**Plantarflexion:** Pointing the toes downward.

**Plateau:** A flat surface located within a joint.

**Posterior:** Situated in the back of the body.

**Proximal:** Situated nearer to the center of the body or the point of attachment.

**Radius:** One of the large bones of the forearm extending from the lateral elbow to the thumb side of the wrist.

**Sagittal:** The plane parallel to the long axis of the body that divides the body into right and left halves.

**Scaphoid:** A bone of the wrist that articulates with the radius below the thumb.

**Shank:** The part of the leg from the knee to the ankle.

**Superior:** Situated above, or closer to the head.

**Talo-calcaneal joint:** The joint between the talus and the calcaneus.

**Talo-crural joint:** The joint between the talus and the tibia/fibula.

**Talo-navicular joint:** The joint between the talus and the navicular.

**Talus:** Bone of the hindfoot that articulates with the tibia/fibula, navicular and calcaneus.

**Tarsal:** Bone of the foot.

**Tendon:** Fibrous tissue connecting a bone to a muscle.

**Tibia:** The larger bone of the lower leg on the medial side between the knee and ankle.

**Tibio-fibular joint:** Two joints located proximally and distally that connect the tibia and the fibula.

**Trabecular:** See cancellous bone.

**Transverse:** The plane perpendicular to the long axis of the body that divides the body into superior and inferior sections.

**Vascularization:** Supply of blood vessels.

**Ventral:** The front of an organism.

---

## **APPENDIX B – Estimated Radii of Curvature**

---

**Table B.1: Estimated Radii of Curvature at the Strain Gauge Locations**

The nodes closest to the gauge locations were selected on the FE models of the talus and calcaneus. The radius of curvature at each gauge location was estimated by fitting a 3D circle to the strain gauge node and one node before and after in the upwards, downwards, and diagonal directions. The radius of the smallest circle that was generated at each gauge location is presented. The original plantar calcaneus gauge location reports the smallest radius of curvature at the location where this gauge was intended to be placed, located slightly laterally to the actual gauge location.

<b>Gauge Location</b>	<b>Smallest Radius of Curvature (mm)</b>
<b>Tibia</b>	11.0
<b>Fibula</b>	15.9
<b>Lateral Calcaneus</b>	41.4
<b>Medial Calcaneus</b>	20.9
<b>Plantar Calcaneus</b>	6.5
<b>Original Plantar Calcaneus</b>	12.9
<b>Lateral Talus</b>	14.6
<b>Medial Talus</b>	11.1

---

## **APPENDIX C – Strain Gauge Attachment Protocol**

---

Gauges were fixed to the specimen using the following protocol (Quenneville, 2009):

1. The area of interest was sanded and wiped down with alcohol. Since the locations where the gauges were placed were in a moist environment, this process was repeated several times until the area was completely dry.
2. A layer of cyanoacrylate was pressed against the area of interest with a piece of tape and was allowed to dry. This created a flat, smooth and dry surface.
3. The tape was peeled away, the surface was lightly sanded and the area was wiped with alcohol again.
4. The strain gauge was placed on a clean surface and another piece of tape was applied to the top. Cyanoacrylate was applied to the backing of the strain gauge and the surface of the bone and allowed to dry for 1 minute.
5. The appropriate gauge in the rosette was aligned with the laser line and a small amount of cyanoacrylate was applied to the bone at the site of attachment. The gauge was pressed down onto the site with even pressure for 2 minutes.
6. The gauge was allowed to sit for 5 minutes and the tape was removed.
7. More cyanoacrylate was applied to the top surface of the strain gauge, a CT-sensitive 1/8” acrylic ball was placed on top of the gauge and the glue was allowed to dry.

### **References**

- QUENNEVILLE, C. E. 2009. *Experimental and Numerical Assessments of Injury Criteria for Short-Duration High-Force Impact Loading of the Tibia*. PhD, University of Western Ontario.

---

## APPENDIX D – Technical Drawings for Test Frame

---

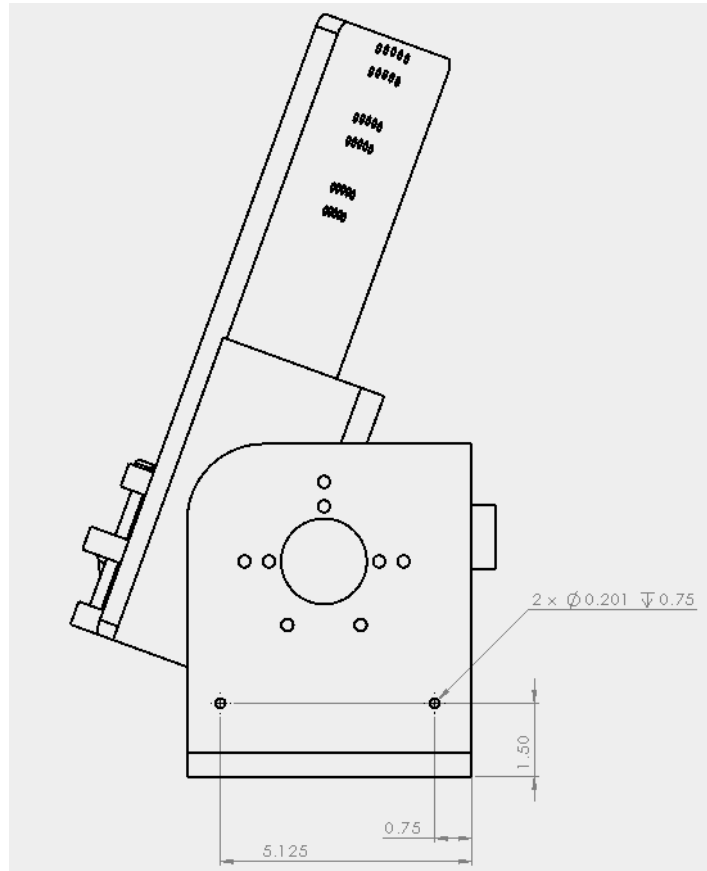


**Figure D.1: Dimensioned Drawing of Ankle Positioner Modifications**  
All dimensions in inches, made of acrylic.

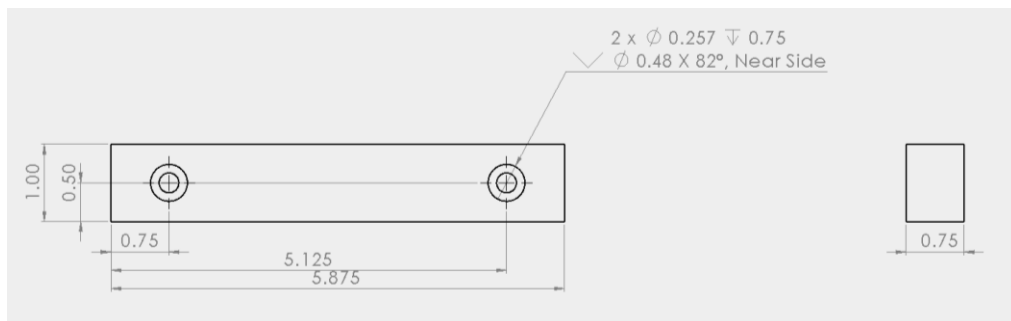


**Figure D.2: Dimensioned Drawing of Ankle Positioner Bottom Rail**  
All dimensions in inches, made of acrylic.

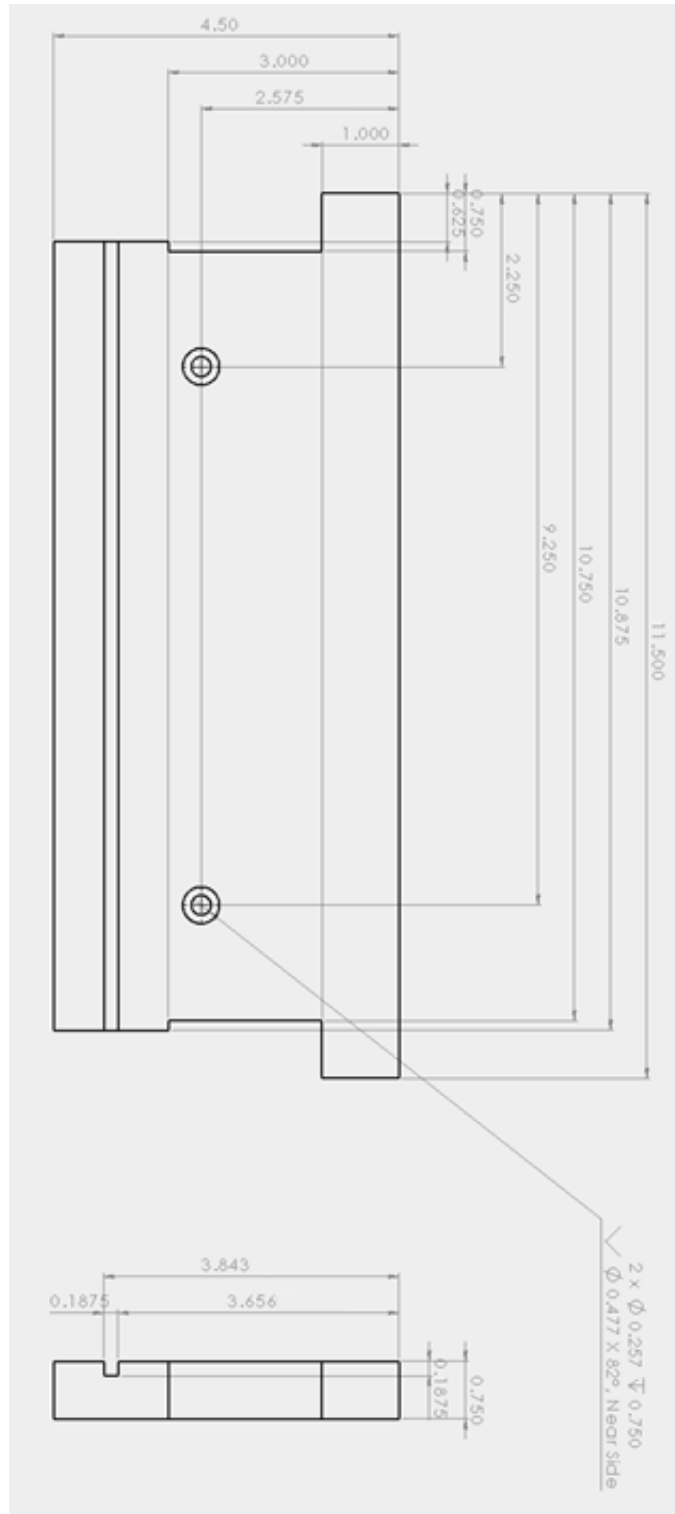


**Figure D.3: Dimensioned Drawing of Ankle Positioner Top Rail Piece**  
All dimensions in inches, made of acrylic.

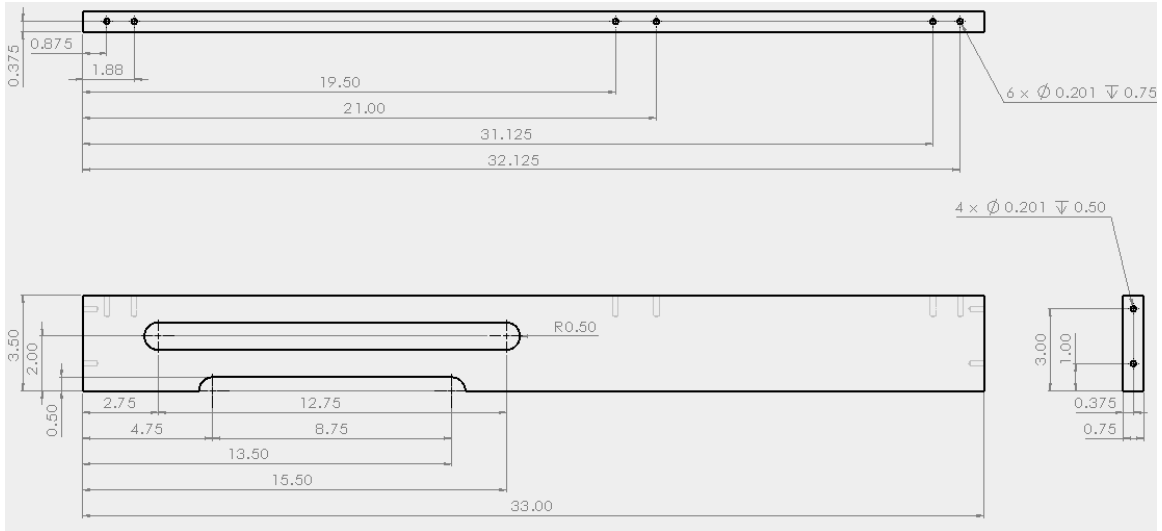


**Figure D.4: Dimensioned Drawing of Test Frame Bottom Struts**  
All dimensions in inches, made of acrylic.

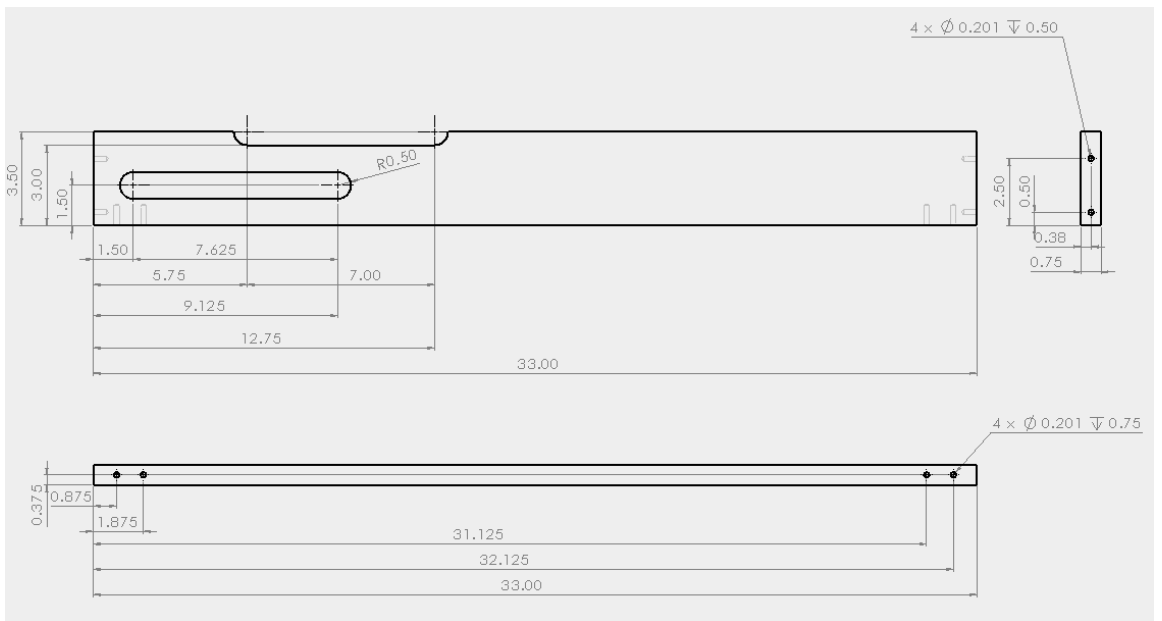


**Figure D.5: Dimensioned Drawing of Test Frame Top Struts**  
All dimensions in inches, made of acrylic.

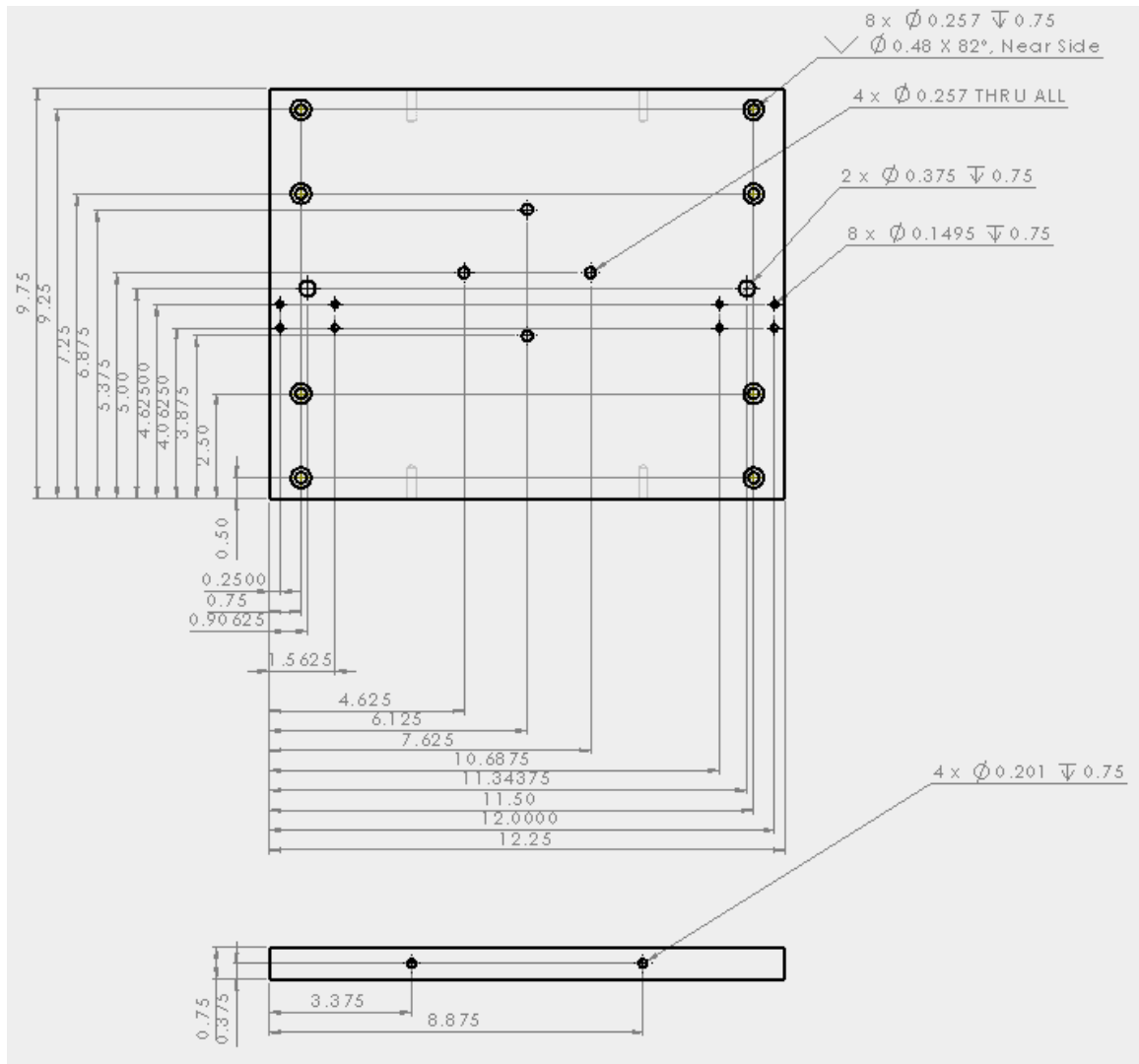


**Figure D.6: Dimensioned Drawing of Test Frame Front End Plate**

All dimensions in inches, made of acrylic.

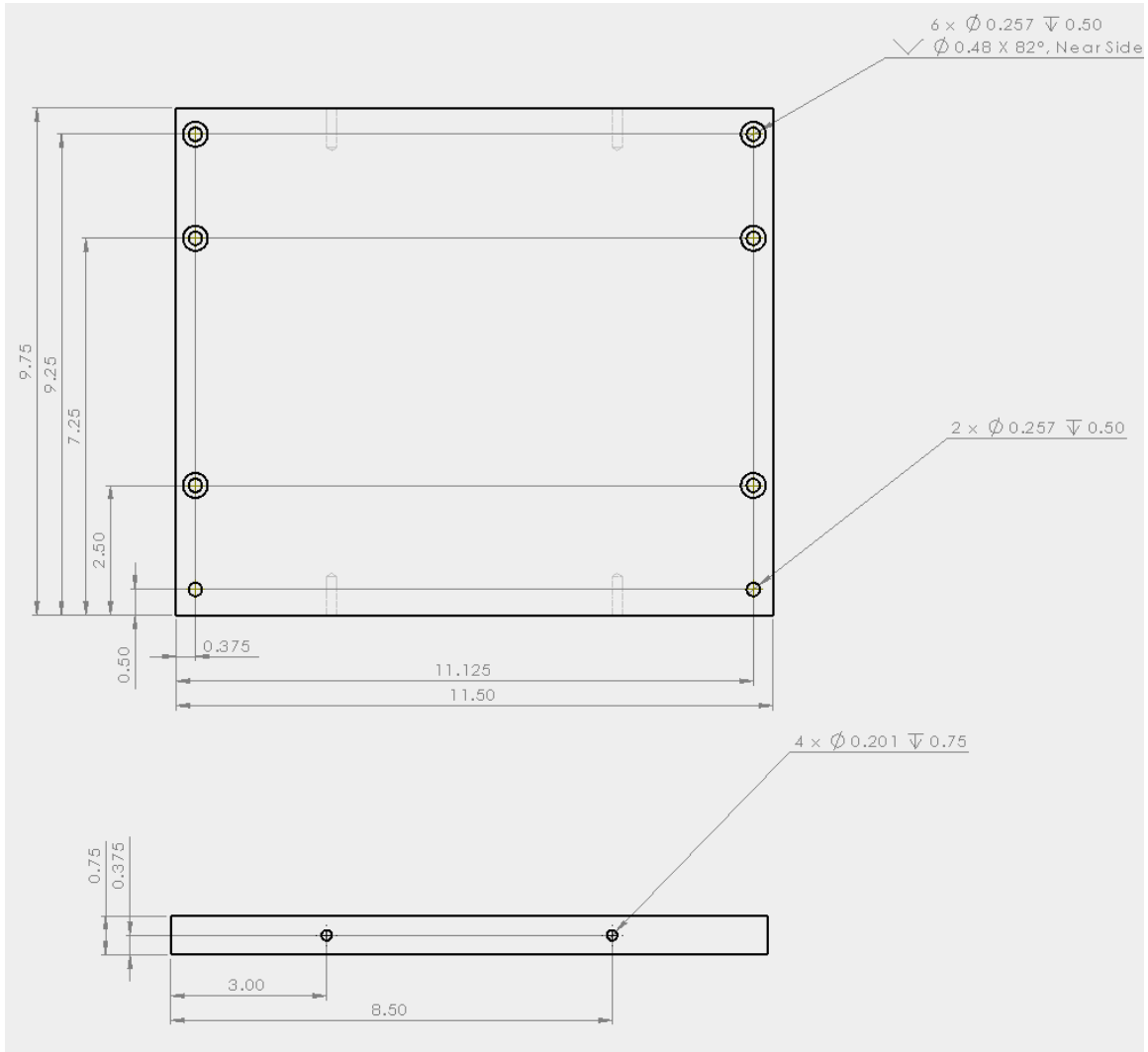


**Figure D.7: Dimensioned Drawing of Test Frame Back End Plate**  
All dimensions in inches, made of acrylic.

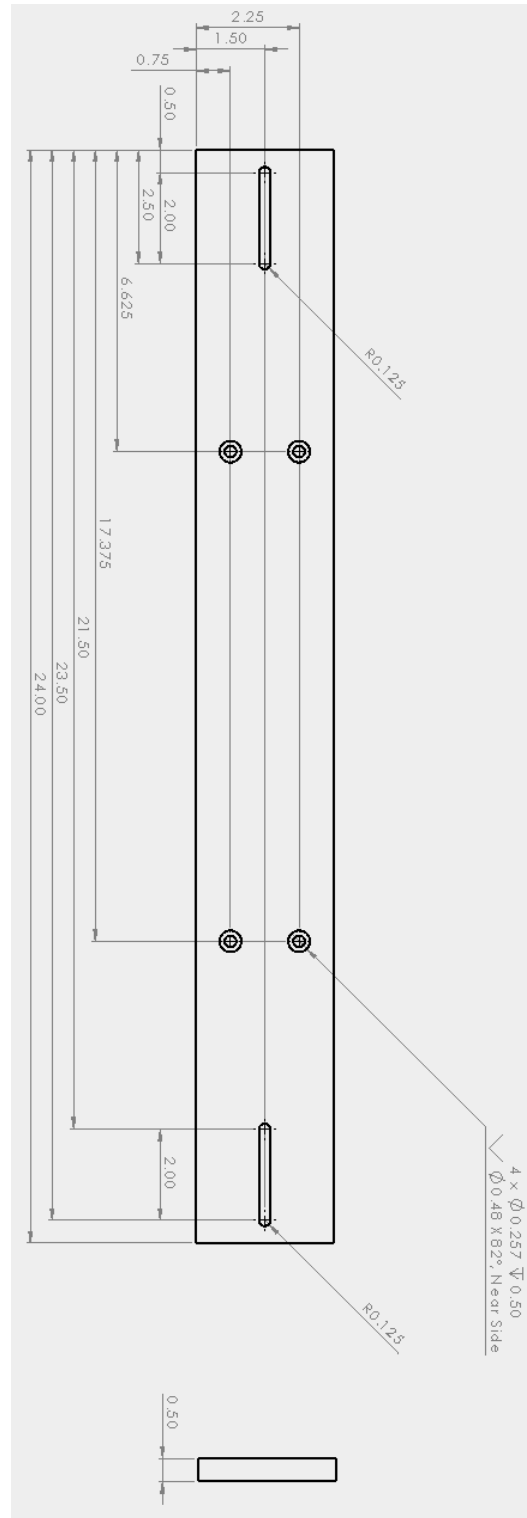


**Figure D.8: Dimensioned Drawing of Test Frame Slotting Wing**  
All dimensions in inches, made of acrylic.

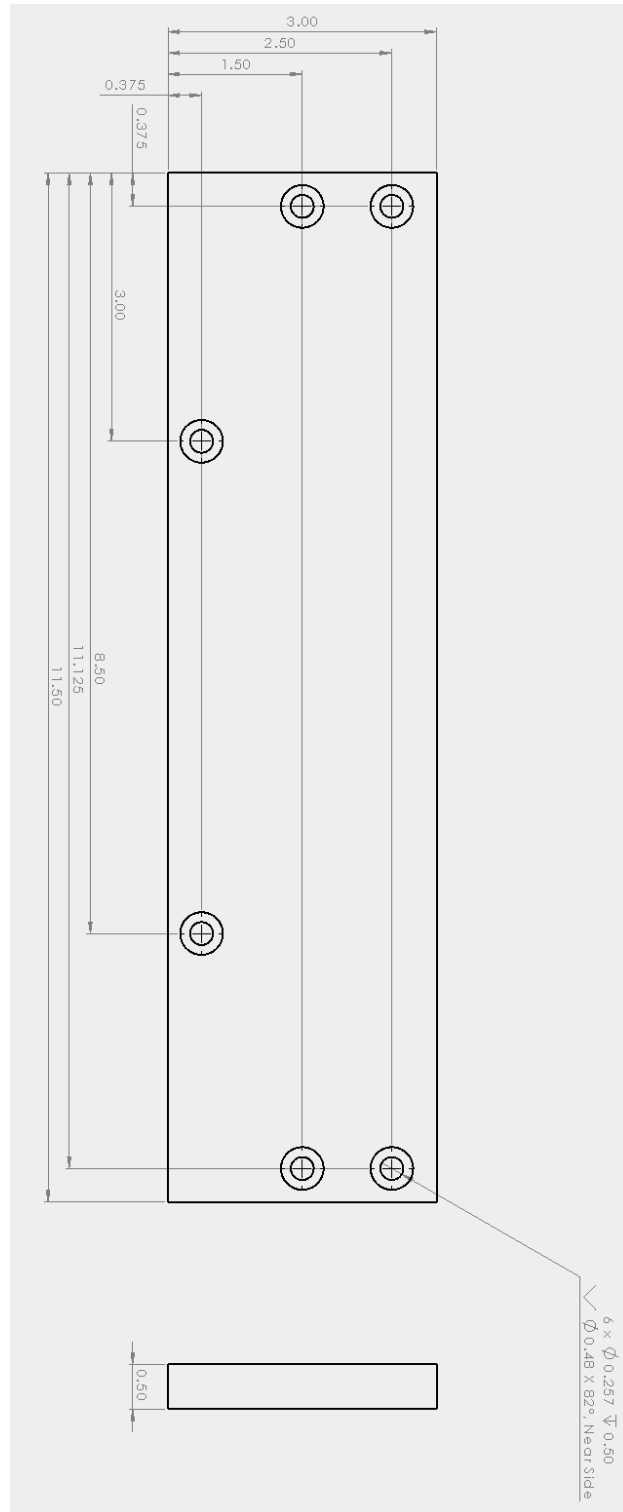


**Figure D.9: Dimensioned Drawing of Test Frame Cross Members**  
All dimensions in inches, made of acrylic.

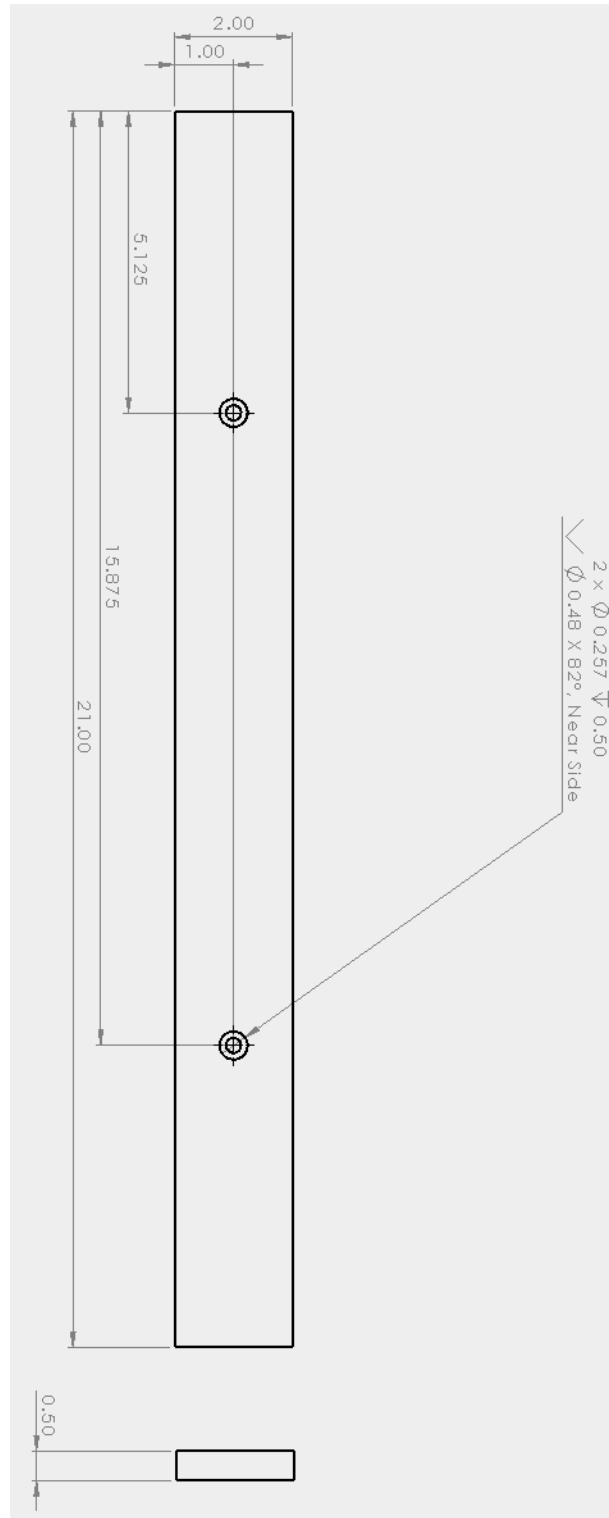


**Figure D.10: Dimensioned Drawing of Test Frame Clamping Bar**  
All dimensions in inches, made of aluminium.

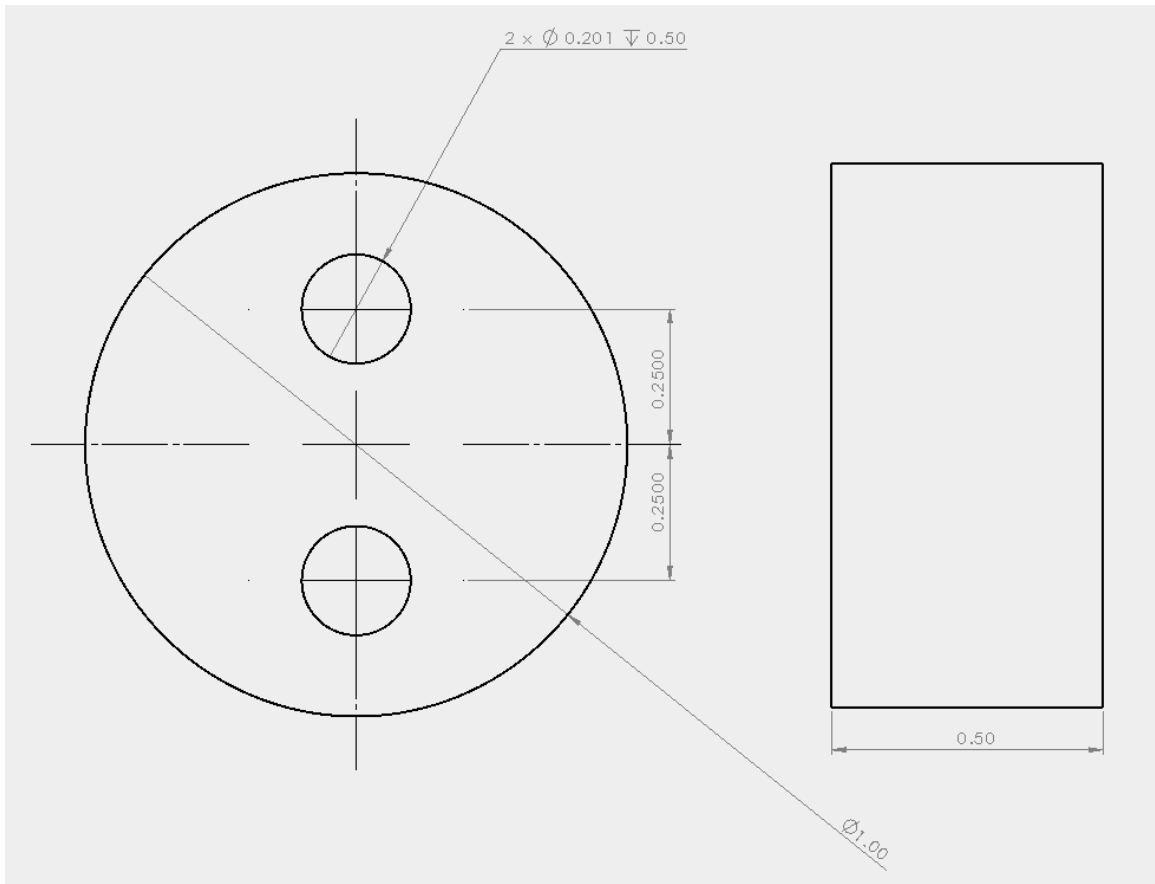


**Figure D.11: Dimensioned Drawing of Test Frame Pegs**  
All dimensions in inches, made of acrylic.

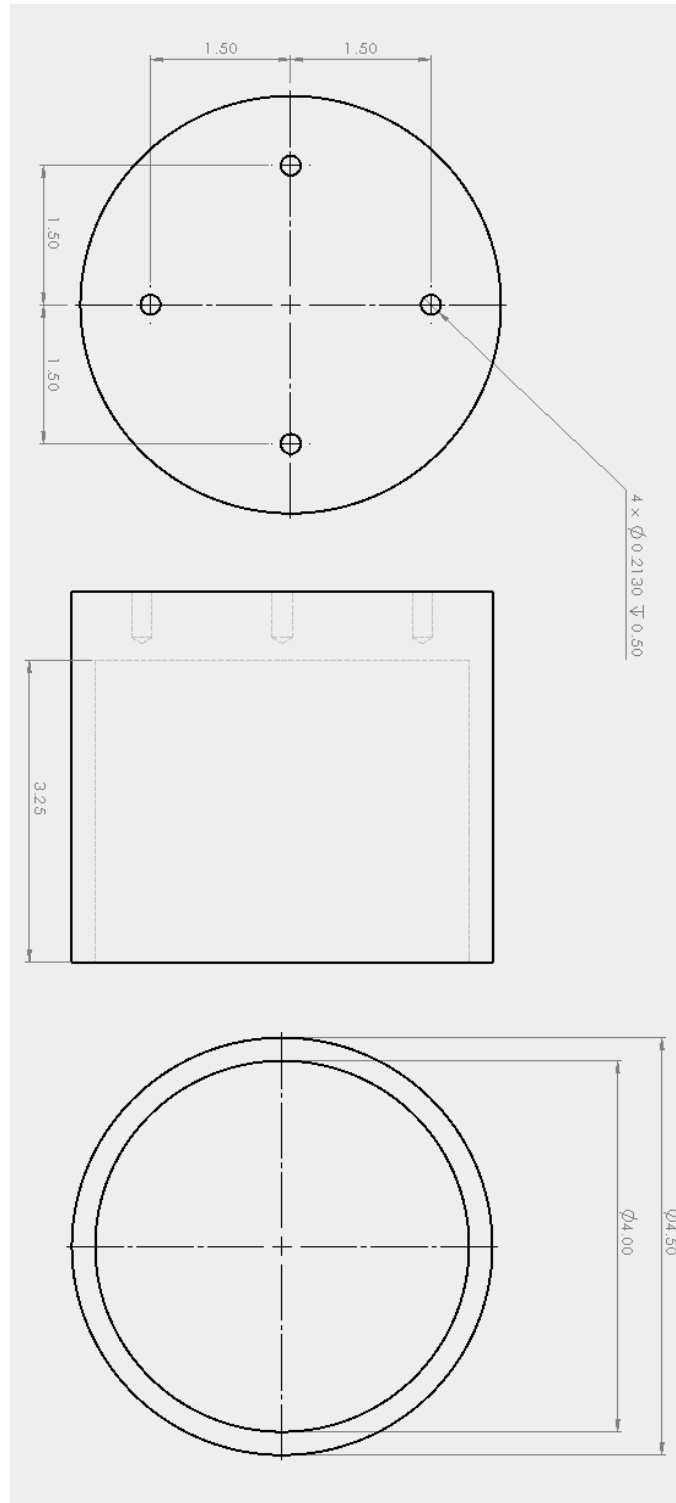


**Figure D.12: Dimensioned Drawing of Test Frame Potting Fixture**  
All dimensions in inches, made of aluminium.

## APPENDIX E – Full Strain Table

**Table E.1: Principal Strains and Direction of Principal Strain**

1<sup>st</sup> and 2<sup>nd</sup> principal strains ( $\mu\epsilon$ ) and the angle of the 1<sup>st</sup> principal strain ( $^\circ$ ) are presented. Neut, INV-ER, EV-ER, PF and DF-INV denote neutral, inversion-external rotation, eversion-external rotation, plantarflexion and dorsiflexion-inversion, respectively.

	1st	2nd	Angle	1st	2nd	Angle	1st	2nd	Angle
	<b>Tibia</b>			<b>Fibula</b>			<b>Plantar Calcaneus</b>		
<b>Neut 1</b>	10	-5	49	115	-64	-29	152	-166	25
<b>Neut 2</b>	117	-105	60	239	-141	-35	141	-145	29
<b>Neut 3</b>	69	-79	58	253	-149	-34	129	-231	13
<b>Neut 4</b>	36	-37	57	248	-144	-32	41	-225	-3
<b>INV-ER</b>	105	-113	60	4	-12	-50	345	-315	34
<b>EV-ER</b>	44	-39	19	53	-42	-12	78	-36	-59
<b>DF-INV</b>	46	-15	-27	79	-86	61	389	-156	40
<b>PF</b>	17	-17	57	186	-117	-44	175	-228	3
<b>Post-Neut</b>	16	-2	73	216	-134	-27	110	-108	25
	<b>Medial Calcaneus</b>			<b>Lateral Calcaneus</b>					
<b>Neut 1</b>	95	-178	53	229	-241	-68			
<b>Neut 2</b>	18	-73	-80	245	-312	-65			
<b>Neut 3</b>	15	-67	63	217	-298	-61			
<b>Neut 4</b>	55	-95	48	190	-274	-57			
<b>INV-ER</b>	165	-485	56	133	2	48			
<b>EV-ER</b>	89	-135	54	247	-317	-60			
<b>DF-INV</b>	224	-396	54	115	-57	-65			
<b>PF</b>	107	-154	83	236	-260	-80			
<b>Post-Neut</b>	64	-169	60	268	-280	-71			
	<b>Medial Talar Neck</b>			<b>Talar Sulcus</b>					
<b>Neut 1</b>	213	-357	86	164	-56	30			
<b>Neut 2</b>	210	-314	-89	260	-66	47			
<b>Neut 3</b>	236	-350	-89	263	-71	43			
<b>Neut 4</b>	204	-309	88	257	-64	39			
<b>INV-ER</b>	27	-51	43	1	-19	-41			
<b>EV-ER</b>	242	-401	61	313	-5	64			
<b>DF-INV</b>	45	-68	-85	171	-187	13			
<b>PF</b>	237	-232	-75	163	-81	52			
<b>Post-Neut</b>	284	-467	88	276	-127	28			

## APPENDIX F – Full Euler Angle and Displacement Tables

**Table F.1: Experimental Euler Angles and Displacements of the Talus and Calcaneus**

The complete list of Euler angles and displacements of the calcaneus and talus in each tested posture are provided. INV-ER, EV-ER, PF and DF-INV denote inversion-external rotation, eversion-external rotation, plantarflexion and dorsiflexion-inversion, respectively. The z, y and x Euler angles are about the axes most closely aligned with the dorsiflexion/plantarflexion, inversion/eversion and internal/external rotation directions, respectively. Positive rotation about z, y and x indicate plantarflexion, eversion and external rotation.

<b>CALCANEUS</b>							
<b>Posture</b>	<b>Euler Angles (°)</b>			<b>Displacement (mm)</b>			
	<b>Z</b>	<b>Y</b>	<b>X</b>	<b>X</b>	<b>Y</b>	<b>Z</b>	<b>Total</b>
<b>INV-ER</b>	0.2	-11	3.1	-0.4	0.4	-10.1	10.1
<b>EV-ER</b>	0.7	6.7	9.8	-0.7	1.4	0.4	1.6
<b>PF</b>	20	-4.1	-3.8	17.8	-16.6	-0.5	24.3
<b>DF-INV</b>	-14.5	-10.3	-0.8	-9.8	17.3	-9.3	21.9
<b>TALUS</b>							
<b>Posture</b>	<b>Euler Angles (°)</b>			<b>Displacement (mm)</b>			
	<b>Z</b>	<b>Y</b>	<b>X</b>	<b>X</b>	<b>Y</b>	<b>Z</b>	<b>Total</b>
<b>INV-ER</b>	-5.2	0.3	8.7	-1.5	1.0	-4.2	4.6
<b>EV-ER</b>	1	-0.7	3.2	0.8	0.8	-1.2	1.7
<b>PF</b>	20.8	-9.7	1.6	9.6	1.9	0.9	9.9
<b>DF-INV</b>	-21.4	7.7	3.8	-9.4	2.4	-3.9	10.5

**Note:** some of the displacement results presented here are smaller than the resolution of the CT scanner, and this is due to the transforms that were applied to normalize all coordinate systems to the neutral tibiofibular coordinate system.

---

## **APPENDIX G – Previously-Validated Tibia Mesh Evaluation**

---

### **DISTAL EPIPHYSIS**

**Jacobian:** 0.11 – 9.11 with a mean of 1.5. Six elements with a Jacobian less than 0.15.

**Angular Deviation:**  $-79^{\circ}$  to  $86^{\circ}$  with a mean of  $0^{\circ}$ . Eighteen elements with deviations between  $80^{\circ}$  and  $90^{\circ}$ .

**Aspect Ratio:** 1.1 – 14.3 with a mean of 3. Five elements with aspect ratios of 10.

### **DIAPHYSIS**

**Jacobian:** 0.29 – 15.36 with a mean of 3. One element with a Jacobian less than 0.3.

**Angular Deviation:**  $-68^{\circ}$  to  $70^{\circ}$  with a mean of  $0^{\circ}$ .

**Aspect Ratio:** 1.1 – 23.1 with a mean of 6. Ratios greater than 20 were only present in a small number of elements at the center of the diaphysis.

**Total Number of elements:** 320120